Mechanisms and Machine Science 44

Jaroslav Beran
Martin Bílek
Petr Žabka *Editors*

Advances in Mechanism Design II

Proceedings of the XII International Conference on the Theory of Machines and Mechanisms

Springer

Mechanisms and Machine Science

Volume 44

Series editor

Marco Ceccarelli
LARM: Laboratory of Robotics and Mechatronics
DICeM: University of Cassino and South Latium
Via Di Biasio 43, 03043 Cassino (Fr), Italy
e-mail: ceccarelli@unicas.it

More information about this series at http://www.springer.com/series/8779

Jaroslav Beran · Martin Bílek
Petr Žabka
Editors

Advances in Mechanism Design II

Proceedings of the XII International Conference on the Theory of Machines and Mechanisms

Springer

Editors
Jaroslav Beran
Textile Machine Design Department
Technical University of Liberec
Liberec
Czech Republic

Petr Žabka
Faculty of Mechanical Engineering
Technical University of Liberec
Liberec
Czech Republic

Martin Bílek
Textile Machine Design Department
Technical University of Liberec
Liberec
Czech Republic

ISSN 2211-0984 ISSN 2211-0992 (electronic)
Mechanisms and Machine Science
ISBN 978-3-319-44086-6 ISBN 978-3-319-44087-3 (eBook)
DOI 10.1007/978-3-319-44087-3

Library of Congress Control Number: 2016947391

Printed on acid-free paper

This Springer imprint is published by Springer Nature
The registered company is Springer International Publishing AG Switzerland

Preface

The international conference on the theory of machines and mechanisms has been held since 1973 in regular four-year intervals. The expert agenda of the conference focuses on a wide range of problems including theoretical and practical findings related to theories pertaining to machines and mechanisms. A person involved in the creation of this conference was important personality and leading expert in mechanics and mechanism theories doc. Ing. Jaroslav Charvát, CSc. He was not only a renowned expert regarding mechanism theories, but he was also an excellent teacher and promoter of mechanics for the professional and lay public. He impressed students with his lectures and boosted their enthusiasm for the study field. His scientific and research activities were focused to a great extent on mechanisms of textile machines. He has regularly contributed to expert magazines. He is the author of many monographs and scripts, and he has actively attended conferences and seminars. He has been responsible to a significant extent for the development of young technical intelligence and has contributed to the development of the field of textile machine mechanics.

The 12th international conference on the theory of machines and mechanisms was held from September 6–8, 2016, at the Liberec Technical University, Liberec, Czech Republic. The conference was organized under the auspices of the Czech National Committee for Theories of Machines and Mechanisms IFToMM, the Czech Society for Mechanics and VUTS a.s. Liberec. The lectures focused particularly on the areas of analysis, synthesis of articulated, cam, planar and spatial mechanisms.

A major part included a focus on problems related to the dynamics of machines and mechanisms as well as mechatronics and biomechanical systems. Robotic systems were another major focus on the conference.

During the conference, the Meeting of the Technical Committee for Linkages and Mechanical Controls of IFToMM and the Meeting of the Czech Society for Mechanics took place.

In this book, contributions from the conference have been included into six main parts.

- General Theory of Machines and Mechanisms, Analysis and Synthesis of Planar and Spatial Mechanisms, Linkages and Cams, Robots and Manipulators
- Dynamics of Machines and Mechanisms, Rotor Dynamics
- Computational Mechanics
- Vibration and Noise in Machines
- Optimization of Mechanisms and Machines, Mechanisms of Textile Machines
- Mechatronics, Control and Monitoring Systems of Machines

As it has for more than 48 years, this volume of proceedings offers both a broad perspective on the state of the art in the field and an in-depth look at its leading edge research. It is our privilege to be able to offer this collection and we express our sincere thanks to the contributing authors for making this series a continuing success.

We appreciate the interest in this conference and believe it will bring many suggestions for further extension of knowledge in the field of machines and mechanisms theory and will provide new ideas for international cooperation in this field.

Liberec, Czech Republic Jaroslav Beran

Scientific Committee

J. Beran—Chairman (CZ)
M. Bílek—Secretary (CZ)
V. Arakelyan (FR)
M. Ceccarelli (IT)
B. Corves (DE)
J.C. Garcia-Prada (ES)
A. Gronowicz (PL)
J. Horáček (CZ)
T. Leinonen (FI)
M. Lima (PT)
E.CH. Lovasz (RO)
K.H. Modler (DE)
V. Natarajan (IN)
L. Pešek (CZ)
Š. Segľa (SK)
J. Stadnicki (PL)
I. Tempea (RO)
H. Terada (JP)
D. Tesar (US)
M. Václavík (CZ)
J. Vimmr (CZ)
J. Zapoměl (CZ)
V. Zeman (CZ)

The conference is organized under the patronage of:

Technical University of Liberec
Studentská 1402/2
461 17 Liberec 1
Czech Republic
http://www.tul.cz

Czech Society of Mechanics
Dolejškova 5
182 00 Praha 8
Czech Republic
http://www.csm.cz

IFToMM
International Federation for the Promotion of Mechanism and Machine Science
http://www.iftomm.org
Czech National Commitee of IFToMM
Institute of Thermomechanics AS CR, v. v. i.
Dolejškova 5
182 00 Praha 8
Czech Republic
http://www.it.cas.cz/IFToMM-TC-NO/

VÚTS, a.s.
Svárovská 619
460 01 Liberec 11
Czech Republic
http://www.vuts.cz

Contents

Part I
General Theory of Machines and Mechanisms, Analysis and Synthesis of Planar and Spatial Mechanisms, Linkages and Cams, Robots and Manipulators

IFToMM in MMS Developments

Marco Ceccarelli

Abstract The paper presents IFToMM and its activity as influential in Mechanism and Machine Science (MMS) and its future developments. IFToMM is the international federation of a worldwide community working in MMS with achievements in research, formation, practice and technological transfer. The role of IFToMM is discussed as influential not only in aggregating people with commonly shared activities but also in leading international collaboration for innovative trends in MMS.

Keywords Mechanism and machine science · IFToMM · Trends in MMS

1 Introduction

Two main facts can be highlighted in order to claim that MMS (Mechanism and Machine Science) is still necessary with a strong activity in formation, research, and practice, namely they are:

- Human beings operate and interact with their environments and using many systems with actions of mechanical nature so that mechanical systems will always be an essential part of systems that assist or substitute human beings in their actions and other tasks.
- There is a continuous need to update problems and solutions in Technology since Society continuously evolves with new and updated needs and requirements so that even mechanical systems are expected to be updated for new and/or updated functioning through a continuous evolution and update of knowledge, means, and operation for the successful applications of mechanical systems.

(IFToMM President 2016–2019)

M. Ceccarelli (✉)
University of Cassino and South Latium, Cassino, Italy
e-mail: ceccarelli@unicas.it

J. Beran et al. (eds.), *Advances in Mechanism Design II*,
Mechanisms and Machine Science 44, DOI 10.1007/978-3-319-44087-3_1

MMS can be understood as an evolution of TMM with a broader content and vision of a Science, including disciplines with synergy and integration purposes. The modernity of MMS has augmented TMM with new vision and means but also with many new disciplines, of which the most significant can be recognized in Robotics; Mechatronics; Computational Kinematics; Computer Graphics; Computer Simulation; CAD/CAM for TMM; Tribology; Multibody Dynamics, Medical Devices, Micro and Nano Machines, Energy Sustainable Systems, and Service Systems. In 2000 the evolution of the name from TMM to MMS brought also a change in the denomination of the IFToMM Federation from "IFToMM: the International Federation for TMM" to "IFToMM, the International Federation for the Promotion of MMS" [1].

Aggregation of people in communities is a need and motivation for the success of activity with common features and purposes. IFToMM as international federation of national/territory communities is the world aggregation of people working in MMS with a common vision that collaboration and activity share are helpful not only to achieve better results but to disseminate efficiently the achievements for a successful improvement of a peaceful society.

In this paper, a significant role of IFToMM is presented in MMS activities within technological achievements by using historical outlines and general considerations that are also based on the author's experience [2–5].

2 MMS and Its Future Developments

The meaning of MMS can be clarified by looking at IFToMM terminology with the terms [6]:

- Mechanism and Machine Science: Branch of science, which deals with the theory and practice of the geometry, motion, dynamics, and control of machines, mechanisms, and elements and systems thereof, together with their application in industry and other contexts, e.g. in Biomechanics and the environment. Related processes, such as the conversion and transfer of energy and information, also pertain to this field.
- Machine: mechanical system that performs a specific task, such as the forming of material, and the transference and transformation of motion and force.
- Mechanism: system of bodies designed to convert motions of, and forces on, one or several bodies into constrained motions of, and forces on, other bodies.

Today, a modern machine is understood as a combination of systems of different natures and this integration has led to the modern concept of Mechatronics, Fig. 1. Thus, most of the recent advances in machinery are sometimes considered to be in fields other than MMS. But Mechanism Design can still be recognized as a fundamental aspect for developing successful systems that operate in the mechanical world of human beings.

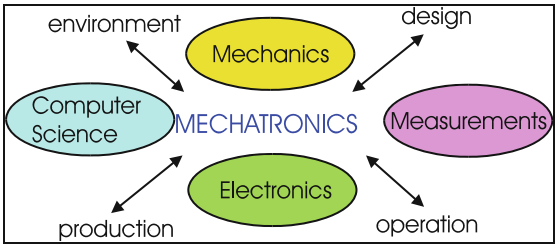

Fig. 1 A scheme for the mechatronic structure of modern (mechanical) systems

Future developments in MMS can be summarized with trends and challenges mainly in:

- 3D Kinematics
- Modeling and mathematization for MMS
- Multi-d.o.f. multibody systems
- Spatial mechanisms and manipulators
- Unconventional mechanisms
- Scaled mechanisms
- System design with multidisciplinary integration
- Bio-mechanical/mimetic systems
- Tribology issues
- Creative design
- Human-machine interactions for user/task-oriented systems
- Reconsideration and reformulation of theories and mechanism solutions.

Those topics and many others in MMS are also motivated by needs for formation and activity of professionals, who will be able to conceive and transmit innovation both into production, service frames and diary life.

Formation in MMS requires attention to modern methodologies that can efficiently use computer and software means, which are still evolving rapidly. Thus, there is a need to update also the teaching means that makes use of simulations and computer oriented formulation. In addition, mechatronic layout of modern mechanical systems suggests that mechanisms should be taught as integrated with other components like actuators and sensors since the beginning of the formation.

The mission of academy needs to be revitalized and better understood as a result of high expertise of teachers that can be reached also with intense research activity and links to the professional and industrial world. This requires more attention and vision not only from the academy but mainly from the society as a whole that through governing leaders should give more and more support to the formation system and research institutions.

Activity by professionals asks for novel applications and high performance machines since they are continually needed in evolving/updating systems and engineering tasks. In addition, there is a need to make understandable new methodologies to professionals for practical implementation both in their use and results.

In general, MMS activity will be directed for further developments by searching for:

- information and understanding of the functionality and impact of systems
- algorithms for design, operation, and evaluation of systems with user/task-oriented performance
- performance evaluation and economic merit of systems as constrained by environmental limits
- transfer of innovation
- human-machine interfaces and interactions.

Thus, mechanical aspects will have a significant role in modern systems mainly referring to:

– Human-machine interactions and user/task-oriented performance
– Mechanical tasks in motion operations
– Structure design for sizing dimensions.

Therefore, 'hot' topics of MMS can be considered:

- to analyze and to investigate operation and performance of modern (mechatronic) systems
- to analyze and to investigate the actions against the environment and within the mechatronic system.
- to focus on safety and comfort issues both for the system and for the human operators
- to consider the interactions mainly from mechanical viewpoints
- to size system actions according to task/user oriented requirements
- to consider complex motions such as spatial movement at high acceleration in novel environments
- to look at integrated systems via suitable modeling of components of other aspects than of a mechanical nature.

Trends in system composition can be summarized as in the examples in Table 1. In the future more than today, the presence of mechanical components will be reduced percentage-wise but nevertheless they will still be necessary and indeed be fundamental for the use and operation of systems.

An important area demanding new system designs can be recognized for service operations that can be understood in terms of set of actions and behaviors towards achieving a service task [2, 3]. Those service actions and tasks can be much more articulated and varied than traditional industrial applications.

Table 1 Examples of evolution of system composition

1960–2010	Mechanics (%)	Electronics/informatics (%)
Cars	90–50	10–50
Calculators	100–10	0–90
Cameras	100–10	0–90

A service task can be understood as the ultimate goal of the design and operation of a service machine, that can be conceived not only as a robot. A service task may be identified with well defined properties and by a large variety of situations. The multi-disciplinary for a service system is much wider than in any other engineering fields, since it includes technical aspects, human attitudes (of operators and/or users), human-machine interactions, and environment issues. Indeed, in developing and operating service robots, other than technical expertise, it is more and more necessary that competences from other fields of human life and environmental considerations be incorporated.

Referring to technical aspects, Fig. 2 summarizes the multi-disciplinary in terms of interactions with the environment and human beings, and in terms of a careful consideration of the environment. Those interactions should be understood not only in terms of engineering issues (mainly mechanical ones) but by looking at more general aspects, such as for example psychological attitudes and social impacts.

In particular, the main flow of technical design activity is indicated in the central streamline as referring to data identification in both technical and non-technical aspects, considerations of technical constraints/issues, analysis of service operation and goal, design activity and system programming, with final checks by operators and users. The core character on technical design activity is indicated by aspects and activities that are grouped in the two lateral blocks concerning with interactions with human beings and the environment, respectively. Each block will refer to aspects that even with non-technical concerns must be included in the machine development with proper models and problem formulation.

All the above considerations can be considered as attaining also to the process of building and transferring innovation, which will be understood not only as a technical advance but more widely as an enhancement of the quality of life in all its aspects with the help and support of technical means.

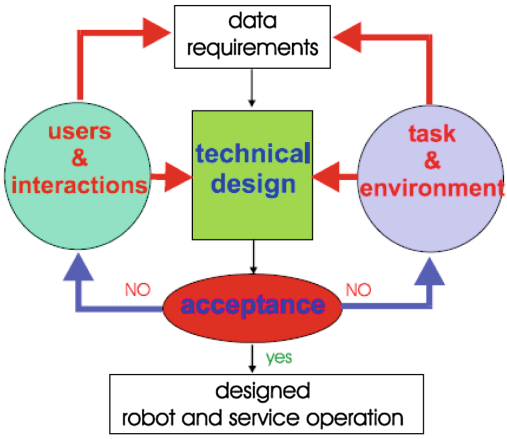

Fig. 2 A general flowchart with new peculiarities for designing and operating service systems

3 IFToMM and Its Role in MMS

The names of IFToMM and MMS are related to fields of Mechanical Engineering concerning with mechanisms in a broad sense.

The developments in TMM have stimulated cooperation around the world at various levels. One of the most relevant results has been the foundation of IFToMM in 1969, Fig. 3. IFToMM was founded as a Federation of territorial organizations but as based on the activity of individuals within a family frame with the aim to facilitate co-operation and exchange of opinions and research results in all the fields of TMM. Many individuals have contributed and still contribute to the success of IFToMM and related activity, (see IFToMM webpage: www.iftomm.org) under a coordination of IFToMM Presidents over time [5].

The foundation of IFToMM was the result of an intense activity for stimulating and promoting international collaboration, more than what had been done previously. The process started in the late 1950s', as documented by several letters that are stored in the IFToMM Archive at CISM in Udine, Italy. A first World Congress on TMM (Theory of Mechanisms and Machines) was held in 1965 in Varna,

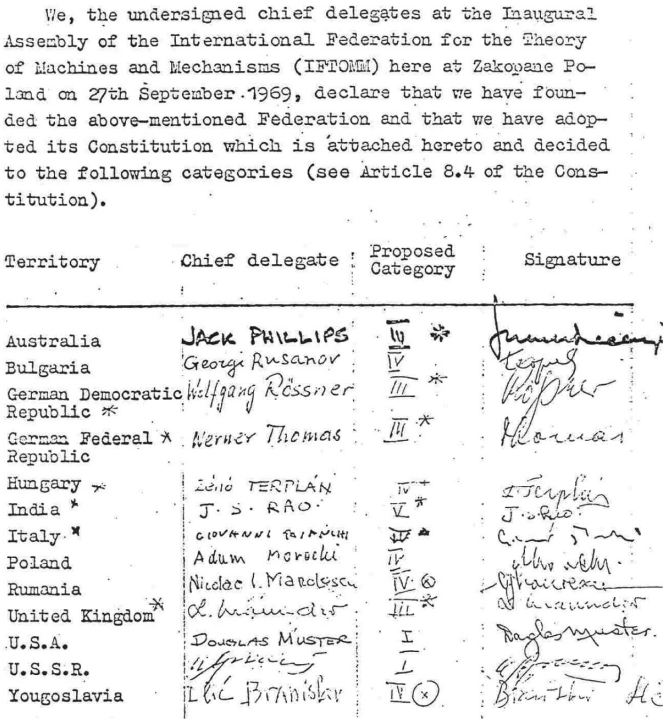

We, the undersigned chief delegates at the Inaugural Assembly of the International Federation for the Theory of Machines and Mechanisms (IFTOMM) here at Zakopane Poland on 27th September 1969, declare that we have founded the above-mentioned Federation and that we have adopted its Constitution which is attached hereto and decided to the following categories (see Article 8.4 of the Constitution).

Territory	Chief delegate	Proposed Category	Signature
Australia	JACK PHILLIPS	III *	
Bulgaria	Georgi Rusanov	IV	
German Democratic Republic *	Wolfgang Rössner	III *	
German Federal Republic *	Werner Thomas	III *	
Hungary *	Zénó TERPLÁN	IV *	
India *	J. S. RAO	V *	
Italy *	GIOVANNI PAPPALARDO	IV *	
Poland	Adam Morecki	IV	
Rumania	Nicolae I. Mandescu	IV ⊗	
United Kingdom *	[illegible]	III *	
U.S.A.	DOUGLAS MUSTER	I	
U.S.S.R.	[illegible]	I	
Yougoslavia	Ilić Branislav	IV (×)	

Fig. 3 The foundation act of IFToMM, the International Federation for the Theory of Machines and Mechanisms, in Zakopane (Poland) on 27 September 1969 (*courtesy* of IFToMM Archive)

Bulgaria during which the foundation of IFToMM was planned as later it was agreed during the Second World Congress on TMM in Zakopane, Poland. The Congress series was immediately recognized as the IFToMM World Congresses and in 2015 we have celebrated the 14th event with the participation of delegates from 47 Member Organizations and from more than 50 countries.

IFToMM activity has grown in many aspects, as for example concerning the number of member organizations (from the 13 founder members to the current 47 members), the size and scale of conference events (with many other conferences, even on specific topics, at national and international levels, in addition to the MMS World Congress), and the number and focus of technical committees working on specific discipline areas of MMS.

IFToMM was founded in 1969 and today a fourth generation of IFToMMists starts to be active. Knowing the History of IFToMM and how we arrived at today's modus operandi gives a greater awareness of community identity and significance [2, 3, 5].

The IFToMM community evolved from a family-like structure of few enthusiastic pioneers/visionaries and founders into a scientific worldwide community through the following generations:

- 1950's–'79 First generation: founding fathers and their friend colleagues up to the 4-th IFToMM World Congress in Newcastle-upon-Tyne in 1975 with prof. Leonard Maunder as Congress Chair.
- 1980–95 Second Generation: students and people educated by founding fathers and their friend colleagues; up to the 9-th World Congress in Milan in 1995 with prof. Alberto Rovetta as Congress Chair.
- 1996–2011 Third Generation: educated people in the frame of IFToMM and within IFToMM activity with 48 national organizations as IFToMM members, with Prof. Carlos Lopez-Cajùn. As General Chair for 2011 Congress.
- Today–Fourth Generation: educated people in local frames with international activities that are linked to IFToMM and within IFToMM activity through 47 organizations as IFToMM members.

IFToMM officers (who are the Chairs of IFToMM Member Organizations, the Chairs of TCs and PCs, and the members of the Executive Council) have contributed and still contribute as leaders for the mission of IFToMM, which is stated in the 1-st article of the Constitution as: 'The mission of IFToMM is the promotion of Mechanism and Machine Science'. A complete list of IFToMM officers over time is available in [7] and updates in the IFToMM webpage.

The structure of IFToMM is summarized in Fig. 4 with the IFToMM Bodies that are indicated in IFToMM constitution according to IFToMM mission to provide leadership for cooperation and development of modern results in the Mechanism and Machine Sciences by assisting and enhancing international collaboration.

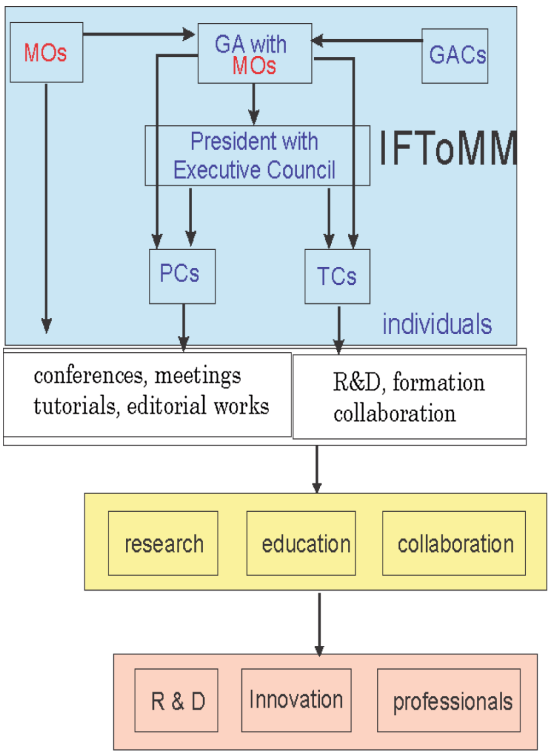

Fig. 4 A scheme for structure and activity of IFToMM

The bodies of IFToMM can be described synthetically as:

- General Assembly: it is the supreme body of the Federation and determines its policy. It is composed of the Chief Delegates of IFToMM Organization members (in 2016 they are 47) and members of the Executive Council.
- Executive Council: it manages the affairs of the Federation between the sessions of the General Assembly. It is elected every four years, meets annually and works also with telemeetings, and is composed of the President, Vice-President, Secretary-General, Treasurer, and six ordinary members.
- Permanent Commissions (PCs) and Technical Committees (TCs): Each PC and TC is composed of a Chairperson, appointed by the Executive Council, Deputy Chair, a Secretary and members, nominated by the Chairperson and appointed by the Executive Council. A Chairperson shall not serve for more than two terms consecutively. The general goals for the work of the PCs and TCs are aimed at promoting their fields of interest by attracting researchers and practitioners, including young individuals, in order:
  - to define new directions in research and development within their technical areas;
  - to establish contacts between researchers and engineers;

- to initiate and develop bases and procedures for modern problems;
- to promote the exchange of information;
- to organize national and international symposia, conferences, summer schools, and meetings.

In 2016 13 TCs are active in the fields of: Biomechanical Engineering, Computational Kinematics, Gearing and Transmissions, Linkages and Mechanical Controls, Micromachines, Multibody Dynamics, Reliability,, Robotics and Mechatronics, Rotordynamics, Sustainable Energy Systems, Transportation Machinery, Tribology, and Vibrations. Additional TCs are under consideration for hot topics with an IFToMM significant community. The PCs are on: Communications, Publications and Archiving, Education, History of MMS, and Standardization of Terminology.

Main aspects of the IFToMM activity are emphasized in Fig. 4 as related to Research, Formation, and Collaboration for final goals in R&D frames, Innovation, and Professionals Formation. Indeed, they are related to each other since a good teaching for a modern professionals formation needs to be well based on a successful research activity that today requires collaborations in teams even within international frames for shared approaches and results.

IFToMM activity can be summarized mainly in:

- conference events, in wide form and specific subjects not only as linked to TCs, at local and international frames, within series and in one shot events. A World Congress is organized every 4 years and the next one is 15th IFToMM World Congress that is scheduled in June 2019 in Kracow, Poland
- meetings and visit exchanges, including joint teaching
- project collaborations in research programs and in teaching plans
- organization of fields of interests for aggregation of an international community and planning actions as the above ones
- publications for dissemination purposes of research results and knowledge transfer. This is achieved at the moment through 5 affiliated journal and two book series specifically dedicated to MMS and IFToMM community. The journals are: Mechanism and Machine Theory (http://www.elsevier.com), Open-access Mechanical Sciences (http://www.mech-sci.net), Chinese Journal of Mechanical Engineering (http://www.cjmenet.com), Advances in Vibration Engineering (http://www.tvi-in.com/index.asp), Mechanics Based Design of Structures and Machines (http://www.tandf.co.uk/journals/titles/15397734.asp). The book series are published by Springer on MMS (http://www.springer.com/series/8779) and on History of MMS (http://www.springer.com/series/7481).

IFToMM significance can be summarized as being the unique world federation in MMS with the following motivations:

- Yesterday: To start and facilitate international collaboration between Eastern and Western countries

- Today: To help and enhance international collaboration and modern results on MMS
- Tomorrow: To leader cooperation and development in MMS Mechanism and Machine Science.

4 Conclusions

Not everything is new or recently developed in MMS, although innovation seems to be a priority today. But this does not mean that there is not interest for MMS, nor that there is no need to work on developing and enhancing knowledge and application of MMS. New challenges are determined for MMS in the new needs of Technology and Society both in term of developing new solutions and updating past solutions. An awareness of the historical background can give not only a conscious understanding of past efforts and solutions, including their paternity, but even more importantly it can help to find/develop ideas for new and updated problems to be solved. But the rapidly evolving needs of Technology and Society will require a continuous re-thinking and re-conceiving of methodologies and solutions in suitable updated applications. Thus, the main challenges for future success in MMS may be recognized in the community capability of being able to keep updating the field and therefore in being ready to solve new and updated problems with new ideas or by refreshing past solutions, as has been done successfully in the past. IFToMM is the international body that made MMS very successful and widespread in the second half o 20th century and it can have still an influential role in guiding/coordinating future development sin MMS. IFToMM is the frame that made MMS very successful in the second half of the 20-th century and it can have still an influential role in guiding/coordinating future developments.

References and Further Reading Sources

1. Ceccarelli, M.: From TMM to MMS: a vision of IFToMM. Bull. IFToMM Newsl. 10(1). (http://www.iftomm.org) (2001)
2. Ceccarelli, M.: President Report for IFToMM General Assembly. IFToMM Archive, Udine (2011)
3. Ceccarelli, M.: Problems and issues for service robots in new applications. Int. J. Soc. Rob. **3** (3), 299–312 (2011)
4. Ceccarelli, M.: Twenty-five years of activity in IFToMM. J. Theory Mech. Mach. (http://tmm.spbstu.ru) St. Petersburg State University **11**(2), 3–14 (2013)
5. Ceccarelli, M.: A short account of history of IFToMM and its role in MMS. Mech. Mach. Theory **89**, 75–91 (2015)
6. IFToMM 2003: Special Issue 'Standardization and Terminology', Mechanism and Machine Theory, vol. 38(7–10) (2003)

7. Ceccarelli, M. (ed.): Proceedings of HMM2004 International Symposium on History of Machines and Mechanisms. Kluwer, Dordrecht (2004)
8. Bautista Paz, E., Ceccarelli, M., Echavarri Otero, J., Munoz Sanz, J.J.: A Brief Illustrated History of Machines and Mechanisms. Springer, Dordrecht (2010)
9. Ceccarelli, M.: IFToMM celebration for 40-th year celebration. Mech. Mach. Theory **45** (2010), 119–127 (2010)
10. Crossley, F.R.E.: The early days of IFToMM. In: Proceedings of 8-th IFToMM World Congress, Prague, vol. 1, pp. 4–9 (1991)
11. Koetsier, T.: Mechanism and machine Science: its history and its identity. In: Proceedings of HMM2000—the First IFToMM International Symposium on History of Machines and Mechanisms, pp. 5–24. Springer, Dordrecht (2000)
12. Maunder, L.: The progress of IFToMM. Mech. Mach. Theory **15**, 415–417 (1980)
13. Maunder, L.: Report: the scientific activity of IFToMM. Mech. Mach. Theory **23**, 329–332 (1988)
14. Morecki, A.: Past present and future of IFToMM. Mech. Mach. Theory **30**, 1–9 (1995)
15. Morecki, A.: International friendly thinkers organization (who likes) machines and mechanisms (IFToMM)—where are we going? In: Proceedings of 10-th IFToMM World Congress, Oulu (1999)

General Algorithm for Computing the Theoretical Centering Precision of the Gripping Devices

E.-C. Lovasz, V. Mesaroş-Anghel, C.M. Gruescu, C.E. Moldovan and M. Ceccarelli

Abstract The paper shows a study about the theoretical centering precision for gripping devices. The deviation of the absolute axial centering is taken into account as a centering precision parameter and a general computing algorithm is developed for it. For previously developed gripping devices, using parallelogram and four-bar linkages with coupler driven jaws is computed the variation of the axial centering deviation.

Keywords Centering precision · Axial centering deviation · Gripping device · Four-bar linkage

1 Introduction

The industrial gripping devices usually use a reduced number of jaws 2 or 3 with equivalent dexterity of 40–90 % in comparison with the human hand having 5 fingers [1]. In [2], the gripping devices are classified in regard with the motion type of the jaws in translating, rotating (oscillating), planar motion and combinations of them. Konstantinov in [3] systematized the mechanisms used in gripping devices, which contains structural linkages, gears and screw-nut mechanisms. In [4] are

E.-C. Lovasz (✉) · V. Mesaroş-Anghel · C.M. Gruescu · C.E. Moldovan
Politehnica University of Timişoara, Timişoara, Romania
e-mail: erwin.lovasz@upt.ro

V. Mesaroş-Anghel
e-mail: voicu.mesaros-anghel@upt.ro

C.M. Gruescu
e-mail: corina.gruescu@upt.ro

C.E. Moldovan
e-mail: cristian.moldovan@upt.ro

M. Ceccarelli
University of Cassino, Cassino, Italy
e-mail: ceccarelli@unicas.it

J. Beran et al. (eds.), *Advances in Mechanism Design II*,
Mechanisms and Machine Science 44, DOI 10.1007/978-3-319-44087-3_2

shown some examples, which use in addition cam mechanisms in the structure of the gripping devices.

For all of these gripping devices an important industrial characteristic is the capability of centering precision. The centering precision is implicitly fulfilled in the case of the translational jaws and can be minimized for other motion types of the jaws. This aim is pursued by Qingsen in [5], and Brukher in [6], through proper designing of the gripping device mechanism provided by Pankin in [7] or through shaping the jaws. Recent researches develop special gripping devices used in soft robotics for performing gentle tasks [8] or for handling highly elastic objects [9]. For simple or complex anthropomorphic structures, underactuated grasping devices are used [10, 11], etc.

In [5], Qingsen presents a study of designing a grooved cam profile for increasing the centering precision. Simionescu in [12] shows a study of the centering precision of a conveniently chosen four-bar linkage used for acting a gripping device.

2 General Algorithm for Computing the Axial Centering Deviation

The centering is defined as the property of the gripping device to superpose the characteristic axis of the grasped object with his characteristic axis. The centering precision implies the computation of the axial centering deviation between the characteristic axis of the cylindrical grasped object and the characteristic axis of the grasping device. For this purpose it is considered the bisecting line of the prism in the top point M of the prism-jaw. The absolute axial centering deviation is the distance from the intersection of the bisecting line with the Ox-axis to the origin of the reference system axes xOy, identical with the characteristic axis of the grasping device (see Fig. 1).

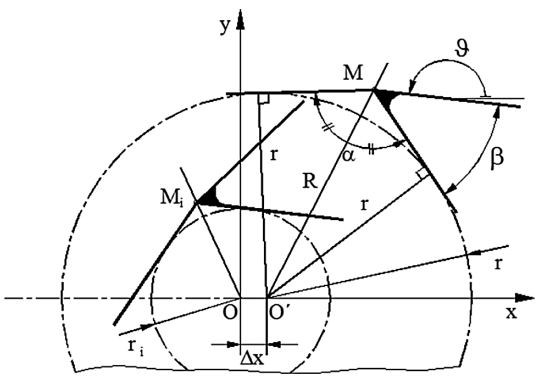

Fig. 1 Axial centering deviation

The absolute axial centering deviation Δx computation, based on the notations in Fig. 1, follows by considering the vector equation:

$$\mathrm{M} = \Delta x + \frac{r}{\sin(\alpha/2)} \cdot e^{i(\vartheta-\beta-\alpha/2)}. \tag{1}$$

The coordinates x_M and y_M of the top point of the prism-jaw M and the pose angle ϑ of the coupler connecting element depend on the structure of the gripping mechanism. The prism angle of the jaw α (usually $\alpha = 120°$) and the connection angle β of the coupler with the jaw are imposed by design conditions.

From the Eq. (1) can be computed the radius of the grasped object and the corresponding absolute axial centering deviation:

$$\begin{aligned} r &= y_M \cdot \frac{\sin(\alpha/2)}{\sin(\vartheta - \beta - \alpha/2)}, \\ \Delta x &= x_M + \frac{r}{\sin(\alpha/2)} \cdot \cos(\vartheta - \beta - \alpha/2). \end{aligned} \tag{2}$$

2.1 Gripping Device Using Parallelogram Linkages

The grapping device contains 2 parallelogram linkages symmetrically placed in respect with the axial direction of the structure and uses a symmetrical acting chain [13], as shown in Fig. 2. The motion of the coupler keeps parallel with the axial direction of the gripping device. The jaws prisms are fixed with the couplers.

The particularity of this parallelogram linkage consists in the constant value of the coupler angle:

$$\vartheta(\varphi) = \pi \tag{3}$$

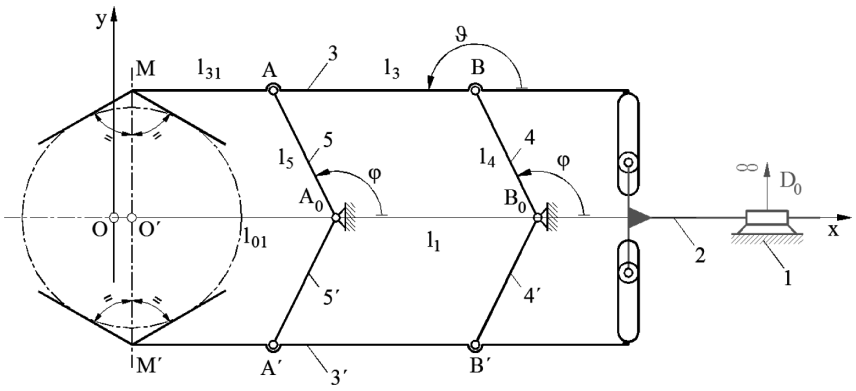

Fig. 2 Kinematic schema of the gripping device using parallel linkages

and the same positional angle of the both cranks.

The coupler point M coordinates of the parallelogram linkage in the xOy coordinate system of the gripping device results from the vector equation:

$$M = l_{01} + l_1 + l_4 \cdot e^{i\cdot\varphi} + (l_3 + l_{31}) \cdot e^{i\cdot\vartheta(\varphi)}, \tag{4}$$

and by considering the relationship (3) as:

$$x_M = (l_{01} + l_1) + l_4 \cdot \cos\varphi - (l_3 + l_{31}), \quad y_M = l_4 \cdot \sin\varphi. \tag{5}$$

2.2 Gripping Device Using Four-Bar Linkages

This type of gripping device (see Fig. 3) contains also 2 symmetrical four-bar linkages with coupler driven motion of the jaws and using symmetrical actuating chains [1, 14].

The positional analysis of the four-bar linkage, used for acting the coupler jaws, allows the computing of the coordinates of the top point M according to the kinematic parameters of the linkage. The vector equation of the four-bar linkage A_0ABB_0 in its own coordinate system, shown in Fig. 3, is:

$$l_1 + l_4 \cdot e^{i\cdot\phi} + l_5 \cdot e^{i\cdot(\vartheta+\delta)} = l_6 \cdot e^{i\cdot\psi}. \tag{6}$$

By considering the complex conjugate equation of the vector Eq. (3) follows the coupler (5) positional angle ϑ depending on the rocker (4) angle φ:

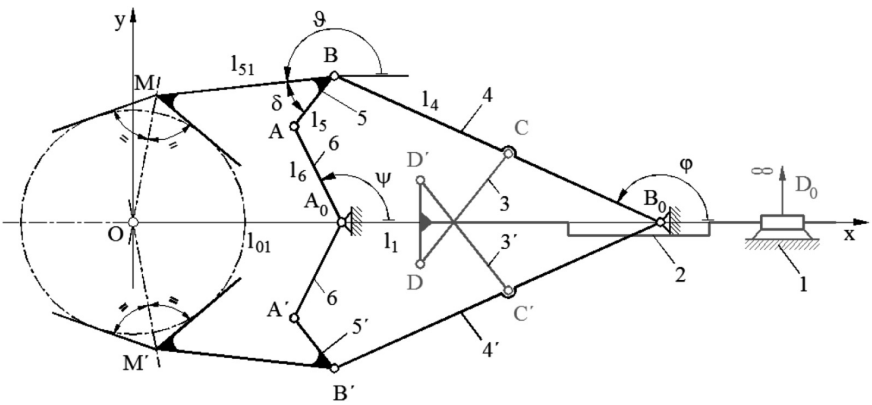

Fig. 3 Kinematic schema of the grasping device using four-bar linkages with coupler jaws

$$\vartheta(\phi) = -\delta + \frac{B_1(\phi) + \sqrt{A_1(\phi) + B_1(\phi) - C_1(\phi)}}{A_1(\phi) - C_1(\phi)}. \tag{7}$$

with:

$$\begin{aligned} A_1(\phi) &= 2l_5(l_1 + l_4\cos\phi), \quad B_1(\phi) = 2l_4l_5\sin\phi, \\ C_1(\phi) &= l_1^2 + l_4^2 + l_5^2 - l_6^2 + 2l_1l_4\cos\phi. \end{aligned} \tag{8}$$

The coordinates of the coupler point M of the four-bar linkage in the gripping device coordinate system xOy follows from the vector equation:

$$M = l_{01} + l_1 + l_4 \cdot e^{i\cdot\phi} + l_{51} \cdot e^{i\cdot\vartheta(\phi)}, \tag{9}$$

in the form:

$$\begin{aligned} x_M &= l_{01} + l_1 + l_4 \cdot \cos\phi + l_{51} \cdot \cos\vartheta(\phi), \\ y_M &= l_4 \cdot \sin\phi + l_{51} \cdot \sin\vartheta(\phi). \end{aligned} \tag{10}$$

3 Numerical Examples

The numerical examples show the variation of the absolute axial centering deviation in respect with the grasped object radius Δx(r) for the both grasping mechanism devices, presented in Sects. 2.1 and 2.2.

The considered radii of the grasped cylindrical object are in the range of 2.5–35 mm and the angle of the jaws prisms is chosen α = 120° for both examples.

3.1 Gripping Device Using Parallelogram Linkages

The geometrical parameters of the gripping device using parallelogram linkages are shown in Table 1.

In Fig. 4a is represented the variation of the absolute axial centering deviation symmetrically distributed for the considered mechanism. The centering condition is fulfilled only for one radius of the grasped object (r = 26.66 mm), as expected.

Table 1 Geometrical parameters of the parallelogram linkage

Parameters	l_1 (mm)	l_{01} (mm)	l_3 (mm)	l_{31} (mm)	l_4 (mm)	l_5 (mm)	β (°)
Parallelogram linkage	70	129.5	70	90	50	50	30

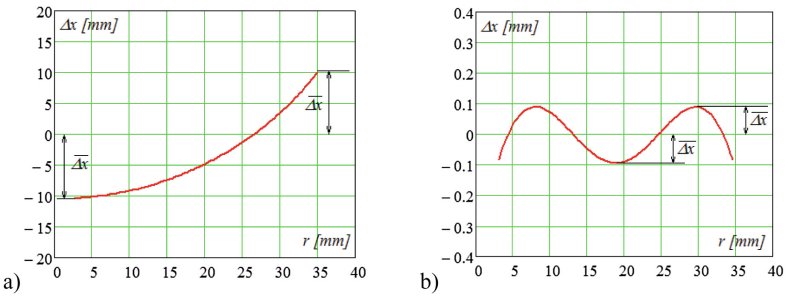

Fig. 4 Absolute axial centering deviation for parallelogram (**a**) and four-bar (**b**) linkage

Table 2 Geometrical parameters of the parallelogram linkage

Parameters	l_1 (mm)	l_{01} (mm)	l_4 (mm)	l_5 (mm)	l_{51} (mm)	l_6 (mm)	β (°)	δ (°)
Four-bar linkage	100	79.79	117.2	9.1	66.36	26.3	10.84	19.162

3.2 Gripping Device Using Four-Bar Linkage

The geometrical parameters of the gripping device using four-bar linkages are shown in Table 2 and the design assembly was patented in [15].

Figure 4b shows the variation of the absolute axial centering deviation for the four-bar linkages. The centering condition is fulfilled for four radii of the grasped cylindrical object. For these radii the four-bar linkage was computed by using four pose synthesis in [1, 14].

4 Conclusions

The paper presents a general algorithm for computing the absolute axial centering deviation, as theoretical precision parameter. Some known gripping devices were considered and numerically analyzed to validate the proposed algorithm.

References

1. Warnecke, H.J., Schraft, R.D.: Industrieroboter. Krausskopf-Verlag GmbH, Mainz (1979)
2. Mesaroş-Anghel, V.: Contribution to the synthesis of four-bar linkages used for designing of the grasping devices of the industrial robots (Contribuţii la sinteza mecanismelor articulate aplicate în construcţia dispozitivelor de prehensiune ale roboţilor industriali). PhD Thesis, Politehnica University of Timişoara, Romania (1991). Accessible on http://www.dmg-lib.org/

3. Konstantinov, M.S., Galabov, W.B.: Kriterien zum Entwurf von Greifmechanismen für maniupulatoren und Industrieroboter, Maschinenbautechnick, pp. 534–535 (1978)
4. Ceccarelli, M.: Fundamentals of Mechanics of Robotic Manipulation. Kluwer Academic Publishers, Dordrecht (2004)
5. Qingsen, H.: A linkage mechanism for concentric gripping cylindrical components. In: Proceedings of the 12 National symposium on Industrial Robots and the 6th International Symposium on Robotised Technologies, Paris, 9–11 June 1982
6. Brukher, E.: Maschinell betatigte Zange zum Greifen von Rundkorpen, Deutschland, Patent 3717091, 21 May 1987
7. Pankin, E.P.: Universalnoe zahvatnoe ustroino. Mehanizatiea i avtomatizatiea proizvotsva **11**, 10 (1989)
8. Zhou, X., Majidi, C., O'Reilly, O.M.: Soft hands: an analysis of some gripping mechanisms in soft robot design. Int. J. Solids Struct. **64–65**, 155–165 (2015)
9. Tilli, J., Brando, A., Fantoni, G.: Gripping device for heavy and deformable materials handling: concept, design, selection and test. Proc. CIRP **21**, 373–378 (2014)
10. Wu, L., Carbone, G., Ceccarelli, M.: Design an under actuated mechanism for a 1 active DOF finger operation. Mech. Mach. Theory **44**(2), 336–348 (2009)
11. Butterfass, J., Grebenstein, M., Liu, H., Hirzinger, G.: DLR-Hand II: next generation of a Dextrous robot hand. In: Proceedings of the IEEE, International Conference on Robotics and Automation, Seoul, Korea (2001)
12. Simionescu, I., Ionescu, C.: Optimum design of self centering grippers. UPB Sci. Bull. Ser. D **73**(1), 43–52 (2011)
13. Kovacs, F.W., Varga, S., Pau, V.-C.: Introduction in Robotics (Introducere în robotică). Printech Publisher, Bucharest (2000)
14. Mesaroş-Anghel, V., Lovasz, E.-C., Gruescu, C.M., Moldovan, C.E.: Optimal Design of a Grasping Device through Simplified Pose Synthesis of a Four-Bar Linkage, MTM & Robotics 2016. Series: Mechanisms and Machine Science. Springer (2016)
15. Mesaroş-Anghel, V., Mesaroş-Anghel, T., Groza, I.-R., Cioabă, V., Mareş, A., Czika, Z.: Grasping device with centering (Dispozitiv de prehensiune cu centrare), Brevet nr.102291/26.06.1989, Romania (1989)

Design and Development of a Heddle Shaft Mechanism for Air-Jet Weaving Machines

F. Schwarzfischer, S. Kurtenbach, J. Onischke and B. Corves

Abstract Air-jet weaving is the most productive weaving procedure. However, it is also the most energy-intensive procedure. In order to save energy newly developed high-volume-low-pressure relay nozzles can be used. The application of these nozzles requires changes in the heddle shaft movement. The design and development of a suitable mechanism to drive the heddle shaft is presented. After the determination of requirements a structural synthesis is conducted. The outcome of the structural synthesis is a set of mechanisms which in principal can solve the motion task. Subsequently a dimensional synthesis is performed to determine the kinematic parameters of each structure. The different mechanisms are then compared to each other. The most suited mechanism is a combination of a linkage and a cam mechanism. In order to improve the dynamic behavior of the heddle shaft mechanism a Fourier analysis of the shaft motion is carried out. The Fourier series of the shaft motion is then truncated and the disk cam profile is redesigned in order to drive the shaft with the desired harmonic motion. The result of the design and development process is a new heddle shaft mechanism for air-jet weaving machines with high-volume-low-pressure (HVLP) relay nozzles.

Keywords Mechanism design · Cam design · Air-jet weaving machine · Heddle frame mechanism

F. Schwarzfischer · S. Kurtenbach · J. Onischke · B. Corves (✉)
RWTH Aachen University, Aachen, Germany
e-mail: corves@igm.rwth-aachen.de

F. Schwarzfischer
e-mail: schwarzfischer@igm.rwth-aachen.de

S. Kurtenbach
e-mail: kurtenbach@igm.rwth-aachen.de

J. Onischke
e-mail: onischke@igm.rwth-aachen.de

J. Beran et al. (eds.), *Advances in Mechanism Design II*,
Mechanisms and Machine Science 44, DOI 10.1007/978-3-319-44087-3_3

1 Introduction

Weaving is one of the oldest techniques for the production of fabric. Sets of yarns are interlaced at right angles to form cloth. Nowadays weaving is no longer handcraft but executed automatically by weaving machines. Figure 1 shows the basic structure of a weaving machine. The warp yarns are unrolled from the warp beam. Then they are guided through the weaving machine in longitudinal direction. Each warp yarn is threaded through one heddle eye. The heddle eyes are part of the heddles, which are mounted on the heddle frames.

The minimum number of heddle frames is two, as shown in Fig. 1. In case of complex weaving patterns, more heddle frames are required. The heddle frames move the warp yarns in vertical direction in order to create the shed. At maximum displacement of the heddle frames, the shed is called "open shed". The filling yarn is then inserted at right angle to the warp yarns into the open shed. The reed performs a rotating motion and beats the filling yarn against the woven cloth that has already been formed. The heddle frames switch position and the filling yarn is inserted into the newly opened shed. A new cycle starts. The cloth take-up roll serves to wind up the woven cloth [1].

Weaving machines can be classified with respect to the method of the insertion of the filling yarn. Common methods are shuttle weaving, projectile waving, rapier weaving and jet weaving. Jet weaving uses a fluid to transport the filling yarn through the open weaving shed and can be subdivided into water-jet and air-jet weaving. In the latter method the filling yarn is accelerated by a main nozzle and guided through the open shed by relay nozzles [1].

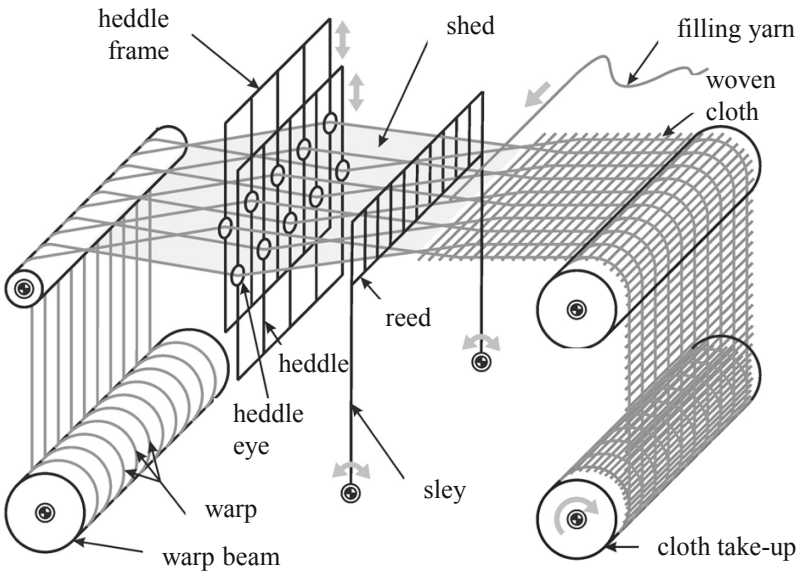

Fig. 1 Basic structure of a weaving machine

Air-jet weaving is the most productive weaving procedure. However, it is also the most energy-intensive procedure. In order to save energy newly developed high-volume-low-pressure relay nozzles can be used. The application of these nozzles requires changes in the heddle shaft movement. This is due to their increased external dimensions, which require a movement of the relay nozzles [2]. The purpose of this study was the development of a heddle frame mechanism with a new motion profile to allow the application of the new relay nozzles.

2 Materials and Methods

In order to develop the heddle shaft mechanism, a mechanism synthesis had to be conducted. The requirements for the mechanism were identified by conducting measurements on the real weaving machine and by simulating the machine using the newly developed HVLP relay nozzles.

2.1 Requirement Elicitation

To measure the movement of the reed and the current heddle frame movement an optical coordinate-measuring device was utilized. The measured reed movement was used as an input for an existing kinematic model of the weaving machine. The necessary heddle frame movement to allow the application of the new HVLP relay nozzles was determined. The input of the measured heddle frame movement into the kinematic model of the weaving machine showed the need to change the heddle frame movement. However, the high operating speed should be maintained.

2.2 Design and Development Process

In order to develop the heddle frame mechanism, the motion task was split into subtasks. This step was carried out according to the procedures outlined in [3]. Following the procedure in [4], a morphological box containing solutions for the different subtasks was set up. Combining the solutions of the subtasks, solutions for the complete system were derived. The different solutions for the complete system were compared using qualitative evaluation criteria. In order to reduce the number of solutions, only the best assessed solutions were considered for the following steps. In the next steps, mechanism synthesis had to be carried out for the subtask-solutions containing mechanisms.

2.3 *Mechanism Synthesis*

The mechanism synthesis can be subdivided into the structural and the dimensional synthesis. The determination of mechanisms that in principle can fulfil the motion task is the objective of the structural synthesis. The structural synthesis is followed by the dimensional synthesis. It contains the step of defining the dimensions of the mechanism, which means choosing the length of the links and the positions of the joints. The methods described in [5–7] are used to carry out the dimensional synthesis. In order to determine the dimensioning of cam disks, the Hodograph-Procedure described in [8] is employed. The result of the procedure is the position of the axis of rotation of the cam disk as well as its transfer function. The transfer function of the cam disk is then modified following the procedure outlined in [9, 10]. A so-called high-speed (HS) profile is calculated. Contrary to the normal disk cam profile, the HS transfer function is continuous as it is built up by a finite number of harmonics.

3 Results

The motion task of the heddle frame mechanism is defined by the rotational input motion and the desired output motion, the vertical movement of the heddle frame (s). Figure 2 shows the structure of the motion task.

The complete heddle frame mechanism is shown in Fig. 3. The vertical motion of the heddle frame is created by two guiding mechanisms. These mechanisms are

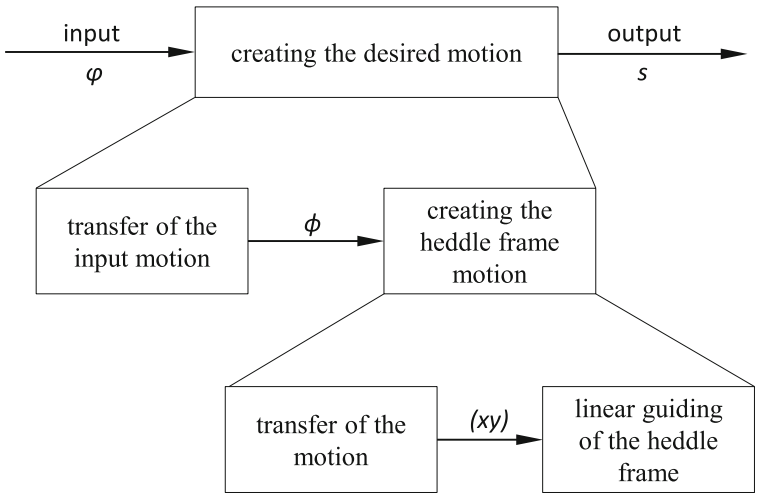

Fig. 2 Structure of the motion task for the heddle frame mechanism

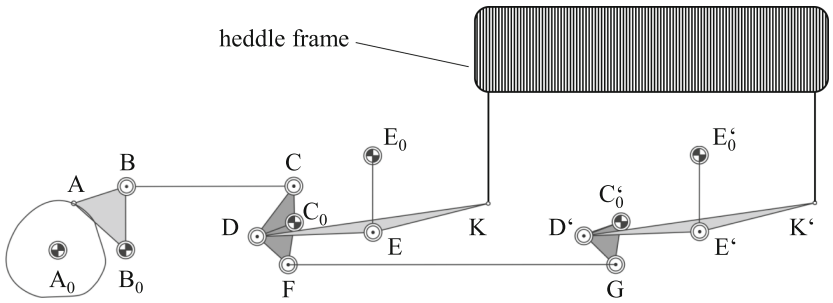

Fig. 3 Heddle frame mechanism

two four-bar linkages C_0–D–E–E_0 and C_0'–D′–E′–E_0'. Both mechanisms are coupled by a four-bar linkage C_0–F–G–C_0' to assure a parallel motion. The heddle frame is connected to the coupler points K and K'. As the four-bar linkages C_0–D–E–E_0 and C_0'–D′–E′–E_0' are almost similar to the Chebyshev lambda mechanism, K and K′ perform an approximate straight-line motion. The guiding mechanisms are driven by another four-bar mechanism B_0–B–C–C_0. The link B_0–B of this mechanism is driven by a cam disk, which transfers the input motion.

In order to decrease vibrations of the heddle frame, a harmonic synthesis of the heddle-frame motion was carried out. Figure 4 shows the heddle frame motion and its amplitude spectrum.

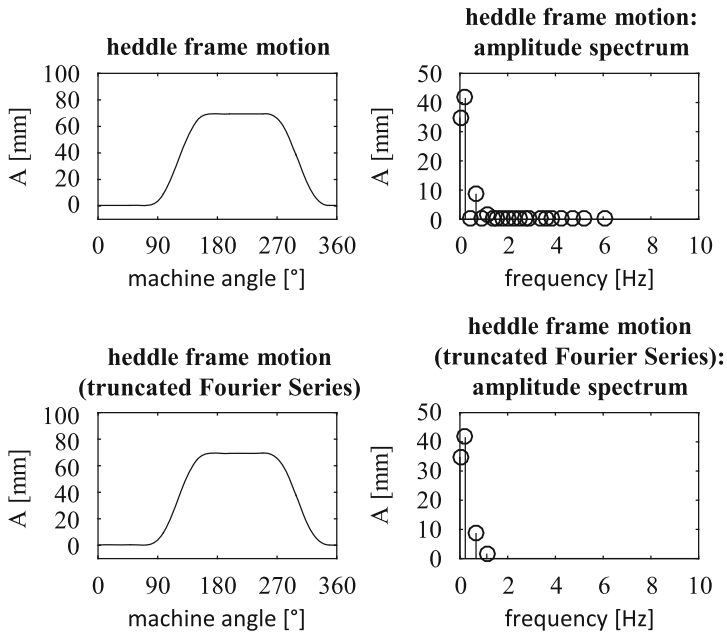

Fig. 4 Heddle frame motion and modified HS heddle frame motion

Furthermore, a modified heddle frame motion is depicted. Although only three harmonics are considered, the modified heddle frame motion is very close to the desired heddle frame motion.

The developed heddle frame mechanism can fulfil the requirements and allows the application of the newly developed HVLP relay nozzles. The mechanism is thin enough to allow the application of various mechanisms in a row, as it is necessary for complex weaving patterns.

4 Conclusion

Newly developed low pressure relay nozzles can contribute to energy savings in air-jet weaving. However, the application of these relay nozzles requires changes in the heddle frame movement of the weaving machine. The design and development of a suitable heddle frame mechanism was outlined in this paper. The mechanism is able to fulfil the requirements for the application of the new relay nozzles. In order to allow the application also for very high operating speeds, transfer function of the heddle frame mechanism was optimized using a HS cam disk.

References

1. Adanur, S.: Handbook of Weaving. CRC Press, Boca Raton (2001)
2. Holtermann, T.: Methode zur Bewertung und Erhöhung der Energieeffizienz von Produktionsprozessen der Textilindustrie. Aachen, Shaker (2014)
3. Koller, R.: Konstruktionslehre für den Maschinenbau. Grundlagen zur Neu- und Weiterentwicklung technischer Produkte mit Beispielen. Springer, Heidelberg (1998)
4. Pahl, G., Beitz, W., Feldhusen, J., Grothe, K.-H.: Engineering Design. A Systematic Approach. Springer, London (2007)
5. Kerle, H., Burkhard, C., Hüsing, M.: Getriebetechnik: Grundlagen, Entwicklung und Anwendung ungleichmäßig übersetzender Getriebe. Vieweg+Teubner, Wiesbaden (2011)
6. Erdman, A., Sandor, G.: Advanced Mechanism Design, Analysis and Synthesis, vol. 2. Prentice Hall Inc., New Jersey (1984)
7. Uicker, J.J., Pennock, G.R., Shigley, J.E.: Theory of Machines and Mechanisms. Oxford University Press, Oxford (2010)
8. Volmer, J.: Getriebetechnik. Vieweg+Teubner, Wiesbaden (1978)
9. Dresig, H., Vul'fson, I.I.: Dynamik der Mechanismen. Deutscher Verlag der Wissenschaften, Berlin (1989)
10. Dresig, H., Fidlin, A.: Schwingungen mechanischer Antriebssysteme. Modellbildung, Berechnung, Analyse, Synthese. Springer, Heidelberg (2014)

On Transfemoral Prosthetic Knee Design Using RRSS Motion and Axode Generation

J. D'Alessio, K. Russell and R.S. Sodhi

Abstract In this work, equation systems for RRSS motion generation and RRSS axode generation are applied to produce a concept transfemoral prosthetic knee. First, an RRSS linkage is synthesized to approximate a series of tibial positions during knee flexion. Next, the fixed and moving axodes of the synthesized RRSS linkage are generated. Because the coupler motion of an RRSS linkage can be replicated by rolling its moving axode over its fixed axode, the axodes for the synthesized RRSS linkage are incorporated as gearing in the concept prosthetic knee. The resulting prosthetic knee approximates the natural spatial motion of the tibia during knee flexion and extension (unlike prosthetic knee designs that include simple pin joints).

Keywords Spatial linkage · RRSS linkage · Motion generation · Axode generation · Transfemoral prosthesis

1 Introduction

Knee motion in the human leg can be described by three rotations and three translations in the principle planes of motion, namely the coronal or frontal plane, the sagittal or side plane and the transverse or horizontal plane (Fig. 1). Natural knee motion initially was characterized by purely planar motion in the sagittal plane [1]. It is now well understood natural knee motion doesn't occur solely in this plane. A complex motion of the principal rotations and translations has been

J. D'Alessio
Onkos Surgical, Parsippany, USA
e-mail: Jdalessio@onkossurgical.com

K. Russell (✉) · R.S. Sodhi
New Jersey Institute of Technology, Newark, USA
e-mail: kevin.russell@njit.edu

R.S. Sodhi
e-mail: rajpal.s.sodhi@njit.edu

J. Beran et al. (eds.), *Advances in Mechanism Design II*,
Mechanisms and Machine Science 44, DOI 10.1007/978-3-319-44087-3_4

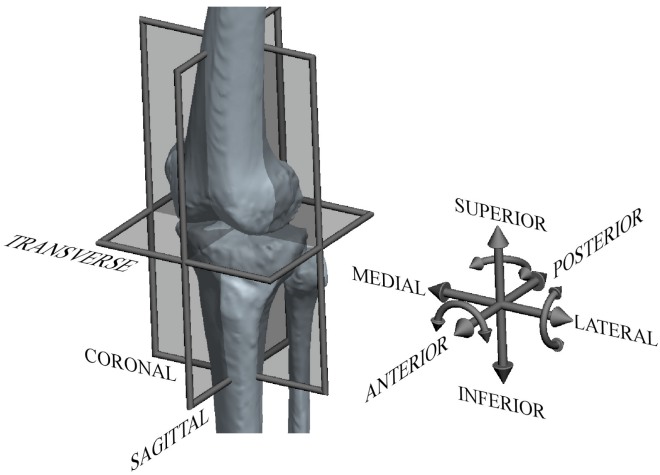

Fig. 1 Planes, rotations and translations for knee motion

documented [2, 3]. Additionally, research has shown that these rotations and translations can be described by showing how the tibia undergoes *screw motion* about the femur [4–7]. The same research has also shown that the position and orientation of this screw axis (called the *finite helical axis*) changes continuously throughout knee motion due to the complex 3D motion occurring in all three planes.

Because knee motion is helical over a continuously-changing axis and does not occur entirely in the sagittal plane, representing the knee as a simple pin or even a polycentric joint (where motion is restricted to pure rotation) in a transfemoral prosthetic leg design results in a prosthesis that does not achieve the natural spatial motion of the tibia. The user of this type of prosthesis will exhibit an unnatural gait to compensate for the unnatural prosthetic knee motion.

2 Design Processes and Models

Figure 2 illustrates the three stages in the prosthetic knee design process and the output from each stage. First, a series of tibial position data are acquired over a determined knee motion range. Next, this data is incorporated in a model to synthesize a spatial *revolute-revolute-spherical-spherical* or RRSS linkage to approximate the tibial positions. After this, the dimensions for the synthesized RRSS linkage are incorporated in a model to generate its fixed and moving axodes over the calculated RRSS motion range. Lastly, the fixed and moving axodes are incorporated into geometry (as gearing) to produce the cam components in the prosthetic knee.

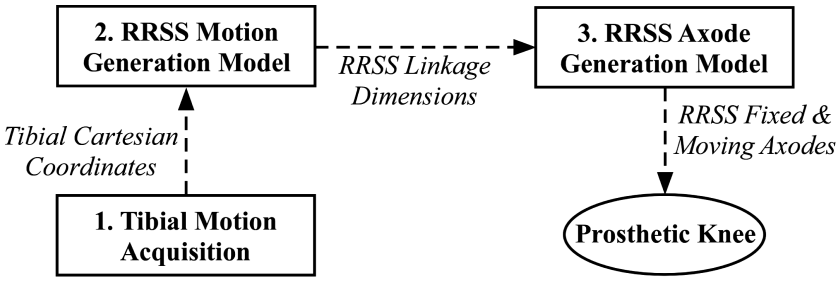

Fig. 2 Stages in transfemoral prosthetic knee design process

Figure 3 illustrates the workstation used in this work to measure tibial-femoral positions. The *localizer* measures and records position coordinates (in spatial Cartesian form) from *trackers*. Trackers are mechanically affixed directly to the tibia and femur bones. A direct tracker-to-bone connection (rather than tracker-to-skin connection), eliminates the bone position error introduced by the motion of leg skin tissue and muscle tissue. In this work, a cadaveric leg specimen was utilized. Not shown in Fig. 3 is the system of pulleys and cables used to support and actuate the cadaver leg from full flexion to full extension.

Russell and Shen [8] presented a motion generation model to synthesize circuit, branch and order defect-free RRSS linkages to approximate N prescribed rigid-body positions. As illustrated in Fig. 2, the tibial position coordinates measured in stage 1 are used as rigid-body positions for stage 2. Given a series of tibial positions, the RRSS motion generation model will calculate the dimensions and driving link rotations of a circuit, branch and order defect-free RRSS linkage that approximates the prescribed tibial positions.

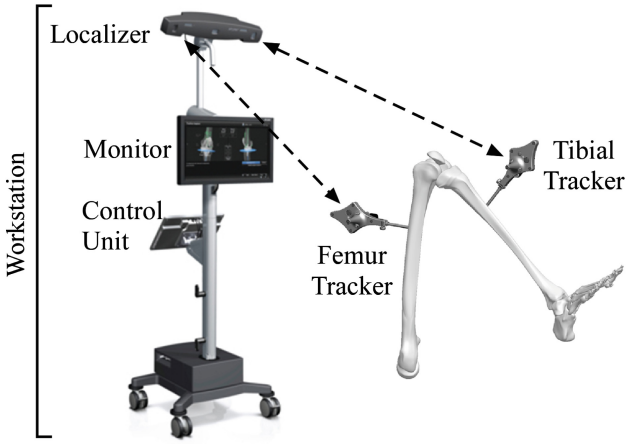

Fig. 3 Tibial-femoral position measurement system

Shen et al. [9] presented a model to generate the fixed and moving axodes for the RRSS linkage. As illustrated in Fig. 2, the RRSS linkage dimensions produced in stage 2 are used as input for stage 3. Given RRSS linkage dimensions and driving link rotations, the RRSS axode generation model will calculate the corresponding fixed and moving axodes. The coupler motion of the RRSS linkage (and subsequently the tibial positions achieved by this linkage) is replicated precisely by rolling the moving axode over the fixed axode [9].

Lastly, the fixed and moving axodes generated in stage 3 are incorporated into the geometry of a transfemoral prosthetic knee to replicate natural tibial motion.

3 Example

A series of tibial positions was measured using the approach in Sect. 2. Table 1 includes the spatial Cartesian coordinates measured for five tibial positions over approximately 37.5° of knee flexion (Fig. 4). This flexion range is adequate to describe the normal range for a standard gait cycle [2].

Table 1 Measured tibial position coordinates

Pos.	p (mm)	q (mm)	r (mm)
1	40.254, 2.718, −146.972	43.729, 2.845, −178.452	22.770, −11.562, −186.178
2	36.416, −6.936, −148.370	39.560, −9.379, −179.790	19.747, −26.032, −185.843
3	30.931, −34.024, −148.506	33.353, −42.460, −178.936	14.963, −61.578, −180.639
4	25.900, −80.564, −135.789	27.553, −97.742, −162.345	9.340, −116.529, −157.674
5	22.384, −117.358, −114.054	23.454, −140.564, −135.580	4.615, −157.026, −126.60

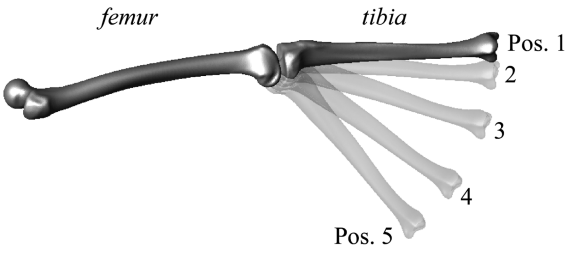

Fig. 4 Tibial displacement range

Table 2 Initial and calculated RRSS linkage dimensions and link rotation values

Variable	Initial values	Calculated values
a_0	−5, −30, −9	−8.277, −30.438, −9.119
a_1	−5, −15, 5.5	−2.525, −15.192, 4.150
ua_0	1, 0, 0	0.962, −0.194, −0.194
ua_1	1, 0, 0	0.962, −0.194, −0.194
b_0	−5, −2.8, −6.3	−5.447, −2.581, −5.130
b_1	−5, −22, 14.5	−3.407, −18.896, 14.761
θ_2–θ_5	10°…10°	0.723°, 3.027°, 8.609°, 15.387°
α_2–α_5	5°…5°	−5.062°, −18.387°, −42.512°, −65.086°

Table 3 Tibial position coordinates achieved by the synthesized RRSS linkage

Pos.	p (mm)	q (mm)	r (mm)
1	40.254, 2.718, −146.972	43.729, 2.845, −178.452	22.770, −11.562, −186.178
2	37.841, −7.915, −148.309	40.869, −10.034, −179.764	20.024, −25.261, −186.103
3	32.360, −35.434, −147.983	34.412, −43.217, −178.614	14.001, −60.045, −181.209
4	25.650, −81.213, −135.511	26.658, −97.927, −162.393	7.394, −115.776, −158.289
5	22.806, −116.926, −113.938	23.582, −140.062, −135.552	5.629, −157.064, −125.80

Next, the measured tibial position coordinates were used to synthesize an RRSS linkage to approximate these coordinates. Table 2 includes the initial and calculated values for the RRSS linkage using the RRSS motion generation model [8]. Table 3 includes the actual tibial position coordinates achieved by the synthesized RRSS linkage (Fig. 5).

Following RRSS motion generation is RRSS axode generation. Figure 5 also includes the fixed and moving axode sections generated using the RRSS axode generation model [9]. The tibial positions in Table 3 are perfectly replicated by rolling the moving axode section over the fixed axode section.

Lastly, the axodes are incorporated in prosthetic knee geometry. In Figs. 5 and 6, the axodes are expressed as noncircular gears (to eliminate slip during knee flexion and extension). Figure 6 also includes the Table 3 tibial positions achieved by the transfemoral prosthetic knee.

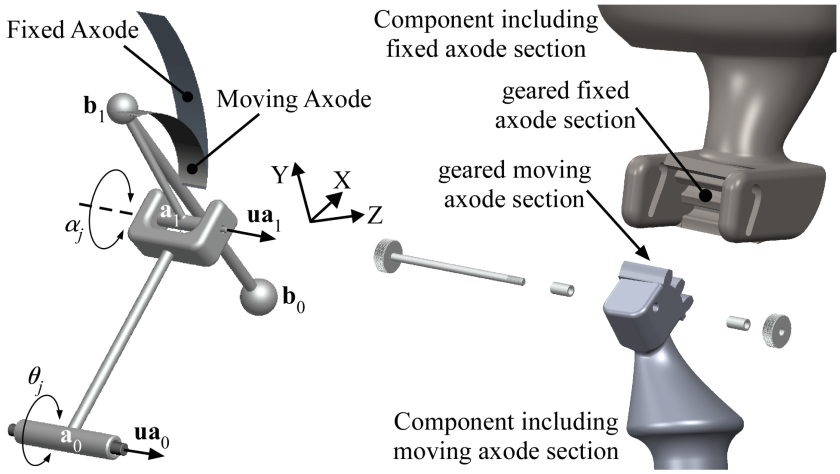

Fig. 5 Synthesized RRSS linkage with fixed and moving axode sections (*left*) and exploded view of transfemoral prosthetic knee (patent pending) with axode sections as gearing (*right*)

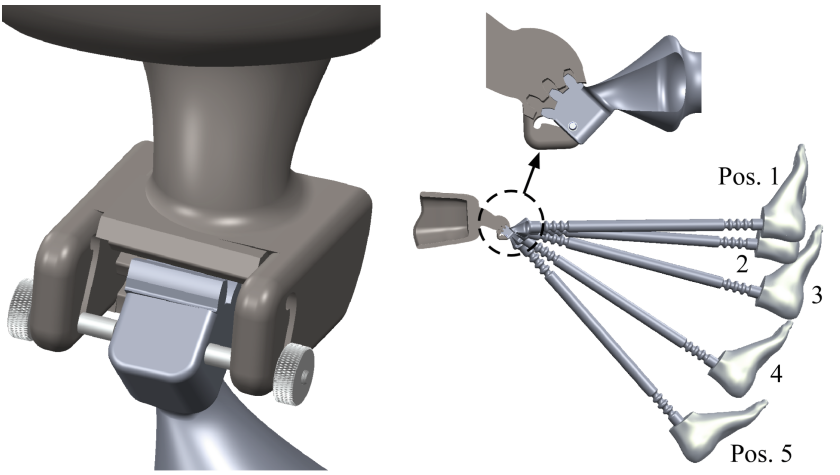

Fig. 6 Assembly view of transfemoral prosthetic knee (patent pending) (*left*) and achieved tibial positions in Table 3 (*right*)

4 Conclusions

Here, the design procedure for a prosthetic knee to achieve natural tibial motion is presented. Given a group of tibial positions, a defect-free RRSS linkage is first synthesized to approximate these positions. The fixed and moving axodes of the synthesized motion generator are calculated next. Lastly, these axodes are incorporated as gearing into a prosthetic knee design.

References

1. Frankel, V.H., Burstein, A.H., Brooks, D.B.: Biomechanics of internal derangement of the knee. J. Bone J. Surg. **53-A**(5), 945–977 (1971)
2. Benoit, D.L., Ramsey, D.K., Lamontagne, M., Xu, L., Wretenberg, P., Renström, P.: In vivo knee kinematics during gait reveals new rotation profiles and smaller translations. Clin. Orthop. Relat. Res. **454**(1), 81–88 (2007)
3. Dennis, D.A., Mahfouz, M.R., Komistek, R.D., Hoff, W.: In vivo determination of normal and anterior cruciate ligament-deficient knee kinematics. J. Biomech. **38**(2), 241–253 (2005)
4. Blankevoort, L., Huiskes, R., De Lange, A.: Helical axes of passive knee joint motions. J. Biomech. **23**(12), 1219–1229 (1990)
5. Hart, R.A., Mote, C.D., Skinner, H.B.: A finite helical axis as a landmark for kinematic reference of the knee. J. Biomech. Eng. **113**(2), 215–222 (1991)
6. Sheehan, F.T.: The finite helical axes of the knee joint (a non-invasive in vivo study using fast-PC MRI). J. Biomech. **40**(5), 1038–1047 (2007)
7. Van Den Bogert, A.J., Reinschmidt, C., Lundberg, A.: Helical axes of skeletal knee joint motion during running. J. Biomech. **41**(8), 1632–1638 (2008)
8. Russell, K., Shen, Q.: Expanded spatial four-link motion and path generation with order and branch defect elimination. Inverse Prob. Sci. Eng. **19**(2), 251–265 (2011)
9. Shen, Q., Russell, K., Lee, W., Sodhi, R.S.: On cam system design to replicate spatial four-bar mechanism coupler motion. Inverse Prob. Sci. Eng. **19**(2), 251–265 (2011)

On Approach Based on Lie Groups and Algebras to the Structural Synthesis of Parallel Robots

L. Rybak, D. Malyshev and A. Chichvarin

Abstract This paper proposes an approach to the structural synthesis of parallel robots based on the Lie algebras of the displacement groups. This approach allows the automation of the synthesis and eliminates the disadvantages of both methods based on the using of displacement subgroups, and methods based on the screw theory. Parallel robot is presented consisting of the moving platform and the stationary base connected via several serial kinematic chains. It is shown that movement of kinematic chain correspond to Lie subgroups of displacement, called displacement subgroups generators. These generators play an important role in determining the possible architectures of parallel mechanisms. Structural synthesis was performed for the case in which the mobile platform speed relative to the fixed basement forms a subalgebra of the Lie algebra of the displacement group of Euclidean space. In this case, we obtain three types of parallel robots. We also consider the case when the speed of mobile platform relative to the fixed basement forms a subspace, which is not a subalgebra of the displacement group of Euclidean space. It is divided into two types of robots. Is discussed case of parallel robot with serial chains generates Lie subalgebras in displacement space synthesis.

Keywords Parallel robot · Lie group · Lie algebra · Kinematic chain · Displacement group

1 Introduction

The type synthesis of parallel mechanisms is an important task of the theory of mechanisms. For synthesis purposes, you can use the formula of mobility, but this approach causes some difficulties in the synthesis of parallel mechanisms with degrees of freedom, less 6. The three most common approach to the synthesis of

L. Rybak (✉) · D. Malyshev · A. Chichvarin
Belgorod State Technological University Named After V.G. Shukhov,
Belgorod, Russia
e-mail: rl_bgtu@intbel.ru

J. Beran et al. (eds.), *Advances in Mechanism Design II*,
Mechanisms and Machine Science 44, DOI 10.1007/978-3-319-44087-3_5

such mechanisms—an approach based on the use of graph theory, screw theory and group theory.

Freudenstein first proposed the use of graph theory for synthesis purposes [1]. He has developed a graph scheme in which vertices correspond to communication mechanisms, and ribs—the hinges. The first graph theory to the development of new architectures of parallel robots applied Earle [2]. But when working with parallel robots graph theory has two major drawbacks: (1) an isomorphism, i.e., the use of compressed graphs, which implies the absence of a direct correspondence between the mechanism and its graph, and (2) the widespread use of the mobility of the formulas are often inapplicable to many spatial arrangements (e.g., parallelograms).

Another currently applied approach is based on the use of groups of motions. Many movements, representing the rigid body, has the structure of a particular group, the group of displacements. Such a group uniquely corresponds to a special matrix of the Euclidean group SE(3). SE(3)—continuous group, and any open set elements SE(3) uniquely corresponds to an open set in R6. In mathematical terms, SE(3)—differentiable manifold, called a Lie group. An exhaustive list of subgroups gave Hervé movements [3]. The importance here is the intersection operation is obtained when subjected to one of several solid elements subgroups. Movements Lie subgroups generated kinematic chains, called generators movements subgroups. These generators play an important role in determining the possible architectures of parallel mechanisms.

2 Methods of the Structural Synthesis of Mechanisms

Synthesis of parallel robots based on the theory of groups is based on the following basic principles: (1) the definition of what is a subgroup of S must have a working body to provide a predetermined number of degrees of freedom; (2) The definition of all possible subgroups with the relevant kinematic chains, which may consist of a robot support, the intersection of which gives a subgroup of S; (3) the definition of motion generator for these subgroups: they are kinematic chains of the robot.

This approach has been used by various researchers, for example, [4–7]. Synthesis based on group theory, it is still an open area of research, as not all groups of structures are developed.

An approach based on group theory, resulted in the opening of many new possible structures. However, the group of motions has a specific properties are not reflected in its structure of a Lie group. Accordingly, an approach based on the theory of groups hard to apply for specific mobility cases, such as paradoxical mechanisms.

It is possible to extend the concept of the group, considering the tangent space at the identity element, which is a vector space, called the Lie algebra of a Lie group. As we proceed from the SE(3), the corresponding Lie algebra se(3) is a vector space of instantaneous velocity, whose elements—the 6-dimensional vectors of the form $(\boldsymbol{\Omega}, \mathbf{v})$, where $\boldsymbol{\Omega}$—the angular velocity of a rigid body, and $\mathbf{v}$—its linear speed. These elements are called kinematic screws. Based on the theory of screws

following synthesis scheme is designed: (1) find a group of power screws S, mutually desired kinematic screw of the mobile platform; (2) determine the power screws robot kinematic chains whose union gives S. (3) to determine all the possible structures of kinematic chains, generating corresponding power screws; (4) as the considered power and instantaneous kinematic screws (and therefore the synthesis based on the screw theory, called the first-order approach), you must check is not instantaneous (full) mobility platform.

The disadvantage of this approach is the difficulty of automation, especially steps 3 and 4. It has the advantage of group theory: after determining the possible restrictions in Step 2, Step 3 movement generators are easily identified. On the other hand, by using an approach based on the group theory, the structure can be skipped, which are not within the sub-Li. However, some authors use this approach to generate a large number of structures with a number of degrees of freedom at least 6, for example, [8–12].

In this paper, we propose an approach designed to eliminate the disadvantages of both methods based on the use of submovements, and methods based on the use of screw groups.

The Euclidean group of motions of the space $SE(3)$ are the following subgroups (Fig. 1).

$R_{P,\hat{u}_1}$—Rotate around a point P, in a plane perpendicular to the axis $\hat{u}_1$; $T_{\hat{u}_1}$—Linear motion along the axis $\hat{u}_1$; $H_{P,\hat{u}_1,p}$—screw displacement of the point P axially $\hat{u}_1$ with a parameter p; $T_{\hat{u}_1^{\perp}}$—linear displacement in a plane perpendicular to the $\hat{u}_1$; $C_{P,\hat{u}_1}$—rotate around a point P, situated on the axis $\hat{u}_1$ in a plane perpendicular

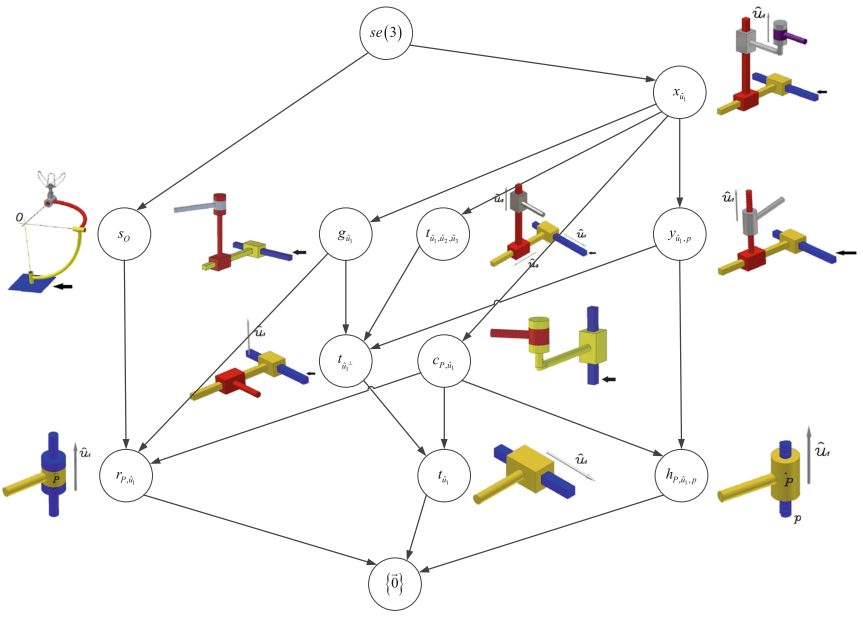

Fig. 1 Subgroups of the group of motions of Euclidean space

to the axis and the linear movement along said; $T_{\hat{u}_1,\hat{u}_2,\hat{u}_3}$—linear motion along three mutually orthogonal axes; $G_{\hat{u}_1}$—linear motion in a plane perpendicular to the axis $\hat{u}_1$ and rotating around this axis; S_O—arbitrary rotation in three-dimensional space around the fixed center O; $Y_{\hat{u}_1,p}$—linear displacement in a plane perpendicular to the axis $\hat{u}_1$ and a helical movement along this axis with a parameter p; $X_{\hat{u}_1}$—linear motion in space and moving along the screw axis $\hat{u}_1$ (Schoenflies movement).

3 An Example of Structural Synthesis of Parallel Robots

Consider a parallel mechanism consisting of the movable platform and the stationary base, connected by a k serial kinematic chain. When the type synthesis of parallel mechanisms consider the case when the mobile platform speed relative to the fixed base forms a subalgebra of the Lie algebra $se(3)$ of the group of motions of Euclidean space $SE(3)$. In this case, you can select the type of parallel mechanisms, for which the required subalgebra $A_R \subset se(3)$ is the intersection of subalgebras generated by a series of connected chains and all these subalgebras are equivalent.

Let $A_R \subset se(3)$—required subalgebra for a given movement. Then $A_R = A_a^{m/b} = \bigcap_{j=1}^{k} A_j^{m/b}$, respectively, $A_a^{m/b} \subset A_j^{m/b}, \quad j = 1, 2\ldots, k$

In this case, the required equivalent subalgebra all subalgebras generated serial kinematic chains,

$$A_R = A_j^{m/b}, \quad j = 1, 2\ldots, k \tag{1}$$

Subalgebras generated by a series of connected chains, represents the space of columns of the Jacobian matrix:

$$A_1^{m/b} = \begin{bmatrix} 0 & 0 & 0 \\ 0 & 0 & 0 \\ 0 & 0 & 0 \\ 0 & 0 & 1 \\ 1 & 0 & 0 \\ 0 & 1 & 0 \end{bmatrix} \quad A_2^{m/b} = \begin{bmatrix} 0 & 0 & 0 \\ 0 & 0 & 0 \\ 0 & 0 & 0 \\ 0 & 1 & 0 \\ 0 & 0 & 1 \\ 1 & 0 & 0 \end{bmatrix} \quad A_3^{m/b} = \begin{bmatrix} 0 & 0 & 0 \\ 0 & 0 & 0 \\ 0 & 0 & 0 \\ 1 & 0 & 0x \\ 0 & 1 & 0 \\ 0 & 0 & 1 \end{bmatrix} \tag{2}$$

It is easy to see that the subalgebra generated by each successive connection chain, as well as their intersection, defined as

$$A_a^{m/b} = \bigcap_{j=1}^{3} A_j^{m/b} = \begin{bmatrix} 0 & 0 & 0 \\ 0 & 0 & 0 \\ 0 & 0 & 0 \\ 1 & 0 & 0 \\ 0 & 0 & 1 \\ 0 & 1 & 0 \end{bmatrix} \tag{3}$$

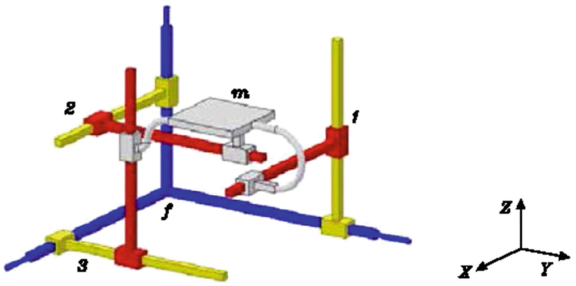

Fig. 2 Parallel mechanism commits linear movement in space, all serial connection circuit that generates a subalgebra spatial movements

They also are equivalent and correspond to spatial movements subalgebra $t_{\hat{u}_1,\hat{u}_2,\hat{u}_3}$.

An example of such mechanism is shown in Fig. 2.

4 Conclusions

It can be concluded that the analyzed approaches to type synthesis of parallel mechanisms, based on the screw theory and movements group theory have significant drawbacks. The method, based on the, movement group theory, it is difficult to apply to some specific cases of mobility, using a method based on the theory of screws, it is necessary to check the instantaneous mobility platform. The proposed method of type synthesis of parallel mechanisms, based on an analysis of the subspace and subalgebras of the Lie algebra, eliminates these drawbacks. An example of structural synthesis of parallel mechanisms for the case, if the mobile platform speed relative to the fixed base forms a subalgebra of the Lie algebra se(3) of the Euclidean space, confirming the effectiveness of this approach.

Acknowledgments This work was supported by the Russian Science Foundation, the agreement No. 16-19-00148.

References

1. Freudenstein, F., Dobrjanskyj, L.: On a theory for the type synthesis of mechanisms, invited contribution. In: Proceedings of Eleventh International Congress of Applied Mechanics, Springer, Berlin, pp. 420–428 (1966)
2. Earl, C.F., Rooney, J.: Some kinematics structures for robot manipulator designs. J. Mech. Transm. Autom. Des. **105**(1), 15–22 (1983)
3. Herve, J.M.: Group mathematics and parallel link mechanisms. In: 9th World Congress on the Theory of Machines and Mechanisms, pp. 2079–2082, Milan, 30 Aug–2 Sept 1995
4. Angeles, J.: The qualitative synthesis of parallel manipulators. ASME J. Mech. Des. **126**(4), 617–624 (2004)

5. Herve, J.M.: Parallel mechanisms with pseudo-planar motion generators. In: Lenarcic, J., Galletti, C. (eds.) Advances in Robot Kinematics, pp. 431–440. Kluwer, Alphen aan den Rijn (2004)
6. Karouia, M., Herve, J.M.: A family of novel orientational 3-dof parallel robots. In: 14th RoManSy, pp. 359–368, Udine, 1–4 July 2002
7. Li Q.-C., Huang, Z.: Mobility analysis of a novel 3–5R parallel mechanism family. ASME J. Mech. Des. **126**(1), 79–82 (2004)
8. Fang, Y., Tsai, L.-W.: Structure synthesis of a class of 3-DOF rotational parallel manipulators. IEEE Trans. Robot. Autom. **20**(1), 117–121 (2004)
9. Frisoli, A., et al.: Synthesis by Screw Algebra of Translating Inparallel Actuated Mechanisms. ARK, Piran, 25–29 June 2000
10. Gao, F., et al.: New kinematic structures for 2-,3-,4- and 5- dof parallel manipulator designs. Mech. Mach. Theory **37**(11), 1395–1411 (2002)
11. Huang, Z., Li, Q.C.: Type synthesis of symmetrical lower mobility parallel mechanisms using the constraint synthesis method. Int. J. Robot. Res. **22**(1), 59–79 (2003)
12. Kong, X., Gosselin, C.M.: Type synthesis of 3 DOF translational parallel manipulators based on screw theory. ASME J. Mech. Des. **126**(1), 83–92 (2004)

Life Estimation of the Contact Surfaces

M. Hejnová and J. Ondrášek

Abstract A life estimation of the contact surfaces is an important part of the cam mechanisms design. The aim of this article is to compare available methods of the life estimation. Every theory has its own experimental constants. Their influence on the resulting life estimation is considerable. The real life of the contact surfaces can be markedly different according to used theory. A solving can be to refine the theories. It is possible to improve the experimental constants by means of the experimental testing.

Keywords Cam mechanism · Service life · Contact surface · Rolling contact fatigue

1 Introduction

VÚTS, a.s. deals with the design of cam mechanisms and cams production more than thirty years. This provides us a lot of experience in design and calculation of both axial and radial cams. In this context, currently we solve the methodology of the life prediction of the cam surface. On this basis, we can determine the life of the cam mechanism respectively time when damage occurs. It is possible to use several methods for life estimation of the cam contact surface. This article deals with two most used available methods.

M. Hejnová (✉) · J. Ondrášek
VÚTS, a.s., Liberec, Czech Republic
e-mail: monika.hejnova@vuts.cz

J. Ondrášek
e-mail: jiri.ondrasek@vuts.cz

J. Beran et al. (eds.), *Advances in Mechanism Design II*,
Mechanisms and Machine Science 44, DOI 10.1007/978-3-319-44087-3_6

Micropitting, steel *14 220*, *11x10*^{6} *cycles*

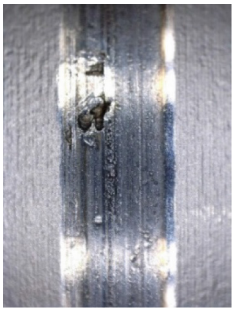

Macropitting, steel *14 220*, *202x10*^{6} *cycles*

Fig. 1 Pitting

2 Surface Fatigue

The surface fatigue [1], called rolling contact fatigue, occurs in functional surfaces that are exposed to repeated loading during movement of functional surfaces of machine components. It may be a relative rolling movement or a combination of sliding and rolling, what is more common in practice.

Pitting is the mechanism of damage, which can lead to the fatigue fracture damage. This type of failure occurs in machine elements, which are cyclically loaded [1].

Micropitting [1] is manifested by the presence of microscopic pits on the material surface in the contact. They are produced due to the repeated cyclic loading of the contact at which occurs to rolling and sliding and they are formed by plastic deformation of the surface asperities. Micropitting is more often observed at materials with higher surface hardness [1]. The micropits are small relative to the size of the contact zone (see Fig. 1), typically 10–20 μm deep and usual size smaller than 100 μm.

Macropitting is presented by cracks formed in a certain depth under the surface [1], where the shear stress is maximal due to Hertzian pressure. It [1] causes the formation of large pits (about 1 mm) on the material surface in the contact. These arise due to the spread of subsurface cracks that leads to flaking larger parts of the material from the surface.

There are another types of the damage mechanisms, e.g. spalling, galling, scuffing, scoring and their combinations. Description of these types of damage is in [1].

3 Theoretical Methods for Life Estimation

The commonly used theoretical models are based on the Hertz's contact theory. On its basic is given the value of the Hertzian pressure, which is decisive at the determining of the save load. At this load it will not occur damage of the functional surfaces of the cam and roller.

Assumptions of Hertz's theory are available in the literature [2]. There is a schematic view of the contact of the two cylinders in Fig. 2. There is a contact of cam and roller at the cam mechanism. The length of the contact area is denoted l, the radii of curvature at point of contact are ${}^{1}\rho_y$, ${}^{2}\rho_y$ and F defines normal reaction between the particular elements of the pair [2].

Assuming a uniform load distribution over the length l, the load in proportion to the length unit will be (1).

$$f = \frac{F}{l} \tag{1}$$

The deflection between two bodies in contact may produce a flat of width $2b$ and length l (see Fig. 2) with coordinates O, x, y, z located in its centre. The flat is situated at the coordinate plane xy where the axis x coincides with the contact area of non-loaded bodies. Contact load distribution $p(y)$ along the elliptic cylinder is (2).

$$p = \frac{2f}{\pi b}\sqrt{1 - \left(\frac{y}{b}\right)^2} \tag{2}$$

Hertzian pressure is a maximum compressive stress p_H defined as (3).

$$p_H = \frac{2f}{\pi b} = \sqrt{\frac{f\left(\left|{}^{2}\rho_y\right| \pm {}^{1}\rho_y\right)}{\pi(\delta_1 + \delta_2)\,{}^{1}\rho_y\left|{}^{2}\rho_y\right|}} \tag{3}$$

Unlike the positive radius of curvature of the roller follower ${}^{1}\rho_y$, the radius of curvature of the cam surface in contact ${}^{2}\rho_y$ may attain both, positive or negative values. Actually this fact is defined in relation (3) by quantity $\left|{}^{2}\rho_y\right|$.

$$\delta_{1,2} = \frac{1 - \mu_{1,2}^2}{E_{1,2}} \tag{4}$$

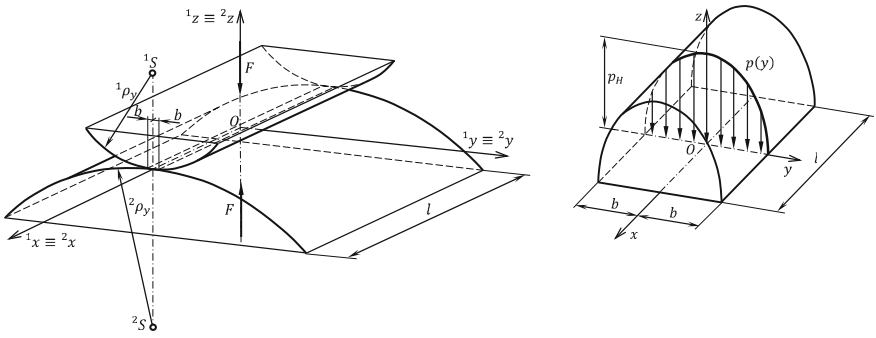

Fig. 2 Contact of cylindrical bodies with parallel axes and pressure distribution in contact

The quantities δ_1, δ_2 are the characteristics of elasticity of the elements in the pair (4), where the Poisson's ratio and the modulus of tension elasticity are denoted as $\mu_{1,2}$ and $E_{1,2}$ respectively. Rearranging relation (3) we get the bisected contact area (5).

$$b = 2\sqrt{\frac{f(\delta_1+\delta_2)^1\rho_y|^2\rho_y|}{\pi\left(|^2\rho_y| \pm {}^1\rho_y\right)}} \tag{5}$$

The next step is to calculate a reduces stress [2]. The reduced stresses σ_{red} (ψ, ς) are limited by the actual strength condition, written in the form (6), where ψ is an angular cam displacement and $\psi \in \langle 0, 2\pi)$. and $\varsigma = |z|/b \geq 0$.

$$\max\sigma_{red}(\psi, \varsigma) < \sigma_h \tag{6}$$

For steel are the usual values $\sigma_c \approx 0.33\ R_m$ and $R_e \approx (0.55{-}0.8)R_m$. However, since the transitory stress limit is $\sigma_h \approx 2\sigma_c \approx 0.66\ R_m$, the relation (6) may be replaced by the inequality (7), where $\psi \in \langle 0, 2\pi)$ and $\varsigma = z/b \geq 0$. This equation states that no destructive action of elastic deformation is produced in the general pair under operation.

$$\max\sigma_{red}(\psi, \varsigma) < R_e \tag{7}$$

3.1 Model A

There were derived equation for values of Hertzian pressure p_H and reduced stress σ_{red}(ψ, ς) in Chap. 5. In the literature [2] is given a condition, when it will not occur damage of the contact surface body in form (8),

$$p_H \leq \frac{K}{N^{1/6}} f(H), \quad K = 4777\,\text{MPa} \tag{8}$$

where a variable N is the life in millions of cycles, parameter H is hardness of the surface in the contact and a function $f(H)$ is expresses an influence of the surface hardness on the Hertzian pressure p_H (MPa). This pressure is given by means of Eq. (3) for cylindrical bodies in contact.

A variable K is the constant empirically determined. The surface hardness H can be expressed by Brinnell's as HB or by Rockwell's as HRC. Thus are for function $f(H)$ formulated empirical equation (9).

$$\begin{aligned} f(H) &= \frac{HB}{1000} \\ f(H) &= 0.251 + \frac{HRC}{100}\left[\frac{HRC}{100}\left(2.74 - 1.22\frac{HRC}{100}\right) - 0.6\right] \end{aligned} \tag{9}$$

3.2 Model B

An approach based on a load distribution in the plane contact area of the cylindrical bodies is in the literature [3]. In this model the main compressive stress σ_z takes the highest value for $y = 0\,\text{mm}$ (10).

$$\sigma_z(y=0) = -p_H = -\frac{2f}{\pi b} \tag{10}$$

Substituting of equation for bisected contact area b (5) and Eq. (10) and rearranging we get Eq. (11).

$$\sigma_z^2 = \frac{fE^*}{\pi R_e} \tag{11}$$

For the relative load f is valid (12), where the parameter K_I is the experimental load-stress factor (13).

$$f = \frac{\pi R_e}{E^*}\sigma_z^2 = K_I R_e \tag{12}$$

$$K_I = \frac{\pi}{E^*}\sigma_z^2 \tag{13}$$

Parameter K_I is used to determine safe load F for given number of cycles or for number of cycles which we can expect to destruction at the given load. There is dimension of the equivalent modulus of elasticity E^* and main compressive stress σ_z given by MPa in Eq. (13).

Parameter K_I is possible to use in the equation of the load/life curve, called *S-N* curve to finding of the expected number of the cycles N at the given load (14).

$$\log_{10}(145.03789 \cdot K_I) = \frac{\zeta - \log_{10} N}{\lambda} \tag{14}$$

Stress factors ζ and λ in the Eq. (14) express a slope and an intersection in the *S-N* diagram in logarithmic coordinates. The *S-N* diagram is made from a large amount of the test data. The constant 145.03789 expresses conversion of the metric to anglo-american measurement system. Parameter K_I is in [3] given in K_I (psi).

On basis of Eqs. (13) and (14) we can write the condition for the load level, at which does not occur to damage of the body surface in contact (15).

$$p_H \leq \sqrt{\frac{E^*}{145.03789 \cdot \pi}\left(\frac{10^{\zeta}}{N}\right)^{\frac{1}{\lambda}}}. \tag{15}$$

3.3 Comparison of Results

There is a lot of the tested materials in [3]. In this chapter are presented results for material *12 024*. Material properties of the steel *12 024* are in Table 1. Model A is calculated by Eq. (8), Model B by Eq. (15). Results are in graph on Fig. 3.

We can see a considerable difference in used methods results in the graph (see Fig. 3) for load/life curves. Model A [calculation by Eq. (8)] is more on side of the safety.

Table 1 Material characteristics of the steel *12 024*

Young's modulus of elasticity	E (GPa)	200.0
Shear modulus	G (GPa)	77.52
Poisson's ratio	μ (–)	0.29
Ultimate strength	R_m (Mpa)	400.0
Yield strength	R_e (MPa)	290.0
Rockwell hardness	*HRC*	55
Stress factor 1	λ (–)	13.20
Stress factor 2	ς (–)	61.06

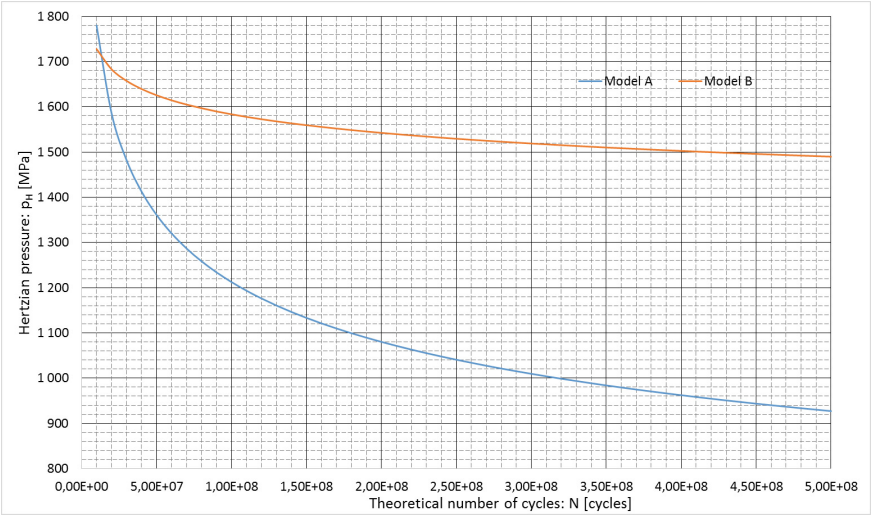

Fig. 3 Load/life curves for steel *12 024*

4 Conclusions

We have used in most cases only Model A for determination of the material for cam producing in VÚTS. Model A is more on the side of safety and this give a space for increasing of the load. Our experience indicate in last time that life estimation only in dependence on surface hardness is not optimal. This article shows that at the choice of the material for cam producing is necessary to take into account another parameters too. On the other side it is difficult to get concrete material parameters, because experimental test for life testing are very time consuming.

Acknowledgments The research work reported here was made possible by FR-TI4/801- project supported by the Ministry of Industry and Trade.

References

1. Hejnova, M.: Service life assessment of the cam mechanisms. Procedia Eng. **96**, 157–163 (2014). doi:10.1016/j.proeng.2014.12.135. Avaliable from: http://www.sciencedirect.com/science/article/pii/S1877705814031944
2. Koloc, Z., Václavík, M.: Vačkové Mechanismy. SNTL—Nakladatelství technické literatury, Praha (1988). 379 s
3. Norton, R.L.: Cam design and manufacturing handbook. Industrial Press Inc., New York (2009). ISBN 978-0-8311-3367-2

Calculation of the Contours of a Radial Double Cam Based on an Approximate Course of the 2nd Derivative of the Displacement Law of a Working Link

P. Jirásko and M. Václavík

Abstract This paper deals with requirements for the production of cam mechanisms or cams that reliably operate in manufacturing machines even for several decades and currently, it is necessary their replacement due to wear. Those machines are usually unique in their construction and they meet the demanding technological requirements of the production even today. The effort of producers or users is to overhaul those machines and so continue to use them. We meet today with the requirements for the manufacture of years proven cam mechanisms with an insufficient or incomplete production documentation. The paper focuses on one such characteristic case.

Keywords Radial cam and double cam · Cam mechanism · Kinematic analysis and synthesis · Approximation

1 Introduction

A significant expansion of cams and cam mechanisms occurred in the seventies and eighties of the last century with the mass deployment of NC machine tools. At that time, the use of computer technology was very limited and it concentrated in research centers or at major manufacturers, for example, at those producing machine tools. The situation in computer technology corresponded to that time with its unique hardware and software components. The conventional and today widespread PC was not in the world. At that time, VÚTS used calculators and first computers from Hewlett-Packard and Olivetti. The same situation was also among

P. Jirásko (✉) · M. Václavík
VÚTS, a.s., Liberec, Czech Republic
e-mail: petr.jirasko@vuts.cz

M. Václavík
e-mail: miroslav.vaclavik@vuts.cz

J. Beran et al. (eds.), *Advances in Mechanism Design II*,
Mechanisms and Machine Science 44, DOI 10.1007/978-3-319-44087-3_7

major manufacturers of machines using cam mechanisms. In such a way, on specific HW computing means, there were developed unique and therefore non-transferable programs with calculation algorithms of production coordinates of the contours of cams. Production data were archived and transferred to machines through punched tapes. After the rapid development of computer technology in the following decades, there often occurred both a loss of production data and "forgetting" of special algorithms and analytical relations describing unique technological movements that were implemented by cam mechanisms.

The special customer's requirement was therefore the manufacture of a cam based on the schematic description of the 2nd derivative of motion function of the working link of a cam mechanism. The paper depicts a methodology for calculating the production coordinates of a radial double cam of that business case.

1.1 General Calculation Methodology of Cam Mechanisms in VÚTS

VÚTS developed the methodology and the associated software to address these cases. It is a system of two communicating sw means that are APROX programs (approximation of a discreetly or numerically defined displacement law with an equidistant step) and KIN (kinematic analysis and synthesis of compound cam mechanisms).

Using the *APROX* program, it can be approximated a function which is defined in a one or several discrete intervals—*blocks*. Inside the selected block, there are chosen *intervals* or *boundary* of intervals. In the intervals, the given function will be approximated using a polynomial of the fifth or seventh degree. The courses of the polynomials can be influenced by the position of *boundary points* or interval boundaries, *boundary values* of polynomials or a degree of a polynomial. The position of the boundary points will be chosen, the boundary values are determined by the program and they can be then corrected. The correction is to be performed in the boundary points of the blocks always there when it is necessary to ensure the mutual sequence of the blocks (in all derivatives according to the degree of the polynomial).

By *kinematic analysis* of the basic cam mechanism with conventional cam it is understood determination of the movement (kinematic quantities) of the working link with rotary (rocker) or sliding (follower) movement for the given movement at the *input* and the defined dimensions of a cam mechanism including the theoretical profile (path of the roller center). Thus, by an *analysis* it is determined the *motion function* of the working link (rocker, follower) in dependence on time or *displacement law* depending on the angle of rotation of the cam at a constant angular velocity equal to 1 (rad/s). The block diagram is in Fig. 1.

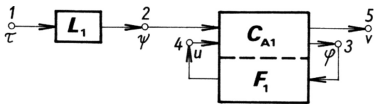

Fig. 1 Block diagram of kinematic analysis [1, 2]

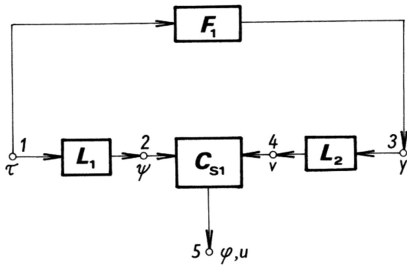

Fig. 2 Block diagram of kinematic synthesis [1, 2]

By *kinematic synthesis* of a basic cam mechanism with conventional cam it is meant the design of a mechanism for the prescribed rotary (rocker) or sliding (follower) movement of the working link and for the given movement of a cam. The result is usually determination of the polar coordinates of the theoretical profile of a cam (path of the roller center of the basic cam mechanism) following the displacement law of the working link or the rocker or follower depending on the constant rotation of the cam. The block diagram is in Fig. 2.

In both assignments, linear constraint L_1 defines the sense of the cam rotation. Function block F_1 in the case of *analysis* it is function relation $u = u(\varphi)$ of the polar coordinates of the theoretical profile of the radial cam and in the case of *synthesis* it is displacement law $y = y(\tau)$ of the working link (rocker, follower) depending on the non-oriented uniform angle of rotation τ or time. Linear constraint L_2 in the case of synthesis it is transformation (translation, scaling) of displacement law F_1. The result of the calculation of *analysis* is according to Fig. 1 *kinematic quantities of the working link* (rocker, follower). The result of the calculation of *synthesis* according to Fig. 2 is *polar coordinates* (φ, u) *of the theoretical profile of a cam* (generally radial, axial, and globoid) iterated to the specified equidistant step of coordinate φ.

2 Specification of the Assignment

By the customer, as production documentation, it is delivered a production drawing according to which the production technology of the blank of a double cam is determined, a cutout is in Fig. 3. (For the reasons of the confidentiality of the customer, merely illustrative cutouts are listed). Other documentation is records for the calculation and for clarity, they are again given partial cutouts in Figs. 4 and 5.

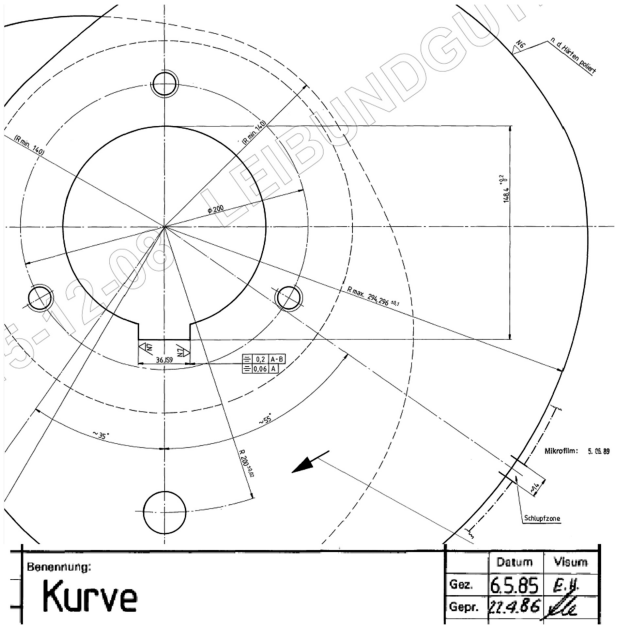

Fig. 3 Cutouts from the drawing of a double cam

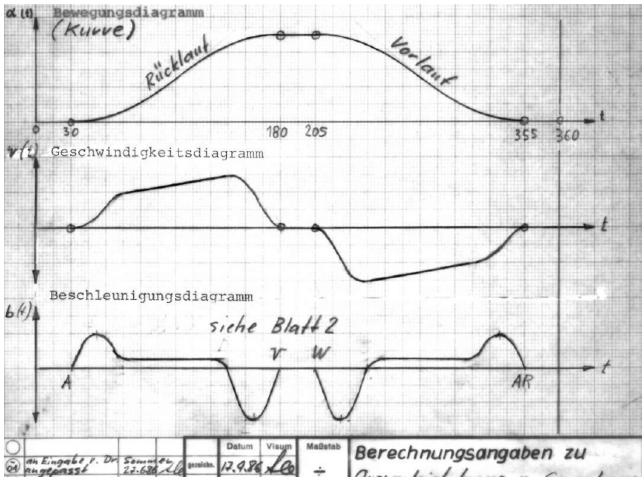

Fig. 4 Scheme of the motion function of the working link

Therefore, it is a schematic representation of the motion function of the working link, which is the rocker of a double cam. Specific usable data for the calculation are only the values of the acceleration polygon with a very course non-equidistant step

Fig. 5 Setting values of the acceleration polygon (partial view)

Bewegungsgesetze		Δ ζ°	Δ α°	b/b max	α̇
Rast		30			0
Beschl. - Polygon		150	+32,5946		
Zwischenwerte	A	0		0	
	B	9		0,2409	
	C	8		0,9511	
	D	11		0,5812	
	E	14		0,6913	
	F	18		0,7613	
	G	22		0,7613	
	H	26		0,6913	

of the independently variable and the geometry of the double cam mechanism (length of the frame, lengths of the rockers of the master and slave cams, roller diameters).

3 The Methodology of Calculation of the Production Coordinates

Due to a limited extent of the paper, we will present only essential documents. Data of the acceleration polygon (see Figs. 4 and 5) are interpolated and subsequently per sections twice numerically integrated. The thus obtained data file is to be approximated per selected sections (sw APROX) by polynomials of the 5th or 7th degree with the check of a positional deviation according to Fig. 6. The file of analytic relations describing the displacement law of the rocker (15 sections of the polynomials) enters the kinematic synthesis of the KIN program according to Fig. 7. The result of the synthesis is the polar coordinates of any arbitrary equidistances of both cams (master and slave) according to the scheme in Fig. 2.

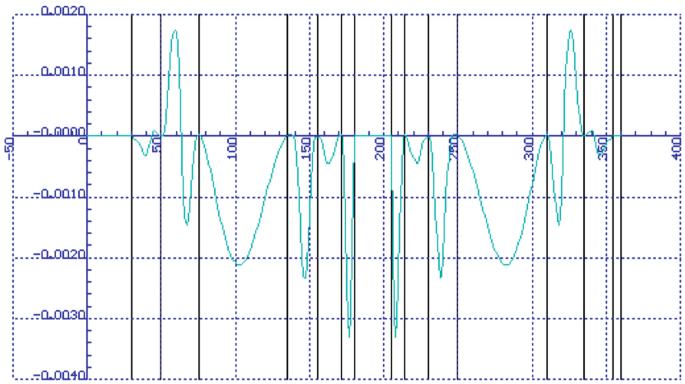

Fig. 6 Positional error with respect to the course of the 2nd derivative of the displacement law of the double cam rocker (15 sections), X-axis (deg), Y-axis (mm)

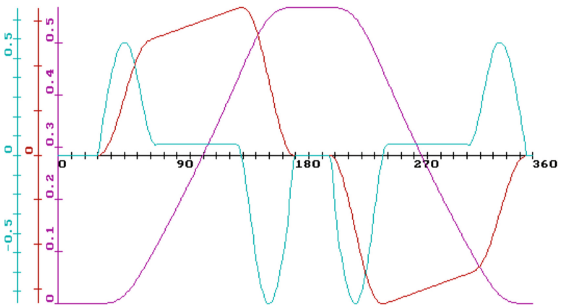

Fig. 7 Displacement law of the double cam rocker entering sw KIN, X-axis (deg), Y0-axis (mm), Y1 (rad/rad), Y2 (rad/rad^2)

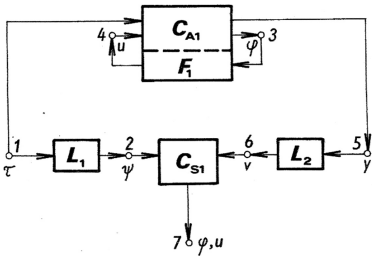

Fig. 8 Task of the analysis of the master cam (sw APROX, sw KIN) with the synthesis of the slave cam (sw KIN) [2]

4 Conclusion

The double cam was produced in the required quality and delivered to full satisfaction of a customer from Western Europe who requires maximum quality. The contract value was in the order of thousands of euros. It was a double cam made from the blank of a diameter of 600 (mm) and a weight of about 350 (kg). The mentioned case is not unique, contracts of a similar type on the basis of insufficient documentation or based on specific worn cams are becoming more common. According to Fig. 8, the creation of the double cam production coordinates is from the measured contour of the master cam by combining *kinematic analysis and synthesis*. This can be done even with worn double cams to which no drawing and calculation documentation is available.

References

1. Koloc, Z., Václavík, M.: Vačkové Mechanismy. SNTL, Praha (1988)
2. Jirásko, P. a kolektiv autorů: Mechatronika pohonů pracovních členů mechanismů, Monografie VÚTS, a.s., ISBN: 978-80-87184-63-9

The Elastic Compression in the Contact Region of a Cam Mechanism General Kinematic Pair

J. Ondrášek

Abstract The paper deals with the elastic compression in the contact region of a general kinematic pair. In the case of a general cam mechanism, the general kinematic pair is formed of the contact of the working surfaces of a cam and a follower. In technical practice, the contact of the cam and the follower is created by the cylinders in contact with the parallel axes for one thing and for another, by the cylinder and the three-dimensional body, which is described locally in contact with the orthogonal radii of curvature. This issue is solved on the basis of the contact mechanics. For both cases, the relations for calculating the elastic compression in the contact regions were defined. This mathematical model is verified through the experimental identification, the general kinematic pair is carried out using a testing device. The aim of the tests was to determine the mutual approach of distant points in the two three-dimensional solids in contact.

Keywords Elastic compression · Contact region · General kinematic pair · Cam mechanism

1 Introduction

In some computational analyses of cam mechanisms, an interaction of a cam contour with a follower has to be considered as a real kinematic pair, i.e. with a backlash and a friction. This occurs, for example, when bearing rating life of the cam mechanism roller is determined. In the case of a model creation of a cam mechanism general kinematic pair, the contact of two cylinders with the parallel axes or a cylindrical body and a non-conforming body may be substituted for the interaction of a cam contour with a follower. The cylinder represents a cam or a cylindrical cam roller and the non-conforming body a crowned cam roller.

J. Ondrášek (✉)
VÚTS, a.s., Liberec, Czech Republic
e-mail: jiri.ondrasek@vuts.cz

J. Beran et al. (eds.), *Advances in Mechanism Design II*,
Mechanisms and Machine Science 44, DOI 10.1007/978-3-319-44087-3_8

Three ways exist for the creation of mathematical models: theoretical, experimental and combination of both. A theoretical mathematical model of the general kinematic pair requires knowledge of some parameters, i.e. a normal displacement and a normal stiffness in a contact region. These parameters may be determined on the basis of a Hertzian contact theory or FEM. In this case, FEM is ineffective.

2 Hertzian Contact Theory

This section gives only basic information on how to determine the compression of two solids in contact. The Hertzian contact stress theory deals with this issue and this theory is described in detail in [1].

When two three-dimensional body are brought into contact they touch initially at a single point or along a line. Under the action of a slightest load, they will deform and contact is made over a finite area which is small compared with the dimensions of both bodies. On the basis of a theory of contact, the shape of the contact area is predicted and the components of deformation and stress in both bodies are calculated in the vicinity of the contact region. For the Hertzian contact stress theory, the fundamental assumptions are, see [1]:

– The shape of each surface in the contact region can be described by a homogeneous quadratic polynomial in two variables:

$$z_i = \mp \frac{1}{2}\left(\frac{1}{\rho_{xi}}x^2 + \frac{1}{\rho_{yi}}y^2\right), \quad i = 1, 2, \tag{1}$$

where ρ_{xi} and ρ_{yi} are the principal radii of curvature of the surface at the rectangular coordinate system origin, see Fig. 1.

– Contact stresses and deformations satisfy the differential equations for stress and strain of homogeneous, isotropic, and elastic bodies in equilibrium. The pressure distribution on the contact area is given by equation:

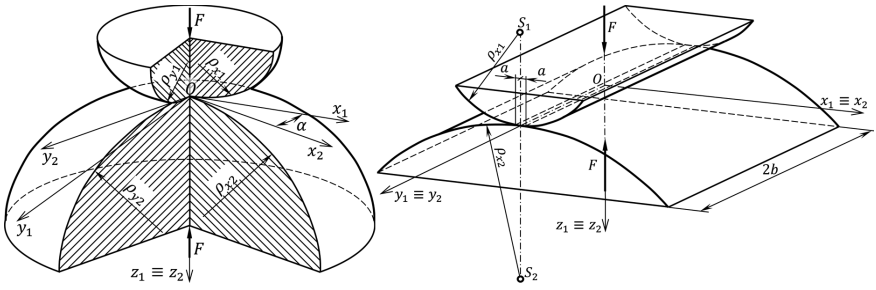

Fig. 1 Contact of two non-conforming bodies and contact of two cylindrical bodies

$$p(x,y) = p_H\sqrt{1-(x/a)^2-(y/b)^2}, \tag{2}$$

where a and b are respective major and minor semi-axes of the elliptical contact area and a maximum value p_H is called Hertzian pressure. In the case of the contact of two cylindrical bodies, the variable y is constant and Eqs. (1) and (2) are the functions just of the variable x.

- Both contacting surfaces are smooth and frictionless.
- The size of the contact area is small compared with the size of both bodies.

The compressive contact of two bodies is caused by application of a normal load F and a contact area is formed. Remote parts T_1 and T_2 of the bodies are approached each other by a distance δ. Points S_1 and S_2 on the approaching contact surfaces are elastically displaced by amount u_{z1} and u_{z2}, as shown in Fig. 2.

On the basis of the Hertzian contact stress theory, the equation of the normal displacement of two non-conforming bodies is derived in the following form:

$$\delta = \delta_1 + \delta_2 = \frac{3F}{2\pi a E^*}K(e), \quad e = \sqrt{1-(b/a)^2}, \quad a > b, \tag{3}$$

where $K(e)$ is complete elliptic integral of the argument e [2], which expresses the eccentricity of the contact ellipse and E^* is the effective modulus of elasticity. The normal stiffness of the contact region is obtained by differentiating the deflection with respect to load F to get compliance, then inverting:

$$k = \left(\frac{\partial\delta}{\partial F}\right)^{-1} = \frac{K(e)}{\pi a E^*}, \quad E^* = \frac{1-\mu_1^2}{E_1} + \frac{1-\mu_2^2}{E_2}, \tag{4}$$

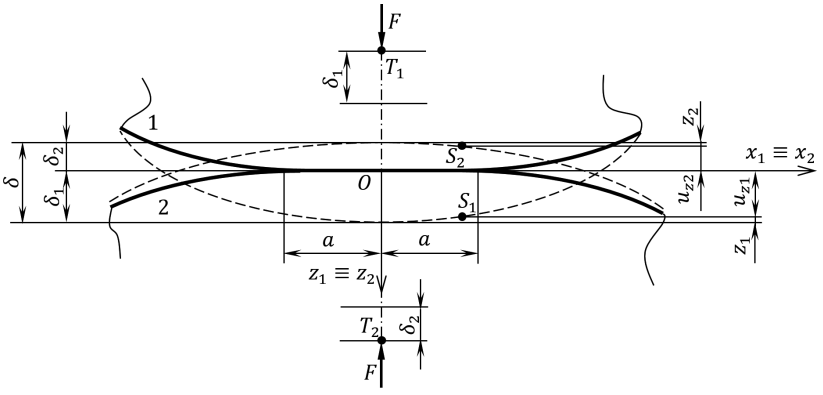

Fig. 2 Contact of two non-conforming bodies after elastic deformation

where E_i and μ_i are the respective Young's modulus of elasticity and Poisson's ratio of the individual solids. In the case of the two cylindrical bodies contact, the normal displacement δ and the normal stiffness k are expressed as:

$$\delta = \delta_1 + \delta_2, \quad \delta_i = \frac{N}{2b} \cdot \frac{1 - \mu_i^2}{\pi E_i} \cdot \left[2 \ln\left(\frac{4L_i}{a}\right) - 1 \right], \quad i = 1, 2, \tag{5}$$

$$k = \left(\frac{\partial \delta}{\partial F}\right)^{-1} = \frac{2b\pi}{\left\{ \frac{1-\mu_1^2}{\pi E_1} \left[2 \ln\left(\frac{4L_1}{a}\right) - 1 \right] + \frac{1-\mu_2^2}{\pi E_2} \left[2 \ln\left(\frac{4L_2}{a}\right) - 1 \right] - \frac{1}{E^*} \right\}}, \tag{6}$$

where variable a denotes the half width of the contact area and the constant L_i is the width of the individual bodies, which may be not equal to the length of the contact area $2b$.

3 Testing jig

To the verification of the validity of the Eqs. (3) and (5) and thus the verification of a general kinematic pair mathematical model, a testing jig has been designed and implemented, see Fig. 3. The aim of the experiments was the determination of the vertical distance change of two fitting pins, which are approached under the action of a normal load F. The lower pin is assigned to the stationary cylindrical body which represents a cam with the radii of curvature ρ_{x2} = 50 mm and the width L_2 = 25 mm and the upper pin to the body which represents a cylindrical or crowned cam rollers with the set of diameters d = {30, 35, 47, 62, 80, 90}.

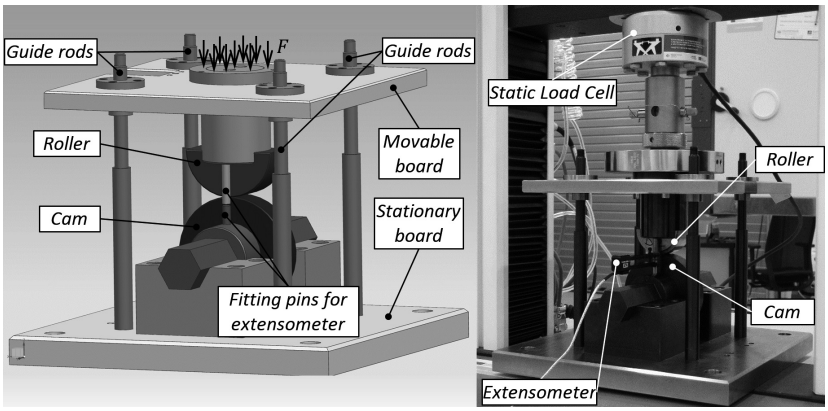

Fig. 3 Testing jig of contact zone deformation of two solids

The vertical displacement of the upper pin was determined by using the *Instron 3369* universal testing machine. The testing jig with the appropriate cam roller and with the connected uniaxial extensometer *Instron 2620-601* to pins was placed between its compressive jaws. Load cycles carried out between compressive forces F_1 and F_2, then strain values were recorded in the interval $\varepsilon_e \in \langle \varepsilon_{e1}; \varepsilon_{e2} \rangle$ [–]. The measured deformation of the contact region of the cam and the roller is defined by the equation: $\delta_e = l_0 \varepsilon_e$, where $l_0 = 12.5$ mm denotes the distance of extensometer contact tips. The percentage deviation between measured δ_e and theoretical δ values of the deformation is defined by the equation:

$$p = \left(\frac{\Delta \delta_e}{\Delta \delta} - 1 \right) \cdot 100\,\% = \left(\frac{\delta_{e2} - \delta_{e1}}{\delta_2 - \delta_1} - 1 \right) \cdot 100\,\% = \left(\frac{\delta_e(F_2) - \delta_e(F_1)}{\delta(F_2) - \delta(F_1)} - 1 \right) \cdot 100\,\%. \tag{8}$$

The typical load cycles are shown in Figs. 4 and 5 where arrows show the process of the loading. From these two examples, the hysteretic characteristic of the load cycle is evident. This is due to the fact that the contacting surfaces are not smooth and frictionless. In the case of the cylindrical cam rollers, the shape of the load cycle lower section is caused by the sum of a manufacturing inaccuracy of individual parts, see Fig. 4. Examples of calculated and measured data are presented in Table 1.

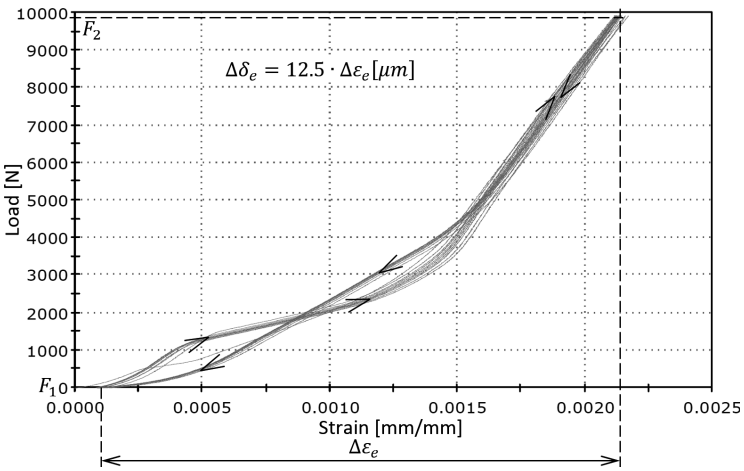

Fig. 4 Loading cycles of two cylindrical bodies

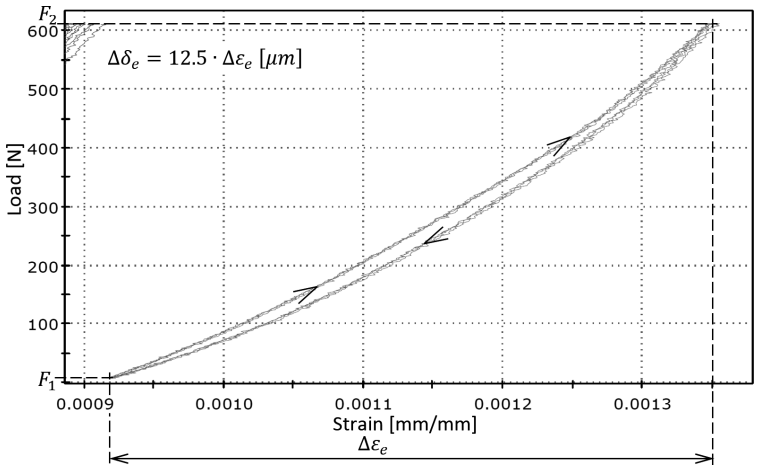

Fig. 5 Loading cycles of three-dimensional body and cylindrical body

Table 1 Contact region deformations of cam and rollers

Dimensions		Cylindrical cam roller				Crowned cam roller: R = 500 mm			
d (mm)	L_1 (mm)	F (kN)	Δδ (μm)	$\Delta\delta_e$ (μm)	p (%)	F (N)	Δδ (μm)	$\Delta\delta_e$ (μm)	p (%)
30	14	1.5–3.0	3.145	3.806	21.2	200–450	1.711	1.794	4.8
35	18	2.0–4.0	3.286	5.050	53.7	200–500	1.989	2.706	36.1
47	24	3.0–6.5	4.276	5.525	29.2	200–700	3.025	3.988	31.8
62	29	2.0–8.5	7.622	10.750	41.0	200–900	3.933	4.825	22.7
80	35	5.0–10.0	5.655	6.706	18.6	200–1000	4.325	5.969	38.0
90	35	3.5–10.0	7.398	9.094	22.9	200–1100	4.726	4.725	0.0

4 Conclusions

The Hertzian contact theory is an important tool for analysis in cam mechanism design. It allows for the prediction of compression and stiffness of a contact region in a general kinematic pair under a load. Then they are used in the definition of a model of the real general kinematic pair of the cam mechanism using the software MSC.ADAMS.

To the verification of the general kinematic pair mathematical model, a testing jig has been designed and implemented. On the basis of measurements, it is evident that the measured data are characterized by a greater value than the calculated data

because the real contact area is formed smaller than the theoretical contact area under the action of a normal load. This is due to the fact, that the contacting surfaces are not smooth and frictionless and the real parts of the testing jig are characterized by a certain degree of manufacturing inaccuracies.

Acknowledgments This paper was created within the work on the project FR-TI4/801—Project supported by the Ministry of Industry and Trade.

References

1. Johnson, K.L.: Contact Mechanics. Cambridge University Press, Cambridge (1985). ISBN 0 521 34796 3
2. Arfken, G.B., Weber, H.J., Harris, F.E.: Mathematical Methods for Physicists, 7th edn., Section 18.8, "Elliptic Integrals", pp. 927–933, Elsevier, Waltham (2013). ISBN 978-0-12384654-9

Design of a Legged Walking Robot with Adjustable Parameters

Y. Zhang, V. Arakelian and J.-P. Le Baron

Abstract In the past decades, an extensive research has been focused on legged walking robots. One of the most attractive trends in the design of walking robots is the development of biped robots with reduced number of degrees of freedom. This paper deals with a new solution of a legged walking mechanism with reduced number of degrees of freedom. It consists of a driven cam system mounted on the body frame and connected with feet via pantograph mechanisms. The introduced adjustable parameters allow one to generate two different steps with variable heights as well as allow the robot to climb stairs. The efficiency of the suggested design principle of the legged walking robot is illustrated by numerical simulations carried out via ADAMS software.

Keywords Mechanism design · Walking robot · Pantograph-leg mechanism · Mechanism with adjustable parameters

1 Introduction

It is well known that legged locomotion is more efficient, speedy, and versatile than the one by track and wheeled vehicles when it operates on a rough terrain, steeps, stairs or avoid obstacles. This research field has attracted great interest of many research groups and companies in the past few decades.

The pioneering works in the field of legged robots were achieved around 1970 by two famous researchers, Kato [1–3] and Vukobratovic [4, 5]. Both works were characterized by the design of relevant experimental systems. In Japan, the first

Y. Zhang · V. Arakelian (✉) · J.-P. Le Baron
Department of M&CSE, INSA-Rennes, Rennes, France
e-mail: vigen.arakelyan@insa-rennes.fr; vigen.arakelyan@irccyn.ec-nantes.fr

Y. Zhang
e-mail: yang.zhang@insa-rennes.fr

V. Arakelian
IRCCyN, UMR CNRS 6597, Nantes, France

J. Beran et al. (eds.), *Advances in Mechanism Design II*,
Mechanisms and Machine Science 44, DOI 10.1007/978-3-319-44087-3_9

anthropomorphic robot, WABOT 1, was demonstrated in 1973 at Waseda University. In Yugoslavia, Belgrade, at the Mihailo Puppin Institute, Miomir Vukobratovic and his team designed the first active exoskeletons and several other devices. In the next decade, the breakthroughs came from the United States [6–9]. Simultaneously, Robert McGhee and Kenneth Waldron, achieved the design of a quasi-industrial system able to walk on natural irregular terrain, which was driven by a human [10, 11]. The idea of studying purely passive mechanical systems was proposed by McGeer [12]. In this paper, McGeer has showed that there exists a class of two-legged machines for which walking is a natural dynamic mode: once started on a shallow slope, such a machine will settle into a steady gait quite comparable to human walking, without active control or energy input. Several researchers have followed the tracks open by Tad McGeer.

The end of the millennium was a period of intense technological activities. Industrial breakthroughs showed to the world that building true humanoids was now possible. In Japan, the first humanoid robot, P2, was exhibited by Honda in 1996, followed by several more: ASIMO (Honda), QRIO (Sony), HRP (Kawada), etc.

To create biped robots walking like a human is necessary to use a large number of actuators. Therefore, these robots are automorphic and flexible. However, there are several drawbacks: complexities of the design and the control system, low energy efficiency due to the masses of motors, as well as an overly high price complicating practical use.

To make a biped robot more attractive, a different methodology can be considered such as constructing a biped robot with reduced number of degrees of freedom [11–15]. In the last decade, at the Laboratory of Robotics and Mechatronics in Cassino University, Marco Ceccarelli and his team have proposed various solutions for Low-Cost Easy-Operation leg design [16–18]. The Chebichev four-bar linkage has been successively used for generation a foot trajectory. In order to amplify the produced motion of the Chebyshev linkage, a pantograph mechanism has been utilized.

This paper is organized as follows. In the first section the leg mechanism is introduced as consisting of a cam mechanism and a pantograph mechanism. Then, the kinematic synthesis of legs is discussed. Finally, the results of numerical simulations are provided.

2 Mechanism Design

The typical walk consists of a repeated gait cycle. The cycle itself contains two phases: a propelling phase and non-propelling phase [18]. In Fig. 1, the thicker line represents the supporting leg (right leg) in propelling phase and the thin line represents the swing leg (left leg) in non-propelling phase. It is known that for design a one-DOF leg mechanism with back-forth and up-down motion capability, the foot point should generate an ovoid curve, which is composed of a straight-line segment and a curved segment (see Fig. 1). The straight-line segment is related to the propelling phase when the corresponding leg touches the ground and could guarantee

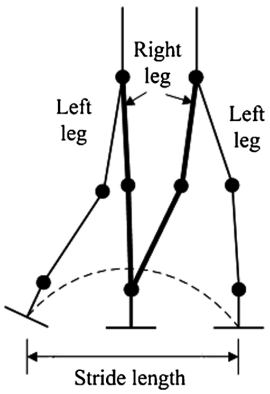

Fig. 1 Two-stage step cycle for human walking gait

stable propelling of the body. The curved segment is related to the non-propelling phase, which is produced by leg when it swings from back to forth [18].

Such a trajectory can be produced by various linkages (Watt, Evans, Chebichev, etc.).

However, these linkages produce only one type of steps with a constant length and height. In addition, in many cases, they provide walking motion only on a horizontal surface.

Therefore, in this paper the proposed one-DOF leg mechanism consists of a cam mechanism with variable angle of inclination connected with a pantograph mechanism permitting to amplify the input motion.

Two adjustable parameters are included in the proposed walking robot: an angle of inclination of the cam mechanism permitting the robot to climb stairs and a pantograph mechanism having the possible to be fixed in two different axes.

Figure 2 shows motions of the proposed leg mechanism with two different points of fixation. As seen from Fig. 2a, b, for the same input trajectories of the point C of the cam mechanism two output trajectories are produced.

The pantograph mechanism is used to amplify the input trajectory of the point C into output trajectory with the same shape of point A. In the suggested design concept, the fixed point can be either B_1 or B_2. Changing the position of the fixed point B_i $(i = 1 \text{ or } 2)$ on the body frame allows one to obtain two output trajectories with different magnitudes. The amplified ratio of the pantograph mechanism depends on the length of links.

For the first case shown in Fig. 2a, the amplify ratio is $k_1 = B_1A/B_1C$ and for the second case shown in Fig. 2b, the amplify ratio is $k_2 = B_2A/B_2C$. Thus, given the need of walking, two different possible steps can be produced with small or large stride length. The choice of adjustable parameters B_i $(i = 1 \text{ or } 2)$ can be carried out taking into account the size of the obstacles and the imposed speed of walking.

The second adjustable parameter is the angle of inclination of the cam mechanism. The rotation of the axis *a-a* of the cam mechanism at an angle of α (Fig. 3)

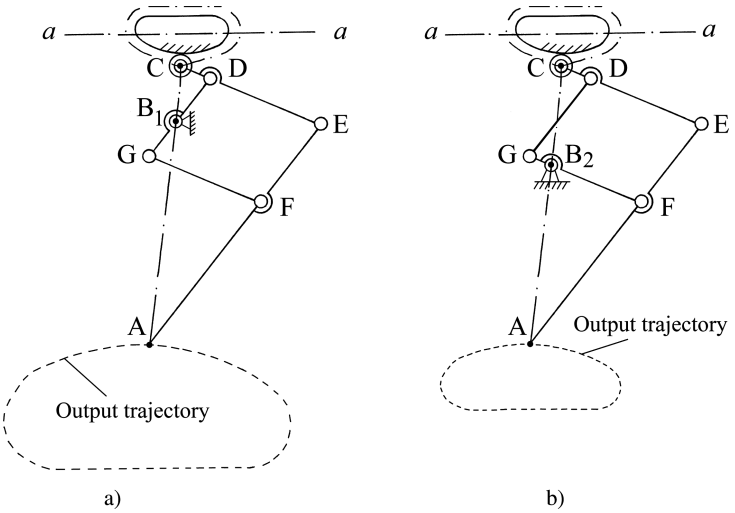

Fig. 2 Leg mechanism with two output trajectories

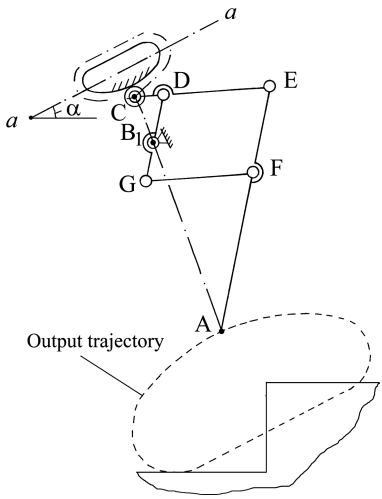

Fig. 3 Leg mechanism with rotated input cam mechanism

allows one to change the orientation of the input trajectory. Such an adjustment allows the walking robot to climb stairs.

The value of the angle α depends on the stair's parameters (height and width). Based on the stair's parameters, the walking robot can be adjusted with inclination angle α as well as with small or large stride length.

To illustrate the efficiency of the suggested walking robot let us consider CAD simulations carried out via ADAMSA software.

3 Numerical Simulations

The CAD model of the legged walking robot was created by CATIA and it was then imported to ADAMS. For the pantograph mechanism, when B_1 is the fixed point, the amplify ratio was 4, and when B_2 is the fixed point, the amplify ratio was 1.

The first two simulations were performed when the robot was walking on the plain road and the fixed point of pantograph mechanism was on B_1 or B_2 respectively. The two motions were inputted on each side of the rolling bars with a speed of 36°/s. The power consumption of input motion during leg's stand phase and swing phase are shown in Figs. 4 and 5.

The second two simulations were performed when the robot was climbing stairs. The two motions were executed on each side of the rolling bars with a speed of 36°/s, the angle between two cams and main body of the robot was adjusted to 20°. Figures 6 and 7 show the power consumption of input motion during leg's stand phase and swing phase.

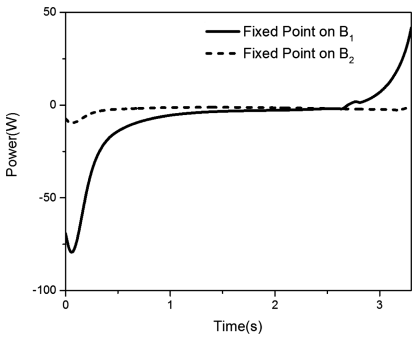

Fig. 4 Power consumption of input motion during leg's stand phase when fixed point on B_1 and B_2

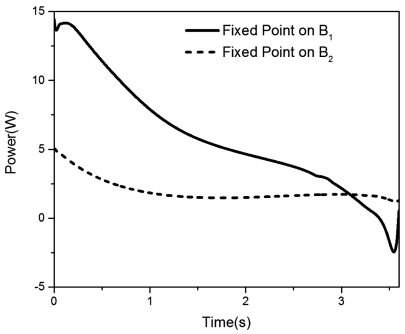

Fig. 5 Power consumption of input motion during leg's swing phase when fixed point on B_1 and B_2

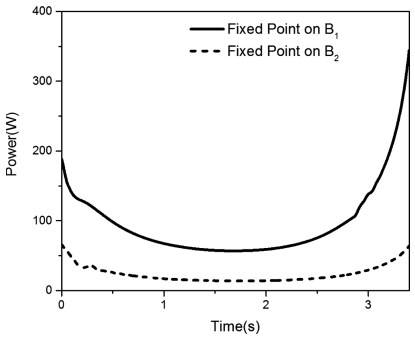

Fig. 6 Power consumption of input motion during leg's stand phase when fixed point on B_1 and B_2

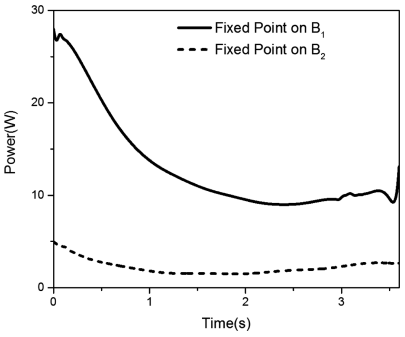

Fig. 7 Power consumption of input motion during leg's swing phase when fixed point on B_1 and B_2

4 Conclusions

In this paper, a one-DOF legged walking robot based on pantograph mechanisms with adjustable parameter is proposed. The introduced adjustable parameters allow one to generate two different steps with variable heights as well as allow the robot to climb stairs. Simulation results showed that the change of fixed point position of pantograph mechanism can significantly change the speeds of walking and climbing stairs, and it also can change the power consumption as well. It means the proposed robot can change its speed and switch to "save energy mode" in some circumstances. On the other hand, the variation of the angle between cams and main body can let the robot be able to climb stairs, and the angle can be adjusted to adapt the slope of stairs. Finally, it is important to note that in the proposed design concept a special attention should be given to the determination of the pressure angle in cam mechanisms to ensure smooth motion.

References

1. Kato, I., Tsuiki, H.: The hydraulically powered biped walking machine with a high carrying capacity. In Proceedings of the Fourth International Symposium on Extremal Control of Human Extremities, Dubrovnik, Yugoslavia, pp. 410–421, Sept 1972

2. Takanishi, A., Ishida, M., Yamazaki, Y., Kato, I.: Realization of dynamic walking by the biped walking robot WL-10RD. In: Japan Industrial Robot Association, N°8, pp. 459–466 (1985)
3. Takanishi, A., Egusa, Y., Tochizawa, M., Takeya, T., Kato, I.: Realization of dynamic biped walking stabilized with trunk motion. ROMANSY **7**, 68–79 (1988)
4. Vukobratovic, M., Juricic, D.: Contribution to the synthesis of biped gait. IEEE Trans. Biomed. Eng. **16**(1), 1–6 (1969)
5. Vukobratovic, M.: Legged locomotion robots and anthropomorphic mechanisms (in English), Mihailo Pupin Institute, Belgrade (1975) (also published in Japanese, Nikkan Shimbun Ltd. Tokyo, 1975; in Russian, "MIR", Moscow, 1976 in Chinese, Beijing, 1983)
6. Raibert, M.H.: Legged robots that balance. MIT Press, Cambridge (1986)
7. Gubina, F., Hemami, H., McGhee, R.B.: On the dynamic stability of biped locomotion. IEEE Trans. Biomed. Eng. BME **21**(2), 102–108 (1974)
8. McGhee, R.B.: Vehicular legged locomotion. In: Saridis, G.N. (ed.) Advances in Automation and Robotics, pp. 259–284. JAI Press, New York (1985)
9. Waldron, K.A.: Force and motion management in legged locomotion. IEEE J. Robot. Autom. **2**(4), 214–230 (1986)
10. Waldron, K.J., McGhee, R.B.: The adaptive suspension vehicle. IEEE Contr. Syst. Mag. **6**, 7–12 (1986)
11. Song, S.M., Waldron, K.J.: Machines that walk: the adaptive suspension vehicle. The MIT Press, Cambridge (1989)
12. McGeer, T.: Passive dynamic walking. Int. J. Robot. Res. **9**(2), 62–82 (1990)
13. Carbone, G., Ceccarelli, M.: Legged Robotic Systems, pp. 553–576. Cutting Edge Robotics ARS Scientific Book, Wien (2005)
14. Funabashi, H., Horie, M., Tachiya, H., Tanio, S.: A synthesis of robotic pantograph mechanisms based on working spaces and static characteristics charts. JSME Int. J. Ser. III, **34** (2) 239–244 (1991)
15. Shieh, W.B., Tsai, L.W., Azarm, S.: Design and optimization of a one-degree-of-freedom six-bar leg mechanism for a walking machine. J. Robot. Syst. **14**(12), 871–880 (1997)
16. Ottaviano, E., Lanni, C., Ceccarelli, M.: Numerical and experimental analysis of a pantograph-leg with a fully-rotative actuating mechanism. In: Proceeding of the 11th World Congress in Mechanism and Machine Science, Tianjin, China, 18–21 Aug 2004
17. Ottaviano, E., Ceccarelli, M., Tavolieri, C.: Kinematic and dynamic analyses of a pantograph-leg for a biped walking machine. In: 7th International Conference on Climbing and Walking Robots CLAWAR, Madrid, Paper A019 (2004)
18. Ling, C., Ceccarelli, M., Takeda, Y.: Operation analysis of a one-DOF pantograph leg mechanism. In: Proceedings of the RAAD 2008, Ancona, Italy, 15–17 Sept 2008

Positioning Control of a Micro Manipulation Robot Based on Voice Command Recognition for the Microscopic Cell Operation

H. Terada, K. Makino, H. Nishizaki, E. Yanase, T. Suzuki and T. Tanzawa

Abstract In the gene manipulation field, to make a genetically-modified mouse, the multi micro manipulation pipettes operation is needed. Especially, to realize more complex cell operations, it is needed that three micro manipulation pipettes are operated simultaneously. Therefore, to realize the simultaneous operation, a micro manipulation robot has been developed. This robot consists of a voice command recognition system and a rectangular-coordinate type structure, and controls the positioning of the third pipette by voice command without manual operations. Then, to eliminate the vibration generated by the feedback loop, a driving actuator uses an oil hydraulic pump which is driven by piezo-electric device to realize the intermediate stop and positioning. Furthermore, it is confirmed that the prototype robot can be driven by voice command recognition.

Keywords Robot · Positioning · Micro manipulation · Voice command recognition · Cell operation

H. Terada (✉) · K. Makino · H. Nishizaki · E. Yanase · T. Suzuki · T. Tanzawa
University of Yamanashi, Yamanashi, Japan
e-mail: terada@yamanashi.ac.jp

K. Makino
e-mail: kohjim@yamanashi.ac.jp

H. Nishizaki
e-mail: hnishi@yamanashi.ac.jp

E. Yanase
e-mail: eririn@alps-lab.org

T. Suzuki
e-mail: t13jm029@yamanashi.ac.jp

T. Tanzawa
e-mail: ttanzawa@yamanashi.ac.jp

J. Beran et al. (eds.), *Advances in Mechanism Design II*,
Mechanisms and Machine Science 44, DOI 10.1007/978-3-319-44087-3_10

1 Introduction

A progress of the gene manipulation technology requires various micromanipulators. Especially, to make a genetically-modified mouse, the multi pipettes operation is needed [1]. At this case, two micro manipulation pipettes are driven by manual operation using oil hydraulic joysticks at the microscopic cell operation [2], and it is required to operate the third micro manipulation pipette. However, an operator drives two pipettes by both hands and foot pedals. The third pipette cannot be operated simultaneously. Therefore, to realize the simultaneous operation, a micro manipulation robot which is controlled by voice command is required.

On the other hand, when the conventional micro manipulation robot systems are driven by stepping motors or friction drive type piezo actuators, the vibration of the microscopic levels is remained [3, 4]. In this report, a micro manipulation robot based on voice command recognition is designed to solve these problems. Especially, a recognition algorithm is proposed to prevent robot malfunction, and that is compared the detected voice to the pre-learning language database. In addition, a prototype robot is tested to verify the reliability of a microscopic motion.

2 Structure of a Microscopic Cell Operation System with a Micro Manipulation Robot

A structure of a microscopic cell operation system with a micro manipulation robot based on voice command recognition is proposed as shown in Fig. 1. To coincide with a manual operation, this robot system consists of a rectangular coordinate structure which is driven by oil hydraulic pumps. When an operator controls a motion of two manual operation devices using the manual haptic devices, that robot is required to hold and to push the cell simultaneously. However, an operator cannot operate this robot by his/her hand, because both haptic devices are grasped. Therefore, this robot is controlled by voice command recognition. Furthermore, when we use the conventional voice coil type micro manipulator, the resolution of a positioning is restricted to 20 μm [5]. However, in recent cell operation fields, the higher positioning accuracy is required. To realize these requirements, the oil hydraulic pump is driven by the piezoelectric actuator which has a displacement magnifying mechanism. Then, the piezoelectric element is controlled by the displacement feedback. However, to eliminate the vibration caused by the displacement feedback of the piezoelectric element, a structure of the oil hydraulic pump is constructed as shown in Fig. 2. This pump generates an oil hydraulic pressure using the diaphragm deformation, and eliminates the small vibration by the silicon oil viscosity.

When the input motions of a step function and a ramp function are used, the response characteristics of the oil hydraulic actuator on the X-axis are shown in

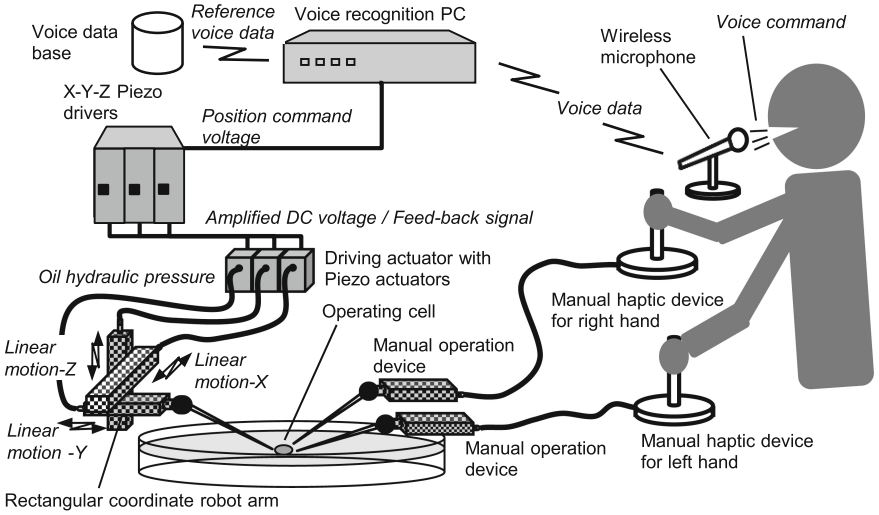

Fig. 1 Microscopic cell operation system with a micro manipulation robot based on voice command recognition

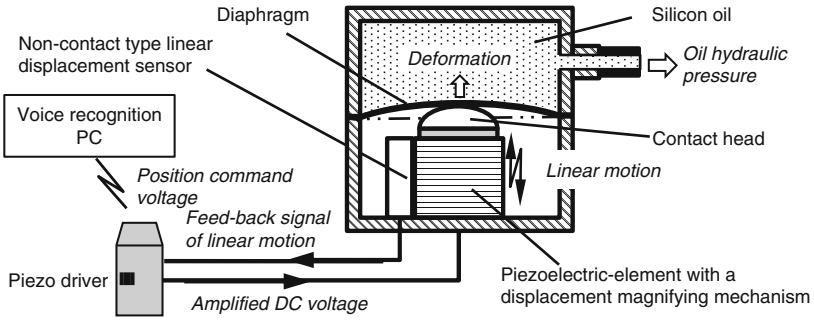

Fig. 2 Structure of an oil hydraulic pump driven by piezo-electric device

Fig. 3. The resolution of an input signal is the 0.7 μm, and the required resolution of an operation is 2.0 μm. In case of a ramp function, the pipette on the X-axis can move very smoothly at 13.0 μm/s, and in case of a step function, the pipette on the X-axis can move very smoothly, too. Then, both time constants are less than 0.5 s; these performances are enough to the human response speed. Furthermore, in cases of the Y-axis and the Z-axis, these response characteristics are the same. However, this motion speed is not enough for the expert operator, so the voice command recognition has to be simplified or to be predicted a command.

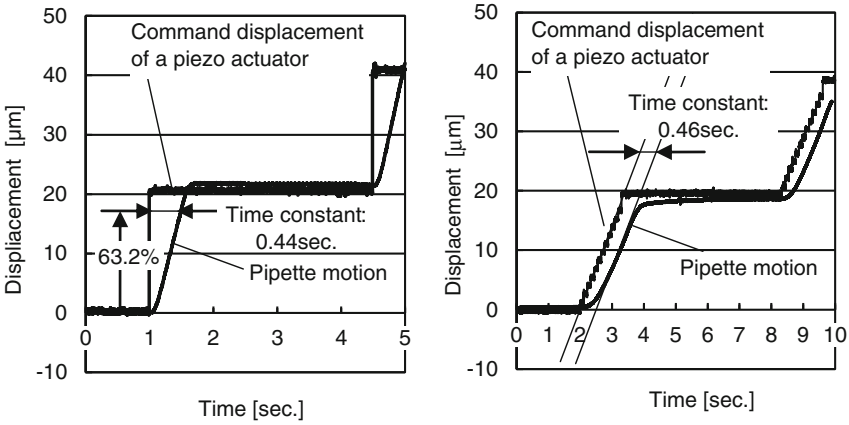

a) Input motion of a step function

b) Input motion of a ramp function

Fig. 3 Response characteristics of an oil hydraulic actuator. **a** Input motion of a step function. **b** Input motion of a ramp function

3 Algorithm of Voice Command Recognition

Japanese language is a phonogram, and it can be divided to the single set of speech sounds or the small syllable, and this language has a unique grammar. Therefore, other language recognition method which is different from the English recognition has to be investigated. To solve this problem, it is popular that the open-source software of Japanese large vocabulary continuous speech recognition is used for the academic research. This open-source is called as "Julius" [6, 7]. It incorporates major speech recognition techniques, and it can perform a large vocabulary continuous speech recognition task in real-time. The command voice is converted to the feature vectors sequence which is shown Mel-Frequency Cepstrum Coefficient [8]. Then, these vectors are matched with the statistic acoustic models. When the vector is matched with that pattern, the motion signal voltage of the commanded axis direction is output.

A flowchart of the voice command recognition is shown in Fig. 4. Especially, under the microscope, the fundamental motion of a pipette is a rectangular coordinate motion, and the arbitrary direction motion on the horizontal plane to adjust the holding position of the cell is sometimes used. In addition, there is some hysteresis loss of each axis motion, and the motion length needs to be compensated. Therefore, in a magnification adjustment, compared with the direction of previous operation and the next operation, the compensation length and direction are determined. Considering this point, the voice command of a robot arm motion is defined as Table 1. In this case, the arbitrary direction on the horizontal plane is commanded using the clock direction. Especially, considering the resolution of D/A, the motion of diagonal direction is approximated by the pulse ratio of the

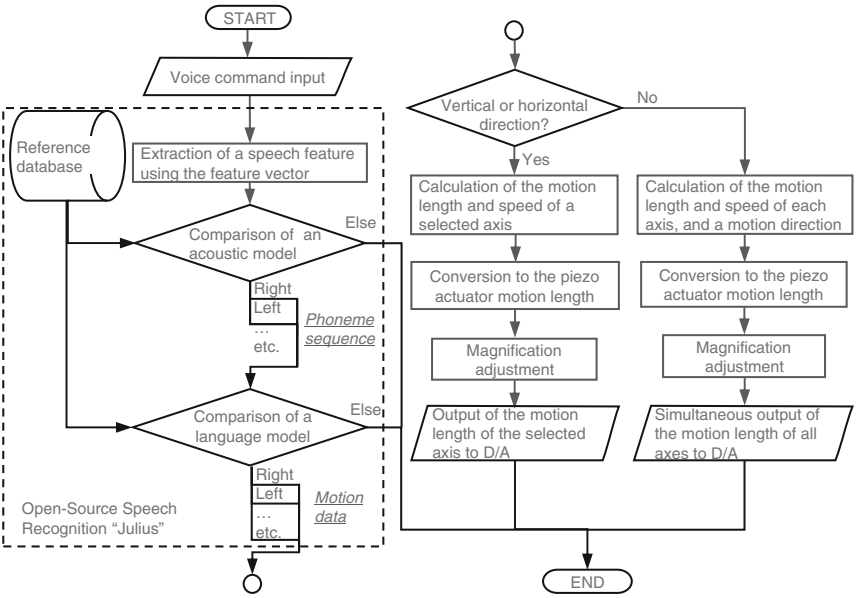

Fig. 4 Flowchart of voice command recognition

horizontal pulse to the vertical pulse. Furthermore, the correct motion rate of each motion is shown, too. Almost direction commands do not have recognition errors. However, the commands of the speed and the motion range are affected by the word order, and the error rate of voice recognition sometimes increases. It is similar to the individual differences in pronunciation, too. Therefore, another word order has to be investigated.

Table 1 Main command of a robot arm motion and the correct motion rate

Class	Command	Command in Japanese	Correct motion rate (%)	Class	Command	Command in Japanese	Correct motion rate (%)
Speed	Quickly	ha-ya-ku	90.0	Arbitrary horizontal direction	One	hi-to-ji	100.0
	Slowly	yu-q-ku-ri	73.3		Two	fu-ta-ji	100.0
					Three	Sa-N-ji	100.0
Motion range	Larger	mo-q-to	60.0		Four	yo-ji	100.0
	Smaller	su-ko-shi	83.3		Five	go-ji	100.0
					Six	ro-ku-ji	93.3
Direction	Right	mi-gi	86.7		Seven	na-na-ji	100.0
	Left	hi-da-ri	100.0		Eight	ha-chi-ji	100.0
	Up	u-e	100.0		Nine	ku-ji	100.0
	Down	shi-ta	100.0		Ten	ju-ji	100.0
	High	ta-ka-ku	100.0		Eleven	ju-i-chi-ji	100.0
	Low	hi-ku-ku	76.7		Twelve	ju-ni-ji	100.0

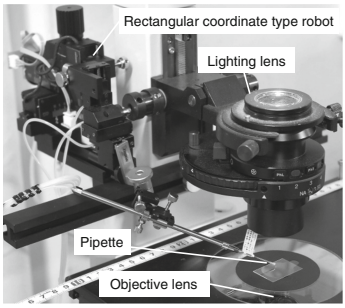

a) Rectangular coordinate type robot arm

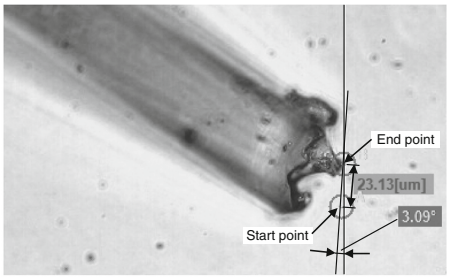

b) Measurement of a pipette motion on the horizontal plane using the microscopic image processing

Fig. 5 Prototype system. **a** Rectangular coordinate type robot arm. **b** Measurement of a pipette motion on the *horizontal plane* using the microscopic image processing

Then, at microscopic cell operation, the positioning error of an arbitrary direction motion on the horizontal plane is measured to evaluate the usefulness of this type robot arm as shown in Fig. 5a. The positioning repeatability of each axis is tested using the image processing under the microscope as shown in Fig. 5b. Therefore, the positioning error of each axis at 10.0 μm linear motion is less than ±2.0 μm. This performance is enough for the cell holding operations.

4 Conclusions

To realize the multi micro manipulation pipettes operation, the micro manipulation robot based on voice command recognition has been developed. It is con-firmed that the operator can control third pipette by voice command smoothly. In future work, to improve the voice recognition rate and to consider the individual differences in pronunciation, we have to optimize the word order. Then, to realize higher response speed, the voice command recognition has to be simplified.

Acknowledgments The authors are grateful to Prof. T. Wakayama, Mr. Y. Kitai and Mr. K. Nakagawa for cooperating to make a control algorithm.

References

1. Wakayama, T.: The technique of “Takumi” to make a clone. Riken-NEWS **303**, 5–7 (2006)
2. NarishigeScientificInstrumentLab.:Three-axisHangingJoystickOilHydraulicMicroma-nipulator. http://products.narishige-group.com/group1/MMO-202ND/injection/english.html
3. Kudoh, K., Gotoh, T., Sato, K., Yamagata, Y., Furutani, K., Higuchi, T.: Development of piezo micromanipulator for cell micromanipulation. J. Mamm. Ova Res. **7**(1), 7–12 (1990)
4. Miura, M., Kashiwagi, K., Niwa, T.: On the automatic micro manipulator system MMS-10. Shimadzu Rev. **44**(1), 51–58 (1987)

5. Kojima, N.: Development of micromanipulator for cell operation. Memoirs Inst. Sci. Technol. Meiji Univ. **31**(5), 67–76 (1992)
6. Kawahara, T., et. al.: http://julius.sourceforge.jp
7. Kawahara, T., et al.: Free software toolkit for Japanese large vocabulary continuous speech recognition. Proc. Int. Conf. Spoken Lang. Process. **4**, 476–479 (2000)
8. Sahidullah, Md, Saha, G.: Design, analysis and experimental evaluation of block based transformation in MFCC computation for speaker recognition. Speech Commun. **54**(4), 543–565 (2012)

Spherical Ultrasonic Motor for Space

U. Nishizawa, S. Toyama and T. Oohashi

Abstract In resent years, space satellites have been widely used in the world. They cause the space debris, which has become a problem because they may collide each other in space. In our study, we have developed a Spherical UltraSonic Motor (SUSM) with 3 DOF in space use to drive the satellite thruster and resolve the space debris problem. When the satellites enter the atmosphere at the end of the life, SUSM controls thrusters for the right direction in falling down to the earth to burn in the air. We have made experiments to evaluate torque, durability and lifetime. It shows that the torque and lifetime meets target value. But durability does not meet the target lifetime. To resolve it, we have applied a new stator lining materials and shifted frequency with 0.4 kHz from resonant frequency. Finally we have succeeded in durability-required specifications.

Keywords Ultrasonic motor · Spherical motor and space application

1 Introduction

Recently many countries launched a lot of space satellites. So, space debris has become a problem in the world. It is because the space debris causes collision of satellites. In our research, we apply our 3DOF Spherical UltraSonic Motor (3DOF SUSM) to resolve this problem. For the use of our motor in outer space, it is necessary to meet space use specifications such as required output torque and durability in the high vacuum. Especially heat is serious problem. By reducing generated heat of the motor by lining material and resonance frequency shift, we are

U. Nishizawa · S. Toyama (✉)
Tokyo A&T University, Tokyo, Japan
e-mail: toyama@cc.tuat.ac.jp

U. Nishizawa
e-mail: n-uichi@cc.tuat.ac.jp

T. Oohashi
National Institute of Tech-Kisarazu College, Kisarazu, Japan
e-mail: oohashi@d.kisarazu.ac.jp

J. Beran et al. (eds.), *Advances in Mechanism Design II*,
Mechanisms and Machine Science 44, DOI 10.1007/978-3-319-44087-3_11

able to rotate the motor under high vacuum environment more than 120 min. The specifications of the motor in this research (high vacuum 10^{-3} Pa, room temperature) is as follows; maximum output torque 25 mN m, continuous working time 120 min, cycles of working more than 300 times.

The temperature changes from −120 to 200 °C in space. It is very important specification for the motor. However, it requires not only improvement of materials but also control method and heat design of it. So, the movement in high or low temperature is the discussion on next stage. In this research, the authors focus on durability of vacuum use in only room temperature. It is also important for special use in space, for example, in the temperature controlled satellite.

2 Spherical Ultrasonic Motor

The 3DOF SUSM used in this study consists of one spherical rotor and three ring-shaped stators. Figures 1 and 2 show an overview of the 3DOF SUSM and the characteristics. The stator consists of a metallic elastic body and piezoelectric elements. When an AC voltage is applied to the piezoelectric vibrator, a standing wave is generated on the elastic body. By applying two AC voltages with some phase difference to the positive and negative sections of the piezoelectric elements, a traveling wave is generated due to combination of the two standing waves. The amplitude of the traveling wave is controlled by the phase difference of these two standing wave; phase difference 0 is standing wave and phase difference 90° is traveling wave with maximum velocity. The velocity of the traveling wave can be controlled by phase difference precisely with every 1°.

The stators and the rotor are in pressure contact with each other. Three stators are aligned with 120° each other, but with 7° under horizontal plane. It is because that the sum of velocity vectors generated by each stator can make arbitrary vector, that is, the motor can rotate about specified vector in three dimensional space with specified speed [1–5]. It has three degree of freedom of rotation. However, exactly speaking, the rotational velocity of the rotor is less than the vector sum due to friction loss.

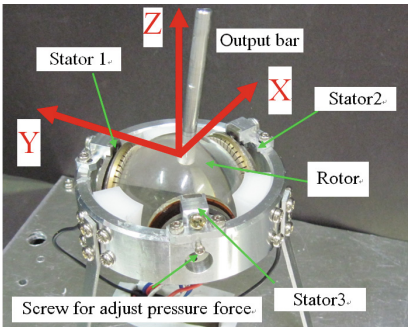

Fig. 1 Spherical ultrasonic motor

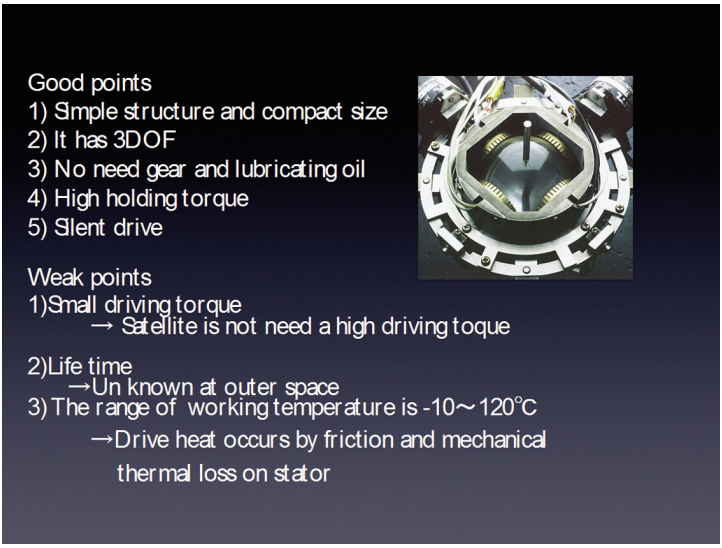

Fig. 2 Characteristics of SUSM

We have made experiments of SUSM in the vacuum chamber (applied voltage 180 Vpp, applied resonant frequency, air pressure 10^{-3} Pa) to measure output torque and rotational speed. An experimental apparatus is shown in Fig. 3. We have applied phase difference 0°, 60°, and −60° to stators to rotate about Y-axis and measured its rotational velocity and output torque. The results are shown in Fig. 4.

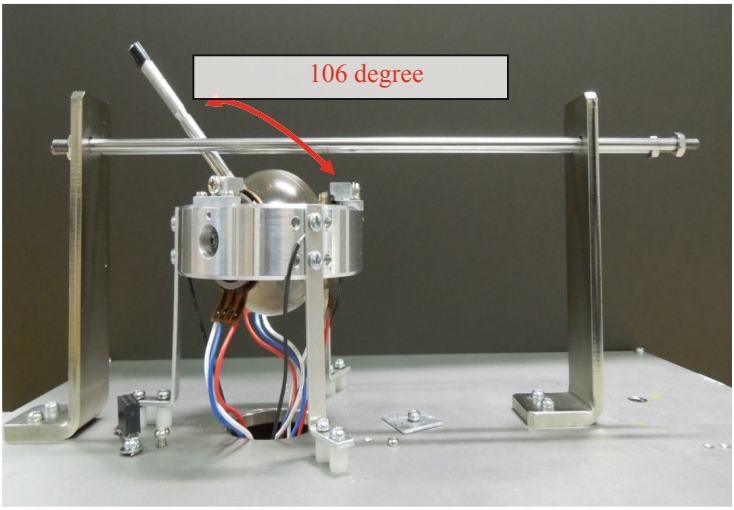

Fig. 3 Experiment equipment for measuring rotational speed

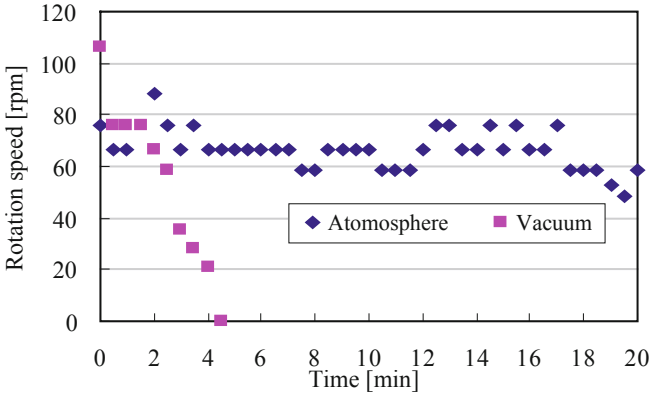

Fig. 4 Durability experiment in the atmosphere versus in vacuum

It shows that lifetime is only 4 min in the vacuum environment and maximum speed is degenerated 17 % comparing to the case in air. But the output torque increased 20 %. It is because that some materials on the surface of the rotor and stator are vapored out and the frictional force increased.

3 Lining Material and Resonant Frequency

We have improved the motor materials for use of space. Firstly, we have applied the new lining material on the surface of rotor as follows; Original (Normal), #1A (Molybdenum disulfide, Type A), FS-1140 (Fluorine resin, Type B), #815-4 (Fluorine resin, Type C), S-6100 (Fluoridation graphite, Type D). These materials have good characteristics suited for space use such as low wear, high frictional force and high durability under high temperature. The experimental results are shown in Fig. 5. The lifetime is extended. But it is much less than required specifications (120 min). It is because that generated heat changes the resonant frequency and stator cannot vibrate nor drive the rotor. All motors generated higher output torque than required specifications.

In order to make lifetime longer, we have applied near resonant frequency (0.4 kHz higher shift) to the stators so that it may make the vibration amplitude smaller to resolve frictional heat. The results are shown in Fig. 6. We have found that it meets the specifications of lifetime.

Generally speaking, the heat source of this motor is contact surface and inside of piezoelectric ceramics. The contact surface of stator and rotor with high pressure produces heat by friction. The improved lining materials reduce the frictional heat. On the other hand, heat generated in the ceramics by inner friction loss with small grains is reduced by the shift of the resonant frequency to suppress the amplitude of the vibration.

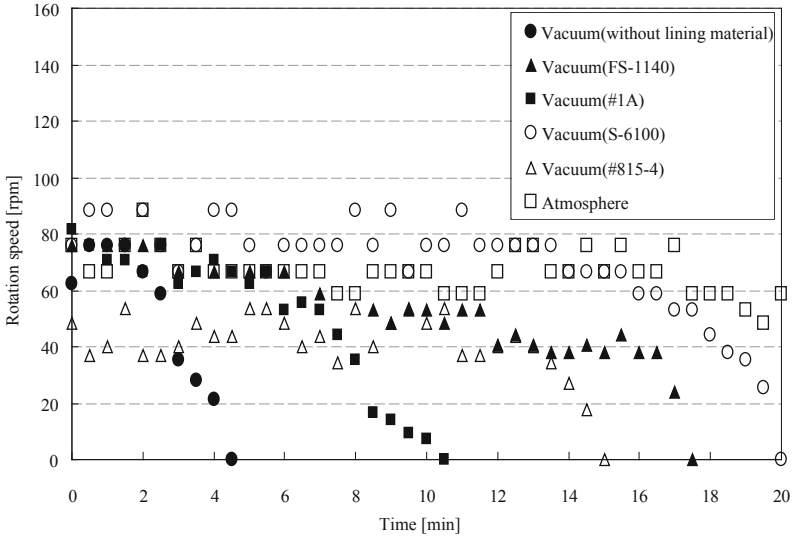

Fig. 5 Durability of motor with lining materials

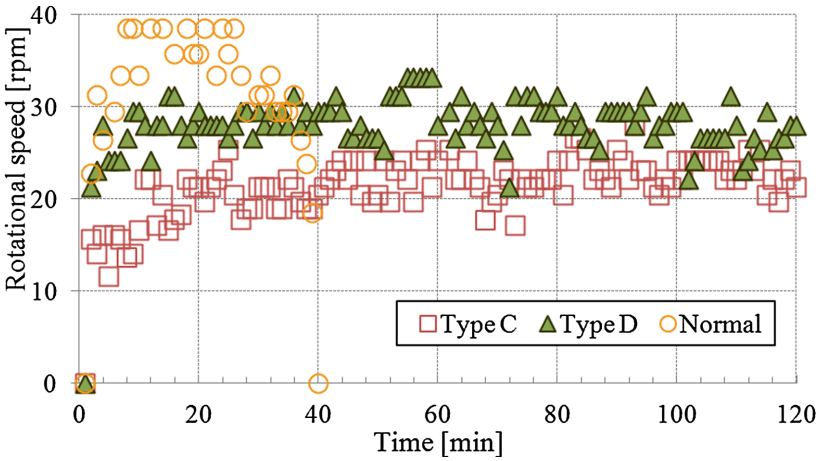

Type C (S-6100), Type D (Fs-1140), Normal (no lining material)

Fig. 6 Durability experiment. Type C (S-6100), Type D (Fs-1140), Normal (no lining material)

4 Conclusions

We have developed a new spherical ultrasonic motor for space use. Applying new lining materials and resonant frequency shift to the stators, it meets the space specifications, that is, maximum output torque 25 mN m, continuous working time 120 min, cycles of working more than 300 times. We have succeeded in showing its potentials for space use.

References

1. Takesue, N., et al.: Position control methods of spherical ultrasonic motor. In: Proceedings of IEEE/RSJ International Conference on Intelligent Robots and Systems, p. 3061 (2010)
2. Sashida, T., Kenjo, T.: An Introduction to Ultrasonic Motors. Oxford Press, Oxford (1993)
3. Purwanto, E., Toyama, S.: Control method of a spherical ultrasonic motor. In: IEEE/ASME International Conference on Advanced Intelligent Mechatronics (AIM 2003), pp. 1321–1326 (2003)
4. Mashimo, T., Awaga, K., Toyama, S.: Development of a spherical ultrasonic motor with an attitude sensing system using optical fibers. In: IEEE International Conference on Robotics and Automation (ICRA2007), p. 4466 (2007)
5. Mashimo, T., Toyama, S., Ishida, H.: Development of an MRI compatible surgical assist manipulator using spherical ultrasonic motor (1st report)-prototype of the spherical ultrasonic motor. J. Japan Soc. Precis. Eng. **73**(2), 275 2007 (in Japanese)

Part II
Dynamics of Machines and Mechanisms, Rotor Dynamics

Multi-physical Analysis of the Forces in the Flexible Rotor Supported by the Magnetorheological Squeeze Film Dampers

P. Ferfecki, J. Zapoměl and M. Marek

Abstract To reduce lateral vibrations of rotating machines, the damping devices are placed between the rotor and its frame. This is enabled by magnetorheological squeeze film dampers. To achieve their optimum performance their damping effect must be adaptable to the current working conditions. In this paper, modelling of the magnetorheological squeeze film damper is based on the assumptions of the classical theory of lubrication except that for the lubricant. The model is completed with the magnetic force acting between the damper rings. Therefore, the magnetostatic approaches to determining the magnetic field in the damper gap at different distinguishing levels were proposed and compared. The developed mathematical model was applied for analysis of a rotating machine with a flexible shaft. The carried out computational simulations confirmed that the developed magnetorheological damper arrives at significant suppression of the rotor vibration in a wide range of running speeds.

Keywords Magnetorheological squeeze film damper · Hydraulic forces · Magnetic forces · Magnetostatic analysis · Flexible rotor · Vibration attenuation

P. Ferfecki (✉) · M. Marek
IT4Innovations, Technical University of Ostrava, Ostrava, Czech Republic
e-mail: petr.ferfecki@vsb.cz

M. Marek
e-mail: martin.marek@vsb.cz

J. Zapoměl
Department of Applied Mechanics, Technical University of Ostrava, Ostrava, Czech Republic
e-mail: jaroslav.zapomel@vsb.cz; zapomel@it.cas.cz

J. Zapoměl
Institute of Thermomechanics, Prague, Czech Republic

J. Beran et al. (eds.), *Advances in Mechanism Design II*,
Mechanisms and Machine Science 44, DOI 10.1007/978-3-319-44087-3_12

1 Introduction

Lateral vibration of flexible rotors can be significantly reduced if damping elements are inserted into its support. For this purpose, magnetorheological (MR) squeeze film dampers can be applied. Their damping effect is controlled by changing induction of the magnetic field passing through the film of the MR fluid.

The mathematical model of a short squeeze film MR damper intended for the analysis of both the steady state and transient rotor vibrations is presented in [1]. Modelling of the MR damper that takes into account both the hydraulic fluid film and magnetic forces is reported in [2, 3].

The development of the enhanced mathematical model of the MR squeeze film damper for rotordynamic applications and learning more on the main forces acting in between the rotor and the MR damping devices are the principal contributions of this article. For this purpose, two magnetostatic modelling approaches have been developed, and the semi-analytical relations defining the magnetic forces acting in the damper were determined.

2 The Hydraulic and Magnetic Forces Between the Damper Rings

The main parts of MR squeeze film dampers (Fig. 1a) for rotordynamic applications are two concentric rings between which there is a layer of MR oil. The outer ring is mounted with the stationary part directly, and the inner one is connected with the squirrel spring carrying the ball bearing. The spring enables the oscillation of the inner damper ring in the radial direction and prevents its rotation together with the shaft. In the damper body the electric coil generating magnetic flux passing through the lubricating oil is imbedded. As its resistance against the flow depends on magnetic induction, the change of the electric current makes it possible to control the hydraulic damping force.

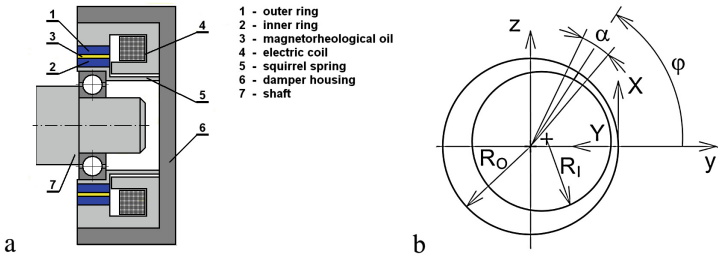

Fig. 1 The scheme of a MR squeeze film damper (**a**) and the damper (xyz) and the fluid film (XYZ) coordinate systems (**b**)

The mathematical model of the studied damping element is based on utilization of the classical theory of lubrication with the exception for the MR oil that is represented by Bingham material, the yielding shear stress of which depends on magnetic induction. Then the pressure distribution in the full oil film referred to a short [1] damper is governed by a Reynolds equation modified for Bingham fluid

$$h^3 p'^3 \pm 3(h^2 \tau_y \mp 4\eta \dot{h} Z) p'^2 \mp 4\tau_y^3 = 0 \quad \text{for } Z > 0. \tag{1}$$

The upper and lower signs in (1) hold for the pressure gradients $p' < 0$, $p' > 0$, respectively. Z is the axial coordinate (Fig. 1b), h is the oil film thickness [4], τ_y, η are the yield shear stress and viscosity of the Bingham liquid, and $(\cdot)$ denotes the first derivative with respect to time. The details on derivation and solution of the modified Reynolds equation (1) can be found in [1].

The stationary value of the yielding shear stress of the MR fluid needed for solving the modified Reynolds equation (1) can be approximated with sufficient accuracy by a power function

$$\tau_y = k_y B^{n_y}. \tag{2}$$

B is the magnetic induction in the damper gap, and k_y, n_y are the material constants of the MR oil.

The mutual interaction between the damper rings is accomplished by the hydraulic and magnetic forces. The hydraulic force is produced due to squeezing the MR oil film and pushes the rings one from another. Its components are obtained by integration of the hydraulic pressure distribution around the circumference and along the length L of the damper

$$F_{MRy} = -2R_I \int_0^{\frac{L}{2}} \int_0^{2\pi} p_d \cos\varphi \mathrm{d}\varphi \mathrm{d}Z, \; F_{MRz} = -2R_I \int_0^{\frac{L}{2}} \int_0^{2\pi} p_d \sin\varphi \mathrm{d}\varphi \mathrm{d}Z. \tag{3}$$

F_{MRy}, F_{MRz} are the y and z components of the hydraulic force, R_I is the inner ring radius, p_d is the pressure distribution in the MR oil film, and φ denotes the circumferential coordinate (Fig. 1b). In cavitated areas, the pressure of the medium is assumed to be constant and equal to the pressure in the ambient space.

Contrary to the hydraulic damping force, the magnetic force is attracting and is induced by the magnetic flux generated in the electric coils.

The 3D approach uses a spatial distribution of the magnetic flux to determine magnetic induction in the damper gap and the force acting between the rings. As the damper permanent magnetization is avoided, the saturation of the magnetic flux and hysteresis are not taken into account. The magnetostatic problem is assumed to be linear and the finite element method was applied for its solving. The discretization of the damper body and the surrounding air environment is evident from Fig. 2a. The total magnitude of the magnetic force acting between the rings in the direction

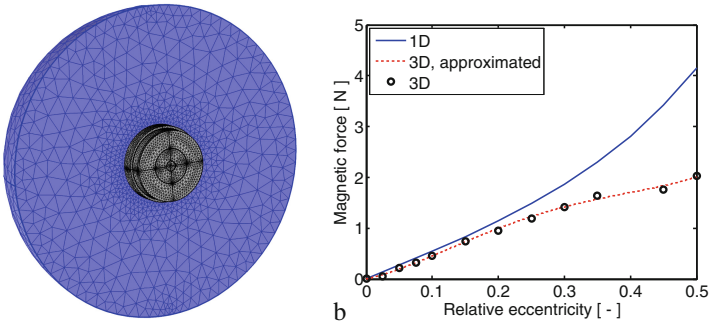

Fig. 2 Discretization of the damper model (**a**) and the magnetic force in dependence on the relative eccentricity (**b**)

of the line of the center was calculated by means of the Maxwell stress tensor and is drawn in Fig. 2b.

At the lowest distinguishing level (1D approach), the inner and outer damper rings can be considered as a divided core of an electromagnet. The semi-analytical relations for the magnetic induction and the magnetic force are based on magnetic reluctance [5] of the MR fluid film of a sufficiently small angular segment between two coaxial cylinders

$$B_i = k_B \mu_0 \mu_r \frac{I}{h_i}, \quad F_{MA,i} = \frac{B_i^2 \alpha L (R_I + R_O)}{4 \mu_0 \mu_r}, \quad i = 1, 2, \ldots, \frac{2\pi}{\alpha} \tag{4}$$

B_i is the magnetic induction in the center of the damper gap and in the center of the angular segment, $F_{MA,i}$ is the magnetic force between the angular segment of the inner and the outer damper rings, I is the electric current, R_O is the outer damper ring radius, h_i is the oil film thickness in the center of the angular segment of the damper gap, k_B is the design parameter, α is the angular segment of the damper gap (Fig. 2b), μ_0 is the vacuum permeability ($4\pi \times 10^{-7}$ H m^{-1}), and μ_r is the magnetic permeability of the MR fluid.

The design parameter was determined from the value of magnetic induction in the middle of the oil film obtained by application of the 3D approach to solve the magnetic problem for the case when the damper rings take a concentric position.

The dependence of the total magnetic force acting between the centers of the inner and outer damper ring computed by application of the 1D approach on the relative eccentricity is drawn in Fig. 2b. It is evident that the difference between the values (Fig. 2b) provided by the 3D and 1D approaches is less than 15 % in the relative eccentricity range 0.0–0.2 in which the MR damper operates.

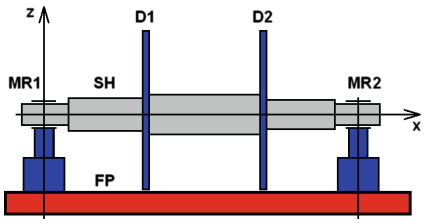

Fig. 3 The scheme of the investigated rotor system

3 The Motion Equation of the Investigated Rotor System

The investigated rotor system (Fig. 3) consists of a flexible shaft (SH) and two discs (D1, D2). The rotor is mounted on a rigid frame (FP), and the squeeze film MR dampers (MR1, MR2) are inserted into its supports.

The task was to investigate the influence of the magnetic attractive and carrying hydraulic damping forces on the vibration amplitude of the rotor.

The rotor turns at constant angular speed, is loaded by its weight, and excited by imbalance of the discs. The mass, diameter, and axial moments of inertia of the discs are considered. The squirrel springs of both dampers are prestressed to be eliminated their deflection caused by the rotor weight.

In the computational model the shaft is considered as flexible and is represented by a beam-like body discretized into finite elements. The discs are assumed to be absolutely rigid and the MR dampers are represented by springs and nonlinear force couplings.

Lateral vibration of the investigated rotor system is described by the equation of motion that takes the form

$$\mathbf{M}\,\ddot{\mathbf{q}} + (\mathbf{B} + \eta_{\mathbf{V}}\,\mathbf{K_{SH}} + \omega\,\mathbf{G})\,\dot{\mathbf{q}} + (\mathbf{K} + \omega\,\mathbf{K_C})\,\mathbf{q} = \mathbf{f_A} + \mathbf{f_{PS}} + \mathbf{f_{MR}} + \mathbf{f_{MA}}. \quad (5)$$

$\mathbf{M}$, $\mathbf{B}$, $\mathbf{K}$, $\mathbf{G}$, $\mathbf{K}_C$, $\mathbf{K}_{SH}$ are the mass, damping, stiffness, gyroscopic, circulation matrices of the rotor, and the stiffness matrix of the shaft, respectively, $\mathbf{f}_A$ is the vector of applied and unbalance forces, $\mathbf{f}_{PS}$ is the vector of prestressed forces, $\mathbf{f}_{MR}$ is the vector of hydraulic MR forces, $\mathbf{f}_{MA}$ is the vector of magnetic forces, $\mathbf{q}$ is the vector of generalized displacements, η_V is the coefficient of viscous damping of the shaft material, ω is the angular speed of the rotor rotation, and $(\cdot)$ denotes the second derivative with respect to time.

A trigonometric collocation method was applied to obtain the steady state solution of the equation of motion (5).

4 Computational Results of the Rotor Dynamics

The frequency responses depicted in Fig. 4a is referred to the center of D1 disc. The responses were determined for the cases when no oil was supplied to the dampers (no damping), and when the MR oil was solidified (over damped).

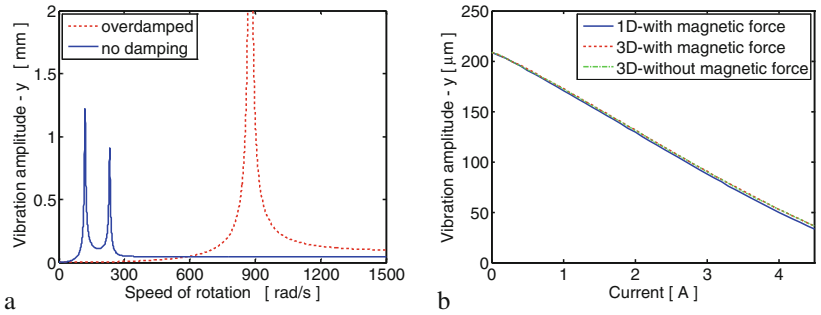

Fig. 4 The frequency responses (**a**) and the vibration amplitude (**b**) in the horizontal direction

The dependence of the vibration amplitude at location of D1 disc referred to the angular speed of the rotor rotation of 120 rad/s on the applied current is drawn in Fig. 4b. The results show that the rising magnitude of the current increases reduction of the vibration amplitude. The computation of the magnetic force by the 3D approach gives almost the same vibration amplitude, and the difference between the 1D and 3D approaches is less than 10 %.

5 Conclusions

It was shown that the magnetic attractive force in the MR damper is much smaller than the hydraulic damping one. The main contribution of this article is the development of a more accurate mathematical model of a short MR squeeze film damper and the procedures for determining the magnetic force based on solving a spatial magnetostatic problem utilizing the finite element method and on application of a semi-analytical relation.

Acknowledgments This work was supported by The Ministry of Education, Youth and Sports from the National Programme of Sustainability (NPU II) project "IT4Innovations excellence in science—LQ1602", and by the Czech Science Foundation 15-06621S.

References

1. Zapoměl, J., Ferfecki, P., Forte, P.: A computational investigation of the transient response of an unbalanced rigid rotor flexibly supported and damped by short magnetorheological squeeze film dampers. Smart Mater. Struct. **21**, 105011 (2012)
2. Zapoměl, J., Ferfecki, P.: A 2D mathematical model of a short magnetorheological squeeze film damper based on representing the lubricating oil by bilinear theoretical material. In: Proceedings of the 14th IFToMM World Congress, Taipei, Taiwan (2015)

3. Wang, G.-J., Feng, N., Meng, G., Hahn, E.-J.: Dynamic performance and control of squeeze mode MR fluid damper-rotor system. Smart Mater. Struct. **14**, 529–539 (2005)
4. Krämer, E.: Dynamics of Rotors and Foundations, Springer, Berlin (1993)
5. Knoepfel, H.E.: MAGNETIC FIELDS A Comprehensive Theoretical Treatise for Practical Use. Wiley, New York (2000)

Experimental Evaluation of a Rotor Model Based Foundation Identification Procedure

M. Yu, N. Feng and E. Hahn

Abstract This paper evaluates experimentally a rotor model based foundation identification procedure (in terms of foundation modal parameters) for rotor bearing foundation systems (RBFS). Earlier experimental evaluations used a deficient rotor model and did not properly consider foundation damping. Demonstrated is the need for an accurate dynamic model of the rotor. It is shown that the proposed approach can identify an equivalent foundation which can predict reasonably well the unbalance response of an experimental RBFS rig over the speed range of interest. The proposed identification procedure shows promise for field applications, but further work is required to identify more accurately the modal damping.

Keywords Experimental evaluation · Foundation identification · Modal parameters · Rotating machinery

1 Introduction

Correct modelling of a RBFS is an invaluable asset for the balancing and efficient running of turbomachinery. A major problem is to properly identify the foundation of existing installations [1]. The approach investigated here requires an accurate rotor model and uses motion measurements at select points on the foundation to identify the modal parameters of an equivalent foundation. Such an approach is

M. Yu
Sun Yat-Sen University, Guangzhou, People's Republic of China

N. Feng
Shandong University, Jinan, People's Republic of China

E. Hahn (✉)
The University of New South Wales, Sydney, Australia
e-mail: e.hahn@unsw.edu.au

J. Beran et al. (eds.), *Advances in Mechanism Design II*,
Mechanisms and Machine Science 44, DOI 10.1007/978-3-319-44087-3_13

attractive, as it can utilize existing monitoring instrumentation. Numerical experiments on a simple RBFS indicate that such an approach is feasible [2], but experimental evaluation is needed to ensure that the approach can cope with the input measurement errors [3]. This paper describes this experimental evaluation.

To this end, an earlier rig [4], which had been used to evaluate the dynamic stiffness parameters of the bearing pedestals of a simple multi disk rotor, was modified to provide a flexible foundation for the rigid bearing pedestals. The modified rig, its commissioning, and the experimental procedure for obtaining the required measurements are described in a previous paper [5]. However, the results in Ref. [5] are only preliminary as they do not properly consider the effect of foundation damping. Also, they are based on a rotor model which does not account for rotor damping, resulting in incorrect force excitation input data. This paper addresses these potentially significant causes of identification error.

2 Notation

$\widetilde{F}$ Harmomic excitation force amplitude vector
$\boldsymbol{I}$ Identity matrix
$\boldsymbol{m}$ Modal mass matrix (diagonal); m_k = modal mass of the kth mode
$\widetilde{X}$ Displacement amplitude vector
$\boldsymbol{\Phi}$ Foundation modal matrix; $\Phi_k = k$th column of $\boldsymbol{\Phi}$
$\boldsymbol{\lambda}$ Eigenvalue matrix (diagonal); $\lambda_k = k$th eigenvalue = ω_k^2
Ω Excitation frequency
$\boldsymbol{\omega}$ Natural frequency matrix (diagonal); $\omega_k = k$th natural frequency
$\boldsymbol{\xi}$ Damping ratio matrix (diagonal); $\xi_k = k$th element of $\boldsymbol{\xi}$

3 The Identification Requirement

For a RBFS with an equivalent foundation having n degrees of freedom (DOF), a harmonic excitation frequency Ω, and periodic response with fundamental frequency Ω, it can be shown [2] that a knowledge of F_j and X_j at a sufficient number of frequencies Ω suffices to identify the elements of $\boldsymbol{\xi}, \boldsymbol{m}, \boldsymbol{\lambda}$ and $\boldsymbol{\Phi}$, which parameters define the desired equivalent foundation. The response is then given by:

$$\widetilde{X} = \boldsymbol{\Phi}[\boldsymbol{m}\left(-\Omega^2\boldsymbol{I} + 2i\Omega\boldsymbol{\omega}\boldsymbol{\xi} + \boldsymbol{\lambda}\right)]^{-1}\boldsymbol{\Phi}^{\mathrm{T}}\widetilde{F} \tag{1}$$

4 Experimental Procedure

Full details of the rig are given in Ref. [5] so only a brief summary is given here. The rig in Fig. 1 consists of a three disc rotor driven via a flexible coupling by a variable speed AC motor. The motor end of the rotor is supported by ball bearings; the other end by a plain journal bearing. Both bearings are mounted in aluminium pedestals which are bolted to an aluminium block which in turn is flexibly connected via steel bars to a heavy steel table. Steel weights bolted to the aluminium block allowed for some tuning of foundation natural frequencies. Motion measurements used appropriately positioned displacement transducers and accelerometers. Figure 2 shows the accelerometer locations and measurement directions. Displacement transducers were mounted at the bearings and facing a notch at the rotor end. Rotor speed, journal bearing oil temperatures and orbit size were monitored. Signals were processed using in house data processing software.

The natural frequencies of the foundation were determined by hammer tests. Six natural frequencies were found in the frequency range from 0 to 512 Hz with resolution of 0.125 Hz as shown in Table 1. None of the accelerometers was able to find all six. There was no longitudinal vibration frequency below 512 Hz. These natural frequencies formed the yardstick frequencies of the yet to be identified

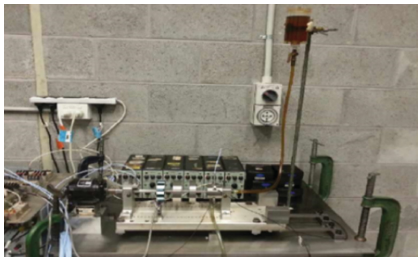

Fig. 1 Rotor bearing foundation rig [5]

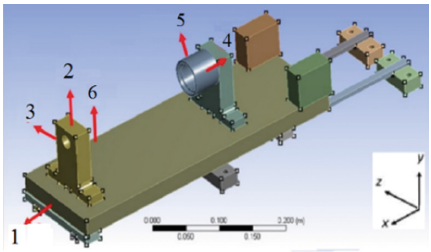

Fig. 2 Accelerometer locations and directions [5]

Table 1 Hammer test and FEM natural frequencies (Hz)

Mode	1st	2nd	3rd	4th	5th	6th
Hammer test	25.500	31.500	40.625	66.625	229.00	481.00
ANSYS FEM	26.102	29.103	49.602	68.137	242.30	462.69

foundation. Also, a finite element model (FEM) of the foundation was used to estimate the first six undamped natural frequencies and corresponding mode shapes of the foundation. Table 1 compares the hammer test and FEM natural frequencies. As expected, agreement is only approximate owing to the limited number of elements which could be accommodated in the FEM; but the results are close enough to provide a qualitative yardstick for the mode shapes. These mode shapes clearly showed that the aluminium block exhibited minimal rotation about the Z axis till the fifth mode and minimal flexure till the sixth mode [5].

The proposed identification procedure presumes a sufficiently accurate dynamic model of the rotor. A discretized rotor model which assumed zero rotor damping was initially accepted as adequate [5] since it had previously proved satisfactory [4]. However, in Ref. [4] all natural frequencies of the rotor were outside the operating speed range, whereas here the first natural frequency of the simply supported rotor (64.73 Hz) is within the operating speed range, necessitating the inclusion of damping in the rotor model to avoid inaccurate excitation force 'measurements' at speeds close to this frequency. With the rotor simply supported in its bearings, its damping ratio was estimated from hammer test signals in the frequency domain, resulting in a value of 0.020267 for the logarithmic decrement of internal shaft damping [6]. This value specified the damping in the updated rotor model.

5 Input Data

As the residual unbalance was unknown, measurements were taken at 'identical' speeds for two rotor rundowns over a speed range from 73 to 20 Hz with known unbalances of 15.189 g mm and 26.81 g mm added to rotor disks 1 and 3 respectively for the second rundown [5]. There were 67 'identical' speeds where speed differences in the two rundowns were less than 0.2 %. Figure 3 shows the magnitudes of the displacement differences obtained from the accelerometers while

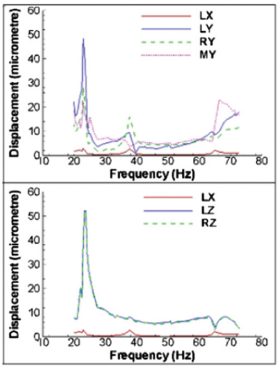

Fig. 3 Magnitude of displacement differences [5]

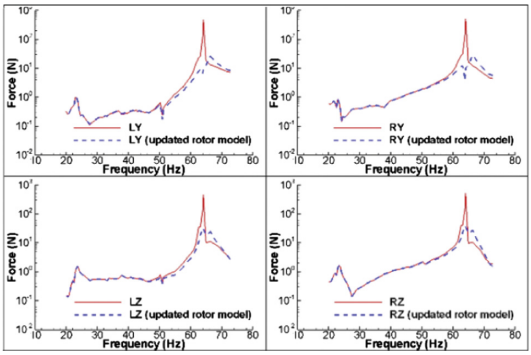

Fig. 4 Magnitude of excitation force differences

Fig. 4 shows the magnitudes of the transmitted force differences for both the undamped rotor model (used to obtain the preliminary results in Ref. [5]) and the now updated rotor model. Hereafter, for the sake of brevity, displacement differences and force differences will simply be referred to as displacements and forces.

In Fig. 4 one can see the significant effect (at speeds near the rotor natural frequency) of updating the rotor model on the transmitted forces, and hence on the force input 'measurements'. In Fig. 3, it can be seen the longitudinal displacement of the foundation (curve *LX*) is very small. The FEM analysis indicated that the longitudinal natural frequency was well above 512 Hz. Hence, accelerometer ***1*** signals could be ignored. Also, since ω_6 (430.75 Hz) was well above the upper bound of the operating speed range (73 Hz), ω_6 could also be ignored leaving the equivalent foundation to have at most 5 DOF. Also, there is minimal difference in the transverse horizontal displacements at the bearing connection points (curve *LZ*) and (curve *RZ*) so that one has, in effect, a 4 DOF foundation. As indicated in Fig. 3, peaks in the transmitted forces still occur around the rotor natural frequency and can be as high as 50 N. To allow for error in the calculated hysteretic damping in the rotor, acceptable data was restricted to speeds at which the transmitted forces were less than 10 N. Also, the selected speeds had speed spacings in excess of 2 rad/s to reduce error bias, leaving data for 42 speeds.

6 Results and Discussion

The identification procedure outlined in Ref. [2] was then applied to identify a 4 DOF equivalent foundation. The identified parameters and actual natural frequencies are given in Table 2. Figure 5 compares the predicted unbalance responses with the measured responses using Eq. (1). The agreement between actual and predicted responses is quite reasonable though there are large discrepancies between the responses around the fourth natural frequency (60–65 Hz), suggesting incorrectly identified damping coupled with error in the identified natural frequency. Even so, the agreement between the responses is far better than that

Table 2 Identified modal parameters (frequencies in Hz; masses in kg)

Mode	Actual	ω_k	Φ_1	Φ_2	Φ_3	Φ_4	ξ_k	m_k
1	25.5	29.55	−4.89	−3.10	−2.85	−2.28	−9.24E-02	117.19
2	31.5	36.04	−0.62	−0.74	−1.78	2.46	−4.73E-02	70.65
3	40.625	37.38	0.16	1.68	2.68	−4.20	1.03E-02	−382.32
4	66.625	64.71	5.50	3.99	5.85	−0.53	−1.80E-02	−2311.99

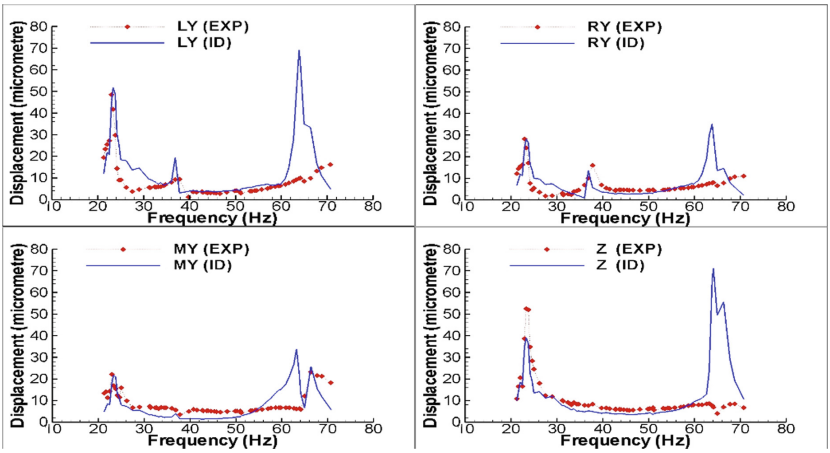

Fig. 5 Measured (EXP) and identified (ID) unbalance responses of the foundation

obtained in Ref. [5] where neither rotor damping nor foundation damping were properly accounted for.

The results in Table 2 and Fig. 5 suggest that the identification procedure needs further improvement and/or that there is too much error in the measurement data to enable better identification. The identified natural frequencies should agree better with the yardstick values since foundation damping is small. Negative damping ratios and modal masses indicate excessive round off error, exacerbated by errors in measurement data. To better understand these results, all modal parameters were reidentified using a different iterative procedure. Again, some of the identified damping ratios and modal masses were negative. The difficulty of identifying the damping ratio is highlighted in this alternative iterative procedure, where the other modal parameters are identified independently of the damping ratio. Its evaluation then involves subtracting two relatively large numbers both of which required extensive computation. Hence further work on perfecting the identification procedure is needed before it can be confidently applied in practice.

7 Conclusions

1. For a laboratory RBFS, a 4 DOF equivalent foundation has been identified which predicts reasonably well the measured unbalance response over the operating speed range.
2. An accurate dynamic model of the rotor, which included rotor damping, was essential to minimise inaccurate force excitation ‘measurements’ at speeds near the rotor natural frequency.
3. Further work is required to better evaluate the foundation modal damping parameter, which is very susceptible to computational round off errors.

References

1. Lees, A., Sinha, J., Friswell, M.: Model-based identification of rotating machines. Mech. Syst. Signal Process. **23**(6), 1884–1893 (2009)
2. Yu, M., Feng, N., Hahn, E.: An equation decoupling approach to identify the equivalent foundation in rotating machinery using modal parameters. J. Sound Vib. **365**, 182–198 (2016)
3. Yu, M., Feng, N., Hahn, E.: Experimental evaluation of a modal parameter based system identification procedure. Mech. Syst. Signal Process. **68–69**, 302–315 (2016)
4. Feng, N., Hahn, E.: Identification of pedestal parameters in rotor-bearing-pedestal systems using known unbalance, In: Proceedings of ASME DETC’01, 9 p (2001)
5. Yu, M., Feng, N., Hahn, E.: Experimental evaluation of a modal parameter based foundation identification procedure. In: Proceedings of the 9th IFToMM International Conference on Rotor Dynamics Mechanisms and Machine Science, 10 p (2014)
6. Lund, J.: Stability and damped critical speeds of a flexible rotor in fluid-film bearings. J. Eng. Ind. **96**(2), 509–517 (1974)

Researching of the Method of Separation of Fine-Grain Particles by Centrifugation in a Liquid Medium

A.B. Kydyrbekuly, L.A. Khajieva and G.E. Ybraev

Abstract In this paper developed the analytical methods of research that used in industrial separation method for the technical rotor installation used for treating a suspension. In this work, the rotor is installed symmetrically to the bearings, on a flexible shaft, and rotates with the angular velocity. The rotor is a round disk on which the cups (tubes) with the suspension are hung symmetrically at a certain distance from the spinning axis. Tubes are rotatable around its horizontal axis. The rotor position is determined relative to a fixed coordinate system. The position of the sample suspension particle is determined relative to the moving coordinate system, coupled with a rotating cup (tube). Angular spin rate of rotor is high enough to ignore the suspension gravitation force, which is much smaller than the centrifugal force. In addition, the shape of the particle is spherical; particle mean free path is much larger than its size; suspension turbulence is absent (laminar mode); the interaction forces between the particles and the walls of the cup (tube) are absent; cup (tube) is quite narrow (diameter $\ll$ length); after settling of on the walls of the cup the particles stop their motion; the friction force between the cups and their axis of rotation are ignored; the friction force between the solid particle and the wall of the cup is also ignored. In contrast to other researcher's papers, in which the particles are moving only in the cup axis, this paper explores the spatial motion of a suspension particle. Suspended containers are symmetrically arranged relative to each other; however, the mass of suspension in them may be different. The number of fine particles in them may not be equal, and the time of particle precipitation differs. All of these factors are the cause of imbalance in the rotor system. For practical use of mathematical model are offered the individual cases and their solutions, which are often encountered in practice. For individual cases, determined the conditions of stability of rotor system using the method of complex amplitudes.

Keywords Suspension · Particles · Rotor system · Suspension separation · Imbalance in the rotor system

A.B. Kydyrbekuly · L.A. Khajieva · G.E. Ybraev (✉)
Al-Farabi Kazakh National University, Almaty, Kazakhstan
e-mail: ybraev.alysher@mail.ru

J. Beran et al. (eds.), *Advances in Mechanism Design II*,
Mechanisms and Machine Science 44, DOI 10.1007/978-3-319-44087-3_14

1 Introduction

Centrifugation method is widely used in many fields of technology and industry. Separation method is particularly widely used in the fields of medicine, biology, chemical and agricultural industries. For example, to study the material composition of ores and soil samples are often used for the separation. Centrifugation is commonly called emulsions separation emulsions [1–3]. This process is carried out in a continuous wall with rotors and can be compared with the process of sedimentation in the gravity field of emulsions. Examples of this process are the separation of the cream from the milk, the water from lubricating oils, separation of massecuite, etc. [4, 5]. Many mathematical models in describing the motion of solids emulsions were limited to the study of planar motion [6–8], which does not give a complete picture of the process. Also, experimental studies [9, 10] show the importance of taking into account fluctuations and their effect on the mechanical system as a whole. In this regard, it was built a number of different analytical and numerical models [11, 12] to describe these processes.

2 Statement of the Problem and the Equations of Motion

The rotor is mounted symmetrically about the supports on the flexible shaft, rotating with the angular velocity ω. The rotor is a circular disc on which at certain distances from the axis of rotation symmetrically suspended containers with suspension.

Containers are can rotate around its horizontal axis (Fig. 1). The angle of rotation is determined by the container from a vertical angle α; $\Omega = \dot{\alpha}$—the angular speed of rotation of the containers, L_{cm}—distance from the rotor axis to the axis of

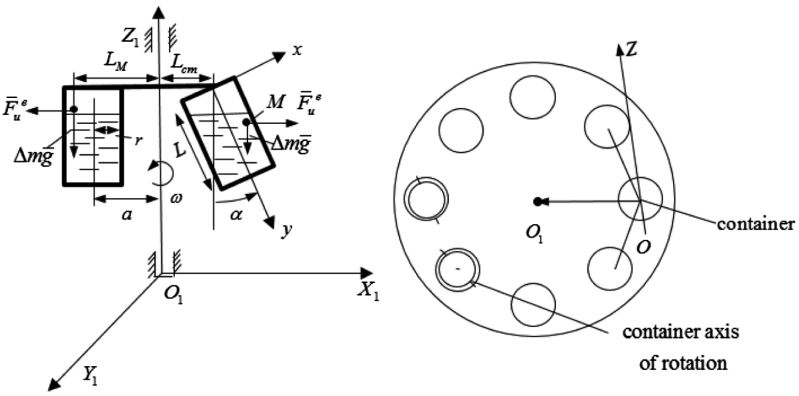

Fig. 1 Scheme the rotor system and disc with containers

rotation of containers, L_M—distance to the particles of the suspension M with a mass Δm, r—containers radius, g—acceleration of gravity, L—containers length.

The rotor position is determined relative to a fixed coordinate system $O_1x_1y_1z_1$ (Fig. 1). The position of the studied particles M is determined by the relative moving coordinate system $Oxyz$. Oy axis is directed along the axis of symmetry of the container bottom, an Oz axis directed along the rotational axis of the container.

In the calculation the following assumptions were used:

(1) the angular speed of the rotor is large enough so that we can ignore the force of gravity suspension ($g \ll \omega^2$);
(2) spherical shape of particles assumed;
(3) particle mean free path is much larger its size;
(4) no turbulence suspension (laminar flow);
(5) the interaction forces between the particles and the walls of the container (test tube) absent;
(6) container (test tube) is rather narrow radius is much smaller than its length ($r_0 \ll L$);
(7) after deposition of the particles on the wall of the container stop moving;
(8) the friction force between the containers and their axes of rotation, as well as a change in gravity from the suspensions disregarded containers;
(9) the force of friction between the solid particles and the container wall disregarded.

Unlike other studies [1, 8, 13], where the movement of the particles only axis of the container, in this paper we investigate the three-dimensional motion of a particle M.

After determining the acceleration vector of the portable moving coordinate system

$$\left.\begin{aligned} W_{ex} &= \omega \sin\alpha \cdot [\omega(x\sin\alpha - y\cos\alpha) - \Omega z] - (L_{cm}\cos\alpha + x)(\omega^2 + \Omega^2) \\ &\quad + \dot{\Omega}(L_{cm}\cos\alpha + x) - z\dot{\omega}\sin\alpha, \\ W_{ey} &= -\omega\cos\alpha \cdot [\omega(x\sin\alpha - y\cos\alpha) - \Omega z] - (L_{cm}\sin\alpha + y)(\omega^2 + \Omega^2) \\ &\quad + \dot{\Omega}(L_{cm}\cos\alpha + x) - z\dot{\omega}\sin\alpha, \\ W_{ez} &= -\Omega \cdot [\omega(x\sin\alpha - y\cos\alpha) - \Omega z] - z(\omega^2 + \Omega^2) + \dot{\omega} \cdot (L_{cm} + y\sin\alpha + x\cos\alpha). \end{aligned}\right\} \quad (1)$$

represent the equation of motion of the particle M in the suspension, taking into account transportation and Coriolis forces of inertia and the assumptions made in the form of:

$$\left.\begin{aligned}
\Delta m\ddot{x} &= -\Delta mg\sin\alpha - 6\pi\eta r_0\dot{x} + \Delta m\{(L_{cm}\cos\alpha + x)(\omega^2+\Omega^2) - \omega\sin\alpha[\omega(x\sin\alpha \\
&\quad - y\cos\alpha) - \Omega z] - \dot{\Omega}(L_{cm}\sin\alpha + y) + 2\Delta m(\omega\cdot\dot{z}\cos\alpha - \dot{y}\Omega), \\
\Delta m\ddot{y} &= \Delta mg\sin\alpha - 6\pi\eta r_0\dot{y} + \Delta m\{(L_{cm}\sin\alpha + y)(\omega^2+\Omega^2) + \omega\cos\alpha[\omega(x\sin\alpha \\
&\quad - y\cos\alpha) - \Omega z] - \dot{\Omega}(L_{cm}\cos\alpha + x) + 2\Delta m(\omega\cdot\dot{z}\sin\alpha + \dot{x}\Omega), \\
\Delta m\ddot{z} &= -6\pi\eta r_0\dot{z} + \Delta m\{z(\omega^2+\Omega^2) + \Omega[\omega(x\sin\alpha \\
&\quad - y\cos\alpha) - \Omega z] - \dot{\omega}(L_{cm} + y\sin\alpha + x\cos\alpha) - 2\Delta m\omega(\dot{y}\sin\alpha + \dot{x}\cos\alpha).
\end{aligned}\right\} \quad (2)$$

where r_0—suspensions particle radius with a mass Δm; η—dynamic viscosity of the fluid (suspension); $6\pi\eta r_0$—friction coefficient of the particle M (coefficient of force environmental resistance) during its movement.

The system (2) is especially nonlinear, since $\omega = \omega(t), \alpha = \alpha(t), \Omega = \Omega(t)$. Moreover the angle of rotation of the container $\alpha(t)$ included in the arguments of trigonometric functions. In view of the above system (2) of the exact solution does not.

Let us consider the special cases.

1. The rotor is rotated at a constant angular speed,$\omega = const$, that is $\alpha \neq 0 = const$, $\dot{\alpha} = \Omega = 0$. At first we define the dependence of the angle α of the angular speed of the rotor ω. For this purpose, we draw up the balance of forces acting on the container (рис.3). Projecting force in the direction of $\tau\tau$ we get (Fig. 2)

$$g\ \sin\alpha = \omega^2(L_{cm} + l\ \sin\alpha)\cos\alpha. \quad (3)$$

where l—distance from the axis of rotation to center of gravity of the container with a suspension of. From here it follows that

$$\omega = \sqrt{\frac{g\cdot tg\alpha}{L_{cm} + l\sin\alpha}}. \quad (4)$$

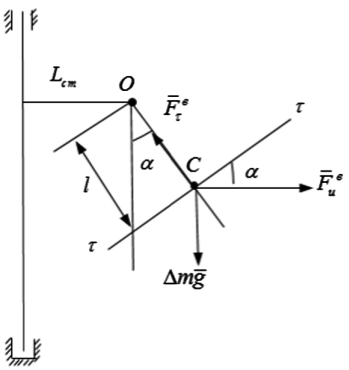

Fig. 2 Determination of forces

If $\omega \to \infty$, $\alpha \to \frac{\pi}{2}$ or $\alpha \to \frac{\pi}{2}$, $\omega \to \infty$. i.e. if $\alpha \to \frac{\pi}{2}$ $\omega \to \infty$, which follows from the physical meaning of the problem. From (3) we find the dependence of the angular speed Ω of the container in ω, α, and other system parameters.

$$\Omega = \frac{2\omega\varepsilon(L_{cm} + l\sin\alpha)}{g\cos\alpha - \omega^2(l\cos 2\alpha - L_{cm}\sin\alpha)}. \tag{5}$$

where $\varepsilon = \dot{\omega}$. Case of indefinite increase of angular velocity $\omega \to \infty$ the angular speed of the container goes to zero $\Omega \to 0$. As is shown above, if $\omega \to \infty$, $\alpha \to \frac{\pi}{2}$; these conclusions are valid, when the angular speed of the rotor increases homogeneous.

The maximum value of the angular velocity of the container we find the angular speed of the rotor. We then obtain

$$\omega^2 = \frac{g\cos\alpha}{l\cos 2\alpha - L_{cm}\sin\alpha}.$$

It follows, that when $\alpha \to \frac{1}{4l}(\sqrt{L_{cm}^2 + 8l^2} - L_{cm})$, the angular velocity increase without limit.

Hence, each value of ω corresponds to the specific value of α. Then from (2) as $\omega = const$, $\alpha = const$, $\Omega = 0$, $\varepsilon = 0$ we will have

$$\left.\begin{aligned} \ddot{x} + 2n\dot{x} &= \omega^2\cos^2\alpha \cdot x - g\sin\alpha + (L_{cm} + y\sin\alpha)\omega^2\cos^2\alpha + 2\omega\cos\alpha\dot{z}, \\ \ddot{y} + 2n\dot{y} &= \omega^2\sin^2\alpha \cdot y + g\cos\alpha + (L_{cm} + x\cos\alpha)\omega^2\sin^2\alpha + 2\omega\sin\alpha\dot{z}, \\ \ddot{z} + 2n\dot{z} &= \omega^2 z - 2\omega(\dot{y}\sin\alpha + \dot{x}\cos\alpha). \end{aligned}\right\} \tag{6}$$

where $n = 3\pi\eta r_0$—friction coefficient. From (6), equating coefficients of the same functions of time $\exp(-\alpha_0 t)$ and the constant terms, is possible get the system of algebraic equations for the unknown $B_1, B_2, B_0, P_1, P_2, P_3$, which solution has the form

$$\left.B_0 = \sin\alpha \cdot C_1 - L_{cm}\cos\alpha, \quad B_1 = -\frac{\sin\alpha}{\alpha_0}C_0, \quad B_2 = -\sin\alpha \cdot k_0, \quad P_1 = P_2 = P_3 = 0.\right\} \tag{7}$$

Considering (7) can be written law of motion of the particle suspensions

$$\left.\begin{aligned} x &= A_1 e^{\alpha_1 t} + A_2 e^{-\beta_1 t} - \frac{\sin\alpha}{\alpha_0}C_0 e^{-\alpha_0 t} - \sin\alpha \cdot k_0 t + \sin\alpha \cdot C_1 - L_{cm}\cos\alpha, \\ y &= A_1 tg\alpha \cdot e^{\alpha_1 t} + A_2 tg\alpha \cdot e^{-\beta_1 t} + \frac{\cos\alpha}{\alpha_0}C_0 e^{-\alpha_0 t} + \cos\alpha \cdot k_0 t - \cos\alpha \cdot C_1 - L_{cm}\sin\alpha, \end{aligned}\right\} \tag{8}$$

$$z = E_1 e^{\alpha_1 t} + E_2 e^{-\beta_1 t}. \tag{9}$$

Using the initial conditions of the problem, we find the integration constants $A_1, A_2, C_0, C_1, E_1, E_2$. For determining A_1, A_2, C_0, C_1 we have four algebraic equations:

$$\left.\begin{aligned} &A_1 + A_2 - \tfrac{\sin\alpha}{\alpha_0} C_0 + \sin\alpha \cdot C_1 = x_0 + L_{cm}\cos\alpha, \\ &\alpha_1 A_1 - \beta_1 A_2 + \sin\alpha \cdot C_0 = \dot{x} - \sin\alpha \cdot k_0, \\ &(A_1 + A_2) tg\alpha + \tfrac{\cos\alpha}{\alpha_0} C_0 - \cos\alpha \cdot C_1 = y_0 + L_{cm}\sin\alpha, \\ &(\alpha_1 A_1 - \beta_1 A_2) tg\alpha - \cos\alpha \cdot C_0 = \dot{y} - \cos\alpha \cdot k_0. \end{aligned}\right\} \tag{10}$$

$$E_1 + E_2 = z_0,\ \alpha_1 E_1 - \beta_1 E_2 = \dot{z}_0.\} \tag{11}$$

The system of algebraic equations (10) and (11) are solved without difficulty. Let us write the final value:

$$\left.\begin{aligned} &A_1 = \frac{b_1\beta_1 + b_2}{2\sqrt{n^2+\omega^2}},\ A_2 = \frac{b_1\alpha_1 - b_2}{2\sqrt{n^2+\omega^2}},\ C_0 = k_0 + \dot{x}_0 \sin\alpha - \dot{y}_0 \cos\alpha, \\ &C_1 = \frac{k_0 + \dot{x}_0 \sin\alpha - \dot{y}_0 \cos\alpha}{\alpha_0} + x_0 \sin\alpha - y_0 \cos\alpha, \end{aligned}\right\} \tag{12}$$

where

$$b_1 = x_0 \cos^2\alpha + y_0 \cos\alpha \sin\alpha + L_{cm}\cos\alpha, \quad b_2 = \dot{x}_0 \cos^2\alpha + \dot{y}_0 \cos\alpha \sin\alpha, \tag{13}$$

$$E_1 = \frac{z_0\beta_1 + \dot{z}_0}{2\sqrt{n^2+\omega^2}},\ E_2 = \frac{z_0\alpha_1 - \dot{z}_0}{2\sqrt{n^2+\omega^2}}. \tag{14}$$

From (22) we find the velocity of the particle suspensions in the direction of the Oy axis:

$$y|_{t=T} = \alpha_1 A_1 tg\alpha \cdot e^{\alpha_1 T} - \beta_1 A_2 tg\alpha \cdot e^{-\beta_1 T} - \alpha_0 \cos\alpha \cdot C_0 e^{-\alpha_0 T} + \cos\alpha \cdot k_0 = 0.$$

If we consider that $\beta_1 - \alpha_0 = n + \sqrt{n^2+\omega^2} - 2n = -n + \sqrt{n^2+\omega^2} = \alpha_1$, $\alpha_1 + \beta_1 = 2\sqrt{n^2+\omega^2}$, and $\omega \gg n$, then ignoring n in exponential functions in comparison with the $(\sqrt{n^2+\omega^2})$, we get

$$\alpha_1 A_1 tg\alpha \cdot e^{2\sqrt{n^2+\omega^2}T} + (\cos\alpha \cdot k_0 - \alpha_0 \cos\alpha \cdot C_0) e^{\sqrt{n^2+\omega^2}T} - \beta_1 A_2 tg\alpha = 0. \tag{15}$$

If we denote $e^{\sqrt{n^2+\omega^2}T} = \xi$, we obtain from (15) is a quadratic equation in the form

$$a\xi^2 + b\xi + c = 0, \tag{16}$$

where $a = \alpha_1 A_1 tg\alpha, \quad b = \cos\alpha \cdot k_0 - \alpha_0 \cos\alpha \cdot C_0, \quad c = -\beta_1 A_2 tg\alpha.$

Here A_1, A_2 and C_0 given by (12):

$$\xi_1 = \frac{-b + \sqrt{b^2 - 4ac}}{2a},\ \xi_2 = \frac{-b - \sqrt{b^2 - 4ac}}{2a},\ T_1 = \frac{\ln \xi_1}{\sqrt{n^2 + \omega^2}},$$
$$T_2 = \frac{\ln \xi_2}{\sqrt{n^2 + \omega^2}}. \tag{17}$$

Thus, the determined time separation of suspensions, taking into account the spatial movement of the solid particles of the suspension.

1. There should be considered a special case, which is more suitable for practical applications and determine the approximate time of separation.

Movements of suspensions of the particle in the direction of the axis Oy. Movement of particles of the suspension in the directions Ox and Oz disregarded. The angular speed of the rotor is large enough so that $\alpha \to \frac{\pi}{2},\ \Omega \to 0$. Then the differential equation of motion of a particle is given by

$$\ddot{y} + \chi\dot{y} - (\omega^2 \sin^2 \alpha + \Omega^2)y = g \cos \alpha + (\omega^2 + \Omega^2)L_{cm} \sin \alpha - \dot{\Omega} L_{cm} \cos \alpha. \tag{18}$$

As In the general case $\omega = \omega(t),\ \alpha = \alpha(t),\ \Omega = \Omega(t)$, Eq. (18) is a differential equation with variable coefficients and finding its exact solution is very difficult. Therefore, to find an approximate solution of Eq. (18) we consider the established mode of the system when $\omega = const$ and $\alpha = const$, $\Omega = 0$. Under these conditions, Eq. (18) takes the form

$$\ddot{y} + x\dot{y} - \omega^2 \sin^2 \alpha \cdot y = g \cos \alpha + L_{cm}\omega^2 \sin \alpha. \tag{19}$$

Linear non-homogeneous differential equation (19) has a solution

$$y = C_1 e^{b_0 t} + C_2 e^{-b_1 t} - A_0, \tag{20}$$

where C_1, C_2—integration constants, which are determined from the initial conditions of the problem and will be equal to:

$$\left.\begin{aligned} b_0 &= -\frac{x}{2} + \sqrt{\frac{x^2}{4} + \omega^2 \sin^2 \alpha}, \quad b_1 = \frac{x}{2} + \sqrt{\frac{x^2}{4} + \omega^2 \sin^2 \alpha}, \quad A_0 = \frac{g \cos \alpha + L_{cm}\omega^2 \sin \alpha}{\omega^2 \sin^2 \alpha}, \\ C_1 &= \frac{b_1(y_0 + A_0) + \dot{y}_0}{b_0 + b_1}, \quad C_2 = \frac{b_0(y_0 + A_0) - \dot{y}_0}{b_0 + b_1}, \quad \omega \neq 0, \alpha \neq 0. \end{aligned}\right\} \tag{21}$$

Then final expression the law of motion of the particle takes the form

$$y = \frac{1}{b_0 + b_1}\{[b_1(y_0 + A_0) + \dot{y}_0]e^{b_0 t} + [b_0(y_0 + A_0) - \dot{y}_0]e^{-b_1 t}\} - A_0. \tag{22}$$

From formula (22) define the precipitation suspension. Thus, from formula (22) we have

$$\frac{(L+A_0)(b_0+b_1)}{b_1(y_0+A_0)+\dot{y}_0} = e^{b_0 T} + \frac{b_0(y_0+A_0)-\dot{y}_0}{b_1(y_0+A_0)+\dot{y}_0} e^{-b_1 T}. \tag{23}$$

Given that the second term on the right-hand side of Eq. (23) by several orders of magnitude smaller than the first term ($b_1 > b_0, \frac{1}{e^{b_1 T}} \to 0$ in $\omega \to \infty$), that taking into account this consideration, (23) we obtain an approximate value of deposition time of suspension:

$$T = \frac{1}{b_0} \ln \left[\frac{(L+A_0)(b_0+b_1)}{b_1(y_0+A_0)+\dot{y}_0} \right]. \tag{24}$$

Thus, the dependence of the angle of rotation of the cup on the angular speed of the rotor, defined law of motion a of the particle suspensions and the deposition of it on the bottom of the cup (while the rotor stops), i.e. the time of separation suspension.

More precise separation of suspensions time can be achieved if coefficients neglected compared with the expression $\sqrt{\frac{\chi^2}{4} + \omega^2 \sin^2 \alpha}$. Then the coefficients b_0 and b_1 are equal to those $b_0 = b_1 = \sqrt{\frac{\chi^2}{4} + \omega^2 \sin^2 \alpha} = b$. In this case, formula (23) takes the form $\xi^2 + p\xi + q = 0$, where

$$p = -\frac{2(L+A_0)b}{b(y_0+A_0)+\dot{y}_0}, \quad q = \frac{b(y_0+A_0)-\dot{y}_0}{b(y_0+A_0)+\dot{y}_0}, \quad \xi_{1,2} = -\frac{p}{2} \pm \sqrt{\frac{p^2}{4} + q},$$
$$T = \frac{\ln \xi}{b}.$$

Consider the case when the rotor shaft is adopted a rigid, but support—elastic, with a corresponding coefficient of elasticity.

Rotor vibrations occur due to an imbalance of suspended containers (cups, test tubes, etc.). While containers are positioned symmetrically with respect to each other, however, the mass of suspensions in them may be different. The number of particles in finely ground them can not be equal, and the time also differs particle precipitation, etc. All of these factors may be the cause of imbalance in the rotor system, which causes oscillation of the rotor.

Figure 3 shows the model is equivalent to the rotor system with containers, taking into account rainfall the particle suspension. The mass, which creates an imbalance denote m_0, rotor mass in m. The position of the rotor center of gravity (the shaft) is determined relative to Oxy. It is assumed that the rotor makes a plane-parallel movement. The position of the shaft in the Oxy coordinate system defined by the x and y.

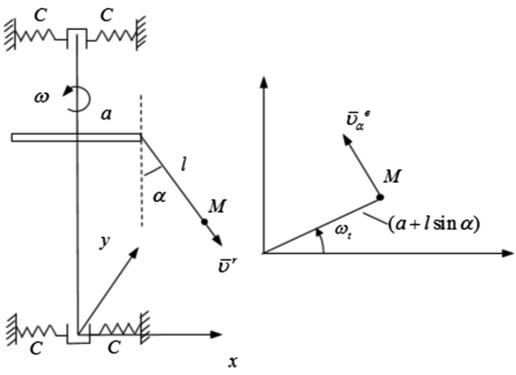

Fig. 3 The equivalent model

Let us introduce the dissipative function in the form

$$\Phi = \frac{\chi}{2}(\dot{x}^2 + \dot{y}^2) + \frac{\chi_0}{2}\dot{\alpha}^2 + \frac{\chi_1}{2}\dot{l}^2. \tag{25}$$

Differential equations of motion systems are nonlinear, finding the exact solution that is very problematic.

In particular, the equations of motion are complicated when the rotation angle of the cup is a function of time $\alpha = \alpha(t)$, as in the case of α include trigonometric functions.

Consider the special case when the angle of rotation of the container fixed $\alpha = const$.

(1) Case $x = x(t),\ y = y(t),\ l = l(t),\ \alpha = const,\ \Omega = 0,\ 0 < \alpha < \frac{\pi}{2}$. In this case, taking into account (25) we obtain the equations of motion of the system

$$\left.\begin{aligned}&(m+m_0)\ddot{x} + \chi\dot{x} + cx + m_0 \sin\alpha\cos\omega t\ddot{l} - 2m_0\omega\sin\omega t\sin\alpha\dot{l}\\&-m_0\omega^2\cos\omega t\sin\alpha l = m_0\omega^2 a\cos\omega t,\\&(m+m_0)\ddot{y} + \chi\dot{y} + cy + m_0\sin\alpha\sin\omega t\ddot{l} + 2m_0\omega\cos\omega t\sin\alpha\dot{l}\\&-m_0\omega^2\sin\omega t\sin\alpha l = m_0\omega^2 a\sin\omega t.\end{aligned}\right\}$$

$$\sin^2\alpha\ddot{l} + 2n_1\dot{l} - \omega^2\sin^2\alpha l + (\ddot{x}\cos\omega t + \ddot{y}\sin\omega t)\sin\alpha = \omega^2 a\sin\alpha + g(1-\cos\alpha). \tag{26}$$

The system (26) is the equation of motion of a system with periodically varying coefficients. When there is a periodically varying parameters growing vibrations of the system, i.e., A so-called parametric oscillation. Eccentricity in this case the system periodically varies, i.e. changing the force of inertia.

The system of Eq. (26) in the literature has been well studied, although the actual results were obtained only for some special cases. Of particular interest is the study of the conditions of stability of the system. For the equation with periodically

varying coefficients of rigidity has a diagram Ainis-Strett, which can be found using the conditions of stability of the system.

You can lead one of the solution methods based on the method of complex amplitudes. The problem is solved in the complex plane, in this case, Eq. (26) will have the form:

$$\left.\begin{aligned} \ddot{z}+2n\dot{z}+k^2z &= -\tfrac{\sin\alpha}{1+\mu}\left(\ddot{l}+2i\omega\dot{l}-\omega^2 l\right)e^{i\omega t}+\tfrac{\omega^2 a}{1+\mu}e^{i\omega t}, \\ \ddot{l}+2n_0\dot{l}-\omega^2 l &= -\tfrac{1}{\sin\alpha}\ddot{z}e^{-i\omega t}+\tfrac{\omega^2 a}{\sin\alpha}+\tfrac{g}{1+\cos\alpha}. \end{aligned}\right\} \tag{27}$$

$$2n=\frac{\chi}{m+m_0},\ k^2=\frac{c}{m+m_0},\ \mu=\frac{m}{m_0},\ 2n_0=\frac{\chi_1}{m_0\sin^2\alpha},\ 2n_1=\frac{\chi_1}{m_0},\ z=x+iy. \tag{28}$$

From the system (27) excluding the $(\ddot{l}-\omega^2 l)$, obtain the

$$\dot{l}=\frac{(n_0+i\omega)}{2(n_0^2+\omega^2)}\left[\frac{\mu\ddot{z}+2(1+\mu)n\dot{z}+k^2(1+\mu)z}{\sin\alpha}\right]e^{-i\omega t}+a_2. \tag{29}$$

The vibrations of the rotor in the complex plane can be represented as

$$z=Ae^{i\omega t}. \tag{30}$$

Substituting (30) into (29) we find

$$l=a_1At+a_2t+C, \tag{31}$$

$$a_1=\frac{n_0+i\omega}{2(n^2+\omega^2)\sin\alpha}[-\mu\omega^2+2(1+\mu)ni\omega+k^2(1+\mu)],\quad a_2=\frac{g(n_0+i\omega)}{2(n_0^2+\omega^2)(1+\cos\alpha)}, \tag{32}$$

C—constant of integration.

Substituting (30) and (31) we obtain

$$A=-\frac{a_2}{a_1}=-\frac{g\sin\alpha}{(1+\cos\alpha)[-\mu\omega^2+2(1+\mu)ni\omega+k^2(1+\mu)]}, \tag{33}$$

$$C=\frac{g(1+\mu)(\omega^2-2n\omega i-k^2)}{\omega^2[-\mu\omega^2+2(1+\mu)ni\omega+k^2(1+\mu)](1+\cos\alpha)}-\frac{a}{\sin\alpha}. \tag{34}$$

Substituting (32), (33) and (34) into (30) and (31) we obtain the motion law of the rotor and the point M of mass m, which moves along the container axis.

The law of motion of the rotor in the direction of the axes Ox and Oy:

$$x = A_0 \cos \omega t - A_1 \sin \omega t, \quad y = A_1 \cos \omega t + A_0 \sin \omega t.\} \tag{35}$$

$$\left.\begin{aligned} A_0 &= \frac{g \sin \alpha(\mu\omega^2 - k^2(1+\mu))}{(1+\cos\alpha)\{[\mu\omega^2 - k^2(1+\mu)]^2 + 4(1+\mu)^2 n^2\omega^2\}}, \\ A_1 &= \frac{2g \sin \alpha(1+\mu)n\omega}{(1+\cos\alpha)\{[\mu\omega^2 - k^2(1+\mu)]^2 + 4(1+\mu)^2 n^2\omega^2\}}, \\ A &= A_0 + iA_1. \end{aligned}\right\} \tag{36}$$

$$l = C = \frac{g(1+\mu)\{(\omega^2 - k^2)[(1+\mu)k^2 - \mu\omega^2] - 2n^2\omega^2(1+\mu)^2]}{\omega^2(1+\cos\alpha)\{[k^2(1+\mu) - \mu\omega^2]^2 + 4(1+\mu)^2 n^2\omega^2\}} - \frac{a}{\sin\alpha}. \tag{37}$$

From (35) it is obvious that the rotor performs harmonic oscillations. The point M a mass m_0 has a certain position in accordance with (37), that is this point is at a distance $l = C$ axis of containers rotation.

3 Conclusions

The important results were obtained within the framework of this study. The problem in this formulation is solved analytically. The analytical dependence of the angular speed of the container, the angle of rotation as a whole. Certain laws of spatial motion of a particle suspension and the deposition of it on the bottom of the container (the stop of the rotor)—the time separation of the suspension. When account is taken of the rotor vibration at fixed angles of rotation of the container was conducted stability analysis method of complex amplitudes, which suggests a harmonic vibration of the rotor.

References

1. Лукьяненко, В.М., Таранец, А.В.: *Промышленные центрифуги*, Москва: Химия, 1974, 376 с
2. Greenspan, H.P.: The Theory of Rotating Fluids. Cambridge University Press, Cambridge (1968)
3. Соколов, В.И.: *Современные промышленные центрифуги*. Москва: Машиностроение, 1967, 524 с
4. Bullen, J., Bruijn, J.M.: Impact of the centrifugal speed of rotation on the quality of white sugar crystals. Zuckerindustrie **129**, 738–741 (2004)
5. Jullienne, L.M.: *Washing sugar in batch A-centrifugals*, Proc. SASTA, pp. 42–43, 1983
6. Please, C.P., Fowkes, N.D., Mason, D.P., Khalique, C.M., Hutchinson, A., Rademeyer, M.C., Loubser R., Davis, S.: Extraction of molasses from sugar crystals in a centrifuge. Math. Modell. Anal. **19**(3), 347–358 (2014)

7. Ратобыльский, В.Ф., Карамзин, В.А. и др.: *О математическом моделировании движения жидкостного сепаратора*,Труды ВНИЭКИПродмаш, Москва, 1983, № 59, с. 87–91
8. Еркова, Л.Н., Смирнов, Н.И.: *Свободное осаждение твёрдых сферических частиц в жидкой среде*, Журнал прикладной химии, т.24, вып.5, 1966, с. 733–738
9. Подольский, В.Г., Эпштейн, Л.Ю.: *Определение динамических нагрузок, возникающих при работе центрифуг*, Химическое и нефтяное машиностроение, 1965, №3
10. Ligier, K.: Methods of diagnosing an acww 1000 sugar centrifuge with the use of vibration processes. Techn. Sci. 11, 289–300 (2008)
11. Zachwieja, J., Ligier, K.: Numerical analysis of vertical rotor dynamics of ACWW 1000 centrifuge. J. Theor. Appl. Mech. **43**(2), 257–275 (2005)
12. Nelson, H.D., McVaugh, J.M.: The dynamics rotor bearing systems using finite elements. J. Eng. Ind. **98**, 593–599 (1976)
13. Trowbridge, M.E.: Centrifugal purification of oils for marine service. Trans. Inst. Mar. Eng. **75** (1), 1–22 (1970)

The Steady State Response of Multi-disc Rotors Damped by Magnetorheological Squeeze Film Dampers

J. Zapoměl and P. Ferfecki

Abstract A frequently used technological solution for suppressing lateral vibrations of rotors produced by unbalance of rotating parts consists in adding damping devices to the rotor supports. Their damping effect must be controllable to achieve their optimum performance. This is enabled by magnetorheological squeeze film dampers. In the developed mathematical model the number of the rotor system state parameters is reduced. The steady state solution of the equation of motion is calculated by the trigonometric collocation method. Modelling the magnetorheological oil by bilinear material, determination of the hydraulic damping forces by means of the Reynolds equation adapted to bilinear material, reduction of the rotor system utilizing the influence coefficients determined by the finite element method, and learning more on suppressing the lateral vibration of flexible rotors by magnetorheological squeeze film dampers are the principle contributions of this article. Reduction of the amplitude of the rotor vibration as a result of controlling the damping force in the supports according to the angular speed was confirmed by computer simulations.

Keywords Multi-disc rotors · Magnetorheological squeeze film dampers · Bilinear material · Model reduction · Controllable vibration suppression

1 Introduction

Magnetorheological squeeze film dampers enable to suppress lateral vibrations of rotors caused by imbalance of rotating parts in a wide range of running speeds [1]. Many journal articles and conference papers deal with their design, function,

J. Zapoměl (✉)
Institute of Thermomechanics, Prague, Czech Republic
e-mail: zapomel@it.cas.cz; jaroslav.zapomel@vsb.cz

J. Zapoměl · P. Ferfecki
VŠB—Technical University of Ostrava, Ostrava, Czech Republic
e-mail: petr.ferfecki@vsb.cz

J. Beran et al. (eds.), *Advances in Mechanism Design II*,
Mechanisms and Machine Science 44, DOI 10.1007/978-3-319-44087-3_15

modelling, experimental investigations, and efficiency [2–4]. Zapoměl et al. [5, 6] reported mathematical models of a short and long squeeze film magnetorheological damper based on modelling the magnetorheological oil by Bingham material. Extension of this work is represented by the development of a new and enhanced model of squeeze film magnetorheological damping devices based on application of bilinear material to represent the magnetorheological oil [7].

This paper deals with application of magnetorheological squeeze film dampers for controllable attenuation of vibration of flexible multi-disc rotors. Modelling the magnetorheological oil by bilinear material; reducing the size of the model rotor system by means of combination of the influence coefficients and the finite element method; and learning more on the effect of magnetorheological squeeze film dampers on suppressing lateral vibrations of complex flexible rotors are the principle contributions of this article.

2 The Magnetorheological Damping Forces

The main parts of magnetorheological squeeze film dampers are two concentric rings between which there is a thin layer of magnetorheological oil. The inner ring is coupled with the shaft by a rolling element bearing and with the damper housing by a squirrel spring. Lateral vibration of the rotor squeezes the oil film, which produces the damping effect. The electric coils, built in the damper housing, generate magnetic flux passing through the lubricating layer. As resistance against the flow of magnetorheological oils depends on magnetic induction, the damping force can be controlled by changing magnitude of the electric current.

Magnetorheological oils belong to the category of fluids with a yielding shear stress. In the developed mathematical model the oil is implemented by bilinear material. The pressure distribution in the full oil film determined on assumptions of the classical theory of lubrication (except for the lubricant) and short dampers is governed by relations (1)–(3) [7]

$$\frac{\partial}{\partial Z}\left(\frac{1}{\eta_C}h^3p'\right) = 12\dot{h}, \tag{1}$$

$$\frac{\partial}{\partial Z}\left[\frac{1}{\eta}\left(h^3p' + 3h^2\tau_y + 8\frac{\tau_C^3}{p'^2} - 12\frac{\tau_y\tau_C^2}{p'^2}\right) - \frac{8}{\eta_C}\frac{\tau_C^3}{p'^2}\right] = 12\dot{h} \quad \text{for } \dot{h}<0, \tag{2}$$

$$Z_C = -\frac{\tau_C h^2}{6\eta_C\dot{h}}. \tag{3}$$

p is the pressure, p' stands for the pressure gradient in the axial direction, Z is the axial coordinate defining position in the oil film, τ_y is the yielding shear stress, τ_C is the shear stress at the core border, η_C, η are the dynamic viscosities of the oil in and outside the core area, respectively, h is the oil film thickness, and $(\cdot)$ denotes the

first derivative with respect to time. The Reynolds equations (1) and (2) hold for the extents of the axial coordinates $0 \le Z \le Z_C$ and $Z_C < Z \le L/2$. L denotes the damper length and Z_C is the axial coordinate where the core touches the rings. More information on solving the modified Reynolds equations can be found in [7].

Based on measurements the dependence of the yielding shear stress on magnetic induction B can be approximated by a power function

$$\tau_y = k_y B^{n_y}, \tag{4}$$

where k_y, n_y are the proportional and exponential material constants. At the simplest distinguishing level the relation between the magnetic induction, electric current I and the thickness of the oil film can be expressed

$$B = k_B \mu_0 \mu_r \frac{I}{h}. \tag{5}$$

μ_0, μ_r are the vacuum and relative permeabilities of the magnetorheological oil, respectively, and k_B is the design parameter.

In areas where the thickness of the oil film rises with time, a cavitation is assumed. In cavitated regions the Reynolds equation does not hold. The pressure is estimated to be constant there and equal to the pressure in the ambient space.

The components of the hydraulic damping forces in the y and z directions (F_{mry}, F_{mrz}, respectively) are calculated by integration of the pressure distribution p_d around the circumference and along the length of the damper

$$F_{mry} = -2R \int_0^{\frac{L}{2}} \int_0^{2\pi} p_d \cos\varphi \, \mathrm{d}\varphi \, \mathrm{d}Z, \quad F_{mrz} = -2R \int_0^{\frac{L}{2}} \int_0^{2\pi} p_d \sin\varphi \, \mathrm{d}\varphi \, \mathrm{d}Z. \tag{6}$$

R is the middle damper gap radius and φ is the circumferential coordinate.

3 Reduction of the Rotor System

In the mathematical model it is assumed that the shaft is flexible and massless, the discs are absolutely rigid, the support damping elements are massless, and the damping (except that in the dampers) has a viscous character.

To reduce the size of the model system, the rotor is represented by a set of nodes coupled by the elements to which elastic and damping properties are assigned. The nodes correspond to the places where the discs and damping elements are mounted on the shaft. Moreover, it is assumed that the rotor is loaded only by the point forces and moments acting in the nodes referred to the discs and rotor journals. The deformation of the shaft in the nodes is described by displacements and rotations in two mutually perpendicular directions.

Lateral vibration of the reduced rotor is governed by the motion equation

$$\mathbf{M}\ddot{\mathbf{x}} + (\mathbf{B}_P - \omega\mathbf{G})\dot{\mathbf{x}} = \mathbf{f}_M + \mathbf{f}_H + \mathbf{f}_A. \tag{7}$$

$\mathbf{M}$, $\mathbf{B}_P$, $\mathbf{G}$ are the mass, external damping and gyroscopic matrices of the reduced system, $\mathbf{f}_H$, $\mathbf{f}_A$, $\mathbf{f}_M$ are the vectors of hydraulic damping, applied and inner forces, respectively, $\mathbf{x}$ is the vector of generalized displacements (lateral displacements and rotations) of the reduced system, ω is the angular speed of the rotor rotation, and $(\cdot)$ denotes the second derivative with respect to time.

The vector of inner forces ($\mathbf{f}_{RM}$) reads in the rotating frame of reference

$$\mathbf{f}_{RM} = -\mathbf{B}_{RM}\dot{\mathbf{x}}_R - \mathbf{K}_R\mathbf{x}_R. \tag{8}$$

$\mathbf{K}_R$, $\mathbf{B}_{RM}$ are the stiffness and material damping matrices and $\mathbf{x}_R$ is the vector of generalized displacements, all related to the rotating frame of reference. Elements of the stiffness matrix $\mathbf{K}_R$ can be determined by application of the procedure described in [8].

$$k_{ij} = \frac{Q_i}{x_j} \quad \text{for } i,j = 1,2,\ldots,n \tag{9}$$

is the element of the reduced stiffness matrix related to the ith row and jth column, x_j is the jth generalized displacement, Q_i is the generalized force corresponding to the ith generalized displacement, and n is the number of degrees of freedom of the reduced system. The generalized displacement x_j is determined by solving the original (not reduced) system loaded by the force or moment corresponding to the generalized force Q_i referred to the reduced system and for the boundary conditions expressing that the generalized displacements in the original system corresponding to x_j of the reduced system for $j = 1, 2, \ldots, n$ are zero except for $j = i$. To determine the generalized displacements x_j the finite element method can be used. The inner damping matrix is set up in the analogue way.

The resulting equation of motion of the reduced rotor system is obtained by the transformation of (8) from rotating to the fixed coordinate system and by its substitution in (7). The transformation utilizes the relationship

$$\mathbf{v} = \mathbf{C}_{RF}\mathbf{v}_R, \tag{10}$$

where $\mathbf{v}$ and $\mathbf{v}_R$ are the vectors related to the fixed and rotating frame of reference, respectively, and $\mathbf{C}_{RF}$ is a block diagonal matrix of the orthogonal transformation. Performing these manipulations arrives in the equation of motion that reads

$$\mathbf{M}\ddot{\mathbf{x}} + (\mathbf{B}_P + \mathbf{B}_M - \omega\mathbf{G})\dot{\mathbf{x}} + (\mathbf{K} + \omega\mathbf{K}_C)\mathbf{x} = \mathbf{f}_H + \mathbf{f}_A. \tag{11}$$

$\mathbf{B}_M$, $\mathbf{K}_C$, $\mathbf{K}$ are the material damping matrix, the circulation matrix, and the stiffness matrix referred to the fixed frame of reference. Because the rotor is axial symmetric, elements of these matrices are constant.

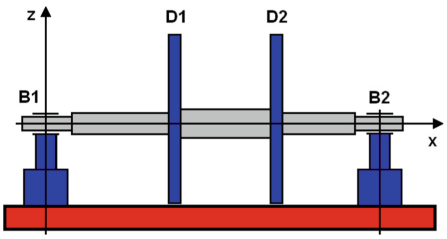

Fig. 1 The investigated rotor system

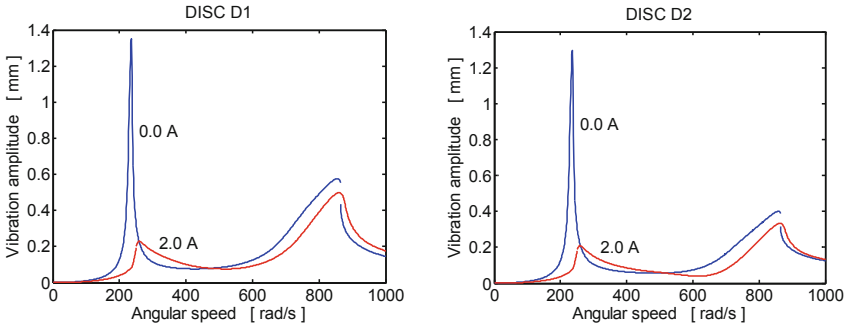

Fig. 2 Frequency response (discs D1—*left*, D2—*right*, vibration in the horizontal direction)

4 The Simulated Rotor System

The investigated rotor system (Fig. 1) consists of a shaft and of two discs. The shaft is coupled with the frame by two magnetorheological squeeze film dampers mounted on both its ends. The rotor turns at constant angular speed, is loaded by its weight and excited by the discs unbalance. In the computational model the shaft is considered as flexible, massless, and the discs as absolutely rigid. The damping elements are implemented by springs and force couplings.

The task was to investigate influence of the damping force on critical speeds of the rotor system.

The frequency responses referred to the discs D1 and D2 vibration in the horizontal direction are drawn in Fig. 2. The results show that rising magnitude of the current enables to reduce the oscillation amplitude.

5 Conclusions

The paper deals with a novel approach to investigation of multi-disc flexible rotors the vibration attenuation of which is controlled by magnetorheological squeeze film dampers placed in the rotor supports. The developed mathematical model is based

on reduction of the primary model system utilizing the influence coefficients determined by the finite element method, on assumptions of the classical theory of lubrication, and representing the magnetorheological oil by bilinear material. The computational simulations showed that adapting the damping forces to the instant operating conditions by means of changing magnitude of the damping forces in the rotor supports enables to reduce the rotor oscillations. The principal advantages of the presented approach consist in the possibility of performing reduction of rotors having a complex geometric configuration and in modelling the magnetorheological oil by bilinear material, which yields stable computational procedures.

Acknowledgments The research work reported here was made possible by the Czech Science Foundation (project no. 15-06621S) and the National Programme of Sustainability (project LQ1602—IT4Innovations excellence in science). The support is highly acknowledged.

References

1. Zapoměl, J., Ferfecki, P., Kozánek, J.: Determination of the transient vibrations of a rigid rotor attenuated by a semiactive magnetorheological damping device by means of computational modelling. Appl. Comput. Mech. **7**(2), 223–234 (2013)
2. Gong, X., Ruan, X., Xuan, S., Yan, Q., Deng, H.: Magnetorheological damper working in squeeze model. Adv. Mech. Eng. **6**, 410158 (2014)
3. Kim, K.J., Lee, C.W., Koo, J.H.: Design and modeling of semi-active squeeze film dampers using magneto-rheological fluids. Smart Mater. Struct. **17**(3), 035006 (2008)
4. Aravindhan, T.S., Gupta, K.: Application of magnetorheological fluid dampers to rotor vibration control. Adv. Vibr. Eng. **5**(4), 369–380 (2006)
5. Zapoměl, J., Ferfecki, P., Forte, P.: A computational investigation of the transient response of an unbalanced rigid rotor flexibly supported and damped by short magnetorheological squeeze film dampers. Smart Mater. Struct. **21**, 105011 (2012)
6. Zapoměl, J., Ferfecki, P.: Mathematical modelling of a long squeeze film magnetorheological damper for rotor systems. Model. Optim. Phys. Syst. **9**, 97–100 (2010)
7. Zapoměl, J., Ferfecki, P.: A 2D mathematical model of a short magnetorheological squeeze film damper based on representing the lubricating oil by bilinear theoretical material. In: Proceedings of the 2015 IFToMM World Congress (Taipei) (2015)
8. Gasch, R., Nordmann, R., Pfützner, H.: Rotordynamik. Springer, Berlin (2002)

Inertia Matrix and Vehicle Driveability

P. Brabec, M. Malý and R. Voženílek

Abstract This paper summarizes the evidence and results of the research focused on determining the inertia matrix (ellipsoid of inertia) of a passenger car aggregate. In the first part of the paper, the measurement results are introduced which are subsequently used for simulation of the whole vehicle dynamic behaviour.

Keywords Measurement · Inertia matrix · Ellipsoid of inertia · Vehicle dynamics

1 Introduction

For determining moments of inertia, various methods are used. Generally, they are based on a principle of dependence between the moment of inertia of a body and the natural oscillation frequency. The basic methods for determining moments of inertia are based on the principle of a physical pendulum, a torsion suspension or a bifilar suspension, eventually a trifilar or a quadrifilar one. When measuring it is supposed that the oscillation is undamped and the time of oscillation is measured [1, 2]. The aim of this research was to suggest a measurement methodology and pursuant to this methodology it would be possible to identify the main weight parameters of the system combustion engine and gearbox (aggregate). When choosing the method for determining the ellipsoid of inertia of the aggregate, the emphasis was placed particularly on the accuracy of measurement. Well specified inertia matrix of the aggregate is very important for further use in computer simulations, such as crash tests. The aggregate (or eventually motor) weight and centre-of-gravity position determination was performed on the basis of measuring the tensile force in

P. Brabec (✉) · M. Malý · R. Voženílek
Technical University of Liberec, Liberec, Czech Republic
e-mail: pavel.brabec@tul.cz

M. Malý
e-mail: miroslav.maly@tul.cz

R. Voženílek
e-mail: robert.vozenilek@tul.cz

J. Beran et al. (eds.), *Advances in Mechanism Design II*,
Mechanisms and Machine Science 44, DOI 10.1007/978-3-319-44087-3_16

individual fibres on the trifilar suspension. For determining the moments of inertia, the indirect method of measuring the time of oscillation of the body hung on the unifilar (torsion) suspension was used. For providing the moments of inertia of bodies of more complex shapes, special preparations were used. These preparations enabled to hung the body in various positions onto the torsion suspension. Therefore, a subframe for gripping the aggregate was used. This aggregate was gripped into the subframe in a defined way so that the axes of the chosen system of coordinates of the aggregate were parallel with the axes of the system of coordinates of the subframe. Because the moments of inertia of the subframe are not insignificant, it was necessary to perform the measuring twice. The first one was performed for the assembly of the subframe with the aggregate. In the second case only the subframe itself was measured by reason of separate parameters evaluation and determination of elements of inertia matrix of the aggregate and the subframe. For determining the inertia matrix, at least six measurements are needed. In our case, at least ten measurements towards an arbitrary axis passing through the beginning were performed so that we would reach the highest accuracy and subsequent calculation of the size and position of the ellipsoid of inertia. In general, for n measurements we will get the matrix of n equations with six unknowns. In this case, these unknowns can be determined from the set of measured data by using the method of least squares [3]. These unknowns are 3 moments of inertia towards the relevant axes: J_x, J_y and J_z and similarly 3 deviation moments: D_{xy}, D_{xz} a D_{yz}.

The methodology was verified when measuring several aggregates or motors, in some cases for more variants of motor accessories layout (thirteen aggregates and one motor designed for passenger vehicles, one motor designed for a commercial vehicle). The measurement was always performed without any filling, which means without (engine) oil and coolant.

In the graphs above, values of axial moments of inertia used for passenger vehicles are illustrated. These were ordinary multi-cylinder combustion engines (three- and four-cylinder ones, spark ignition and diesel ones, supercharged and not-supercharged ones) with both manual and automatic gearboxes. The values are presented in relation to a referential aggregate which was an ordinary light three-cylinder spark ignition engine with the volume of 1.2 dm^3 with a manual five-gear gearbox. The system of coordinates to which the values are attributable is expressed as follows: axis Y is identical with the axis of the crankshaft; axis Z is in plane of axes of cylinders and vertical to axis Y; axis X is vertical to the plane YZ.

From the graphs in Fig. 1 is obvious that the values sizes of axial moments of inertia of the aggregate are not linear dependent on the aggregate weight. The resulting values of moments of inertia and the centre-of-gravity position of the aggregate influence both the weight and also the position of additional devices and motor accessories. Neither relatively low physical parts which (regarding relatively big remoteness) can also influence the size of the overall moment of inertia of the aggregate cannot be neglected. The influence of the accessories was examined with careful attention; therefore, variant measuring of aggregates in different configuration with different accessories was also performed.

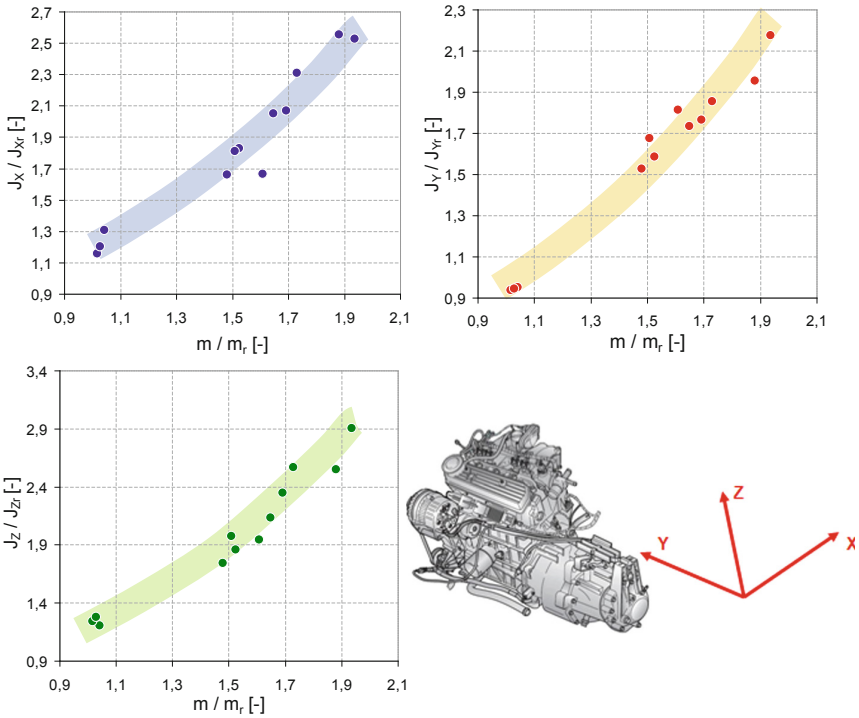

Fig. 1 Values of axial moments of inertia of passenger vehicles aggregate, introduced in relation to the referential aggregate

2 Aggregate and Dynamic Behaviour of a Vehicle

Vehicle driveability—manoeuvrability, comfort, and especially driving stability belong to the main criteria when designing a vehicle. When buying a vehicle, the customer chooses both equipment and accessories, and significant role is also drive unit parameters and the material whole which we have already identified as an aggregate.

The aim of the performed analyses with a number of laboratory measurements was to determine what influence this choice will have on the overall value of the inertia matrix (ellipsoid of inertia) of the whole vehicle and thus on the dynamic behaviour of the vehicle. For comparing behaviour of two variants of a small passenger car, two aggregates were chosen: an ordinary light atmospheric three-cylinder spark ignition engine with the volume of 1.2 dm^3 with a manual five-gear gearbox and an ordinary heavier supercharged four-cylinder diesel engine with the volume of 2 dm^3 with an automatic six-gear gearbox. Then, according to the found values of vehicles inertia [4–6], a virtual vehicle of its weight parameters are illustrated in Table 1 was chosen (Fig. 2).

Table 1 Values of the chosen virtual vehicle

	Virtual vehicle—choice of values for virtual bodywork with a driver (without aggregate)	Virtual vehicle with chosen petrol engine	Virtual vehicle with chosen diesel engine
m (kg)	1050	137	265
J_X (kg m^2)	388	404.6	422.6
J_Y (kg m^2)	1000	1232.6	1408.4
J_Z (kg m^2)	1275	1503.3	1680.6
D_{XY} (kg m^2)	0	−20.9	−36.4
D_{XZ} (kg m^2)	100	140.5	171.8
D_{YZ} (kg m^2)	−10	−12.8	−13.5

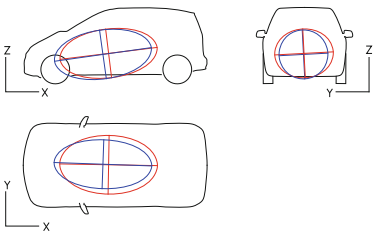

Fig. 2 Illustration of an ellipsoid of inertia for a virtual vehicle (*red*—a vehicle with spark ignition engine, *blue*—a vehicle with diesel engine) (color figure on line)

3 Influence of Inertia Matrix of a Vehicle on Dynamic Behaviour of a Vehicle

Mathematical description of the common vehicle movement represents a very complicated task. For simulations, models which are appropriately simplified are used. For the first approach, a simplified automobile model (often linear) is usually used. A simple model can relatively quickly offer quite good results which are important for a design and a construction of a control system. Then the next level of the model extension can follow. This extended model includes the possibility to assign more parameters of the vehicle. From the previous papers and simulations results it is obvious that for instance a simplified linear simulation model is considerably simpler for modelling. More simplifications were implemented; nevertheless, very good results were reached.

For a comparison, a linear simulation model of a vehicle [7, 8] was used. For comparing the vehicle behaviour with two different aggregates, an avoidance manoeuvre with the same value towards the side (around 2.2 m) was chosen. The vehicle with the diesel engine had bigger lateral force on the front axle and the wheels of the front axle had to turn at a greater angle. The rest of the outputs from the simulation model were about the same. In Fig. 3, the results of the simulation are illustrated. The vehicle with the diesel engine behaves like more understeering.

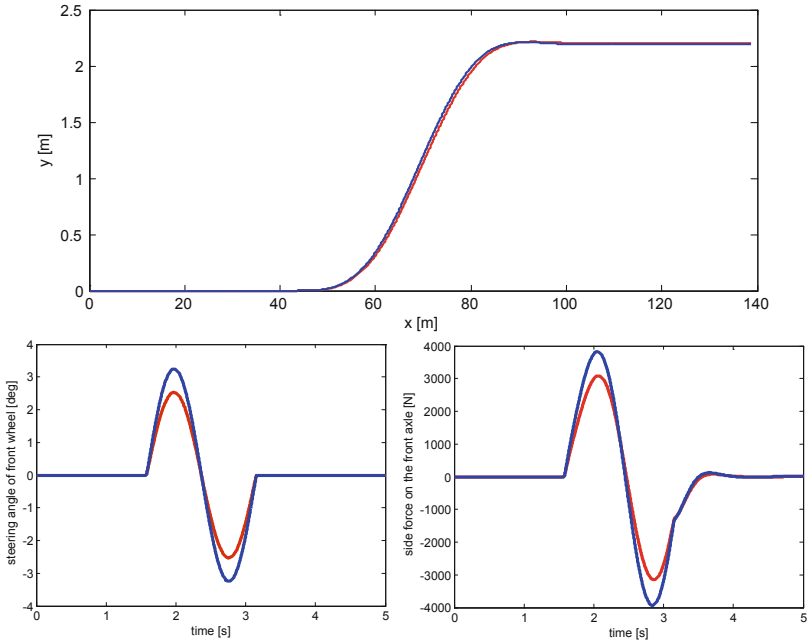

Fig. 3 Simulation results of an avoiding manoeuvre when using the simulation model of the vehicle: *bottom left-hand side*—angular displacement of the front wheels, *bottom right-hand side*—lateral force on the front axle (*red*—spark ignition engine vehicle, *blue*—diesel engine vehicle) (color figure on line)

4 Conclusions

The linear differential motion equations for a simple vehicle model have shown that the rotational vehicle motions will finish quickly if the vehicle weight is small, the moment of inertia around the vertical axis is small and the vehicle wheelbase is big. When dimensioning a motor vehicle, its reaction on both low and high frequencies of the steering-wheel rotation is important. The frequency characteristic is possible to discover both experimentally and by calculation. The evaluation of controllability according to the frequency characteristic process is, among others, performed according to the position of the amplitude maximum. The amplitude excess is the more distinct the lower the system attenuation is. For the given vehicle parameters, the amplitude maximum then depends on the driving speed [9].

It is further noted that on behalf of the fast driving manoeuvre, the amplitude maximum is supposed to lie at higher frequencies. If there is no amplitude excess (regarding the high damping), the decline of amplitude characteristics should appear as long as possible [10]. According to [11] there is no point for the vehicle resonance region in lying far beyond the value 5 $^{s-1}$ by reason of the frequency response of the driver. On the basis of calculations, the assumption was confirmed

that the resonance region position is dependent on design values and operating conditions: it moves towards the higher frequencies due to the small moment of inertia of a vehicle around its vertical axis, long wheelbase, use of tires with high lateral stiffness [9].

Acknowledgments This publication was written at the Technical University of Liberec, Faculty of Mechanical Engineering with the support of the Institutional Endowment for the Long Term Conceptual Development of Research Institutes, as provided by the Ministry of Education, Youth and Sports of the Czech Republic in the year 2016.

References

1. Tag des Fahrwerks, Institut für Kraftfahrwesen Aachen – RWTH Aachen, 09.10.2006
2. Best, A.: Moment of inertia measurement system. MIMS Description and Specification, Anthony Best Dynamics (2004)
3. Brabec, P.: Experimentální určení polohy a rozměrů elipsoidu setrvačnosti hnacího agregátu. *Teze disertační práce*. Technická univerzita v Liberci (2009)
4. Bárta, M.: Měření momentu setrvačnosti vozidel. Diplomová práce, Technická univerzita v Liberci (2015)
5. Laumanns, N.: Integrale Reglerstruktur zum effektiven Abstimmung von Fahrdynamiksystemen. Dissertation, Technischen Hochschule Aachen (2007)
6. Gortz, H.: Identifikation von Fahrzeugträgheitsparametern in Fahrversuchen und auf Prüfständen, Dissertation, Technischen Hochschule Aachen (2007)
7. Vlk, F.: Podvozky motorových vozidel. Nakladatelství a vydavatelství VLK, Brno (2000)
8. Brabec, P., Malý, M., Voženílek, R.: Simulace řízení zadních kol automobilu, *VI.* medzinárodná vedecká konferencia RIADENIE TEKUTINOVÝCH SYSTÉMOV, Žilina (2001)
9. Vlk, F.: Hodnocení řiditelnosti motorových vozidel na základě neustálených jízdních stavů. *Časopis Automobil, ročník XXI*, SNTL (1977)
10. Kohno, T.: On the Vehicle Response to the Steering Kontrol. SAE-Paper, 69 04 88 (1969)
11. Fiala, E.: Die Wechselwirkungen zwischen Fahrzeug und Fater. ATZ, č. 10, s. 345–348 (1967)

Unexpected Vibrations of Relatively Simple Cutting Machine Mechanism

P. Šidlof, Z. Braier, P. Klouček and J. Ondrášek

Abstract Unexpected vibrations and resonance with frequency three times the rpm were detected in a relatively simple cutting machine during process of inertia force reduction (balancing). A knife of the cutting machine is actuated by two identical crank mechanisms at the ends of a crossbeam. The vibrations induced inertial forces larger than the considerable machine imbalance. The crank length to connecting rod length ratio was small enough that the corresponding excitation kinematic acceleration overtone component was practically negligible. The vibration characteristics consisting mainly of the drive shaft gyratory vibrations was determined based on measurements of forces transferred to floor, accelerations of the mechanisms and on a CAD model calculation involving the mechanism main members compliances. Improvements were proposed and tested upon the results with focus on vibrations elimination.

Keywords Measurement · Unexpected vibrations and resonance · Balancing improvement · Inertial forces · Simple cutting machine

1 Introduction

During test measurement of inertia force balancing on a relatively simple cutting machine resonance vibrations with high amplitudes were detected. Vibration frequency was three times the drive shaft rotation frequency of the crank mechanism.

P. Šidlof · Z. Braier (✉) · P. Klouček · J. Ondrášek
VÚTS, a.s., Measurement, Liberec, Czech Republic
e-mail: zdenek.braier@vuts.cz

P. Šidlof
e-mail: pavel.sidlof@vuts.cz

P. Klouček
e-mail: pavel.kloucek@vuts.cz

J. Ondrášek
e-mail: jiri.ondrasek@vuts.cz

J. Beran et al. (eds.), *Advances in Mechanism Design II*,
Mechanisms and Machine Science 44, DOI 10.1007/978-3-319-44087-3_17

The machine was used in practice only at frequencies above or below resonance rpms, since it proved not to work well in this bandwidth.

After the machine was balanced, the resonance frequency increased thus shifting into the frequency used in practice. Although amplitudes of resonance vibrations decreased significantly compared to the unbalanced situation, the resonance caused undesirable increase in the noise.

The problem was solved by measurement and calculation. To measure the original state of the machine and the balanced state, the machine was settled on dynamometers for measurement of forces acting to the ground and equipped with accelerometers measuring the movement of the cutting knife. A laser triangulation displacement sensor to ascertain deflection of the drive shaft was also used. All measurements were done as the function of rotation angle of the drive shaft. Incremental rotary encoder was connected to the end of the drive shaft and measured also the angular velocity of the shaft. Calculations of resonance frequencies were carried out on a model of the machine by use of Adams software [1].

2 Measurements and Calculations

Figure 1 shows a schema of the machine placed on multicomponent dynamometers measuring forces acting on the floor. The electromotor powered from a frequency converter drives the drive shaft via a V-belt. The drive shaft is mounted in two bearings. The drive shaft carries a relatively heavy adjustable eccentric placed to the right of the shaft's centre. The eccentric powers a light feeding mechanism, which is not depicted. Flies and cranks are placed on the overhanging ends of the shaft. By means of long connecting rods these power the crossbeam with the cutting knife fastened in the centre. The crossbeam is guided by two sleeve bearings and is symmetrical. The driving crank mechanisms have very long connecting rods and thus stroke of the cutting knife is almost purely sinusoidal.

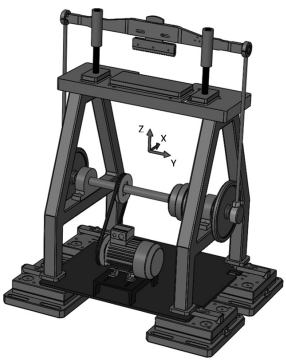

Fig. 1 Schema of the cutting machine settled on multicomponent force platforms

2.1 Measurement Before and After Balancing of the Machine

Four 3-component piezoelectric dynamometers Kistler with excellent dynamic properties (stiffness in the vertical direction ≈2 kN/μm) were used to measure the forces acting to the floor. Sensors of vertical acceleration of the cutter crossbeam were placed near the sleeve bearings. Incremental encoder of angle and angular speed was attached to the drive shaft.

Figures 2 and 3 show the amplitude multispectrum of the measured horizontal force *X* and vertical force *Z* before balancing of the machine in idle run. The forces were evaluated as a sum of corresponding components of forces measured in all the four dynamometers. There are high amplitudes of the fundamental frequency (first harmonic) in spectrum of the *X* force, which are caused by rotational imbalance of the machine. Spectrum of the *Z* force shows high amplitudes in the third harmonic with a maximum at 1350 rpm. The plotted spectrum of the cutter acceleration is very similar to the spectrum of the *Z* force with the exception of the first harmonic, only amplitudes of higher than third harmonic are relatively lower.

Figure 4 shows the course of the *Z* force during resonance depicted depending on the angle of the shaft. The diagram starts at the top dead centre of the cutting knife. The first harmonic is significantly phase-shifted due to unbalanced centrifugal forces. With respect to the geometry of the crank mechanism the ideal force *Z* (without

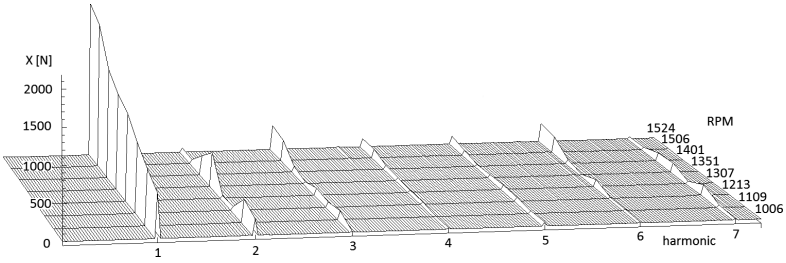

Fig. 2 Amplitude multispectrum of the resulting *X* [N] force before balancing of the machine

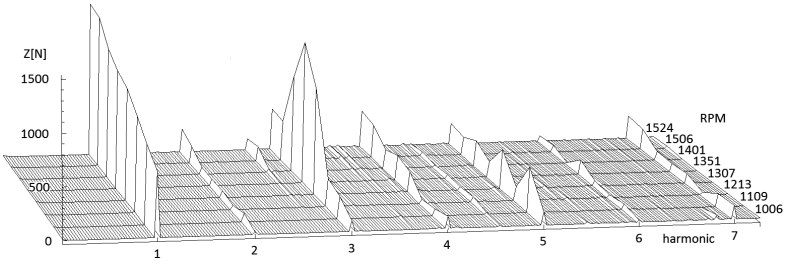

Fig. 3 Amplitude multispectrum of the resulting *Z* [N] force before balancing of the machine

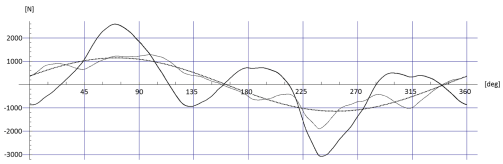

Fig. 4 Resonance force *Z* (*thick line*), force *Z* with filtered-out third harmonic (*thin line*) and first harmonic component of the force (*dotted*) before balancing at 1351 rpm

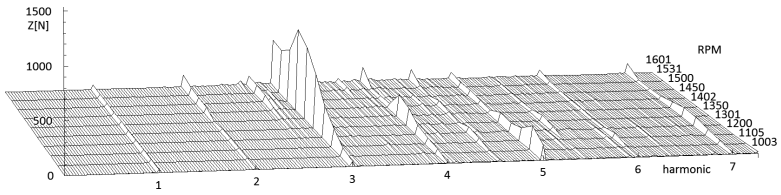

Fig. 5 Multispectrum of the resulting force *Z* [N] after balancing of the machine

effects of flexibility and backlash) should correspond to almost exactly its measured first harmonic, which has an amplitude of 1030 N. The real force, however, has the peak value almost three times higher. The main culprit here is the third harmonic with amplitude of 1370 N, which ideally should not be exceeded at all.

The balancing process include lightening of the adjustable eccentric on the drive shaft, centrifugal forces were balanced and a mechanism with contra-rotating balancing eccentrics was used to balance the vertical inertial force of the crank mechanism. Having employed these adjustments we carried out our measurements again. The horizontal *X* force practically disappeared. On the vertical inertial force *Z* the first harmonic dropped to almost zero (see Fig. 5), but resonance on the third harmonic remained with a peak at 1450 rpm. Although the maximum amplitude dropped to 780 N (by 42 %) the resonance frequency was now shifted to the range of operation rpms of the machine. Figure 6 depicts the *Z* force during resonance. To clarify an approximate calculation was carried out.

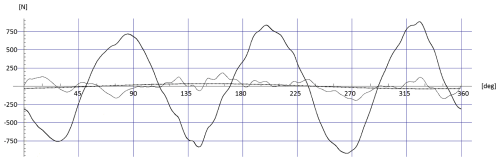

Fig. 6 Resonance force *Z* (*thick line*), force *Z* with filtered-out third harmonic (*thin line*) and first harmonic component of the force (*dotted*) at 1450 rpm after balancing

2.2 Calculation of Resonance Vibrations of the Mechanism

With respect to the complicated effects of flexibility and gyroscopic moments calculation of resonant frequencies of the mechanism was carried out in the Adams software. As input we used the CAD model of the mechanism, where the drive shaft with flywheels, the connecting rods and the cross beam with the cutting knife were considered flexible. First the resonant frequencies with the shaft set at top dead centre of the cutting knife were determined. The corresponding resonant frequency was calculated at 74.6 Hz and main deformations on the mechanism consisted mainly in simple bending of the drive shaft in the vertical plane. Resonant frequency in rotation was determined by use of an approximation approach calculating run-up to a constant angular speed of the drive shaft. For the vibrations to appear a very low modal dumping had to be set in the model. Resonant frequency was found at 72.6 Hz at 1452 rpm, but with amplitudes ten times lower than in reality.

Figure 7 shows the calculated movement of the shaft axes in the place of the connecting rod axes in vertical direction and Fig. 8 shows this process with filtered-out first harmonic. Movement of the shaft axis in the middle of machine is very similar but has an opposite sign and is somewhat larger. The shaft axis moves to a lower extent also in the horizontal direction.

The derived deflection of the shaft depicted in coordinate system fixed to the shaft with z axis in direction of the crank is on Fig. 9. Vectors indicating the concrete deflection have attached a number describing the corresponding angle of the shaft rotation. During one rotation of the shaft the curve runs twice.

Deflection of the shaft without the first harmonic is depicted on Fig. 10. The curve, again, runs twice during one rotation of the shaft.

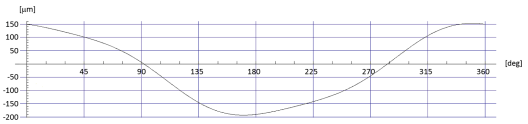

Fig. 7 Calculated movement of the shaft axes in the place of the connecting rod axes in z direction (vertical) at 1452 rpm

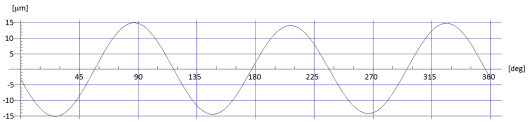

Fig. 8 Calculated movement of the shaft axes in the place of the connecting rod axes in z direction without the first harmonic at 1452 rpm

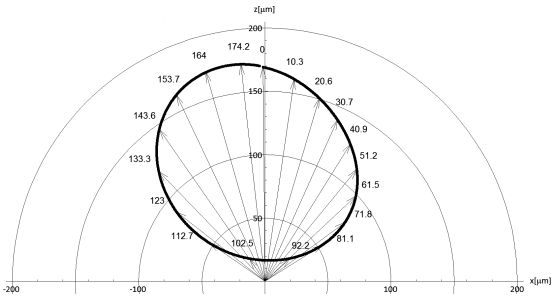

Fig. 9 Deflection of the end of the shaft at 1452 rpm. The z axis is in the direction of the crank

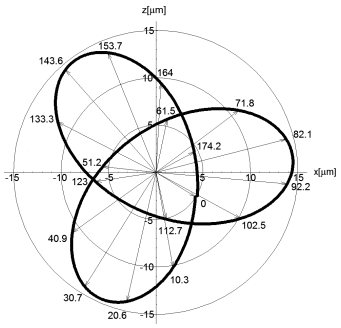

Fig. 10 Deflection of the end of the shaft without the first harmonic at 1452 rpm. The z axis is in the direction of the crank

3 Conclusions

The unexpectedly strong vibrations of the cutting machine mechanism are probably not caused by linear effects, since on a linearized computational model it shows insignificant amplitudes. The vibrations are not random, since they appear also on other similar machines. The measured unevenness of the angular speed of the drive shaft, which might cause the vibrations [2, 3] is very low (below 0.2 %). Also torsional vibration of the shaft is very low. No significant corresponding resonance amplitudes were found in the frame and the base plate with the electromotor and beam of the cutting knife bending vibrations are very low. Products of inertia of imperfectly balanced flywheels, nonlinear effects of backlash in bearings, their non-linear stiffness and solid friction in guiding of the cutting knife in dead centres should not have any significant effect on the vibration with third harmonic [2, 3].

To eliminate vibrations increase of diameter of the shaft between the bearings from the original 35–42 mm had been proposed. The calculated resonance frequency thus increased to 97 Hz at 1895 rpm. Although the calculated frequency for the shaft at 35 mm corresponded very well with the measurement, a resonance appeared on the mechanism with third harmonic at 1600 rpm (80 Hz) with the Z force amplitude of 560 N during tests on a 42 mm shaft.

References

1. MSC-ADAMS. User's Reference Manual. Mechanical Dynamics. http://www.mscsoftware.com/product/adams
2. Brepta, R., Půst, L., Turek, F.: Mechanické kmitání. Technický průvodce 71. Sobotáles, Praha (1994)
3. Juliš, K., Brepta, R. et al.: Mechanika, II. díl: Dynamika, SNTL, Praha (1987)

Effect of Oil Viscosity on Pulsating Flow in Pipe

L. Hružík, A. Bureček and M. Vašina

Abstract The article deals with the influence of oil viscosity on pulsating flow in a pipe. A hydraulic resistance is placed at the end of the pipe. A pulsating pressure signal is generated by proportional directional valve. Time dependencies of pressure drops for different frequencies of the pulsating signal are measured at the beginning and the end of the pipe. A mathematical model of the hydraulic system is constructed using Matlab SimHydraulics software. There are simulated time dependencies of pressures at the beginning and at the end of the pipe. They are subsequently compared with an experiment.

Keywords Pulsating flow · Oil · Viscosity · Pressure · Pipe · Experiment · Simulation

1 Introduction

Pressures, flows and temperatures are important parameters in hydraulics. This article is focused on investigation of other important parameter, i.e. on effect of excitation frequency [1].

With respect to a given hydraulic system, it is possible to measure frequency of pulsations that are generated by elements of the hydraulic system, e.g. by rotary hydraulic pumps and motors. Furthermore there may be systems with high velocity changes of working elements [2]. These velocity changes are mainly controlled by

L. Hružík (✉) · A. Bureček · M. Vašina
Department of Hydromechanics and Hydraulic Equipment, Faculty of Mechanical Engineering, VŠB - Technical University of Ostrava, 17. listopadu 15/2172, 708 33 Ostrava-Poruba, Czech Republic
e-mail: lumir.hruzik@vsb.cz

A. Bureček
e-mail: adam.burecek@vsb.cz

M. Vašina
e-mail: martin.vasina@vsb.cz

J. Beran et al. (eds.), *Advances in Mechanism Design II*,
Mechanisms and Machine Science 44, DOI 10.1007/978-3-319-44087-3_18

proportional valves and servo valves most frequently in combination with a controller. The controller is used to keep constant velocity, acceleration or position on an output element and adjusts quickly a valve. It can lead to pressure and flow pulsations that are subsequently transmitted through hydraulic lines to entire machine. Higher pressure and flow pulsations cause stress of single elements and often lead to their lifetime reduction. If excitation oscillations are approaching to eigenfrequency of a given machine, it can cause resonance of the machine. This resonance can lead to machine destruction too.

There is described a measurement of pressure pulsations of given frequencies in a long pipe in this paper. The pressure pulsations are generated by a proportional control valve. There is also created a mathematical model and performed a simulation of pressure pulsations in the long pipe. Measured and simulated amplitude frequency pressure characteristics are subsequently compared for two oil temperatures.

2 Description of Hydraulic System and Measurement

The investigated experimental equipment (see Fig. 1) enables realization of dynamic processes of the hydraulic system with a long pipe.

A hydraulic aggregate is a pressure liquid source. The aggregate consists of the fixed displacement hydraulic pump HP, the check valve CV, the relief valve RV and the tank T. Mineral oil of viscosity class ISO VG 46 was used as the working liquid in the system. Oil temperature is measured by means of the temperature

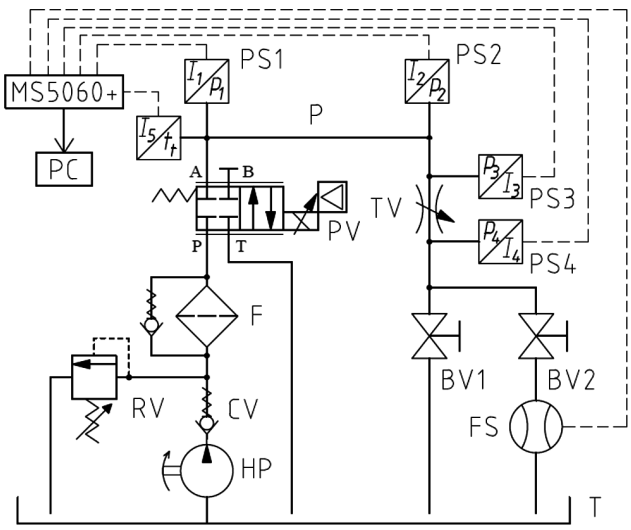

Fig. 1 Scheme of experimental circuit

sensor TS. It is possible to control the flow by means of the proportional control valve PV, which is located behind the filter F. Furthermore the circuit consists of the long steel pipe P, which is equipped by the pressure sensors PS1 and PS2 on its beginning and end. The throttle valve TV is located behind the long pipe P and creates resistance to oil movement on the pipe end. The pressure sensors PS3 and PS4 are located in front of and behind the throttle valve TV. They are used in order to measure the pressure gradient through the throttle valve TV. The system also consists of two ball valves BV1 and BV2. By means of these valves it is possible to ensure the oil flow either directly to the tank T or through the flow sensor FS to the tank T. The flow sensor FS is used to measure Δp-Q characteristic of the throttle valve TV [3].

There was generated pulsating flow by means of the proportional control valve PV in this hydraulic system. A control signal for electronics of the proportional control valve PV was defined using Matlab Simulink software by means of the I/O Humusoft MF634 card. It is possible to control the electronics of the proportional control valve PV by the input voltage $U = (0 \div 10)$ V. The values of the control voltage U for generated pulsating frequencies corresponded to the sine signal with offset of 2 V and the amplitude of 1.5 V. The pressures p_1 and p_2 at the beginning and the end of the pipe P were measured by means of the pressure sensors PS1 and PS2. The length of the pipe P between the pressure sensors PS1 and PS2 is $l = 56$ m in this case. The measurement was performed at pulsations of the frequency $f = (0.5 \div 8)$ Hz with the frequency step $\Delta f = 0.5$ Hz. These pulsations were measured within the indicated frequency range at two oil temperatures (i.e. for $t_{O1} = 30$ °C and $t_{O2} = 45$ °C). These temperatures correspond to the oil kinematic viscosities $v_1 = 65$ mm^2 s^{-1} and $v_2 = 32$ mm^2 s^{-1}.

Δp-Q characteristic of the proportional control valve PV was also measured. The flow Q through the valve at a given pressure gradient Δp and a given valve flow area was determined by means of this characteristic. The dependence of the pressure gradient Δp on the flow Q was also measured for the throttle valve TV and both oil temperatures (see Fig. 2). These characteristics are applied to setting of the elements PV and TV in a mathematical model.

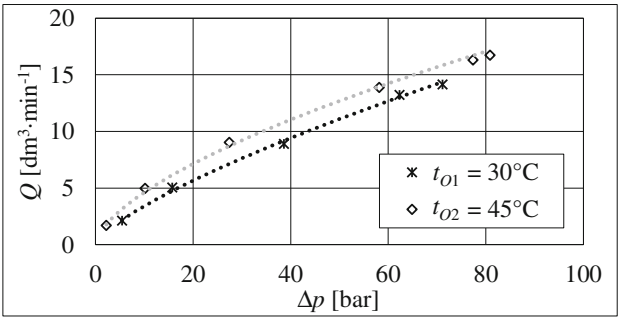

Fig. 2 Measured Δp-Q characteristic of throttle valve at the oil temperatures $t_{O1} = 30$ °C and $t_{O2} = 45$ °C

3 Description of Mathematical Model of Hydraulic System

The mathematical model of the hydraulic system was created using Matlab SimHydraulics software (see Fig. 3), which enables a physical access to a mathematical simulation. Single elements of the hydraulic system are added to the model as mathematical blocks that are described by a system of mathematical equations. In order to obtain a general scheme of the mathematical model, there are created subsystems from some blocks.

Similarly as in the case of a real hydraulic system, the constant pressure source is defined in the form of the hydraulic pump HP and the relief valve RV. Subsequently there is shown the block of the proportional control valve PV that is controlled by the block Pulsating Control Signal. The valve PV generates a pulsating flow in the pipe P, which is defined by the block P in the mathematical model. The pipe P is simulated as a segmented pipe. The mathematical model of the pipe includes expansion of the pipe walls. The pressures are measured at the beginning and the end of the pipe P by means of the subsystems PS1 and PS2. Furthermore there are shown the blocks L1 and L2 of a connecting line between the proportional control valve PV and the pressure sensor PS1 and between the pressure sensor PS2 and the throttle valve TV in the model. The throttle valve TV is defined by means of the Δp-Q characteristic in this model. The flow area of the throttle valve is constant for all measurements and mathematical models. Furthermore the model consists of the block of the tank T, the block Solver Configuration and the block Oil. The block Oil demonstrates a liquid mathematical model that takes into account density, viscosity, bulk modulus and content of free air in oil [4, 5].

An example of the comparison of the measured and simulated time dependencies of the pressures p_1 and p_2 is shown in Fig. 4. It is visible that the mathematical model for the pulsation frequency f = 5 Hz and the oil temperature t_{O1} = 30 °C is practically consistent with the experiment.

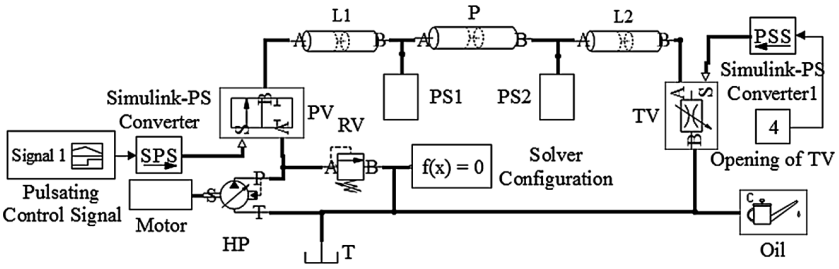

Fig. 3 Mathematical model of the experimental equipment

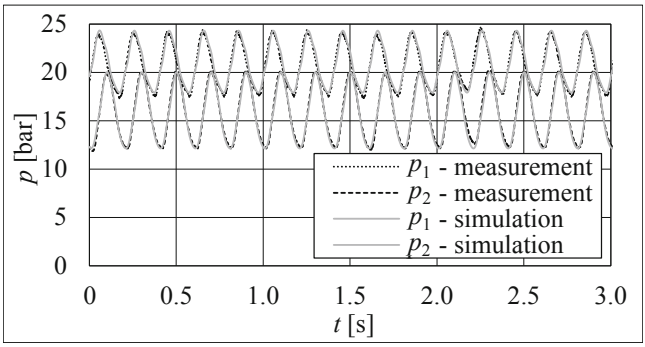

Fig. 4 Comparison of measured and simulated time dependencies of the pressures p_1 and p_2 at the pulsation frequency $f = 5$ Hz and the oil temperature $t_{O1} = 30$ °C

4 Evaluation of Measurement and Comparison with Mathematical Model

The amplitude frequency characteristics were evaluated from measured time dependencies of the pulsating pressure p_1 in front of the pipe P and the pressure p_2 at the pipe end. The pulsation frequency was in the range $f = (0.5 \div 8)$ Hz. These characteristics were subsequently determined by means of the mathematical model. The experimentally measured and mathematically simulated amplitude frequency characteristics at the oil temperature $t_{O1} = 30$ °C are shown in Fig. 5. The system eigenfrequency corresponds with the value of the frequency $f = 5$ Hz. The amplitude pressure ratio Ap_2/Ap_1 was determined on condition of sine time dependencies

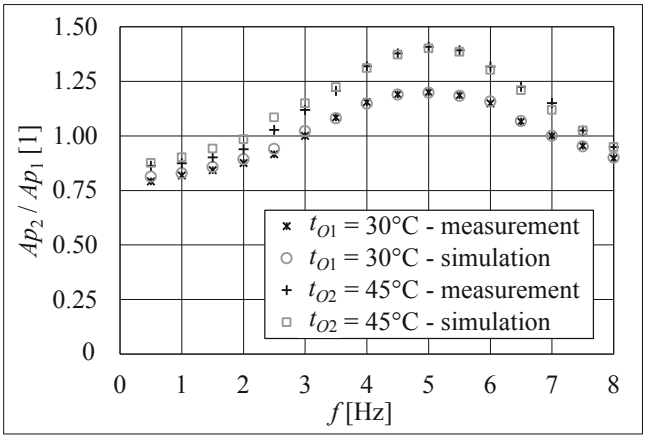

Fig. 5 Comparison of measured and simulated time dependencies of non-stationary components of the pressure amplitudes p_1 and p_2 at the oil temperatures $t_{O1} = 30$ °C and $t_{O2} = 45$ °C

of non-stationary pressure components. Here at the quantity Ap_2 means to the amplitude of non-stationary component of the pressure p_2 and Ap_1 is the amplitude of non-stationary component of the pressure p_1. The ratio of the non-stationary pressure components p_2 and p_1 at the end and at the beginning of the pipe P in the area of the eigenfrequency is $Ap_2/Ap_1 = 1.2$ in this case. It is visible that the mathematical model corresponds to the experiment.

The experimentally measured and mathematically simulated amplitude frequency characteristics at the oil temperature $t_{O2} = 45$ °C are shown in Fig. 5. The eigenfrequency $f = 5$ Hz was not changed during the temperature increasing. The ratio of the non-stationary pressure components p_2 and p_1 at the end and at the beginning of the pipe P in the area of the eigenfrequency was increased to the ratio $Ap_2/Ap_1 = 1.4$. It is visible that the mathematical model corresponds to the experiment.

It is evident (see Fig. 5) that the ratio of the non-stationary pressure components p_2 and p_1 at the end and at the beginning of the pipe P was increased with increasing the oil temperature from $t_{O1} = 30$ °C to $t_{O2} = 45$ °C, i.e. at the decreasing of the oil viscosity from $v_1 = 65$ mm^2 s^{-1} to $v_2 = 32$ mm^2 s^{-1}.

5 Conclusions

The paper was focused on investigation of oil temperature influence on non-stationary pressure components at pulsating flow in a hydraulic system with a long pipe. The throttle valve was located at the pipe end. The ratio of non-stationary pressure components at the end and at the beginning of the pipe was increased with increasing oil temperature, i.e. at decreasing oil viscosity. The increasing of the non-stationary pressure components was obtained for all excitation frequencies. The highest increasing was found in the area of the system eigenfrequency. For this reason the hydraulic system is more dynamically loaded at the higher oil temperature.

Acknowledgments The work presented in this paper was supported by a grant SGS "Experimentální výzkum v oblasti mechaniky tekutin" SP2016/70.

References

1. Gorman, D.G., Reese, J.M., Zhang, Y.L.: Vibration of a flexible pipe conveying viscous pulsating fluid flow. J. Sound Vib. **230**(2), 379–392 (2000)
2. Himr, D., Habán, V.: Damping of self-excited pressure pulsations in petrodiesel pipeline. Appl. Mech. Mater. **630**, 375–382 (2014)
3. Hružík, L.: Pulsating flow in pipe. in: Proceedings Engineering Mechanics 2009 (11–14 May, Svratka), ITAM AS CR, pp. 475–483 (2009)

4. Hružík, L., Bureček, A., Vašina, M.: Non-stationary flow of hydraulic oil in long pipe. In: EPJ Web of Conferences 2014, 67, No. 02042 (2014)
5. MathWorks, The: Matlab simulink user's guide, simhydraulics user's guide. The MathWorks Inc., Natick (2007)

Experimental Research and Mathematical Modeling of Scroll Machine in Air Motor Mode

V.I. Ivlev, S. Yu. Misyurin and A.P. Nelyubin

Abstract Recently the scroll machine is widely used in air and refrigeration compressors, vacuum pumps, because it has a small number of moving parts, high efficiency and low level of noise. The volumetric rotary scroll machine is reversible and can function in air motor mode without any significant construction modification. Scroll air motor is a relatively new concept of pneumatic actuators. There is no technical data comparison with traditional air motors which now on the market. In this paper we describe the experimental bench for determining mechanical and flow performance of scroll air motor under different value of inlet pressure, mechanical losses and exergy efficiency. Mathematical model contains geometrical description of the involute scrolls, chamber volumes, radial and tangential leakage areas as a function of orbital angle; thermodynamical pressure and temperature differential equations of compressed air; and equation of mechanical torque balance on motor shaft. The results of experiments and mathematical modeling are presented and analysed. In the last part of the paper the performances of scroll air motor are compared with such performances of traditional radial and axial piston, vane, turbine air motors.

Keywords Scroll machine · Air motor

V.I. Ivlev · A.P. Nelyubin (✉)
Mechanical Engineering Research Institute RAS, Moscow, Russia
e-mail: nelubin@gmail.com

V.I. Ivlev
e-mail: 6805158@mail.ru

S.Yu.Misyurin
National Research Nuclear University MEPhI, Moscow, Russia
e-mail: ssmmrr@mail.ru

J. Beran et al. (eds.), *Advances in Mechanism Design II*,
Mechanisms and Machine Science 44, DOI 10.1007/978-3-319-44087-3_19

1 Introduction

Compressed air is the second by importance energy medium in industry after electricity. Now about 15–18 % of total consumed electricity in industry is spent to produce the compressed air [1]. Air motors are one of the main consumers of compressed air. As compared with electro- and hydromotors they have simpler construction, light performance weight, high speed ranges, safe explosion, and relatively low cost. They can function without overheating and damage under high loading, "start–stop" and reverse modes. This ensures that air motors can be used in a wide spectrum of applications.

Some demerits which limit use of air motors are their low energy efficiency and high level of noise. The total energy efficiency of pneumatic systems is often lower than 20 %. It can be explained as follows: compression–expansion process of air is essentially irreversible, characterized by a large value of entropy change and lead to thermodynamics losses. Also air leaks, pressure drops in pipes, mechanical friction influence the efficiency.

To improve the energy and other performances of air motors the investigation should be made to search mechanisms, which will be more efficient at conversion potential energy of compressed air to a power on the shaft. Today scroll machine is the most perspective device for a progress in this area.

Scroll machine was invented in 1905 [2], but only after appearance of high precision milling cutter machine tools, they begin intensive put into practice. Now the scroll technique is widely used in air, refrigeration compressors, and vacuum pumps. Because they have a small number of moving parts, high efficiency and a low level of noise as compared with traditional types of compressors (with power motor to 25–30 kWt). The volumetric rotary scroll machine is reversible and can function in air motor mode without any significant construction modification. Scroll air motor is a relatively new concept of pneumatic actuators and is poor investigated [3, 4]. Most works have mainly focused on application scroll machine like expander for realization Organic Rankine Cycle for convert waste heat energy to electricity [5]. In this paper the results of experiments and mathematical modeling of scroll air motor are presented and analysed. In the last part of the paper the performances of scroll air motor are compared with such performances of traditional radial and axial piston, vane, turbine air motors which are on the market. Figure 1 shows a scheme

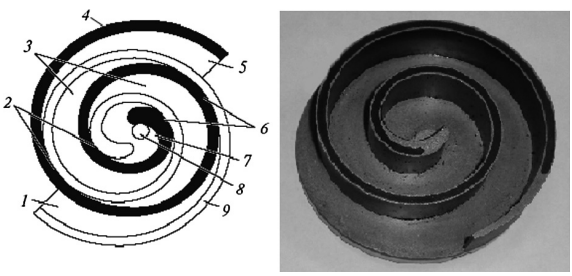

Fig. 1 Scheme of scroll air motor. *1* and *5*—exhaust chambers, *2* and *6*—scroll contact points, *3*—closed expansion chambers, *4*—fixed scroll, *7*—central chamber, *8*—inlet port, *9*—moving scroll

of scroll motor which has two identical involute scrolls (fixed and moving) and photo of moving scroll. As the moving scroll travels along the orbit, these two scrolls can touch at some points and form a series growing chambers. The rotation of moving scroll is provided by a special mechanism like Oldham couple or other.

2 Test System and Experimental Results

The purpose of experimental test of scroll air motor was to obtain mechanical, air consumption and energy performances. A special test bench was developed (the main part of it see on Fig. 2).

The next stationary mode values were measured: input and output pressure and temperature of compressed air, air consumption, output shaft torque, rotation speed. The parameters values of scroll air motor under consideration are: base circle radius = 3.18 mm; scroll thickness = 4.5 mm; scroll pitch = 20 mm; scroll height = 30 mm; involute starting angle = 43° (0.24π); involute end angle = 945° (5.25π); orbiting radius = 5.5 mm; radial clearance = 0.015 mm; flank clearance = 0.01 mm.

Figure 3a shows the power performance N against rotation speed ω under the two constant supply pressure—0.3 and 0.5 Mpa (T_m = 293 K)—curves 1 and 2. Figure 3b shows the specific air consumption $q = G(\omega)/N(\omega)$; G—air consumption bring to normal condition. Figure 3c shows the mechanical η_m and exergy η_e efficiency. Value $\eta_m = M_d/(M_d + M_t)$, M_d—output shaft torque, M_t—friction torque, which consists of two components: viscous friction, depending only on ω and Coulomb friction depending on the normal load acting on moving scroll. These components of friction torque were determined on another special equipment. Value $\eta_e = N_{max}/G_oE$; N_{max}—maximal output power, G_o—mass air consumption under N_{max}, E—specific exergy of input compressed air. Curve 2 corresponds to p_m = 0.3 MPa, curve 3—p_m = 0.5 MPa.

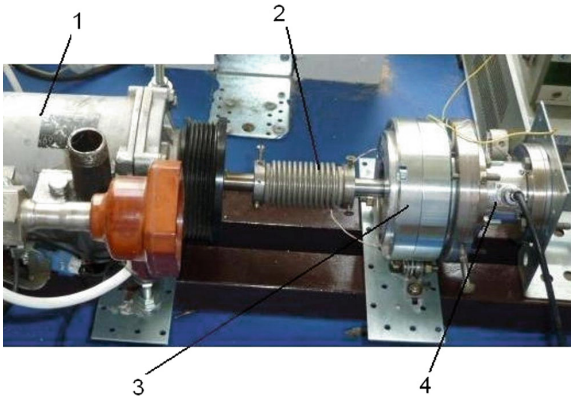

Fig. 2 Test bench. *1*—scroll air motor, *2*—bellow coupling, *3*—controlled electro-power coupling, *4*—torque sensor

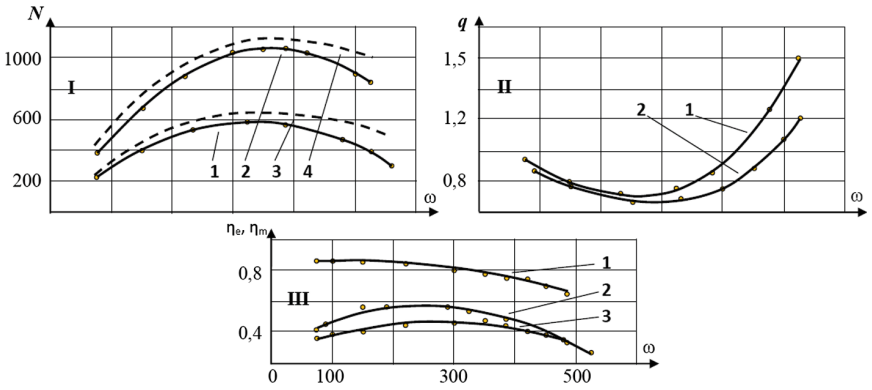

Fig. 3 Power, specific air consumption, energy efficiency performance. N [Wt], q [m^3/min kWt]

3 Mathematical Modeling

The mathematical model contains a system of nonlinear differential equations with variable structure, logical relationships determining the conditions for the connection of the chambers with a feed line or atmosphere, as well as equations describing the scroll elements and their interaction. Thermodynamic equations are written on the basis of the energy conservation law and equation of state for the working medium in the chamber in differential form. For steady-state operation mode, i.e. with a constant angular velocity ω, these equations have the form:

$$\frac{dp_i}{d\alpha} = \frac{k}{\omega V_i}\left[RT_m G_m + T_j G_i^+ - T_i G_i^- - p_i \omega \frac{dV_i}{d\alpha}\right]$$

$$\frac{dT_i}{d\alpha} = \frac{T_i}{\omega p_i V_i}\left[p_i \omega \frac{dV_i}{d\alpha} \omega V_i \frac{dp_i}{d\alpha} - RT_m G_m - RT_j G_i^+ - RT_i G_i^-\right]$$

$$M_c = \frac{1}{2\pi}\int_0^{2\pi}\left(\sum_{i=1}^{z} p_i(\alpha)\frac{dV_i}{d\alpha}\right)d\alpha - M_t(\omega, p_m)$$

Here the equation of motion of the shaft for the case of constant ω is a balance of torques acting on the shaft, M_c is the torque of useful resistance, $M_t(\omega, p_m)$ is the total torque of friction depending on the angular velocity and pressure power p_m (see below), p_i, T_i, V_i are pressure, temperature and volume of the i–th chamber, k is the adiabatic constant, R is the gas constant, α—the angle of rotation of the moving

scroll, G_m is flow of the working medium from the supply line into the central chamber, defined by the Saint-Venant equation.

Similarly, the leakages through axial and radial clearances between the scrolls are calculated: in the chamber of G_i^+ with the temperature of the working medium T_j and from the chamber G_i^-. The volume of the chambers formed by the involute fixed and movable scrolls is determined as follows. The equations of the inner and outer walls of the fixed scroll are written in parametric form. Similar equations are written for the movable scroll considering the eccentricity ε and angle α of the movable scroll. The condition $r_o = (\varepsilon + \delta)/\pi$ always holds, where r_o is the radius of the initial circle of the scrolls, δ is thickness. I.e. the scrolls do not intersect, but only touch. The equations of the scrolls are solved simultaneously, and the coordinates of the touch points of the scrolls are obtained as functions of the angle α, which determines the shape of the chambers. Then the area of the chambers (the area of the curvilinear trapezoid) $S_i(\alpha)$ and respectively the volume $V_i = h\, S_i(\alpha)$ are determined by Green's equation as a function of angle α. Here h is the height of scroll. Also the lengths of the arcs of scrolls are determined that form a chamber for the subsequent calculation of the areas of the channels of leakages. Results of calculation of the power against rotation speed are shown in Fig. 3a (curves 3 and 4). One may see satisfactory quality of this simple model.

Table 1 Performances of traditional types of air motors

Performances	Air motor types				
	Gear motors	Piston motors		Vane motors	Turbine motors
		Radial piston	Axial piston		
Power range kWt	0.5–50	0.1–25	0.4–12	0.05–18	0.01–55
Inlet pressure Mpa	0.3–0.6	0.4–0.7	0.4–0.6	0.4–0.8	0.3–1
(Nominal/free) speed RPM	170/400–3000/5000	750/1600–1100/2300	400/750–2300/4800	550/1200–9000/21500	6000/8500–$(1–1.2) \times 10^5$
Specific air consumption m^3/min kWt	1.1–2.0	0.86–2	0.9–1.7	1.1–2	0.6–4.1
Volume specific power kWt/dm^3	0.23–1.8	0.1–0.45	0.25–0.8	1.05–2.9	Up to 12.5
Inclination of torque curve Nms	$(0.09–3.3) \times 10^{-2}$	6×10^{-3}–1.2	0.01–2.9	2×10^{-4}–0.2	$(0.5–3) \times 10^{-3}$
Exergy efficiency (%)	14–32	15–33	16–27	12–26	10–45

4 Results and Discussion

To estimate the results of test scroll air motor, we must compare its performance with traditional types of air motors. Table 1 presents analysis data of air motors performance of more than twenty companies, some of them [6–14].

It should be noted that our scroll air motor has a rather high energy efficiency. The specific air consumption at 0.5 Mpa was 0.72 m^3/min kWt. This is better than the one of the most efficiency models of piston air motors. Only powerful (40–55 kWt) two-step turbine air motor gives better results—0.65 m^3/min kWt [13]. For turbine motors of comparable power (1–5 kWt) this value is 0.8–1.2 m^3/min kWt.

It has the next main reasons: 1—very small "dead" volume; 2—the leakages from central chamber pass other chambers before come to atmosphere and take part in forming moving torque. Nominal speed of scroll air motor is about 2600–4000 RPM and it take position between piston and vane air motors. The specific power volume is 1.86 kWt/dm^3 (under standard supply pressure 0.6 Mpa), like good models of vane air motors. One important characteristic of air motor is the inclination of its torque curve $K_m = \Delta M(\omega)/\Delta\omega$, which allows us to draw indirect conclusions about the capabilities of a compressed air inlet and exhaust in motor chambers. In our case $K_m = -6.8 \times 10^{-3}$ Nms ($p_m = 0.5$ Mpa). It is a "hard" torque curve, unlike piston air motors with a soft characteristic. Also scroll air motor have a low level of noise and vibration; small pulse of moving torque.

For the most part scroll air motor performance is better (or equal) than traditional types, except cost. If this limitation will be removed, it will find a wide industrial application in the near future.

The study was financially supported by the RFBR project No. 16-29-04401.

References

1. Compressed air technology today is more economical than it has ever been. Deprag Press Release. May 2013. www.deprag.com
2. Creux, L.: Rotary engine. US Patent № 801.182. 1905
3. Wang, J., Yang, L., Mangan, S., Derby, J.: Mathematical modeling study of scroll air motors and energy efficiency analysis—Part I. IEEE/ASME Trans. Mechatron. **16**(1), 112–120 (2011)
4. Yanagisawa, T., Fukuta, M., Ogi, Y.: Performance of an oil-free scroll—type air expander. In: Proceedings of the ImahE Conference on Compressors and their systems, pp. 167–174 (2001)
5. E15H22N4.25. 1 kW Scroll Expander. www.airsquared.com
6. GAST Air Motors / Gear Motors. Labricated and Non-labricated. ISO 9001. Catalog Final 2012, 41 p. www.gastmfg.com
7. Air turbine motors. Sealed Motor Mount Series. www.airturbinetools.com
8. Gardner–Denver Pneumatic Power Motors. Catalog 2011. www.cooperpowertools.com
9. Deprag Air Motors Customized drive solutions. 2012, 28 p. www.deprag.com
10. TONSON Air Motors. Catalog. www.tonson-motor.com

11. Atlas Copco Air Motors. LZB, LZL vane motor. Catalog. 2012, 75 p. www.atlascopco.com
12. Ingersoll Rand MVR and SM (select) Lub—free reversible air motors. www.ingersollrandprodacts.com
13. Ingersoll Rand Turbine Air Starter. Electronic catalog www.murcal.com
14. Pneumatic Rotary Actuators and Air motors. Platform Catalog PDE2613TCUK. Parker pneumatic division Europe

Analysis of the Mechanism of the Drill Hammer

M. Konečný

Abstract This paper describes function of the mechanism of the hammer drill and solving the impact analysis and determining the contact pressure between the parts of the mechanism. The computational model was created by Creo Parametric 2.0., simulation of dynamic effect by the module Mechanism and stress simulation by the module Simulate.

Keywords Pneumatic hammer drill · Impact analysis · Contact pressure

1 Introduction

Use of compressed air is now widespread in many sectors. Pneumatic tools have a high degree of modernization. Manufacturers shall ensure competitiveness, superior technological performance, low price and especially functionality, which is closely related with high reliability. Pneumatic devices in these days widespread throughout the world. It has many advantages over hydraulic mechanisms, electric and solid mechanisms. The market has found a considerable number of companies that are engaged in the production of pneumatic mechanisms and machines.

2 The Drill Hammer

Work pneumatic hammers provides compressed air. It must be applied and regulated. The air supply is provided by a hose that connects to the machine by a thread. Lever built into the handle of the hammer is controlled airflow. The hammer inside air flows into the two chambers. This ensures the flow valve timing as shown in

M. Konečný (✉)
Technical University of Liberec, Liberec, Czech Republic
e-mail: martin.konecny@tul.cz

J. Beran et al. (eds.), *Advances in Mechanism Design II*,
Mechanisms and Machine Science 44, DOI 10.1007/978-3-319-44087-3_20

Fig. 1a, numerically labeled from 1 to 3 parts take care to ensure that the compressed air flow in the first phase of the movement in the chamber above the piston. In the second phase of movement the air flows into the chamber below the piston indicated in Fig. 1b. This cycle must be repeated continually. In the first case, when the compressed air flows into the chamber above the piston (red color component numbers 2), closes the holes in the green part indicated by 3. This process remains until the piston moving downwards opens the exhaust port. The air pressure suddenly in the chamber above the piston drops, part 2 releases closed openings in part 3 and air can flow into the chamber below the piston. To allow air to flow into the lower chamber, the cylinder of the linear motor drilled holes and recessed exhaust port, as can be seen in Fig. 1b. Operation of the distribution valve is provided decreases in pressure in the chamber above the piston and below the piston. The pressure in the chamber drops each time the shock worker is released and the air exhaust hole this hole can escape. A certain volume of the escaping gaps in the exhaust port of the shock worker flows through the tool and blowing debris from the drilled hole.

2.1 *Determination of Dynamic Effects*

The goal of this dynamics analysis is to determine the velocity of the shock worker before impact, the acceleration and kinetic energy. For the calculation of the dynamic effects used data, which the manufacturer says in the manual of the hammer. The stroke of the air motor has a size of 35 mm with frequency 3500 numbers of beats per minute. This value is set for the default position of the shock worker. Technical data was measured at a working pressure of the compressed air of 6.3 bar. The size of the force acting on the shock worker is determine with using analysis of the pneumatic motor. Given the size of this double-acting pneumatic motor and working conditions is the force $\boldsymbol{F_p}$ set at 580 N. Friction between the cylinder of the linear motor and the shock worker has been neglected.

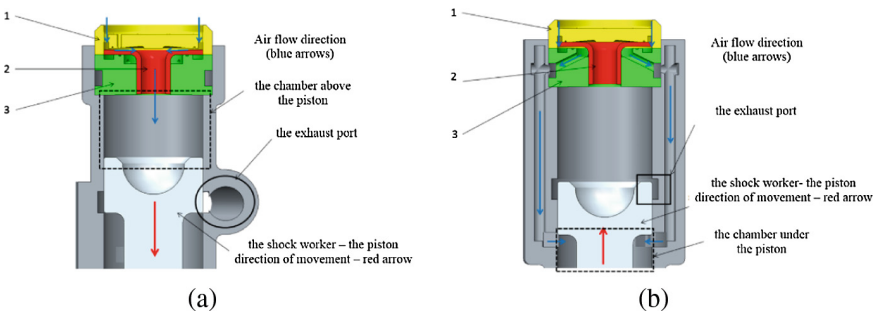

Fig. 1 Scheme of air distribution (Color figure online)

2.1.1 Calculation of Stiffness

In order to perform calculation of impact it is necessary to determine the overall stiffness of the system. The entire assembly is made up of tools and shock worker. Boundary conditions simulate the same deposit, as is in fact the deposit of these parts in real hammer. The end of the tool is used boundary condition fixed. The boundary condition for receiving the hexagonal part of the tool has been defined with clearance 0.1 mm in the direction perpendicular to the longitudinal axis and a permissible displacement of the axis of movement. For shock worker has been defined boundary condition for his large-diameter cylindrical surfaces, which enabled again only a shift in the axis of the tool motion. Boundary conditions for the shock worker is set up without prescribed. This was done due to the desire to get closer to real conditions. Material of the tool and shock worker has been set on hardened steel. Young's modulus for the hardened steel has a value $\boldsymbol{E} = 1.8 \times 10^5$ MPa. System is loaded with the general force $\boldsymbol{F_s}$. The maximal value of the displacement is $\boldsymbol{y} = 0.01145$ mm.

2.1.2 Calculation of Impact Force

After establishing the stiffness of the system of components which are in mutual contact during the impact, there was carried out the calculation of the impact force. For the purpose of this analysis is modified model from the previous analysis. The model is replenished with the subframe and the spring. The spring is inserting between the tool and the subframe. The stiffness of this spring is calculated in the previous stiffness analysis and Eq. (1). The value of stiffness is $\boldsymbol{k_s}$ = 43,626 N mm. The model can be seen in Fig. 2.

$$\boldsymbol{F_s} = \boldsymbol{k_s} * \boldsymbol{y} \tag{1}$$

Insert the spring in the assembly of the calculated stiffness is one of the ways you can check the progress of the impact force by means of software. The tool weight was set to the minimum possible value. This was done because it is already known to the system overall stiffness and thus the weight of the tool is no longer necessary to calculate. The spring was supplemented by a shock absorber with low value of damping. The impact analysis is solved with parameters for the stroke of the pneumatic motor 35 mm, the force $\boldsymbol{F_p}$ 580N, the stiffness of the spring $\boldsymbol{k_s}$ which

Fig. 2 Assembly for the impact analysis, Creo mechanism

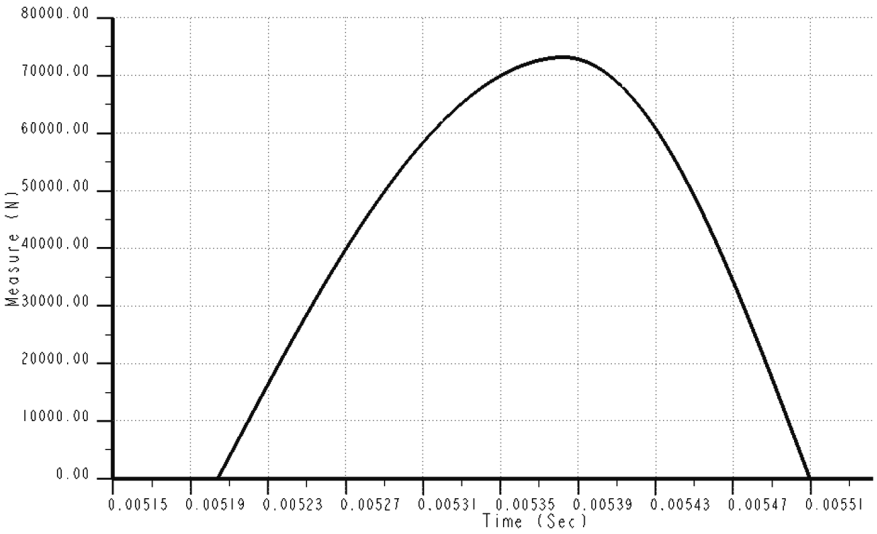

Fig. 3 Course of shock forces of the drill hammer, Creo mechanism

replaced the stiffness of the system and on the cam there has been set up the coefficient of restitution 0.75. The coefficient of restitution has been chosen according to the table for hardened steel.

The course of impact force approximately corresponded to the theoretical course of impact force. As the size and course of the impact force cannot determine exactly is the calculation of certain parts only theoretical. The value of the maximum resultant forces came 73° 192N (Fig. 3).

2.1.3 The Impact Theory

This phenomenon we associate with the emergence of large forces and sharp changes in speed. The impact in technical practice we encounter very often. For example, impact drill, jackhammer, and the like. From a mechanical standpoint it is a complicated phenomenon, which is influenced by many factors [1]. Shock plot spreads in waves and its duration is extremely short. It is a time of about 10^{-4} s. In this short period of time there are changes in speed almost immediately and forces acting in the contact area are enormous. For this reason we can be neglected under the influence of buckling on the long tool. When comparing the course of the force depending on the time when a theoretical calculation nature can observe a great resemblance to a graph obtained from the module Creo Mechanism when the maximal value of the shock force is 73° 192N (Fig. 3).

3 Theoretical Analysis of Contact

For resolving the task was chosen a modified equation for the contact of two balls. The maximum value of the contact pressure was obtained from Eq. (2):

$$p_o = \frac{\sqrt[3]{6}}{\pi}\left(\frac{E_{red}}{R_e}\right)^{\frac{2}{3}} F^{\frac{1}{3}} \tag{2}$$

The size of the force $\boldsymbol{F}$ has been selected 73192N. $\boldsymbol{E_{red}}$ value for two steel balls of the same material is $\boldsymbol{E_{red}} = 1.153846\ 10^5$ MPa ($E = 2.1 \times 10^5$ MPa and $\mu = 0.3$). Furthermore simplification $\boldsymbol{R_e} = \boldsymbol{R_1}$. Size $\boldsymbol{R_1}$ was chosen 75 mm, the value rounding shock worker (3). The tool was considered plane.

$$p_o = \frac{\sqrt[3]{6}}{\pi}\left(\frac{E_{red}}{R_e}\right)^{\frac{2}{3}} F^{\frac{1}{3}} = \frac{\sqrt[3]{6}}{\pi}\left(\frac{1.153846 \times 10^5}{75}\right)^{\frac{2}{3}} (73192)^{\frac{1}{3}} = 3224.4 \text{ MPa} \tag{3}$$

The value of the resulting pressure is approximately 1.5 times greater than the figure recorded in the impact analysis. This value would be correct, assuming that the area of the shock worker is completely straight. Calculated pressure went higher than a contact pressure in the analysis. The formula for calculating the contact of two spheres also does not exactly correspond to the real situation. Due to the fact that the tool is a hole diameter $\boldsymbol{d_d} = 7$ mm, there is a concentration of the largest voltage at the border of the hole. It is possible to say that the result of the contact is approximately analysis results counted according to the formulas. To check whether the counted value analysis is correct, we were made more simplified calculation for contact with the cylinder surface and the planar surface according to the formula (4).

$$p_o^2 = 0.175E\frac{F}{l}\frac{1}{R_e} = 1{,}630{,}185.46 \text{ MPa} \Rightarrow p_o = 1277 \text{ MPa} \tag{4}$$

Again, we consider that the value of $\boldsymbol{R_e} = \boldsymbol{R_1}$, is 75 mm. The length $\boldsymbol{l}$ was considered as a circuit holes $l = \pi \cdot d_d$. As seen, this value of the contact pressure according to the formula 4 is closer to values that can be seen from Fig. 4.

3.1 The FEM Analysis of Contact Pressure

After determining the size of the impact force could be created contact analysis in the module Creo Simulate. The objective of this analysis was to determine the pressures at the contact point with the shock worker and the tool. The analysis used the same model as for the calculation of the overall stiffness. In the report were made slight adjustments. The size of the force has been set at 73° 192N. Defining

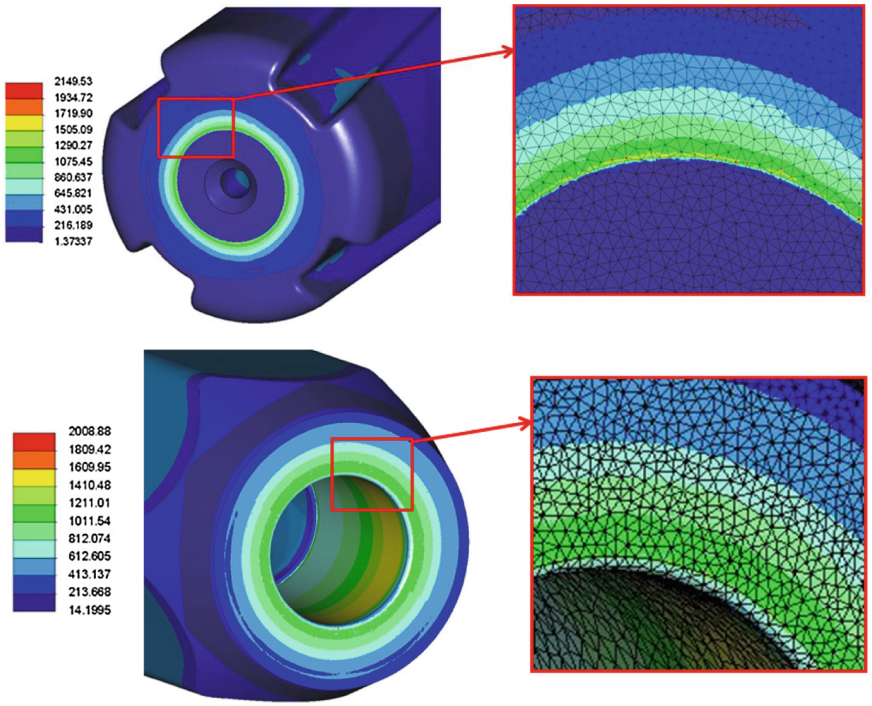

Fig. 4 Detailed distribution of pressures on the shock worker and the tool

Fig. 5 Detailed of the real wear

the contact surface between the tool and the shock worker maintained as the analysis stiffness. The contact area was been awarded on the tool and the shock worker 0.2 mm. The size of elements of concentrated mesh can be seen in Fig. 4.

The result of the contact analysis is visualized in Fig. 4. The critical point of reaching pressure values of almost 2150 MPa in the area of the hole's edge. In other locations the pressure is at lower levels and corresponds to the value of the contact pressure obtained from the formula according to the Hertz theory of contact a ball with the planar surface (4). The measured results were compared with the actual wear part (Fig. 5).

4 Conclusions

Because of limited extent of the article, it is impossible to describe the concerned analysis in detail. Owing to high values of contact pressures acting on a relatively small area, the wear and tear will be fast in the beginning. However, it will result in an enlargement of contact areas consequently, the force will be distributed to a larger area, and the contact pressure will drop down. The wear will also result in toughening of the material, too. The higher will be the wear of the components, the more slowly it will continue subsequently. It is known character of the distribution of the contact pressure. On the difference between the theoretical calculation and the value that are obtained by contact analysis of Creo Simulate probably contributes simplifying assumptions solution that is between the two general surfaces and not exactly correspond to reality. Hertz theory is accurate in case of contact tasks such as spheres with planar surface. The resulting value of the distribution of the contact pressure also affects the by the mesh quality in the contact area and its surroundings. We can see (Fig. 5) that the results come close to the real thing, even if maybe not concerning the value of the pressure, but concerning the proportion of distribution of operating pressures instead of greatest wear suit incidence of the biggest pressure identified in the analysis.

Acknowledgments This publication was written at the Technical University of Liberec, Faculty of Mechanical Engineering with the support of the Institutional Endowment for the Long Term Conceptual Development of Research Institutes, as provided by the Ministry of Education, Youth and Sports of the Czech Republic.

Reference

1. Medvec, A., Stradiot, J., Záhorec, O., Caban, S.: Mechanics III Dynamic, Bratislava SNTL (1988)

Free Vibration Frequency Spectrum of Four-Planetary Gearing Box

L. Půst, L. Pešek and A. Radolfová

Abstract Dynamic analysis of multi-mesh planetary gearings is very important for reduction of noise and vibration. Splitting of force flow into several planet wings is the main advantage of planetary gearings. As it can be devaluated by unequal load sharing on individual planet stages, the floating sun gear and flexible pins of planet gears are applied. This paper shows that dynamic model of such a gearing box is very complicated with many multiple eigenfrequencies. The gained frequency spectrum with multiple eigenvalues is derived and analyzed.

Keywords Planetary gearing · Negative stiffness · Frequency spectrum · Multiple eigenvalues

1 Introduction

Modal and spectral dynamic properties of planetary gearboxes are more complicated than parallel-axis gear transmission systems and therefore they need deeper dynamic analysis. The main advantage of planetary gearing is in splitting of force flow into several planet stages and so minimizing of weight. In order to prevent unequal load sharing on planet stages, floating sun gear and flexible pins of planet gears are applied. Dynamic model of such a gearing box is very complicated mainly since it has several multiple eigenfrequencies in its spectrum.

In this paper, the solution of spectral properties of the plane type of gearings with four planetary subsystems and with fixed planet carrier is presented. As the all

L. Půst (✉) · L. Pešek · A. Radolfová
Institute of Thermomechanics AS CR, v.v.i., Dolejškova 5,
18200 Praha 8, Prague, Czech Republic
e-mail: pust@it.cas.cz

L. Pešek
e-mail: pesek@it.cas.cz

A. Radolfová
e-mail: radolfov@it.cas.cz

J. Beran et al. (eds.), *Advances in Mechanism Design II*,
Mechanisms and Machine Science 44, DOI 10.1007/978-3-319-44087-3_21

wheels have helical gearings, fluctuation of teeth contact stiffness over a mesh cycle can be neglected. Steady contacts in gearings are asserted by means of preloading due to the constant moment loads on the sun and on outer rig gears.

Application of floating sun gear causes that in addition to the deformations in mesh contact in the direction of tangent to the base circle there is also a radial motion component perpendicular to this tangential deformation. Restoring forces at displacement in this radial direction are usually not taken into account at mathematical modelling. The new radial stiffness of gear contact has been therefore introduced both for external and internal tooth systems.

2 Type of Investigated Gearbox

The plane type of gearings with four planetary subsystems and with fixed planet carrier has been solved—Fig. 1. All the wheels have helical gearings. As these gearings have a very small variation of contact stiffness, teeth contact stiffness is supposed to be constant. The main aim of the complex study is analysis of influence of planetary pins compliance (stiffness k_c) and of free (or weekly supported, stiffness k_c) axis of sun wheel on gearbox dynamic properties. The second aim is to prepare the theoretical base for evaluation of measurements data gained at the planned experiments on new gearing box prototype.

3 Radial Stiffness of Two Gearing Wheels

Mutual radial motion of two gearing wheels changes pressure angle α as shown in Fig. 2, where $r_3^* = r_3 \cos(\alpha)$, $r_2^* = r_2 \cos(\alpha)$ are radiuses of base, (r_3, r_2 of pitch) circles. The radial shift Δy determines change $\Delta\alpha$ of pressure angle α. The radial component F_r of the contact force F increases:

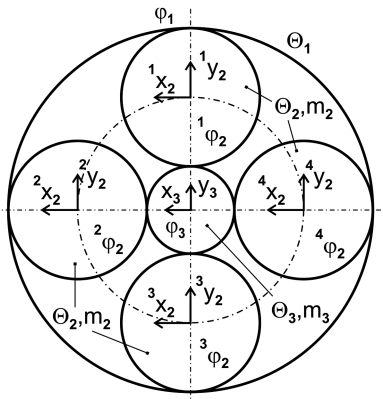

Fig. 1 Four-planetary gearing

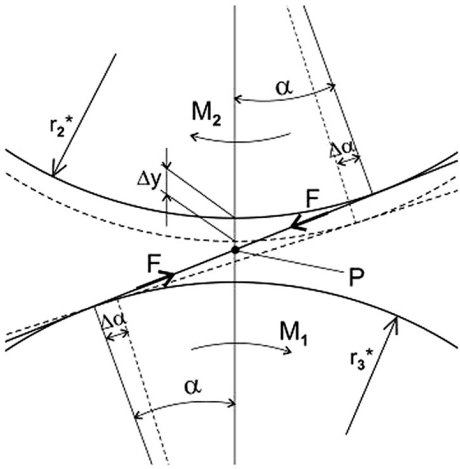

Fig. 2 External mesh

$$\Delta F_r = F(\sin(\alpha - |\Delta\alpha|) - \sin(\alpha)) \cong -F\cos(\alpha)\sin(|\Delta\alpha|) \tag{1}$$

Also the change of radial shift Δy is connected with $\Delta\alpha$. The approaching of base circles Δy_c and of axes Δy_a of both wheels are the same $\Delta y_c = \Delta y_a = \Delta y$:

$$\Delta y = \frac{r_3^* + r_2^*}{\cos(\alpha)} - \frac{r_3^* + r_2^*}{\cos(\alpha - |\Delta\alpha|)} \cong \frac{(r_3^* + r_2^*)\sin(\alpha)\sin(|\Delta\alpha|)}{\cos^2(\alpha)}. \tag{1a}$$

The ratio of ΔF_r and Δy, gives negative radial stiffness k_r:

$$k_r = \frac{\Delta F_r}{\Delta y} = \frac{\Delta F_r}{\Delta y_c} = \frac{\Delta F_r}{\Delta y_a} = \frac{-F\cos^3(\alpha)}{(r_3^* + r_2^*)\sin(\alpha)} = \frac{-F\cos^2(\alpha)}{(r_3 + r_2)\sin(\alpha)}. \tag{2}$$

Similar relations are valid also for the radial contact stiffness between ring and planetary wheel that is an internal gearing contact, where the pressure angle α increases $\Delta\alpha > 0$ at wheels penetrating $\Delta y = \Delta y_c$. In such a case the radial contact stiffness k_r is positive. However, the approaching of base circles Δy_c at internal gearing contact is connected with increase of wheel axes distance $\Delta y_a = -\Delta y_c$ and therefore the radial contact stiffness $k_r = \frac{\Delta F_r}{\Delta y_a}$ of this internal gearing has again negative sign similar to the external mesh.

In the mesh, there are perpendicular friction forces besides pressure forces. These forces act along the whole length of pressure line. The friction forces in the addendum part of the pressure line have opposite direction than in the dedendum part, they are roughly in balance and therefore the friction forces result is small and can be neglected in the following solution.

3.1 Radial Free Vibration

The first step in solution of dynamics of the four planetary gearing system (Fig. 1) is analysis of one separate planet wheel. We shall use the same value for external and internal tooth contacts $k_r = -40{,}000$ N/m. Equations of motion of free radial vibration of one planet wing, at assumption that the ring wheel axis is stiff, are

$$m_3\ddot{y}_3 - k_r(y_3 - y_2) + k_3 y_3 = 0, \quad m_2\ddot{y}_2 + k_r y_3 + k_c y_2 = 0. \tag{3}$$

It is a 2DOF system, which can serve as a mathematical model of the upper planet subsystem labeled by a left upper index " ^{1} " in Fig. 1. Mathematical models of other three planet subsystems labeled by " $^{2,\,3,\,4}$ " have similar structure but the variables must be exchanged according to the orientation of planet wings [1].

3.2 Free Tangential Vibration

Tangential motion and rotation of wheels are influenced by stiffness of tooth meshes k_1, k_2 and stiffness of flexible wheel's pins k_3, k_c. As planet and sun wheel both rotate and translate, the masses of planet and of sun wheel as well their moments of inertia must be considered. Differential equations of one planet wing motion are described in [2]. Here the direct derivation of mathematical model of the entire four planetary gearing box is applied.

4 Free Vibration of Four-Planetary Gearing Box

Mathematical description of free vibration of gearing box can be constructed by means of Lagrange equations written for n generalized coordinates of motion q_j

$$\frac{d}{dt}\left(\frac{\partial T}{\partial \dot{q}_j}\right) - \frac{\partial T}{\partial q_j} + \frac{\partial V}{\partial q_j} = 0 \quad j = 1, \ldots, n \tag{4}$$

where T is kinetic energy of investigated system, V is potential energy.

Let us investigate dynamic properties of a gearing box shown in Fig. 1 without any external driving and braking aggregate. The coordinate vector q is:

$$q = [\varphi_1\ {}^{1}y_2\ {}^{1}x_2\ {}^{1}\varphi_2\ {}^{2}y_2\ {}^{2}x_2\ {}^{2}\varphi_2\ {}^{3}y_2\ {}^{3}x_2\ {}^{3}\varphi_2\ {}^{4}y_2\ {}^{4}x_2\ {}^{4}\varphi_2\ y_3\ x_3\ \varphi_3]^T. \tag{5}$$

Kinetic energy of the four-planets gearing system with 16 DOF is

$$T = \frac{1}{2}\left[\begin{array}{l}\Theta_1\dot{\varphi}_1^2 + m_2({}^1\dot{y}_2^2 + {}^1\dot{x}_2^2 + {}^2\dot{y}_2^2 + {}^2\dot{x}_2^2 + {}^3\dot{y}_2^2 + {}^3\dot{x}_2^2 + {}^4\dot{y}_2^2 + {}^4\dot{x}_2^2) \\ + \Theta_2({}^1\dot{\varphi}_2^2 + {}^2\dot{\varphi}_2^2 + {}^3\dot{\varphi}_2^2 + {}^4\dot{\varphi}_2^2) + m_3(\dot{y}_3^2 + \dot{x}_3^2) + \Theta_3\dot{\varphi}_3^2\end{array}\right]. \tag{6}$$

Potential energy V of the same 16 DOF gearing system is a function of all angular and transversal coordinates given in the coordinate vector q and contains also tooth mesh stiffness parameters $k_1,\ k_2$, stiffness k_c of flexible planet pins and stiffness k_3 of sun gear support. The axis of ring wheel is supposed to be sufficiently stiff with no transversal displacements ($y_1 = 0,\ x_1 = 0$). Potential energy consists of radial and potential parts $V = V_{rad} + V_{\tan}$. The complete potential energy is

$$V = \frac{1}{2}\left[\begin{array}{l}k_r\left[(y_3 - {}^1y_2)^2 + (x_3 - {}^2x_2)^2 + (y_3 - {}^3y_2)^2 + (x_3 - {}^4x_2)^2\right] \\ \quad + k_r\left[{}^1y_2^2 + {}^2x_2^2 + {}^3y_2^2 + {}^4x_2^2\right] + k_c({}^1y_2^2 + {}^1x_2^2 + {}^2y_2^2 + {}^2x_2^2 + {}^3y_2^2 + {}^3x_2^2 + {}^4y_2^2 + {}^4x_2^2) \\ \quad + k_1[(r_1\varphi_1 - r_2{}^1\varphi_2 - {}^1x_2)^2 + (r_1\varphi_1 - r_2{}^2\varphi_2 + {}^2y_2)^2 + (r_1\varphi_1 - r_2{}^3\varphi_2 - {}^3x_2)^2 \\ \quad + (r_1\varphi_1 - r_2{}^4\varphi_2 + {}^4y_2)^2] + k_2[(r_3\varphi_3 - x_3 - r_2{}^1\varphi_2 + {}^1x_2)^2 \\ \quad + (r_3\varphi_3 + y_3 - r_2{}^2\varphi_2 + {}^2y_2)^2 + (r_3\varphi_3 + x_3 - r_2{}^3\varphi_2 - {}^3x_2)^2 \\ \quad + (r_3\varphi_3 + y_3 - r_2{}^4\varphi_2 + {}^4y_2)^2] + k_3(y_3^2 + x_3^2)\end{array}\right] \tag{7}$$

Introducing expressions (6) and (7) into Lagrange equations. (4) we get 16 differential equations of motion

$$\begin{array}{l}
\Theta_1\ddot{\varphi}_1 + k_1r_1[4r_1\varphi_1 - r_2({}^1\varphi_2 + {}^2\varphi_2 + {}^3\varphi_2 + {}^4\varphi_2) - {}^1x_2 + {}^2y_2 + {}^3x_2 - {}^4y_2] = 0, \\
m_2{}^1\ddot{y}_2 + (k_c + 2k_r){}^1y_2 - k_ry_3 = 0, \\
m_2{}^1\ddot{x}_2 - k_1r_1\varphi_1 + (k_1 - k_2)r_2{}^1\varphi_2 + (k_1 + k_2 + k_c){}^1x_2 + k_2r_3\varphi_3 - k_2x_3 = 0, \\
\Theta_2{}^1\ddot{\varphi}_2 - k_1r_2r_1\varphi_1 + (k_1 + k_2)r_2{}^1\varphi_2 - (k_2 - k_1)r_2{}^1x_2 + k_2r_2x_3 - k_2r_2r_3\varphi_3 = 0, \\
m_2{}^2\ddot{y}_2 + k_1r_1\varphi_1 - (k_1 - k_2)r_2{}^2\varphi_2 + (k_1 + k_2 + k_c){}^2y_2 - k_2r_3\varphi_3 - k_2y_3 = 0, \\
m_2{}^2\ddot{x}_2 + (k_c + 2k_r){}^2x_2 - k_rx_3 = 0, \\
\Theta_2{}^2\ddot{\varphi}_2 - k_1r_2r_1\varphi_1 + (k_1 + k_2)r_2{}^2\varphi_2 + (k_2 - k_1)r_2{}^2y_2 - k_2r_2y_3 - k_2r_2r_3\varphi_3 = 0, \\
m_2{}^3\ddot{y}_2 + (k_c + 2k_r){}^3y_2 - k_ry_3 = 0, \\
m_2{}^3\ddot{x}_2 + k_1r_1\varphi_1 - (k_1 - k_2)r_2{}^3\varphi_2 + (k_1 + k_2 + k_c){}^3x_2 - k_2r_3\varphi_3 - k_2x_3 = 0, \\
\Theta_2{}^3\ddot{\varphi}_2 - k_1r_2r_1\varphi_1 + (k_1 + k_2)r_2{}^3\varphi_2 + (k_2 - k_1)r_2{}^3x_2 - k_2r_2x_3 - k_2r_2r_3\varphi_3 = 0, \\
m_2{}^4\ddot{y}_2 - k_1r_1\varphi_1 + (k_1 - k_2)r_2{}^4\varphi_2 + (k_1 + k_2 + k_c){}^4y_2 + k_2r_3\varphi_3 - k_2y_3 = 0, \\
m_2{}^4\ddot{x}_2 + (k_c + 2k_r){}^4x_2 - k_rx_3 = 0, \\
\Theta_2{}^4\ddot{\varphi}_2 - k_1r_2r_1\varphi_1 + (k_1 + k_2)r_2{}^4\varphi_2 + (k_1 - k_2)r_2{}^4y_2 + k_2r_3y_3 - k_2r_2r_3\varphi_3 = 0, \\
m_3\ddot{y}_3 + k_2[-r_2({}^2\varphi_2 - {}^4\varphi_2) + 2y_3 - {}^2y_2 - {}^4y_2] + k_3y_3 + k_r(2y_3 - {}^1y_2 - {}^3y_2) = 0 \\
m_3\ddot{x}_3 + k_2[r_2({}^1\varphi_2 - {}^3\varphi_2) + 2x_3 - {}^1x_2 - {}^3x_2] + k_3x_3 + k_r(2x_3 - {}^2x_2 - {}^4x_2) = 0 \\
\Theta_3\ddot{\varphi}_3 + k_2r_3(4r_3\varphi_3 - r_2{}^1\varphi_2 - r_2{}^2\varphi_2 - r_2{}^3\varphi_2 - r_2{}^4\varphi_2 + {}^1x_2 - {}^2y_2 - {}^3x_2 + {}^4y_2) = 0,
\end{array} \tag{8}$$

These equations of motion can be rewritten into a matrix form

$$M\,\ddot{q} + K\,q = 0 \tag{9}$$

with the coordinate vector q given by (5) and with the diagonal inertia matrix M

$$M = diag[\backslash \Theta_1, m_2, m_2, \Theta_2, m_2, m_2, \Theta_2, m_2, m_2, \Theta_2, m_2, m_2, \Theta_2, m_3, m_3, \Theta_3 \backslash] \tag{10}$$

and with the full stiffness matrix K which is of order 16.

The roots of characteristic determinant

$$\left| -\Omega^2 M + K \right| = 0 \tag{11}$$

give eigen-frequencies of investigated planetary gearbox.

If the parameters of the example of planetary gearbox are:

Tangential mesh stiffness $k_1 = k_2 = 4e + 9$ N/m, radial stiffness $k_r = -4e + 4$ N/m, planet pin stiffness $k_c = 5e + 9$ N/m, radiuses $r_1 = 0.3$ m, $r_2 = 0.12$ m, $r_3 = 0.06$ m, masses $m_1 = 250$ kg, $m_2 = 42$ kg, $m_3 = 25$ kg, moments of inertia $\Theta_1 = 200$ kgm^2, $\Theta_2 = 0.5$ kgm^2, $\Theta_3 = 0.05$ kgm^2, then by means of program "eig" in system Matlab we get eigenfrequencies of investigated planetary gearing—see Table 1.

The first eigen-frequency has zero value and corresponds to the revolution of all gearing wheels. The remaining fifteen non-zero eigen-frequencies correspond to the vibrations superposed on this rotation. There are three twofold frequencies 856, 2673, 3780 Hz and one fourfold frequency 1779 Hz.

The used program "eig" in Matlab system ascertains corresponding modes of vibrations in a normalized form. In the case when all the eigenvalues are distinct, one mode shape orthogonal to the rest of eigenmodes belongs to each one of them. But there are some multi-fold eigen-frequencies in the planet gearings frequency spectrum, which need special mode shape procedure [3, 4]. There is no difficulty for computer programs to extract multiple eigenvalues, but it makes certain complication in ascertaining of eigenvectors. If the system has a repeated eingen value, we get a corresponding number of different, independent eigenvectors. Any linear combination of these vectors is also an eigenvector. Therefore the eigenvector matrix U is not unique. Different procedures are proposed in literature, the simplest one seems to be the perturbation method [4, p. 382] based on splitting the multiple

Table 1 Eigen frequencies

	f_1	f_2	f_3	f_4	f_5	f_6	f_7	f_8
Hz	0.0	856	856	1225	1779	1779	1779	1779
	f_9	f_{10}	f_{11}	f_{12}	f_{13}	f_{14}	f_{15}	f_{16}
Hz	2415	2673	2673	2869	2947	3780	3780	5908

eigenvalue into several separated eigenfrequencies located close to each other and having separate mode shapes. If in the above mentioned mathematical model of planetary gearing is completed with moderately increasing e.g. stiffness k_c of flexible planet pins, then the frequency spectrum differs a little from the original in Table 1, all eigenvalues are distinct and eigenmodes can be easily determined.

5 Conclusion

It is shown that the solution of vibrations of planetary gearing box with the weakly supported sun wheel needs to include radial gear mesh stiffness into mathematical model and that this stiffness is negative. After deriving 16 differential equations of gearing motion, the free frequency spectrum is ascertained. Several multiple eigenfrequencies were discovered and the method for ascertaining of adjoined eigenmode shapes is indicated.

Acknowledgments The work has been supported by the grant project TA04011656.

References

1. Půst, L., Pešek, L., Radolfová, A.: Negative stiffness in gear contact. Appl. Comput. Mech. **9**(2), 141–150 (2015)
2. Půst, L. Pešek, L. Radolfová, A.: Free vibration of planetary gearing. In Proceedings of Dynamesi 2015, IT ASCR, pp. 45–54. Prague (2015)
3. Newland, D.E.: Mechanical vibration analysis and computation, Longman Scientific and Technical, Harlow Essex, England (1989)
4. Collatz, L.: Eigenwertaufgaben mit technischen Anwendungen. Akademische Verlagsgesellschaft, Leipzig (1949)

Speed Control of 3-Phase Induction Motor in Presence of Sommerfeld Effect

A. Bisoi, R. Bhattacharyya and A.K. Samantaray

Abstract This paper considers the dynamics of an unbalanced rotor disk which is supported on a flexible foundation and is driven by a three-phase induction motor (IM). At resonance, the structural vibration amplitudes of the system are high and most of the motor power is spent to excite the structural mode of vibration. If the motor is improperly sized then it may not be possible for it to drive the rotor through this resonance. Even if the motor is sufficiently powerful, it first approaches the natural frequency and then suddenly jumps to a much higher value. This classic phenomenon is called the Sommerfeld effect. IM control laws often neglect this phenomenon. We develop a controller for such situation. The source-structure interaction involving the power transfer mechanism is modeled through bond graph and simulation results are presented.

Keywords Sommerfeld effect · Induction motor · Bond graph · V/f control

1 Introduction

During an experiment on an unbalanced motor placed on an elastic table, Arnold Sommerfeld came across a peculiar phenomenon. He found that near the structural resonance, there is considerable motor power consumption without much change in rotor speeds and at a critical power input, the motor speed jumps to a high value and keeps increasing with increase in voltage. This jump phenomenon was later named as Sommerfeld effect [1]. Sommerfeld effect at the stability threshold of a non-ideal system with DC motor was studied in [2, 3]. Bond graph technique [4] is very

A. Bisoi · R. Bhattacharyya (✉) · A.K. Samantaray (✉)
Indian Institute of Technology, Kharagpur, India
e-mail: rbmail@mech.iitkgp.ernet.in

A.K. Samantaray
e-mail: samantaray@mech.iitkgp.ernet.in

A. Bisoi
e-mail: alfabisoi@gmail.com

J. Beran et al. (eds.), *Advances in Mechanism Design II*,
Mechanisms and Machine Science 44, DOI 10.1007/978-3-319-44087-3_22

useful for modelling multi-disciplinary systems and has been used in the past for motor-rotor interaction modelling [5].

2 Model Description

Here, dynamics of a system with a 3-phase squirrel cage motor (see Fig. 1) attached with an unbalanced disk mounted on a flexible foundation is studied.

The disk's mass centre at C is at distance e from the geometric centre of disk at G. The total mass of the disk is denoted by m. The geometric centre of the disk is coupled with the motor and the rotor is supported by a bearing offering constant viscous resistance R_b. The foundation is flexible. The mass, stiffness and damping coefficients of the foundation are M, K_f and R_f, respectively. Parameters considered for this system are listed in Table 1.

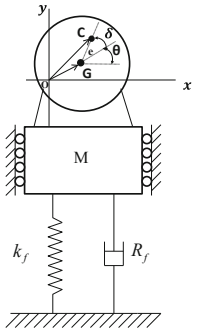

Fig. 1 Motor on a flexible foundation

Table 1 The system parameters, their descriptions and values

Parameter	Description	Value
K_f	Stiffness coefficient of foundation	15×10^4 N/m
R_f	Damping coefficient of foundation	100 Ns/m
K_{pad}	Stiffness coefficient of pad	1×10^{10} N/m
R_{pad}	Damping coefficient of pad	1×10^3 Ns/m
m	Mass of the disk	8 kg
M	Total mass of the foundation	20 kg
I_p	Polar moment of inertia of disk	0.1 kgm^2
e	Eccentricity in rotor disk	0.005 m
R_b	Bearing rotational damping coefficient	0.0002 Nms/rad
R_s	Stator resistance	0.55 Ω
R_r	Rotor equivalent resistance	0.568 Ω
I_s	Stator coil inductance	0.0048 H
I_r	Rotor equivalent inductance	0.0025 H
L_m	Mutual induction	0.1 H
T_L	Initial load torque	0.01 Nm

2.1 Equations of Motion

Let the position of the mass center G be (x_m, y_m) and geometric center C be (x, y). It follows from Fig. 1 that $y_m = y + e\sin(\theta + \delta)$ and $\dot{y}_m = \dot{y} - e\cos(\theta + \delta)\dot{\theta}$ where, $\theta = \omega t$ is the angle between the x-axis and the line passing from the geometric centre through the mass centre of the rotor, ω is the rotor speed, and δ is an arbitrary phase angle. The equations of motion of the system may be written as (2, 3, 5)

$$(M+m)\ddot{y} + R_f\dot{y} + K_f y = me\omega^2\cos(\omega t) + me\ddot{\theta}\sin(\omega t) \tag{1}$$

$$I_p\ddot{\theta} = T(\dot{\theta}) - R_b\dot{\theta} + me\ddot{y}\sin(\theta) \tag{2}$$

where $T(\dot{\theta})$ is the output torque from the motor. From Eq. 1, natural frequency $\omega_n = \sqrt{K_f/(M+m)}$. Substituting $y = A\cos(\omega t - \phi)$ in Eq. (1) yields

$$\tan(\phi) = \frac{\omega R_f}{K_f - (M+m)\omega^2} \quad \text{and} \quad A = \frac{me\omega^2}{\sqrt{(\omega R_f)^2 + \left(K_f - (M+m)\omega^2\right)^2}} \tag{3}$$

where A is the vibration amplitude of the foundation and ϕ is a phase.

Bond graph modelling of the system

An existing model of three phase six pole induction motor is used here (5). According to Maxwell-Faraday equation

$$\nabla \times E_s = \left(-\frac{\partial B}{\partial t}\right) \text{ as seen from stator} \quad \nabla \times E_r = \left(-\frac{\partial B}{\partial t}\right) \text{ as seen from rotor} \tag{4}$$

where E_s and E_r are stator electric field and rotor electric field, respectively, B is the magnetic field, and Φ is the magnetic flux. For number of turns n_s, we get potential differences (5) across terminals as

$$\begin{aligned} V_{1s} &= -n_s\dot{\Phi}_{1s}, \quad V_{2s} = -n_s\left(\dot{\Phi}_{2s}\cos\frac{2\pi}{3} + \dot{\Phi}_{3s}\sin\frac{2\pi}{3}\right), \\ V_{3s} &= -n_s\left(\dot{\Phi}_{2s}\cos\frac{4\pi}{3} + \dot{\Phi}_{3s}\sin\frac{4\pi}{3}\right) \end{aligned} \tag{5}$$

Three phase voltage supply and delta connection sub-models which are used in the integrated model are shown in Figs. 2 and 3, respectively. Here, TF moduli $\mu_{d1} = \cos\omega t$, $\mu_{d2} = \cos(\omega t - 2\pi/3)$ and $\mu_{d3} = os(\omega t - 4\pi/3)$.

In Fig. 3, e/o and e/i are the output and input voltage ports. The integrated bond graph model of the squirrel cage induction motor attached with an unbalance rotor placed on a flexible foundation is shown Fig. 4 where i_α and i_β are the currents in

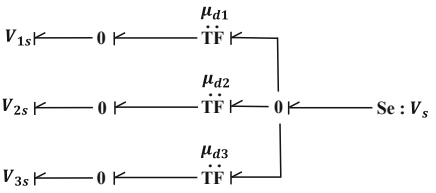

Fig. 2 The 3-phase supply sub-model

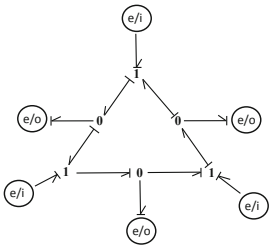

Fig. 3 Delta connection sub-model

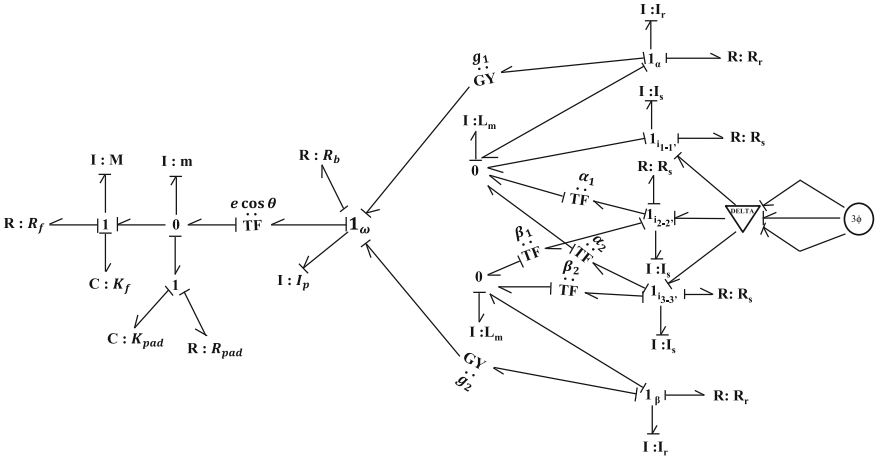

Fig. 4 Integrated bond graph model

the rotor in x and y directions, $i_{1-1'}$, $i_{2-2'}$ and $i_{3-3'}$ are the currents in the 3 different phases of stator side. The equivalent rotor inductance equivalent rotor resistance are reduced as $I_r = (n_s/n_r)^2 I_{r'}$ and $R_r = (n_s/n_r)^2 R_{r'}$ where $I_{r'}$ and $R_{r'}$ are actual rotor inductance and actual rotor resistance of the motor, respectively, and n_s and n_r are number of stator and rotor poles. In case of squirrel cage induction motors, $n_s = n_r$. Three phase voltage supply to two phase supply transformation is given as

$$\begin{bmatrix} i_{\alpha r} \\ i_{\beta r} \end{bmatrix} = \frac{\sqrt{2}}{\sqrt{3}} \begin{bmatrix} \cos 0 & \cos 2\pi/3 & \cos 4\pi/3 \\ \sin 0 & \sin 2\pi/3 & \sin 4\pi/3 \end{bmatrix} \begin{bmatrix} i_{s1} \\ i_{s2} \\ i_{s3} \end{bmatrix} \tag{6}$$

Thus, the values of transformer moduli used in bond graph model are $\alpha_1 = \sec 2\pi/3$, $\beta_1 = \csc 2\pi/3$, $\alpha_2 = \sec 4\pi/3$, $\beta_2 = \csc 4\pi/3$. Contribution of voltage from mutual inductance is modeled by GY elements. Moduli of Gyrators are given as $g_1 = L_m di_\beta/dt$ and $g_2 = L_m di_\alpha/dt$. More details of this model are available in (4, 5).

Simulation results

Using the data in Table 1, $\omega_n = 73.1$ rad/s. The variables used to plot the results are normalized transverse displacement of foundation $A^* = 2\omega_n^2 A/(\pi^2 g)$ and normalized shaft spin speed $\omega^* = \omega/\omega_n$, where g is the acceleration due to gravity. For supply voltage V_s = 53.3 V and frequency 60 Hz (377 rad/s), the rotor speed gets stuck at the resonance as shown in Fig. 5. The corresponding results for V_s = 53.4 V are shown in Fig. 6, where vibration amplitude reduces and rotor speed jumps to near synchronous speed (372 rad/s).

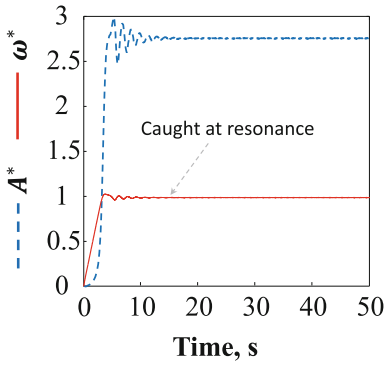

Fig. 5 Transient response during coasting up for V_s = 53.3 V

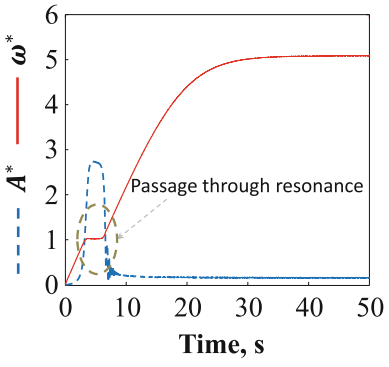

Fig. 6 Transient response during coasting up for V_s = 53.4 V

3 Speed Control of Induction Motor

Generally there are two types of speed control methods for induction motor. One is scalar control and the other is vector control method. Volts-per-hertz, commonly called V/f is the most popular method of IM control. It is widely used in industrial and domestic applications. In pure V/f approach, the voltage and frequency ratio is kept constant; the constant being specified according to motor rating in order to avoid coil burnout. Some transient simulations with V/f control of IM are shown in Figs. 7 and 8 with V/f constant chosen as 1 (f is in rad/s). In Fig. 7, the reference speed is 60 rad/s, supply voltage V_s = 60 V. The simulation results show that the motor speed reaches nearly the synchronous speed. Similar result is obtained when the reference speed is set to 80 rad/s (V_s = 80 V) and the steady speed reached is nearly the synchronous speed as shown in Fig. 8. Thus, the resonance is passed without the system being caught at it.

When the reference speed is kept just above the resonance speed, the response does not settle to any steady value. This happens due to Sommerfeld effect which excludes some speed zones from stable operation. Such cases for reference speed of 74 rad/s (resonance is at 71.3 rad/s) are shown in Figs. 9 and 10.

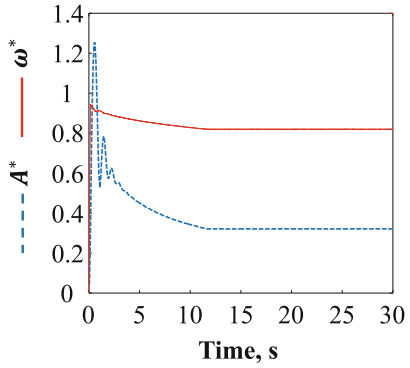

Fig. 7 Transient response during coasting up for reference speed of 60 rad/s

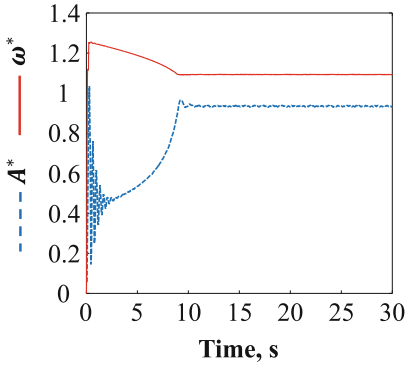

Fig. 8 Transient response during coasting up for reference speed of 80 rad/s

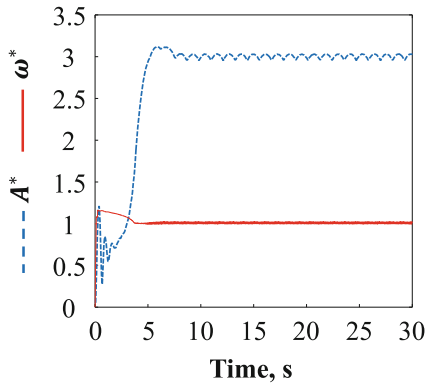

Fig. 9 Transient response during coasting up for reference speed of 74 rad/s

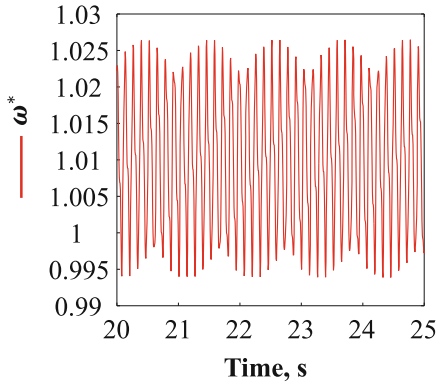

Fig. 10 A zoomed part of rotor speed response at reference speed of 74 rad/s

4 Conclusions

Many engineering applications require speed control of unbalanced rotors driven by induction motors. One example is a heavy-duty vibration generator where use of peizo-elements can be expensive. We show that passage through resonance can be a problem by simple voltage variation approach due to the existence of Sommerfeld effect. The v/f speed controller is shown to be able to regulate the rotor speed even in the regimes near the structural resonance.

References

1. Sommerfeld, A.: Beiträge Zum Dynamischen Ausbau Der Festigkeitslehe, Physikal Zeitschr **3**, 266 (1902)
2. Samantaray, A.K.: Steady-state dynamics of a non-ideal rotor with internal damping and gyroscopic effects. Int. J. Non-Linear Mech. **56**(4), 443 (2008)

3. Karthikeyan, M., Bisoi, A., Samantaray, A.K., Bhattacharyya, R.: Sommerfeld effect characterization in rotors with non-ideal drive from ideal drive response and power balance. Mech. Mach. Theory **91**, 269 (2015)
4. Mukherjee, A., Karmakar, R., Samantaray, A.K.: Bond graph in modeling, simulation and fault identification. CRC Press (2012)
5. Mukherjee, A., Karmakar, R., Samantaray, A.K.: Modelling of basic induction motors and source loading in rotor-motor systems with regenerative force field. Simul. Pract. Theor. **7**, 563 (1999)

Part III
Computational Mechanics

Various Strategies of Elastic Forces Evaluation in the Absolute Nodal Coordinate Formulation

R. Bulín and M. Hajžman

Abstract This paper deals with the description of the absolute nodal coordinate formulation (ANCF) which is suitable for the flexible bodies modelling considering large deformation. As it is shown for beam ANCF elements, this formulation leads to the nonlinear expression of elastic forces, which could be the main disadvantage of the ANCF. The evaluation of these forces can be done by numerical integration in each computational step or by analytical derivation with the help of a software for symbolic operations. The computational performance of various elastic forces evaluation strategies is investigated using a benchmark problem of falling flexible pendulum.

Keywords Absolute nodal coordinate formulation · Elastic forces · Benchmark · Flexible beam

1 Introduction

An absolute nodal coordinate formulation (ANCF) [3] is a suitable approach to the modelling of beams, cables, wires and fibers in the framework of robot, manipulator and mechanism design. The ANCF is based on the usage of global displacements and slopes as nodal coordinates. It belongs to the modern approaches of flexible multibody dynamics and allows to model flexible bodies performing a large motion including deformation.

Dynamical models employing ANCF are characterized by constant mass matrices and highly nonlinear stiffness matrices. Therefore the issue of the formulation of elastic forces is very important and it is the motivation for the work presented in this paper. There are several types of ANCF beam elements [2]. This

R. Bulín (✉) · M. Hajžman
University of West Bohemia, Pilsen, Czech Republic
e-mail: rbulin@kme.zcu.cz

M. Hajžman
e-mail: mhajzman@kme.zcu.cz

J. Beran et al. (eds.), *Advances in Mechanism Design II*,
Mechanisms and Machine Science 44, DOI 10.1007/978-3-319-44087-3_23

paper is focused on a lower order ANCF element, which can be used for modelling of thin cables, fibers and wires. This element respects bending and axial stiffness and can be also extended by adding torsional stiffness [4].

2 Absolute Nodal Coordinate Formulation

A spatial lower order ANCF element of length l with two nodes uses components of position vector $\mathbf{r}$ of nodes and its derivation with respect to local parameter $x \in \langle 0, l \rangle$ (slopes) as the nodal coordinates. This can be expressed as

$$\mathbf{e} = \left[\mathbf{r}^{(i)T}, \mathbf{r}_{,x}^{(i)T}, \mathbf{r}^{(j)T}, \mathbf{r}_{,x}^{(j)T}\right]^T, \tag{1}$$

where $\mathbf{e}$ is the vector of nodal coordinates, $\mathbf{r}^{(i)}$ is the position vector of node i and $\mathbf{r}_{,x}^{(i)} = \frac{\partial \mathbf{r}^{(i)}}{\partial x} = \boldsymbol{\tau}^{(i)}$ represents the slope at node i (note, that each element has node i and j). This implies that each element has 12 degrees of freedom, 6 at each node. Global position $\mathbf{r} = \left[r_x, r_y, r_z\right]^T$ of an arbitrary beam point determined by parameter x can be written as

$$\mathbf{r}(x) = \mathbf{S}(x)\mathbf{e}, \quad \mathbf{S}(x) = [s_1\mathbf{I}, s_2\mathbf{I}, s_3\mathbf{I}, s_4\mathbf{I}], \tag{2}$$

where $\mathbf{S}$ is the global shape function matrix of size 3×12, $\mathbf{I}$ is the identity matrix of size 3×3 and the shape functions can be derived in the form

$$\begin{aligned} s_1 &= 1 - 3\xi^2 + 2\xi^3, & s_2 &= l\left(\xi - 2\xi^2 + \xi^3\right), \\ s_3 &= 3\xi^2 - 2\xi^3, & s_4 &= l\left(-\xi^2 + \xi^3\right), \qquad \xi = x/l. \end{aligned} \tag{3}$$

It must be noted, that a cubic polynomials in x are employed to describe all three components of the displacement and the element can be considered as isoparametric.

Standard procedures (e.g. the Lagrange equations or the principle of virtual work) can be used in order to derive a mathematical model of the spatial ANCF element. Kinetic energy of the element with material density ρ is

$$E_k = \frac{1}{2}\int_0^l \rho A \dot{\mathbf{r}}^T \dot{\mathbf{r}} \mathrm{d}x = \frac{1}{2}\dot{\mathbf{e}}^T \int_0^l \rho A \mathbf{S}^T \mathbf{S} \mathrm{d}x \, \dot{\mathbf{e}} = \frac{1}{2}\dot{\mathbf{e}}^T \mathbf{M}_e \dot{\mathbf{e}}, \tag{4}$$

where $\mathbf{M}_e$ is the element mass matrix.

Strain energy E_p of the element is used for the derivation of elastic forces in the ANCF beam model and the form of an adopted elasticity model determines the complexity of the whole model. The most common approach employs the

separation of the strain energy of longitudinal deformation E_{pl} and the strain energy of transverse (bending) deformation E_{pt} as

$$E_p = E_{pl} + E_{pt} = \frac{1}{2}\int_0^l EA\varepsilon_x^2 \mathrm{d}x + \frac{1}{2}\int_0^l EI\kappa^2 \mathrm{d}x, \tag{5}$$

where E is the Young modulus, A is the area of the cross-section and I is the second moment of the area about a transverse axis. In this particular case, it is assumed that the second moments of the area for both transverse axes z and y are equal, so it is applied $I = I_{zz} = I_{yy}$. The axial strain ε_x and the curvature κ can be in general case expressed as [2]

$$\varepsilon_x = \frac{1}{2}\left(\mathbf{r}_{,x}^T\mathbf{r}_{,x} - 1\right) = \frac{1}{2}\left(f^2 - 1\right), \quad \kappa = \left|\frac{\mathrm{d}^2\mathbf{r}}{\mathrm{d}s^2}\right| = \frac{\left|\mathbf{r}_{,x} \times \mathbf{r}_{,xx}\right|}{\left|\mathbf{r}_{,x}\right|^3}, \tag{6}$$

where $f = \frac{\mathrm{d}s}{\mathrm{d}x}$ represents the deformation gradient for longitudinal strain and $\mathrm{d}s$ is the infinitesimal arc length. Note, that the axial strain is defined by Green strain tensor. The strain energy leads to nonlinear elastic forces that must be evaluated in each integration step.

3 Evaluation of Elastic Forces

Based on the general expression of axial strain (6), the vector of longitudinal elastic forces of the element e has the form

$$\begin{aligned}\mathbf{Q}_l^e &= \frac{\partial E_{pl}}{\partial \mathbf{e}} = EA\int_0^l \left(\frac{\partial \varepsilon_x}{\partial \mathbf{e}}\right)^T \varepsilon_x \mathrm{d}x \\ &= EA\int_0^l \left(\mathbf{S}_{,x}^T\mathbf{S}_{,x}\mathbf{e}\right)\left[\frac{1}{2}\left(\mathbf{e}^T\mathbf{S}_{,x}^T\mathbf{S}_{,x}\mathbf{e} - 1\right)\right]\mathrm{d}x = \mathbf{K}_l(\mathbf{e})\mathbf{e}.\end{aligned} \tag{7}$$

The integral in Eq. (7) can be derived analytically or by using some software for symbolic operations (MATLAB R2012a was used in this work). It can be shown that the resultant nonlinear longitudinal stiffness matrix is a full matrix and its elements are quadratic functions of the nodal coordinates. The evaluation of such a vector of elastic forces in each time step can be computationally demanding. That is why it is suitable to approximate the integral in (7) by using the Gaussian quadrature. As it is noted in [1], the matrix $\mathbf{K}_l(\mathbf{e})$ is not unique and another derivation of this matrix in case of planar ANCF beam is shown there. It is based on

the separation of vector of nodal coordinates $\mathbf{e}$ to sum of two vectors—arbitrary rigid-body displacement and flexible deformation. This approach leads to simpler form of matrix $\mathbf{K}_l(\mathbf{e})$ in case of planar elements and is referred to as L2 model.

The vector of transverse elastic forces of element e has the form

$$\mathbf{Q}_t^e = \frac{\partial E_{pt}}{\partial \mathbf{e}} = EI \int_0^l \left(\frac{\partial \kappa}{\partial \mathbf{e}}\right)^T \kappa \, \mathrm{d}x. \tag{8}$$

Since the general expression of curvature κ in Eq. (6) is of a complex form, the integral in Eq. (8) is difficult to solve even with the help of the software for symbolic operations. But, as it is mentioned in [2], the derivation of curvature $\frac{\partial \kappa}{\partial \mathbf{e}}$ can be obtained in closed form. The vector of transverse elastic forces can be then evaluated using Gaussian quadrature with the use of several precomputed terms. As it is described in [1], significant simplification can be achieved when the longitudinal deformation within the element is assumed constant while developing the vector of transverse elastic forces. Then, the deformation gradient $f = \frac{\mathrm{d}s}{\mathrm{d}x}$ has a constant value $\bar{f}$ and the curvature can be simplified as

$$\kappa = \left|\frac{\mathrm{d}^2\mathbf{r}}{\mathrm{d}s^2}\right| = \left|\frac{\mathrm{d}^2\mathbf{r}}{\mathrm{d}x^2} \cdot \frac{\mathrm{d}^2x}{\mathrm{d}s^2}\right| = \frac{1}{\bar{f}^2}\mathbf{r}_{,xx} = \frac{1}{\bar{f}^2}\mathbf{S}_{,xx}\mathbf{e}. \tag{6}$$

This approach is referred to as T2 model and it is recommended to use sufficient number of elements to meet the mentioned assumption.

4 Benchmark Problem of a Flexible Pendulum

An in-house software for the numerical simulation of chosen mechanical systems with flexible beams modelled by spatial lower order ANCF beam elements was created in MATLAB. A falling flexible pendulum as a standard benchmark example for the testing of the created code was implemented and several simulation results are described in this section. The scheme of the pendulum is in Fig. 1 and its parameters are $l = 2$ m, $\rho = 4000$ kg m^3, $a = 0.01$ m, $E = 10^8$ Pa, $g = 9.81$ m s^{-2}. The simulation time is 2 s. The equations of motion were solved using *ode23t* function in MATLAB with implicit error settings. The numerical solution was performed using HP Compaq Elite 8300 with Intel Core i5-3570 CPU and 16 GB RAM.

Three strategies of the elastic forces evaluation were tested. First model denoted as GL-T uses Gaussian quadrature to evaluate both longitudinal and transverse elastic forces (L is the number of Gaussian points used for determination of $\mathbf{Q}_l^e$ and T is the number of points for $\mathbf{Q}_t^e$). Second model denoted as ST2 uses symbolically determined longitudinal elastic forces and T2 model [1] for transverse forces. The

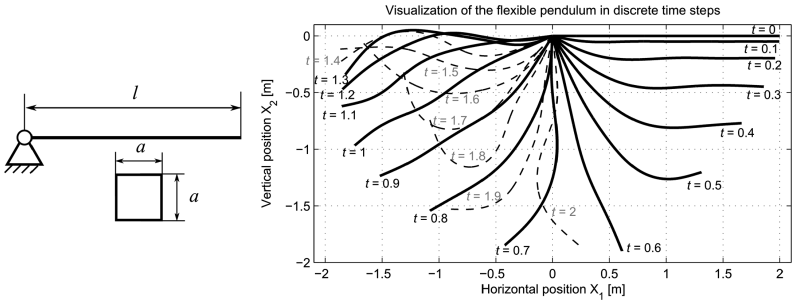

Fig. 1 The scheme of the flexible pendulum with its cross-section and the visualization of the pendulum in discrete time steps

last model is denoted as L2T2 and the strategy of evaluation of the elastic forces is evident from the name of the model and corresponds with [1].

The visualization of the flexible pendulum obtained from solution of the G10-10 model is shown in Fig. 1. The computational times for each model and maximum difference over time from G10-10 model are summarized in Table 1. It is obvious, that results from G2-2 model are rather different, because it uses only two Gaussian points to approximate cubic terms in general. Other differences between models are rather small. It seems reasonable to use more Gaussian points for longitudinal force approximation (5 points), because their evaluation is relatively fast. The vertical displacement of the pendulum tip for selected models and the difference of vertical displacement of the tip is shown in Fig. 2.

Table 1 The summary of computational demands for various approaches to elastic forces

Model	Number of elements	Computational time (s)	Computational time for longitudinal forces (s)	Computational time for transverse forces (s)	Maximum difference from G10-10 model (m)
G2-2	10	107.5	14.6	60.5	3.36×10^{-1}
G3-3	10	185.7	26.3	116.1	4.16×10^{-3}
G4-4	10	233.4	33.8	154.1	1.84×10^{-4}
G5-5	10	285.2	42.2	192.9	3.29×10^{-5}
G10-10	10	492.5	76.5	367.2	Reference model
ST2	10	355.0	261.1	48.1	1.02×10^{-4}
L2T2	10	109.8	14.8	50.3	1.02×10^{-2}
L2T2	20	481.4	67.5	233.4	7.72×10^{-3}

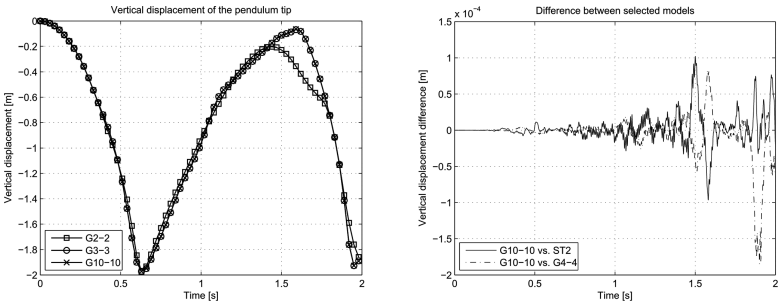

Fig. 2 The vertical displacement of the pendulum tip for selected models and the difference of vertical displacement of the tip for selected models

5 Conclusions

In this paper, the ANCF beam element suitable for problems of flexible multibody dynamics was described and various strategies of evaluation of the elastic forces were shown. According to resultant computational times of various models it is recommended to use five Gaussian points to approximate longitudinal elastic forces and at least three points for transverse forces. Another option for transverse force evaluation is to use T2 model [1]. The symbolical evaluation of longitudinal forces leads to full stiffness matrix, whose evaluation is relatively slow.

Acknowledgments The first author was supported by the project LO1506 of the Czech Ministry of Education, Youth and Sports and the second author was supported by the project 15-20134S of the Czech Science Foundation.

References

1. Berzeri, M., Shabana, A.A.: Development of simple models for the elastic force in the absolute nodal co-ordinate formulation. J. Sound Vib. **235**, 539–565 (2000)
2. Gerstmayr, J., Shabana, A.A.: Analysis of thin beams and cables using absolute nodal co-ordinate formulation. Nonlinear Dyn. **45**, 109–130 (2006)
3. Shabana, A.A.: Dynamics of Multibody Systems, 3rd edn. Cambridge UP (2005)
4. Yoo, W.-S., Dmitrochenko, O., Park, S.-J., Lim, O.-K.: A new thin spatial beam element using the absolute nodal coordinates: application to a rotating strip. Mech. Based Des. Struct. Mach. **33**, 339–422 (2005)

Nonlinear Vibration of Nuclear Fuel Rods

Š. Dyk and V. Zeman

Abstract From mechanical point of view, nuclear fuel rod (FR) is a complex system consisting of two subsystems—fuel rod cladding (thin walled zirconium tube) and a fuel pellets stack placed inside the cladding placed with a small radial clearance. Both subsystems are beam-type continua that possibly impact-interact during the vibration caused by fuel assembly support plates motion. The FR is supported at eight levels by prestressed spacer grid cells. The paper focuses on complex mathematical modelling of such a system including all the nonlinearities given by possible impacts between cladding and fuel pellets stack and possible loose of contact between cladding and spacer grid cells due to low prestress. In all the contact points, friction-vibration interactions respect three possible phases—stick, slip and separation—depending on the slip velocity and normal contact force. The model is used for estimation of a fretting wear of the cladding in contact with spacer grids.

Keywords Nuclear fuel rods · Nonlinear vibration · Impact · Friction forces · Wear

1 Introduction and Model Description

A fuel rod (FR) is a key part of nuclear fuel assembly as it is the component where the nuclear reaction occurs. Basically, there are two types of FAs—hexagonal and square-type, where the type refers to shape of FA's cross section. The paper deals with modelling of hexagonal-type FAs (see Fig. 1) that consists of 312 FRs, 18 guide thimbles, one centre tube and six angle-pieces that stiffen the FA's construction. At eight levels, regularly placed on the axis of the FA, there are spacer

Š. Dyk (✉) · V. Zeman
NTIS, University of West Bohemia, Pilsen, Czech Republic
e-mail: sdyk@ntis.zcu.cz

V. Zeman
e-mail: zemanv@kme.zcu.cz

J. Beran et al. (eds.), *Advances in Mechanism Design II*,
Mechanisms and Machine Science 44, DOI 10.1007/978-3-319-44087-3_24

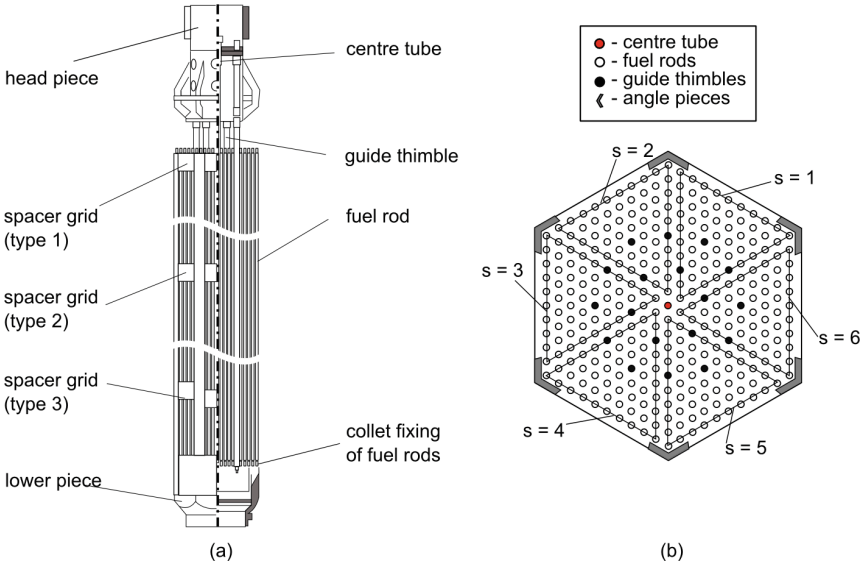

Fig. 1 A hexagonal-type fuel assembly—side view (**a**) and cross-section (**b**)

grids (SGs) that fix all the components in hexagonal cross section. Whole FA is submerged into coolant liquid (in case of VVER reactors, there is water as a coolant). In VVER-1000 reactors, there are 163 FAs in a reactor core that are fixed in lower and upper mounting plates. Due to pressure pulsations of coolant, the mounting plates are excited and their motion can be computed using global reactor model [1]. A SGs motion is investigated using linearized model of the chosen FA [2]. Obtained kinematical excitation is used in a detailed nonlinear model of one chosen FR.

A fretting wear of Zr FR cladding has been analysed in [3], but the modelling of FR vibration did not include friction forces in contact points whose effect was approximated by proportional damping. Friction forces can significantly influence results of numerical simulation. In the model described in this paper, friction and impact forces are fully considered.

A mechanical scheme of a nuclear fuel rod is shown in the Fig. 2. It consists of a FR cladding (C) in the form of long thin-walled Zr tube and fuel pellets stack (P) placed inside the C. The subsystem P is axially coupled with the C by hold-down fixation spring. Between both subsystems, there is a little radial clearance δ, that is considered to be constant through whole length of the FR. Both subsystems C and P are fixed at the bottom-end to the lower piece that is fixed in the moving lower FA support plate. At eight levels g, the cladding is supported by three spacer grid cells as shown in the Fig. 2.

Both subsystems are modelled using finite element method (FEM) for Euler-Bernoulli type one-dimensional continua. In each discrete node, all the six degrees of freedom are respected (axial displacement and two lateral displacements,

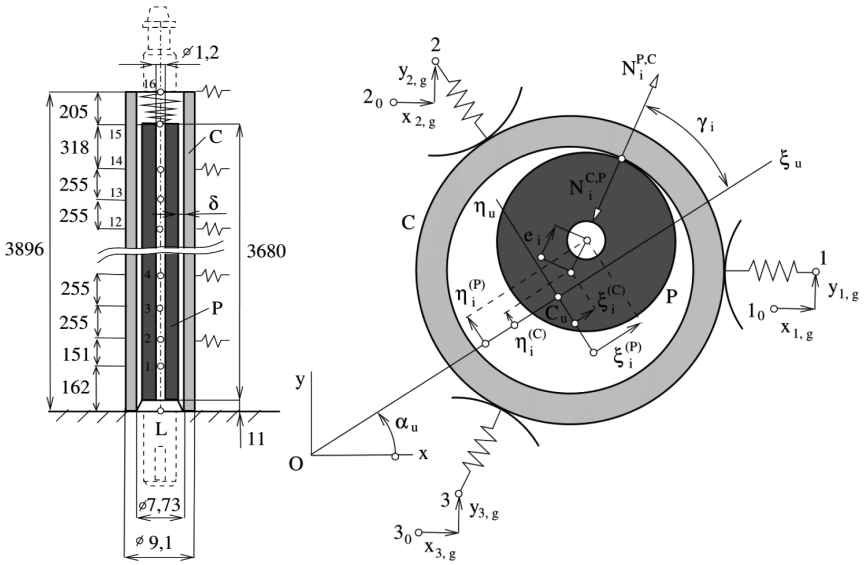

Fig. 2 Schematic mechanical model of the FR in side-view and a cross-section of the FR at the level of spacer grid *g*

torsional rotational angle and flexural bending angles). The mathematical model of the system including all above mentioned nonlinearities can be written in the form of set of second order ordinary differential equations

$$\begin{aligned}
&\begin{bmatrix} \mathbf{M}_F^{(C)} & 0 \\ 0 & \mathbf{M}_F^{(P)} \end{bmatrix} \begin{bmatrix} \ddot{\mathbf{q}}_F^{(C)} \\ \ddot{\mathbf{q}}_F^{(P)} \end{bmatrix} + \begin{bmatrix} \mathbf{B}_F^{(C)} & 0 \\ 0 & \mathbf{B}_F^{(P)} \end{bmatrix} \begin{bmatrix} \dot{\mathbf{q}}_F^{(C)} \\ \dot{\mathbf{q}}_F^{(P)} \end{bmatrix} \\
&+ \left(\begin{bmatrix} \mathbf{K}_F^{(C)} & 0 \\ 0 & \mathbf{K}_F^{(P)} \end{bmatrix} \begin{bmatrix} \mathbf{q}_F^{(C)} \\ \mathbf{q}_F^{(P)} \end{bmatrix} + \mathbf{K}_{fix} \right) = \begin{bmatrix} \mathbf{f}_L^{(C)}(t) \\ \mathbf{f}_L^{(P)}(t) \end{bmatrix} + \begin{bmatrix} \mathbf{f}_{SG}\left(\mathbf{q}_F^{(C)}, \dot{\mathbf{q}}_F^{(C)}, t \right) \\ 0 \end{bmatrix} \\
&+ \begin{bmatrix} \mathbf{f}_{P,C}\left(\mathbf{q}_F^{(C)}, \dot{\mathbf{q}}_F^{(C)}, \mathbf{q}_F^{(P)}, \dot{\mathbf{q}}_F^{(P)} \right) \\ \mathbf{f}_{C,P}\left(\mathbf{q}_F^{(C)}, \dot{\mathbf{q}}_F^{(C)}, \mathbf{q}_F^{(P)}, \dot{\mathbf{q}}_F^{(P)} \right) \end{bmatrix},
\end{aligned} \tag{1}$$

where $\mathbf{q}_F^{(X)}, X = C, P$ are vectors of generalized coordinates of the free nodes $i = 1, 2, \ldots 16$, see Fig. 2, matrices $\mathbf{M}_F^{(X)}, \mathbf{B}_F^{(X)}, \mathbf{K}_F^{(X)}, X = C, P$, are mass, damping and stiffness matrices, respectively, of both subsystems and $\mathbf{K}_{fix}$ is stiffness matrix of fixation spring. At the right hand side of (1), there are vectors $\mathbf{f}_L^{(X)}(t), X = C, P$ of kinematical excitation by motion of the lower node L, and vector $\mathbf{f}_{SG}\left(\mathbf{q}_F^{(C)}, \dot{\mathbf{q}}_F^{(C)}, t \right)$ express forces caused by all the SGs. Last vector in (1) is vector of impact forces between subsystems P and C. The latter two vectors include both generalized displacements and generalized velocities of the subsystems which expresses

nonlinear character of the contact forces. The model (1) can be formally rewritten into standard matrix form

$$\mathbf{M}\ddot{\mathbf{q}}(t) + \mathbf{B}\mathbf{q}(t) + \mathbf{K}\mathbf{q}(t) = \mathbf{f}(\mathbf{q}(t), \dot{\mathbf{q}}(t), t), \tag{2}$$

that can be solved numerically after transformation to the form of the set of double number of first order equations.

2 Application and Results

The computational model of the system was implemented in MATLAB software. To describe a qualitative and quantitative changes in fuel rod vibration during an operational cycle, five states were determined, see Table 1. The initial state (I) is characterized by maximal radial clearance, maximal prestress of SG cells and minimal force of fixation spring. During the operational-cycle, the fuel pellets swell and thus the radial clearance is getting smaller and at the end (state V), there is a zero clearance. Due to swell effect, the fixation spring force is getting larger as the prestress grows. The prestress of SG cells is getting smaller due to wear in contact points. Between these two states, the parameters are considered to change linearly, see Table 1.

The fretting wear of the fuel rod cladding in the cell $j = 1, 2, 3$ and at the level of the spacer grid $g = 1, 2, \ldots 8$ can be estimated in the form [3]

$$\Delta m_{j,g} = \mu \frac{f(\omega)}{f_0} W_{j,g} \tag{3}$$

where μ is loss of FR cladding mass in one contact surface generated by the work of friction force 1 J at the excitation frequency ω,$f(\omega)$ is experimentally obtained friction coefficient at the same frequency [4], f_0 is calculated friction coefficient and $W_{j,g}$ is the work of friction forces.

Figure 3 shows the fretting wear per a steady state part of simulation domain (0,3 s) and its evolution during an operational cycle of the reactor. The work of friction forces in (3) is obtained using nonlinear response of the system described by (1).

Table 1 Combination of system parameters considered for different states during reactor operational cycle

State number	Radial clearance between C and P (μm)	Prestress of SG cells (N)	Fixation spring hold-down force (N)
I	65	20	5
II	48.75	16.25	6.25
III	32.5	12.5	7.5
IV	16.5	8.75	8.75
V	0	5	10

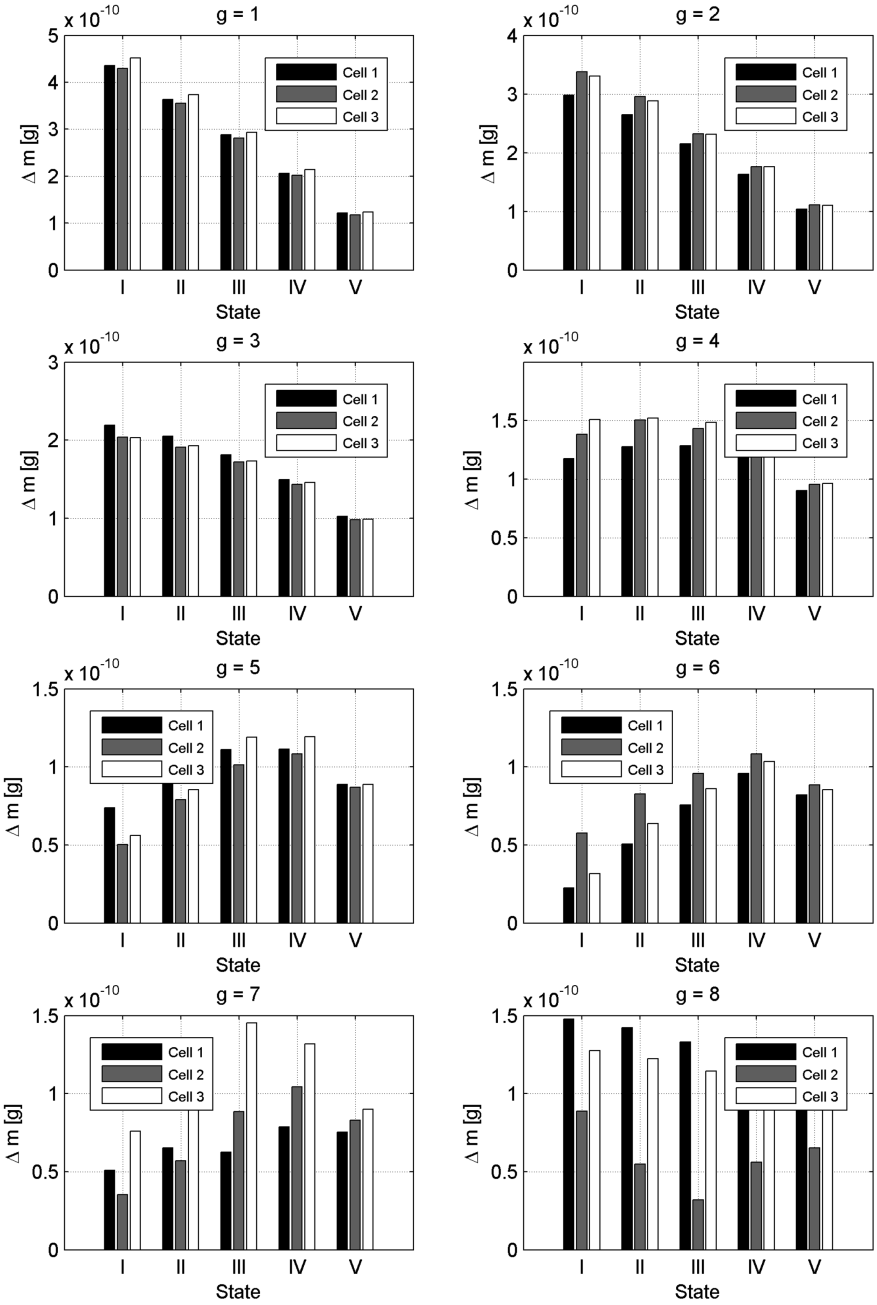

Fig. 3 Fretting wear per the simulation time at all the SG levels and in all the contact points

3 Conclusions

The contribution describes mathematical model of fuel rod in hexagonal-type fuel assembly that respects all the mechanical nonlinearities; impact and friction forces between fuel pellets stack and fuel rod cladding and between fuel rod cladding and spacer grid cells. Numerical simulation in time domain was performed to estimate the fretting wear of Zr cladding and its wall thickness that is very important for judgement of fuel operational-life left. The analysis shows the evolution of the wear during an operational cycle of the reactor based on estimated evolution of mechanical parameters such as a clearance between P and C, fixation spring force and prestress of spacer grid cells.

Acknowledgments This publication was supported by the project LO1506 of the Czech Ministry of Education, Youth and Sports.

References

1. Hlaváč, Z., Zeman, V.: Vibration of Nuclear Fuel Assemblies: Modelling, Methods, Application. LAP Lambert Academic Publishing, Saarbruecken (2013)
2. Zeman, V., Hlaváč, Z.: Dynamic response of nuclear fuel assembly excited by pressure pulsations. Appl. Comput. Mech. **6**, 212–230 (2012)
3. Zeman, V., Dyk, Š., Hlaváč, Z.: Mathematical modelling of nonlinear vibration and fretting wear of the nuclear fuel rods. Arch. Appl. Mech. **86**, 657–668 (2016)
4. Pečínka, L., Svoboda, J., Zeman, V.: Fretting wear of the Zr fuel rod cladding. In: Proceedings of the 2014 22nd International Conference of Nuclear Engineering ICONE22 (2014)

Thermal Field Simulation of Repair Threads in a Hole in the Cover of a Pressure Vessel by Welding Using Sysweld

R. Jančo and P. Élesztős

Abstract This paper deals with the analysis of residual strain and stress after welding. It was done using the SYSWELD software, which is based on the finite element methods. The welding solution has been divided into two phases. In our simulation we have used the Goldak model for a heat source. After the correct allocation of all inputs the process can be initiated. The results of this phase of the solution are the distribution of the thermal fields and the percentages of the separate metallurgical phases. The results of these solutions are presented in this paper.

Keywords Welding · Goldak model · Finite element method · SYSWELD

1 Introduction

The use of numerical, mainly finite elements and experimental approaches to characterize weld residual stresses is fairly widespread, but limitations to these methods are not fully known and they need to be recognized. However, when the two approaches are combined, and the results corroborate each other sufficiently well, the resulting residual stress distribution can be confidently used for assessment.

The use of numerical techniques to simulate the welding process is not new and the increase in computing power has seen the size and complexity of the models increase.

Simulation of the welding process, considering the moving electrode, is actually a three-dimensional problem requiring a lot of computer time and effort. Alternative

R. Jančo (✉) · P. Élesztős
Faculty of Mechanical Engineering, Institute of Applied Mechanics and Mechatronics, Slovak University of Technology in Bratislava, Nám. Slobody 17, 812 31 Bratislava, Slovak Republic
e-mail: roland.janco@stuba.sk

P. Élesztős
e-mail: pavel.elesztos@stuba.sk

J. Beran et al. (eds.), *Advances in Mechanism Design II*,
Mechanisms and Machine Science 44, DOI 10.1007/978-3-319-44087-3_25

two-dimensional, quasi-steady state models based on simple transformations are widely used instead of the three-dimensional unsteady welding process. The two-dimensional problem involves the analysis of the thermal and stress distributions in the normal plane to the weld direction in the case of thick plate components and on the surface for thin plate configurations. The accuracy of the two-dimensional cross-sectional model increases as the weld speed increases, which corresponds to simulating the condition of a negligible temperature gradient in the direction of the weld [1, 2].

An algorithm for the analysis of non-linear heat transfer was presented by Bathe and Khosgoftaar [3] with an iterative solution procedure for time integration for a general three-dimensional configuration. This has been used by researchers for obtaining transient temperature distributions during a welding process by modeling heat input due to a weld torch as an internal heat generation or as a surface boundary condition. Goldak [4] demonstrated the application of elliptical power density distribution of heat flux input with reference to two-dimensional in-plane, cross-sectional and three-dimensional geometric configurations. This concept of weld heat input has been used by many researchers [5, 6].

This paper describes a finite element analysis of the repair threads in a hole in the cover of a pressure vessel by welding using the commercial finite element packages SYSWELD [7]. The geometry of the symmetry part of the cover of pressure vessels has been modeled in 3D. The heat source is defined by the Goldak model [2]. Some results from this analysis are presented in this paper

2 Heat Transfer Analysis

The use of analytical, mainly finite elements and experimental approaches to characterize weld residual stresses is fairly widespread, but limitations to these methods are not fully known and they need to be recognized. However, when the two approaches are combined, and the results corroborate each other sufficiently well, the resulting residual stress distribution can be confidently used for assessment. To determine the thermal field during the welding process, two different analyses are required, namely heat conduction and phase transformation analyses. The most significant factors affecting both analyses are the heat input rate, the moving speed of the heat source and the thickness of the base material.

The fundamental behavior of heat conduction is that a flux [8]. Q'' (W/m^2), of energy flows from a hot region to cooler regions, linearly dependent on the temperature gradient, ∇T:

$$Q'' = k\nabla T \tag{1}$$

where k is the thermal conductivity of the material. The energy required to change the temperature of the material is defined by specific heat c or enthalpy H. The conservation of energy is expressed in differential form having the terms for specific

heat, thermal flux and a distributed volume heat-source term $Q'''(W/m^3)$ and it is given as

$$\rho c\dot{T} - \nabla(k\nabla T) - Q'' = 0 \tag{2}$$

where $\dot{T} = \partial T/\partial t$ with t being the time parameter and ρ the density of the materials.

3 Finite Element Analysis and Model

In the FEM analysis, the boundary conditions are applied to the model by specifying the value of the heat transfer coefficient and the surrounding temperatures at the elements and nodes, respectively, of the "skin elements" by creating a mesh at the boundaries of the domain studies.

When applied to the heat Eq. (2), the finite element method involves the solution of a system of differential equations [8]:

$$C\dot{T} + KT = Q \tag{3}$$

The above Eq. (3) can be written as

$$R = Q - C\dot{T} - KT = 0 \tag{4}$$

where R is a vector containing all the residual nodal forces (temperature). For non-linear analysis, Eq. (4) is to be solved by an iterative method at each time step. T is the nodal temperature vector, $\dot{T}$ is the time derivative of the temperature, C is the specific heat matrix, K is the conductivity matrix and Q is the vector of nodal power equivalent to an internal heat source and boundary conditions.

A 3D model for transient analysis is shown in Fig. 1. This model contained 120356 linear elements.

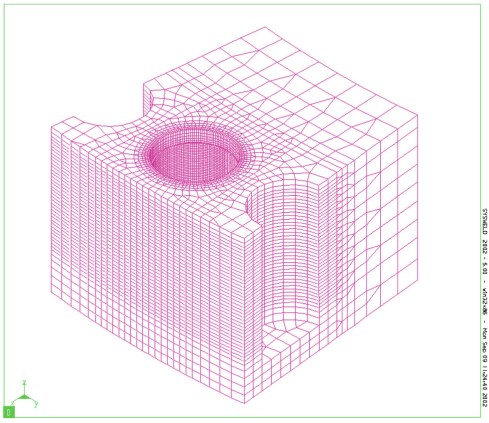

Fig. 1 3D model for finite element analysis

3.1 Material Properties

The temperature dependent value of thermal conductivity, specified heat capacity, thermal expansion coefficient and Young's modulus can be found in Table 1. Density was assumed to be 7700 kg m^{-3} and Poisson's ratio to be 0.3, both independent of temperature. Other material properties are in [9].

3.2 Heat Source Model

In this model the heat source distribution is comprised of two different ellipses in Fig. 2, i.e. one is in the front quadrant of the heat source and the other is in the rear quadrant. The power densities of the double-ellipsoidal heat source, q_f (x, y, z) and

Table 1 Thermo-mechanical properties

Temp (°C)	Weld	Parent	Weld	Parent	Weld	Parent
	Specific heat (kJ/kg/°C)		Coefficient of thermal expansion $\times 10^6$ (1/K)		Young's modulus (GPa)	
20	0.460	0.428	14.0	14.6	171	195
100	0.468	0.468	15.0	15.4	165	191
300	0.486	0.559	16.3	16.9	150	179
500	0.503	0.690	18.2	17.8	135	164
900	0.540	0.650	23.6	19.0	97	116
1000	0.547	0.670	24.7	19.3	83	100
1400	0.593	0.670	29.5	20.2	1.7	2.0
1500	0.593	0.670	30.9	20.4	1.5	1.8

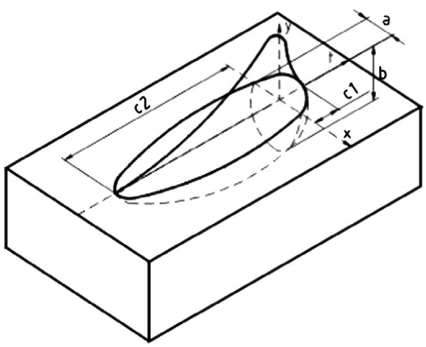

Fig. 2 Goldak model of heat source

q_r (x, y, z) describe the Goldak heat flux distribution inside the front and rear quadrant of the heat source and can be expressed as [2]:

$$q_f(x,y,z) = \frac{6\sqrt{3}\,f_f Q}{abc_f\pi\sqrt{\pi}} e^{-\frac{3x^2}{a^2}} e^{-\frac{3y^2}{b^2}} e^{-\frac{3(z-v(\tau-t))^2}{c_f^2}} \tag{5}$$

$$q_r(x,y,z) = \frac{6\sqrt{3}\,f_r Q}{abc_r\pi\sqrt{\pi}} e^{-\frac{3x^2}{a^2}} e^{-\frac{3y^2}{b^2}} e^{-\frac{3(z-v(\tau-t))^2}{c_r^2}} \tag{6}$$

where Q is the energy input rate, f_f and f_r are the fractional factor of the heat deposit in the front and rear quadrant, a, b, c_f and c_r are heat source parameters, v is welding rate and τ is total time of welding. Parameters of heat source are in [9].

4 Results

In the numerical simulation the Goldak heat source moves along the helical with 91 screw-threads. Total time of transient thermal and mechanical analysis for one-layer welding is 21160 s. Results from thermal analysis are the thermal fields in Figs. 3 and 4, and phase distributions in Figs. 6, 7 and 8. In Fig. 5 the temperature change is along the depth of the neighbor hole and a selected point in the outside surface of numerical model (top and lateral surface).

In Fig. 8 the result for mechanical analysis with consideration of thermal field and metallurgical phase fractions from thermal analysis is presented. In the mechanical solution the isotropic hardening model for plastic deformations was considered.

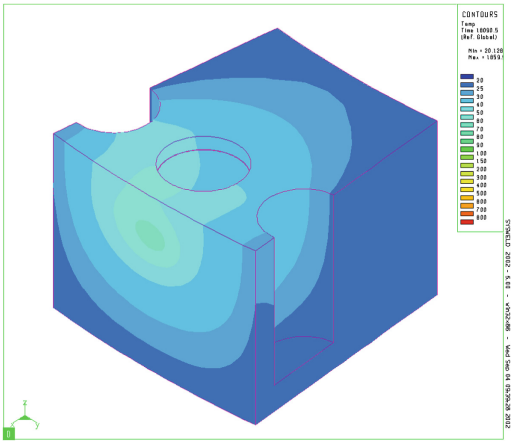

Fig. 3 Temperature field in time 16090 s of welding

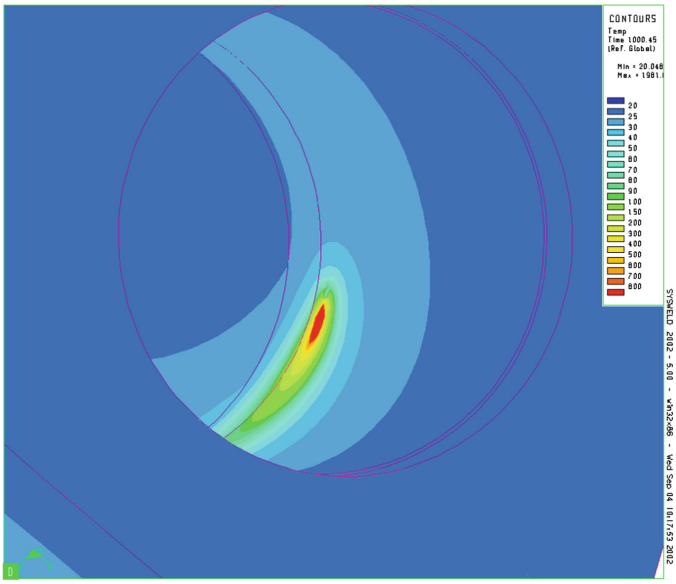

Fig. 4 Temperature field in time 1000 s of welding

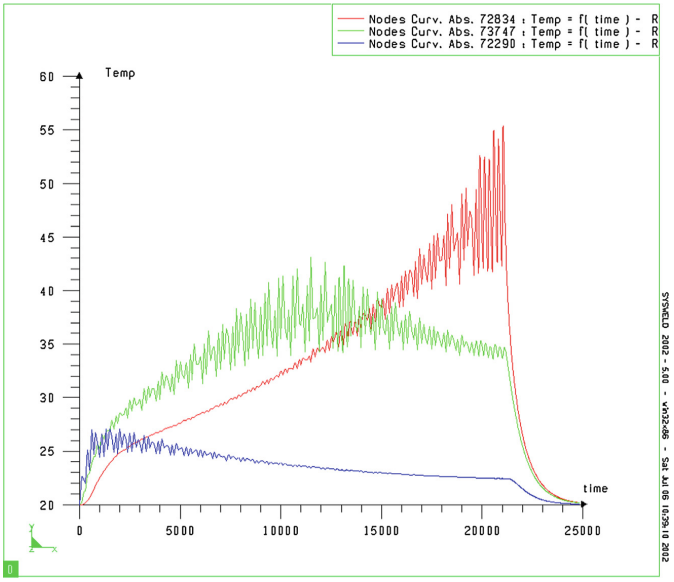

Fig. 5 Change of temperature along the length of the repair hole with cooling phase of solution

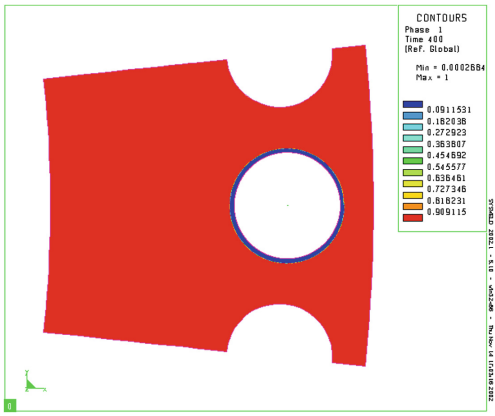

Fig. 6 Distribution of sorbite phase after welding of first layer

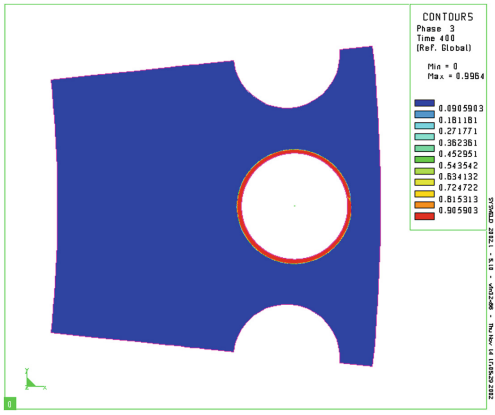

Fig. 7 Distribution of tempered martensite phase after welding of first layer

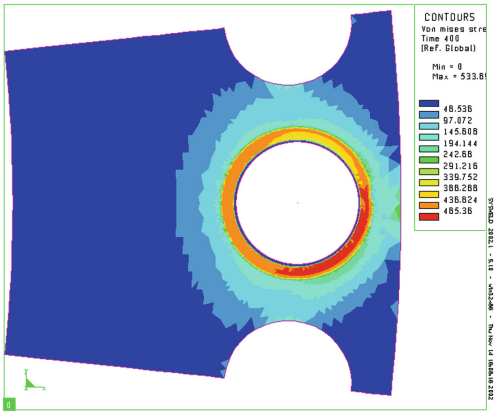

Fig. 8 Von Mises stress after welding of first layer

5 Conclusions

Parameters of the Goldak model of heat source were determined from experimental measurements in selected points using thermocouples. Good agreement was obtained between the measurement and numerically calculated value in thermal and mechanical results. In this paper one of the methods of repair is presented for a hole with an incorrect screw-thread by using welding. After creating welding layers in the repair hole in the cover of pressure vessels we cut a new screw-thread. An isotropic hardening model was used for the solution of mechanical stress, which leads to an over-conservative estimate of stress.

Acknowledgments The publication is the result of the project implementation: Research of friction stir welding (FSW) application as an alternative to melting welding methods no. 26240220031 supported by the Research & Development Operational Programme funded by the ERDF. The paper was supported by a grant from Grant Agency of VEGA no. 1/0740/16.

References

1. Argyris, J.H., Szimmat, J., Willam, K.J.: Computational aspects of welding stress analysis. Comp. Meth. Appl. Mech. Engng **33**, 635–666 (1982)
2. Goldak, J., Chakravarti, A., Bibby, M.A.: A new finite element model for welding heat sources. Metall. Trans. **15B**, 299–305 (1984)
3. Bathe, K.J., Khoshgoftaar, M.R.: Finite element formulation and solution of non-linear heat transfer. Nucl. Engng Des. **51**, 389–401 (1979)
4. Goldak, J., Bibby, M., Moore, J., House, R., Patel, B.: Computational modeling of heat flow in welds. Metall. Trans. **17B**, 587–600 (1984)
5. Leung, C.K., Pick, R.F., Mok, D.H.B.: Finite element modeling of a single pass but well. Weld. Res. Coun. Bull. **256**, 1–10 (1990)
6. Sonti, N., Amateau, M.F.: Finite element modeling of heat flow in deep penetration laser weld in aluminium alloys. Numer. Heat Transf. Part A **16**, 351–370 (1989)
7. SYSWELD v2004. ESI Group
8. Frewin, M.R., Scott, D.A.: Finite element model of pulsed laser welding., Weld J. **78**, 15–22 (1999)
9. Voštiar, V., Jančo, R., Élesztös, P.: Numerical simulation of repair of coil nest by welding, In: Proceedings 7th International scientific conference on Mechanical Engineering 2013, ISBN 80-227-1960-9, Bratislava (2003)

Simulation of Isothermal Compression Test

I. Matoušek and O. Matúšek

Abstract Paper deals with an issue of computer simulation of glass pressing. Attention is paid to accuracy of numerical outputs. Simple forming process—isothermal compression of a glass cylinder is chosen for virtual modelling. The constitutive behaviour of shaped glass is assumed to be nonlinear viscoelastic, based on general Maxwell model. Both viscoelastic response and relaxation behaviour of samples made of lead crystal are evaluated. Computer outputs are verified with experimental measurements in the viscosity range of 10^7–10^{10} Pa s. In this paper results at temperature 611 °C (corresponding viscosity $10^{7.4}$ Pa s) and 587 °C (viscosity 10^8 Pa s) are presented. Uniaxial deformation was carried out at various constant pressing rates (in the interval 0.1–8 mm s^{-1}).

Keywords Glass melt · Isotropic compression method · FEM · Viscoelastic material model

1 Introduction

Virtual modelling of technological processes has been already regarded as a powerful tool for research and development. Its application in pre-manufacture stage allows reducing physical testing, the rate of rejects and material waste as well as accelerating cost-effective product development. Fundamental problem of virtual modelling of glass forming processes is accuracy of numerical outputs.

Critical factor is not only a definition of boundary conditions (heat transfer on the outside of formed glass melt, etc.) but also a specification of material properties of glass melt to be formed. Though glass melt is a viscoelastic material in the whole range of the forming, in the range of temperatures above transition interval the

I. Matoušek (✉) · O. Matúšek
Technical University of Liberec, Liberec, Czech Republic
e-mail: ivo.matousek@tul.cz

O. Matúšek
e-mail: ondrej.matusek@tul.cz

J. Beran et al. (eds.), *Advances in Mechanism Design II*,
Mechanisms and Machine Science 44, DOI 10.1007/978-3-319-44087-3_26

elastic part of deformation is supposed to be almost negligible—and therefore glass is usually allowed to be generally incompressible Non Newtonian fluid.

To get more realistic outputs of virtual modelling the non-linear viscoelastic model of a general Maxwell type is used for description of constitutive glass melt behaviour.

2 Experimental Equipment

For the investigation of viscoelastic behaviour of glass melt (in the temperature range corresponding to the viscosity of 10^7–10^{10} Pa s) the simplest practically relevant process: uniaxial isothermal compression method was used. The principle of this method is simple. The glass sample is compressed in defined manner by working piston and its force response dependence on constant piston velocity and temperature is measured.

The measurement was realised on a benchtop tensile tester LLOYD 50 LR [1] with a maximum piston load 50 kN and maximum piston speed 8 mm s^{-1}. To get reliable outputs strictly isothermal conditions had to be ensured during the experiment. Therefore forming tools and glass samples were heated up in a cylindrical laboratory furnace. That is an integral part of a laboratory pressing apparatus. Temperature of pressing plates and glass samples was held constant by an electronic temperature controller. Actual temperature was monitored by thermocouples (type K—chromel-alumel), two of them were soldered into the working surfaces of pistons and third one was located close to the free cylindrical surface of the glass sample. To avoid sticking of the glass melt 0.24 mm thick mica foils were put in between the glass and working surfaces.

3 Experimental Results

As a result of experimental measurements the set of curves describing viscoelastic response of glass samples to applied loading was obtained (measurements were realised in the viscosity range of 10^7–10^{10} Pa s) [2]. In Fig. 1a viscoelastic response of glass sample (diameter D = 20 mm, height h = 20 mm) made of lead crystal (24 % PbO) to the constant piston speed (from the interval of 0.1–8 mm s^{-1}) at temperature 611 °C (corresponding to the viscosity $10^{7.4}$ Pa s) is shown (an independent variable is true, respectively real compression, i.e. displacement after its correction on system deformation [3]). Experimentally determined viscous-elastic response of glass allows direct evaluation of some technological and material characteristics, such as true strain rates (Fig. 1c), or instantaneous values of the elastic moduli (Fig. 1b). Instantaneous Young elastic modulus E(t) was evaluated by means of equation:

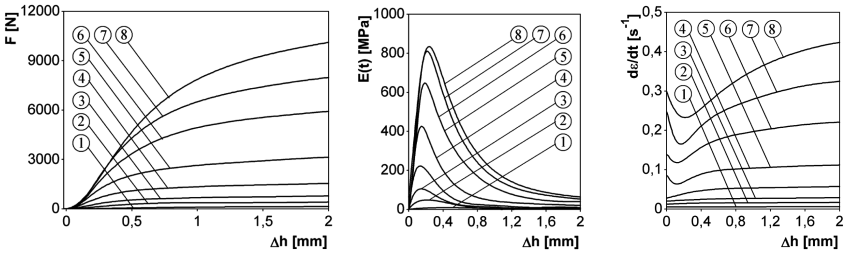

Fig. 1 Viscoelastic response (**a**), instantaneous elastic modulus (**b**) and true compression speed (**c**) versus real sample compression under various piston speeds: *curves* (*1*)—0.1; (*2*)—0.3; (*3*)—0.5; (*4*)—1; (*5*)—2; (*6*)—4; (*7*)—6; (*8*)—8 mm s^{-1}, viscosity $10^{7.4}$ Pa s (lead crystal)

$$E(t) = \frac{d\sigma(t)}{d\varepsilon(t)} = \frac{d(F(t)/A(t))}{d(\Delta h(t)/h(t))} \tag{1}$$

where F(t) is the pressing loads at time t, h(t) the sample height at time t; A(t) an actual value of the cross section; $\Delta h = h_0 - h(t)$ is an instantaneous altitudinal deformation and h_0 is an initial height.

Actual value of instantaneous elastic modulus depends markedly on the compression rate, it tends to the constant value $E(\infty)$ asymptotically. The course of the instantaneous elastic modulus on piston speed at viscosity $10^{7.4}$ Pa s is shown in Fig. 2—elastic modulus $E(\infty)$ was evaluated to be approx. 1.15 GPa (value ca. 1 GPa was measured with ultrasonic method).

Besides the analysis of the elastic response the attention was also paid to the evaluation of relaxation behaviour of glass melt. The course of stress relaxation curves depends markedly on the level of compression of shaped sample (Fig. 3) and

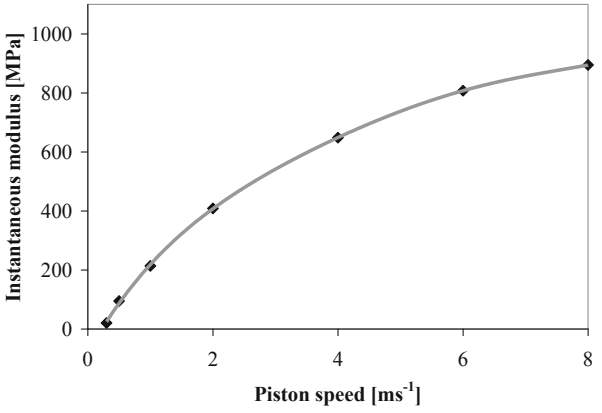

Fig. 2 Dependence of instantaneous elastic modulus on the applied piston speed (strain rate)

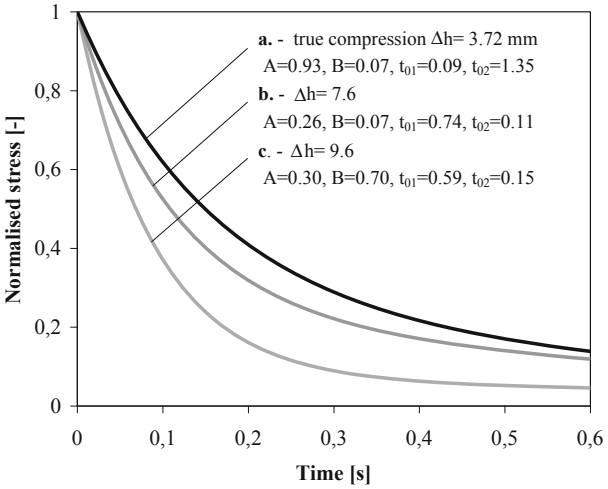

Fig. 3 Normalised curves of the stress relaxation for different Δh at $v = 2$ m s^{-1} and $\eta = 10^{7.4}$ Pa s

piston speed. Measured data can be described by a multiple Maxwell model—in our case by coupling two Maxwell elements in parallel [4]:

$$\sigma_t = \sigma_0[A\exp(t/t_{01}) + B\exp(t/t_{02})], \tag{2}$$

where σ_t is the stress at time t, σ_0 is initial stress, t_{0i} is the relaxation time.

4 Computer Modelling

Virtual model was created in customized commercial code MSC MARC. The constitutive behaviour of shaped glass is assumed to be of non-linear viscoelastic, based on the general Maxwell model. Due to lower sample stiffness the working pistons were regarded as a rigid body. The lead crystal glass material properties specified in the model are: $E = 1.15 \times 10^9$ Pa (Young's elastic modulus), $\nu = 0.36$ (Poisson's ratio), $c_p = 1182$ J kg^{-1} K^{-1} (specific heat), $\rho = 2780$ kg m^{-3} (density at temperature 611 °C).

Friction conditions between pistons working surfaces and sample were defined through the shear-based model (frictional stress is a fraction of the equivalent stress in the formed material) [5]. Samples were subjected to the true compression rate (Fig. 1c). Friction coefficient was changed in the whole range of values (0–1) subsequently.

Computations were performed for three different cases:

- no mechanical heating,
- total viscous heat dissipation,
- real viscous heat dissipation incl. friction, heat flux out of outer surface:

$$Q_{dis} = \zeta_p(\eta, h, dh/dt) \int_0^t F(t) \frac{dh(t)}{dt} dt \tag{3}$$

where Q_{dis} is dissipated heat, $\zeta_p(\eta, h, dh/dt)$ is a variable fraction of viscous work converted into heat (function comes from complex analysis of relaxation behaviour—see Fig. 3), *F(t)* is an actual force, *dh/dt* actual compression rate, t is time.

After compression load the shape of the sample is changed, except idealised frictionless case, from the cylindrical at the beginning to the barrel-shaped later on gradually (Fig. 4a). Values of friction coefficient influence sample shape dominantly in the initial stage, later the final shape is settled with the flow of material in the area of sample casing. Enlargement of initially contact surface (base of cylinder) does not exceed value of 1 mm in diameter (for maximum compression—9 mm—under real friction conditions—Fig. 4b). Time behaviour of the force response to applied piston velocity 2 mm s^{-1} (compression rate defined in accordance with Fig. 1c) for all mentioned cases is drawn up in Fig. 5. Curves 2 and 3 correspond to the extreme cases—without (curve 2) and with (curve 3) consideration of total heat dissipation. Total (theoretical) dissipated viscous heat for compression 9.6 mm at piston speed 2 mm s^{-1} exceeds value of 128 J that corresponds to the theoretical average temperature growth ca. 6.3 °C; 45 J or 2.2 °C

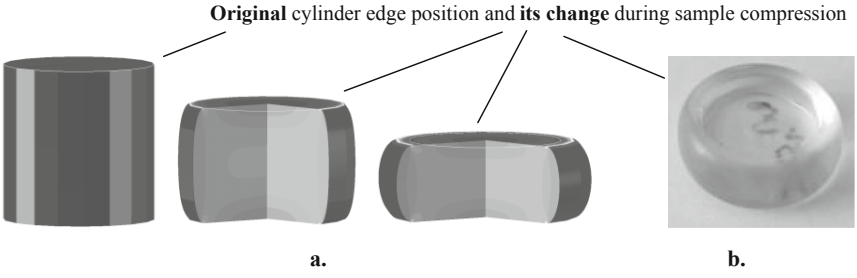

Fig. 4 Progression of the sample shape made of lead crystal at viscosity $10^{7.4}$ Pa s for piston speed 2 mm s^{-2}, incl. identification of change of position of original cylinder edge: **a** FEM model—initial state, compression 5 and 9.6 mm, **b** real sample

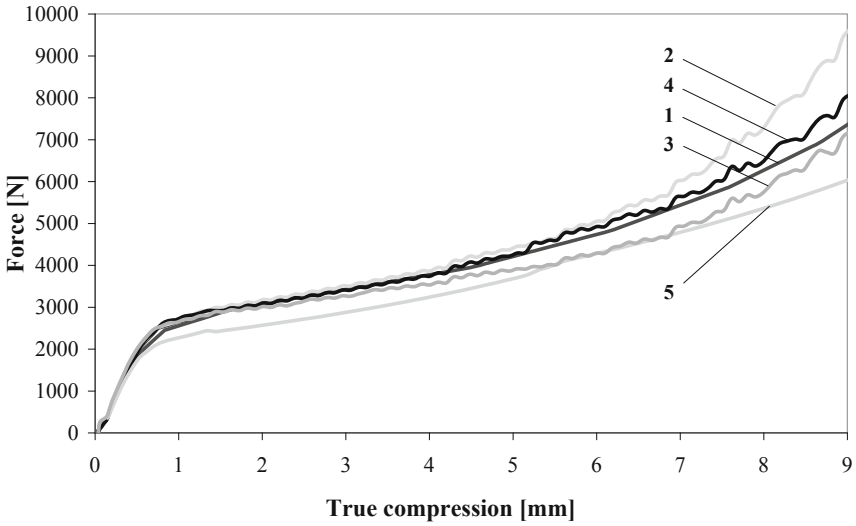

Fig. 5 Viscoelastic response of lead crystal at viscosity $10^{7.4}$ Pa s for the piston speed 2 mm s^{-2}: *1* experimental data, *2* FEM—without consideration of energy dissipation, *3* FEM—with considering of total viscous heat dissipation, *4* FEM—real process simulation, *5* FEM—without mechanical heating and without friction

(Δh = 9.6 mm, v = 1 mm s^{-1}); 15 J or 0.8 °C (Δh = 9.6 mm, v = 0.5 mm s^{-1}) and 327 J and 15.8 °C respectively at compression 7.6 mm and piston speed 4 mm s^{-1}.

In all cases mentioned above the friction coefficient supposed to be 0.9. However the value of friction coefficient, except idealised—frictionless case (curve 5), does not influence time behaviour of the force response significantly. Difference between extreme cases—friction coefficient f = 0 and f = 1 does not exceed value of 10 %.

Curve 4 approximates real time behaviour of the force response very well although only Newtonian viscosity was considered in this case. However, it is evident that above compression 8 mm curve 4 starts to deviate from experimental data. At higher compression acceleration of this process is expected due to shear thinning.

The results of virtual modelling of lead glass viscoelastic response to various compression rate—piston speed respectively—from the interval 0.5–4 mm s^{-1} are presented in Fig. 5. For all cases analysed (used identical conditions as for piston speed 2 mm s^{-1}—curve 4 in Fig. 5) the obtained data are in good accordance with experiment realised (Fig. 6).

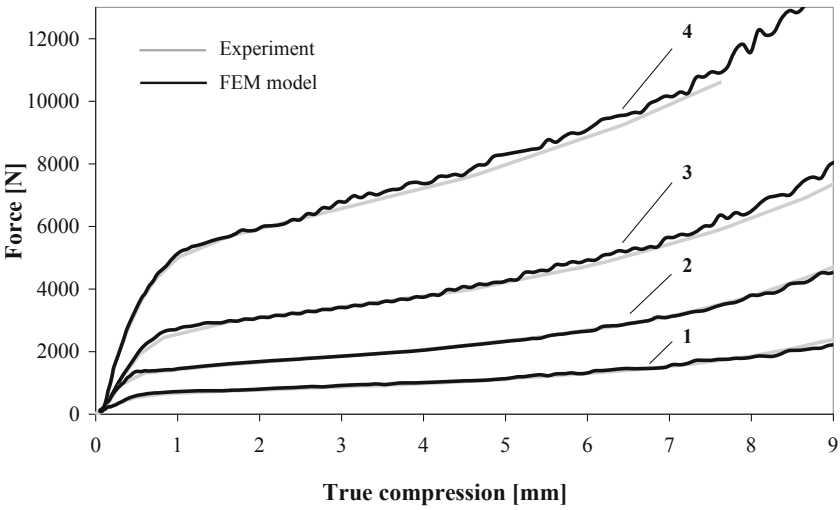

Fig. 6 Viscoelastic response of lead crystal at viscosity $10^{7.4}$ Pa s for variable piston speeds: 0.5 mm s^{-1} (*1*), 1 mm s^{-1} (*2*), 2 mm s^{-1} (*3*), and 4 mm s^{-1} (*4*) respectively

5 Conclusion

In the paper the viscoelastic response of samples made of lead crystal at viscosity $10^{7.4}$ Pa s are analysed by means of FEM. For definition of glass melt constitutive behaviour viscoelastic model of Maxwell type was used. Realised experimental results prove relatively high accordance with simulated outputs of viscoelastic response. Although curves describing viscoelastic response of glass sample to subjected load have tendency to deviate from experimental measurements at higher compression critical values for initiation of shear thinning behaviour were not exceeded in the range of strains applied during the experiment.

Acknowledgments This publication was written at the Technical University of Liberec as part of the project "Research and development in the field of glass-producing machines, industrial and service robotics" (SGS 21128/115) with the support of the Specific University Research Grant, as provided by the Ministry of Education, Youth and Sports of the Czech Republic in the year 2016.

References

1. Vítová, M.: Forming process and rheological properties of glass. In: Proceedings of 12th International Conference on Glass Making Machinery, 2006, p. 173 (in Czech)
2. Vítová, M., Matoušek, I.: Rheological response. Ceram. Silikáty **53**(1), 59 (2009)
3. Bruckner, R., Yue, Y., Habeckm, A.: Load-dependent flow behaviour of silicate glass melts. Glastechnische Berichte **67**(5), 114 (1994)
4. Sobotka, Z.: Reologie hmot a konstrukcí, Academia (1981) (in Czech)
5. MSC Marc 2008. User manual

Influence of Bubbles in the Shock Liquid at Its Compressibility

M. Sivčák and T. Hruš

Abstract The article elaborates simplified thoughts of the effect of the size of the air bubbles and their interactions on the shock fluid compressibility. When fluid flows through the throttle hole, pressure drop occurs and the dissolved air is released from the liquid in the form of bubbles. These bubbles can influence the stiffness of the liquid. If such effect occurs e.g. in a hydraulic shock absorbers, than the damper stops perform its function. This phenomenon is called the delay. Releasing the air into the liquid can be observed even at low piston speed of the damper. However for low piston speeds the delay does not occur, the liquid and containing air bubbles behave as incompressible.

Keywords Air bubbles · Shock liquid · Cavitation · Delay

1 Introduction

The aim of this work is to verify the possibility of formation of the delay [1] in the damper using elementary physical laws. We assume that the delay is created by the compression of free air bubbles in the shock liquid. Releasing the air into the liquid can be observed even at low piston speed of the damper. However for low piston speeds the delay does not occur, the liquid and containing air bubbles behave as incompressible. We want verify whether the fluid stiffness depends on bubble radius and whether the bubbles are grouping into the bigger assemblies.

M. Sivčák (✉) · T. Hruš
Technical University of Liberec, Liberec, Czech Republic
e-mail: michal.sivcak@tul.cz

T. Hruš
e-mail: tomas.hrus@tul.cz

J. Beran et al. (eds.), *Advances in Mechanism Design II*,
Mechanisms and Machine Science 44, DOI 10.1007/978-3-319-44087-3_27

2 Volume-Stiffness of the Bubbles

The set of n equal bubbles (each with radius R_n, pressure p_n and volume V_n) is described by three simple equations

1. the ideal gas law

$$p_n n V_n = p_0 V_0; \tag{1}$$

2. the relation between surface tension, radius and pressure

$$(p_n - p_k) R_n = 2\sigma; \tag{2}$$

3. the equation for volume of the bubble

$$V_n = \frac{4}{3}\pi R_n^3. \tag{3}$$

By substituting p_n from (2) and V_n from (3) into (1) we can obtain the ideal gas law in this form

$$3n\mathrm{p}_k \mathrm{V}_n + 2 \cdot 6^{\frac{2}{3}} \sqrt[3]{\pi} n \sigma V_n^{\frac{2}{3}} - 3 p_0 V_0 = 0. \tag{4}$$

This enables us to find volume of bubble V_n as a function of pressure p_n. Volume stifness k_n of the bubble is given by

$$k_n = \left(\frac{\mathrm{d}V_n}{\mathrm{d}p_k} \right)^{-1}. \tag{5}$$

A set of n bubbles has a lower stiffness given by equation

$$K_n = \frac{1}{n \frac{1}{k_n}} = \frac{k_n}{n}. \tag{6}$$

An important question is *the change* of volume stiffness by changing the number of bubbles n

$$RATIO = \frac{K_n}{K_1}. \tag{7}$$

Exact forms of Eqs. (5), (6) and (7) are very complicated and not "human-readable".

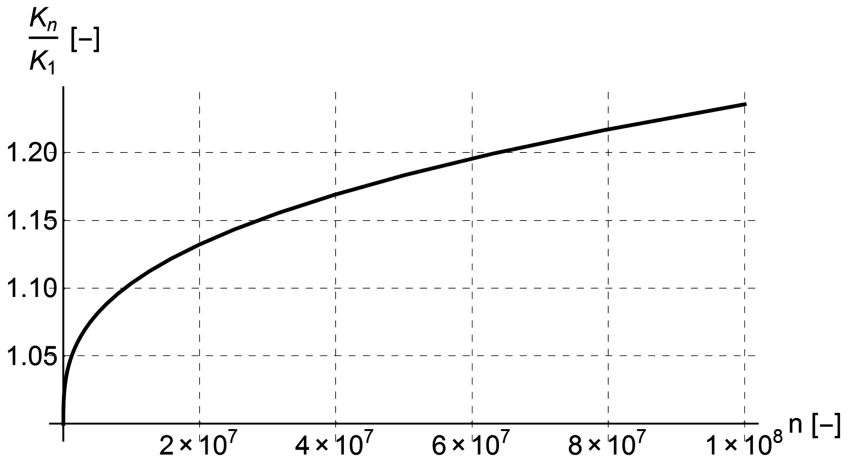

Fig. 1 Stiffness of a set of n equal bubbles (K_n) compared with stiffness of one bubble (K_1). The mass of gas in the bubbles is the same

Assuming values

$$\sigma = 40 \times 10^{-3}\,\mathrm{N/m}, \tag{8}$$

$$p_k = 10^5\,\mathrm{Pa}, \tag{9}$$

$$R_0 = 3\,\mathrm{mm}, \tag{10}$$

we get the numerical result shown in Fig. 1. By decreasing number of bubbles, the volume stiffness of the gas is growing.

3 The Equilibrium State of Two Bubbles

The equilibrium position of two connected bubbles occurs if their potential energy is minimal. For this expression it is necessary to derive dependency of the potential energy on the distance between midpoints of the bubbles s12. The minimum must be subsequently applied as follows

$$\frac{\mathrm{d}Ep(s_{12})}{\mathrm{d}s_{12}} = 0. \tag{11}$$

Potential energy of two connected bubbles will be equal to sum of surface and pressure energy.

$$Ep = S\sigma + p_1 V_1 + p_2 V_2, \tag{12}$$

where S is total surface of the bubbles. Gas pressure energy inside the bubble is constant (we assume the validity of the equation of state) and thus irrelevant for searching of the energy minimum, just as surface tension.

Therefore the relation is determined by the equation

$$\frac{\mathrm{d}S}{\mathrm{d}s_{12}} = 0. \tag{13}$$

Let's introduce the marking (Fig. 2) where index 1 is spherical cap of the small bubble, index 2 for spherical cap of the bigger bubble and index 3 for spherical cap belonging to both bubbles.

Provided that formula (1) is valid, the following is true for our bubbles:

$$p_{i0} V_{i0} = p_i V_i. \tag{14}$$

The initial state of the two bubbles is determined by their size before merging

$$V_{i0} p_{i0} = \frac{4\pi R_{i0}^3}{3} \cdot \left(p_k + \frac{2\sigma}{R_{i0}} \right), \quad i = 1, 2 \tag{15}$$

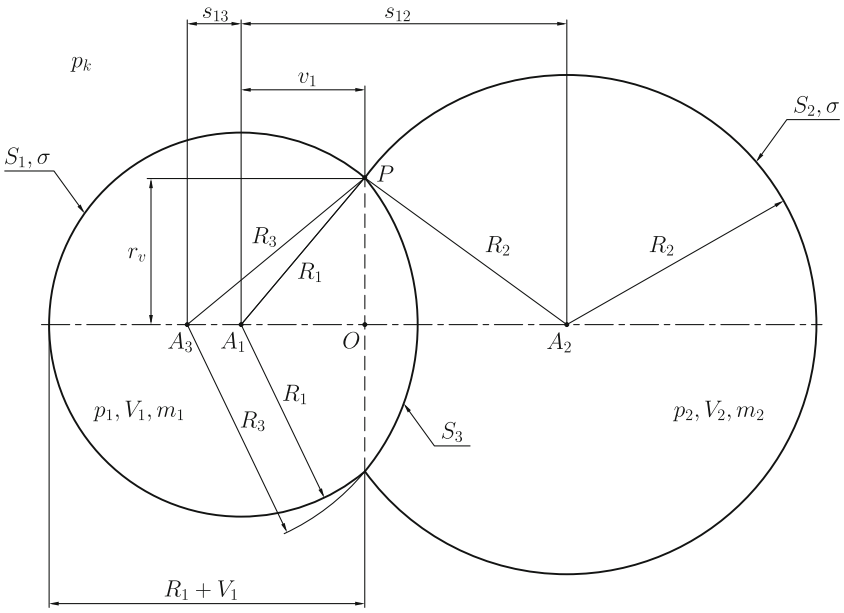

Fig. 2 Interaction between two bubbles

Pressure inside the bubble p_i is sum of pressure of surrounding fluid and addition due to surface tension

$$p_i = p_k + \frac{2\sigma}{R_i}, \tag{16}$$

Volume V_i is dependent on volumes of individual spherical caps.

$$V_i = \frac{\pi v_i\left(3r_v^2 + h_i^2\right)}{6} - \frac{\pi v_3\left(3r_v^2 + h_3^2\right)}{6}(-1)^i, \tag{17}$$

where h_i, h_3 are heights of the spherical caps and r_v is spherical cap radius

$$h_1 = R_1 + v_1, \quad h_2 = R_2 + s_{12} - v_1, \quad h_3 = R_3 - s_{13} - v_1 \tag{18}$$

and

$$r_v = \sqrt{R_1^2 - v_1^3}. \tag{19}$$

On the basis of force equilibrium it is possible to derive that radius R_3 is function of radii of outer spherical caps.

$$R_3 = \frac{2R_1R_2}{R_2 - R_1}, \tag{20}$$

distances s_{13} and v_1 are derived from the geometry on the Fig. 2 as follows

$$s_{13} = -v_1 + \sqrt{v_1^2 - R_1^2 + R_3^2}, \tag{21}$$

$$v_1 = \frac{R_1^2 - R_2^2 + s_{12}^2}{2s_{12}}. \tag{22}$$

The bubble surface will be calculated as a sum of surfaces of individual spherical caps, where the surface of the third cap must be counted twice.

$$S = 2\pi R_1 h_1 + 2\pi R_2 h_2 + 4\pi R_3 h_3. \tag{23}$$

By substituting Eqs. (15)–(22) in the Eqs. (14) and (23) we get a system of three equations which are depending only on R_1, R_2 and s_{12}.

$$p_{i0}V_{i0} = p_i(R_1, R_2, s_{12}) \cdot V_i(R_1, R_2, s_{12}), \tag{24}$$

$$S = S(R_1, R_2, s_{12}), \tag{25}$$

Differentiating (25) by s_{12} with respect to (13) we get

$$\frac{\mathrm{d}S}{\mathrm{d}s_{12}} = \frac{\partial S}{\partial s_{12}} + \frac{\partial S}{\partial R_1}\frac{\mathrm{d}R_1}{\mathrm{d}s_{12}} + \frac{\partial S}{\partial R_2}\frac{\mathrm{d}R_2}{\mathrm{d}s_{12}} = 0. \tag{26}$$

We express unknown derivatives of radius by distance implicitly using derivatives of expressions (24). Because the solutions are difficult to read we call them f_1 and f_2.

$$\frac{\mathrm{d}(23)}{\mathrm{d}s_{12}} = 0 = f_i\left(R_1, R_2, s_{12}, \frac{\mathrm{d}R_1}{\mathrm{d}s_{12}}, \frac{\mathrm{d}R_2}{\mathrm{d}s_{12}}\right). \tag{27}$$

Equations (24), (26) and (27) form a system of five nonlinear algebraic equations with solution of equilibrium state

$$s_{12} = R_1 + R_2. \tag{28}$$

4 Conclusions

It is theoretically confirmed (Fig. 1) that stiffness of fluid with smaller bubbles is higher than the same amount of air in a smaller number of larger bubbles. The assumption that bubbles in fluid are clustering and, therefore, the stiffness of fluid is decreased, was not confirmed. The result (28) means that two bubbles located in fluid tend not to merge. Because bubbles in fluid do merge, the reason for drop of stiffness will be more complicated and we will focus on this phenomenon further.

Acknowledgments This publication was written at the Technical University of Liberec, Faculty of Mechanical Engineering with the support of the Institutional Endowment for the Long Term Conceptual Development of Research Institutes, as provided by the Ministry of Education, Youth and Sports of the Czech Republic in the year 2016.

Reference

1. Šklíba, J., Svoboda, R.: On the problem of dependence of damper force on the concentration of free air in working liquid. In: Springer Proceedings in Physics, Vibrations Problems, ICOVP-2007, 2008. ISBN 978-1-4020-9091-2

Procedure for Seismic Analysis of Liquid Storage Tanks Using FEM Approach and Analytical Models

M. Sivý and M. Musil

Abstract Liquid storage tanks are important components of liquid transmission and distribution systems and therefore should be properly designed to withstand various loadings. One of which is seismic excitation. The paper deals with the seismic analysis of the flexible circular vertical ground-supported liquid storage tank with the aim to determine the dynamic properties (e.g. natural frequencies and their respective mode shapes of the tank and the liquid) and the seismic characteristics (e.g. hydrodynamic pressure distribution, base shear, overturning moment and maximum wave height). During seismic activity, a specific interaction occurs between the tank and the liquid. It is expressed as a vibration of the tank and contained liquid. One (lower) part of liquid moves in unison with the structure, the second (upper) part representing the free surface tends to experience a sloshing effect. The paper is also dedicated to comparing the acquired results from the seismic analysis computed by FE method (ANSYS) with methods using analytical models (spring-mass and pendulum) and Eurocode 8, respectively.

Keywords Liquid storage tanks · Eurocode 8 · Spring-mass model · Seismic characteristics

1 Introduction

Large capacity tanks are used as storage for liquid, non-flammable, non-toxic liquids to highly flammable, toxic chemicals with explosive nature before subsequent treatment or application. They are widely used almost in the industrial sector (e.g. nuclear power plants). Storage tanks should be properly designed to withstand static or dynamic loadings. One of them, which is of interest to many researchers, is the

M. Sivý (✉) · M. Musil
Slovak University of Technology, Bratislava, Slovak Republic
e-mail: martin.sivy@stuba.sk

M. Musil
e-mail: milos.musil@stuba.sk

J. Beran et al. (eds.), *Advances in Mechanism Design II*,
Mechanisms and Machine Science 44, DOI 10.1007/978-3-319-44087-3_28

seismic excitation. Past earthquakes and their destructive consequences, e.g. breakdown of water supplies, uncontrolled fires with subsequent ignition to adjacent tanks and buildings, clouds of toxic chemicals, resulted in a huge effort to describe tank behaviour during a seismic event in an effort to prevent pollution, radiation or loss of human lives etc.

The aim of the investigation has been to develop methods to evaluate earthquake resistance of liquid storage tanks and to provide codes for engineers engaged in the construction of these systems. Some of the proposed procedures and recommendations have been underlain in international (AWWA, ACI, API, Eurocode 8 etc.) or national standards (PNM34080183).

2 Seismic Analysis of Liquid Storage Tank

Dynamic analysis of a tank containing liquid is a complex problem involving fluid-structure interaction. Following numerous studies, simplified equivalent models were proposed which provide a satisfactory solution. Fundamental scientific findings of the seismic effects were published by Housner [1]. The tank-liquid system is simplified by a spring-mass model (two SDOF systems) in which the total liquid mass is divided into two zones—impulsive and convective. The impulsive part represents effects of the portion of the liquid which moves in unison with the tank. It behaves like a mass rigidly connected to the tank wall. The convective part represents the free surface which causes the sloshing effect (Fig. 1).

This procedure is valid only for rigid tanks on rigid foundations. Whereas the walls of rigid tanks move in unison with the ground, motion of flexible tanks is different. Flexibility affects the hydrodynamics effects and may increase the seismic characteristics significantly. The wall deflection configuration of tanks does not

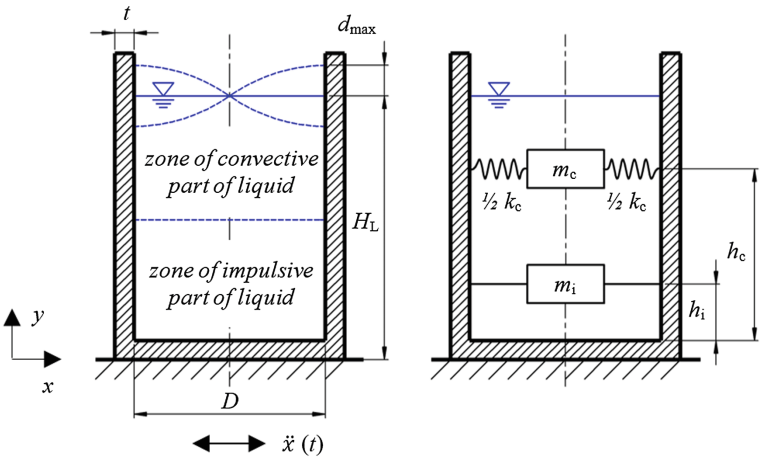

Fig. 1 Model of investigated liquid storage tank and equivalent mechanical model

remain the same but vary from the base to the top of the tank. Flexibility of the tank-liquid system must be taken into account in simplify the equivalent models using an additional flexible mass connected to the tank wall with springs of appropriate stiffness [2, 3]. All formulations of the necessary model parameters can be found in the referenced publications.

The following subchapters are focused on the determination of seismic characteristics using procedures presented in Eurocode 8—section four dedicated to earthquake resistance of tanks. The investigated model is a flexible (steel) cylindrical tank of diameter D (32 m), height H (20 m) and wall thickness t (0.025 m). It is filled to a height of H_L (16 m) with water. The base is fixed to a rigid foundation and is assumed to be excited by a 1 m s^{-2} horizontal component of ground acceleration with an importance factor of III with respect to Eurocode 8.

2.1 Basic Seismic Characteristics

The total base shear is defined as the total dynamic force exerted by the liquid on the tank wall and can be defined as

$$Q = (m_i + m_w + m_r)S_e\left(T_{imp}\right) + m_c S_e(T_{con}) \tag{1}$$

where m_w and m_r represent the wall and the roof mass, $S_e\left(T_{imp}\right)$ and $S_e(T_{con})$ are spectral accelerations, obtained from the elastic response spectrum, respectively.

Hydrodynamic overturning moments immediately above or below the base of a structure (representing the total dynamic force exerted by the liquid on the tank) may be determined as follows

$$\begin{aligned} M &= (m_i h_i + m_w h_w + m_r h_r)S_e\left(T_{imp}\right) + m_c h_c S_e(T_{con}) \\ M' &= \left(m_i h_i' + m_w h_w + m_r h_r\right)S_e\left(T_{imp}\right) + m_c h_c' S_e(T_{con}) \end{aligned} \tag{2}$$

where h_w and h_r are the heights of wall and roof centers of gravity, respectively.

2.2 Hydrodynamic Pressure

According to Eurocode 8, hydrodynamic pressure of flexible tanks is usually expressed as the sum of three contributions, namely rigid impulsive, flexible and convective. The flexibility of the tank wall has a direct impact on the impulsive liquid that experiences accelerations that may be greater than peak ground acceleration (flexible component varies with response acceleration whilst the rigid impulsive component varies only with a ground acceleration). The flexible component of the hydrodynamic pressure has a tendency to shift a peak ordinate from the

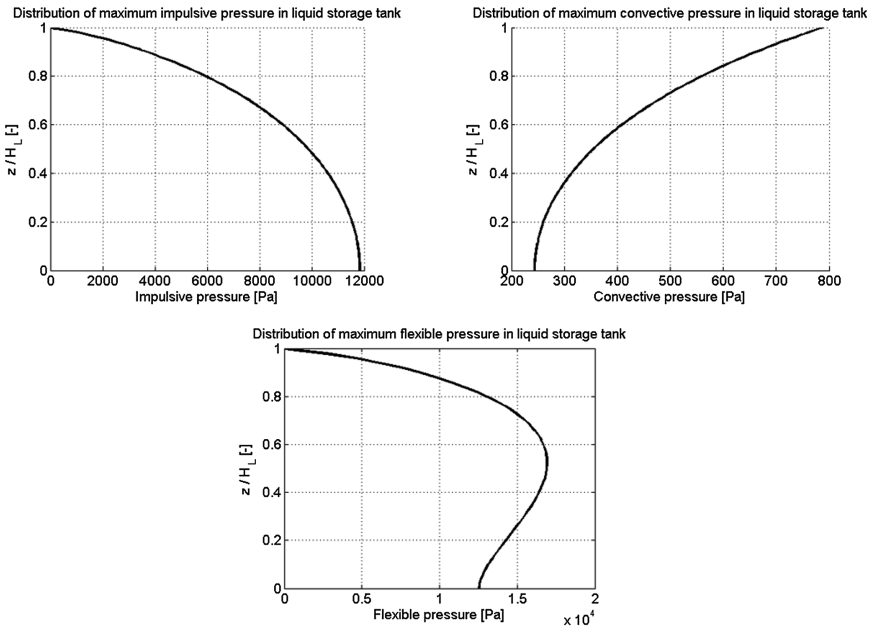

Fig. 2 Contributions of hydrodynamic pressure along the free surface height

base to the top. Due to a weak coupling between the second and third component of hydrodynamic pressure, the flexible component may be determined independently.

During lateral base excitation, the tank wall is subject to lateral hydrodynamic pressure. The spatial-temporal distributions of rigid impulsive, flexible and convective pressures are given respectively by

$$\begin{aligned} p_{\mathrm{i}}(\xi,\varsigma,\theta,t) &= C_i(\xi,\varsigma)\rho_{\mathrm{L}}H_{\mathrm{L}}A_{\mathrm{g}}(t)\cos\theta \\ p_{\mathrm{f}}(\varsigma,\theta,t) &= \rho_{\mathrm{L}}H_{\mathrm{L}}\psi\cos\theta\sum_{n=0}^{\infty}d_n\cos(v_n\varsigma)A_{\mathrm{fn}}(t) \\ p_{\mathrm{c}}(\xi,\varsigma,\theta,t) &= \rho_{\mathrm{L}}\sum_{n=0}^{\infty}\psi_n\cos\mathrm{h}(\lambda_n\gamma\varsigma)J_1(\lambda_n\xi)\cos\theta A_{cn}(t) \end{aligned} \tag{5}$$

where $A_g(t)$ denotes the ground acceleration time-history, $A_{cn}(t)$ is the acceleration time-history of SDOF oscillator with natural frequency ω_{cn} and A_{fn} (t) is the pseudo-acceleration function with the natural frequency of the tank-liquid system. The rest of the parameters are introduced in [3]. Figure 2 presents the maximum contributions of hydrodynamic pressure along the free surface height of the model.

2.3 Natural Frequencies and Modes of Vibration

Natural frequencies of impulsive and convective responses are taken as

$$T_i = C_i \frac{\sqrt{\rho_L} H_L}{\sqrt{t/R}\sqrt{E}} \quad T_c = C_c \sqrt{R} \tag{6}$$

where ρ_L is the density of the liquid, E is a modulus of elasticity of the tank material. C_i and C_c represent coefficients for their respective slenderness H_L/R.

When liquid oscillates in unison with the tank, an impulsive frequency occurs. It represents the most unfavourable response to the system, which behaves like a cantilever beam with a mass equivalent to the mass of the tank and liquid. The response of the investigated system (Fig. 3) occurs at 5.629 Hz (in ANSYS 5.505 Hz).

Sloshing of the convective liquid can rupture the roof or top of the tank. Hence, the *freeboard* between free liquid surface and top of the tank must be designed assuming a *maximum displacement of sloshing wave* within the calculations. Sloshing is described by infinite antisymmetric mode shapes. Figure 4 presents the

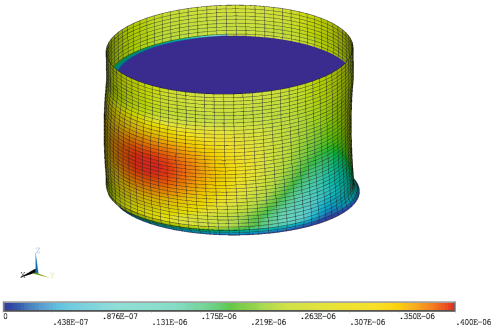

Fig. 3 Mode of vibration at the impulsive frequency of the investigated liquid storage tank

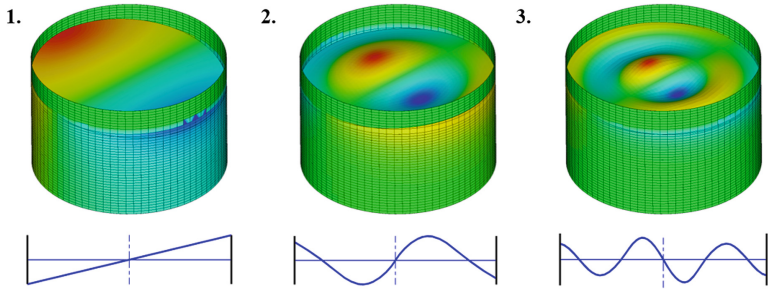

Fig. 4 First three modes of vibration of the convective liquid mass

Table 1 Comparison of the natural frequencies considering the first convective liquid mass

	ANSYS (Hz)	Eurocode 8 (Hz)	Pendulum model (Hz)
1	0.1649	0.1648	0.1734
2	0.2883	0.2877	0.2877
3	0.3659	0.3641	0.3641

first three theoretic and computed eigenmodes of the model. These modes of vibration occur at the frequencies listed in Table 1 and are compared with methods using Eurocode 8 (spring-mass model) [3] and pendulum model [4], respectively.

3 Conclusions

The aim of this paper was to perform a seismic analysis on a model of circular vertical ground supported liquid storage tank according to Eurocode 8. Seismic analysis was one of the analyses which should be carried out to provide satisfactory performance of tanks, especially in earthquake prone regions.

Due to the different responses (wall flexibility), rigid and flexible tanks should be appropriately distinguished. This difference is significant especially when investigating the hydrodynamic pressure and tank oscillation. On the other hand, response of the convective liquid mass and its contribution to hydrodynamic pressure is not affected by wall flexibility. For design purposes, these effects can be evaluated by considering the tank to be rigid. But the seismic characteristics of the flexible tank assumed that the tank was rigid can be non-conservative.

The situation, when liquid oscillates in unison with the tank, represents an unfavourable response to the system. Due to the sloshing effect, it is necessary to determine the sloshing wave height to prevent ruptures and fluid spilling.

The seismic analysis was performed using Matlab and ANSYS. Results were compared with procedures presented in Eurocode 8 (spring-mass model) and pendulum model. The results between each solution represented good conformity.

Acknowledgments The paper was supported by the grant from Grant Agency of VEGA no. 1/0742/15 entitled “Analysis for seismic resistance of liquid storage tanks with nonlinear and time-dependent parameters”.

References

1. Housner, G.W.: Earthquake Pressures on Fluid Containers. California Institute of Technology (1954)
2. Veletsos, A.S.: Seismic Response and Design of Liquid Storage Tanks. Guidelines for the Seismic Design of Oil and Gas Pipeline Systems. Technical Council on Lifeline Earthquake Engineering (ASCE) (1984)

3. Eurocode 8: Design of Structures for Earthquakes Resistance: Part 4—Silos, Tanks and Pipelines. CEN (2006)
4. Ibrahim, R.A.: Liquid Sloshing Dynamics Theory and Applications. Cambridge University Press, Cambridge (2005)

Part IV
Vibration and Noise in Machines

Forced Response Reduction of a Compressor Blisk Rotor Employing Intentional Mistuning

B. Beirow, A. Kühhorn and J. Nipkau

Abstract Using the example of a compressor test blisk with 29 blades different sources of mistuning and their consequences for the forced response are analysed under consideration of aeroelastic effects. In particular the impact of superimposing intentional structural mistuning by both random structural mistuning and aerodynamic mistuning is studied. For this purpose reduced order models of the blisk are adjusted for different mistuning distributions. The mistuning itself is characterized by assigning individual stiffness parameters to each blade. The aeroelastic coupling is included employing aerodynamic influence coefficients. By means of genetic algorithm optimizations, structural mistuning patterns are found which yield a mitigation of the forced response below that of the tuned design reference. Ideally a nearly 50 % reduction of maximum response magnitudes is computed for the fundamental bending mode and large mistuning. The solutions found have been proven to be robust with respect to additional random and aerodynamic mistuning in case of large intentional structural mistuning.

Keywords Blade vibration · Blisk · Mistuning · Forced response · Compressor

1 Introduction

The fabrication of aero-engine compressor rotors as one piece has become increasingly significant in recent years, since it allows for higher rotational speeds associated with higher pressure ratios and an enhanced efficiency. However, regarding the forced response computation of these blade integrated disks (blisks) due to aerodynamic excitation, engineers are exposed to a number of particularities.

B. Beirow (✉) · A. Kühhorn
Brandenburg University of Technology, Cottbus, Germany
e-mail: beirow@b-tu.de

J. Nipkau
Rolls-Royce Deutschland Ltd. & Co KG, Blankenfelde-Mahlow, Germany
e-mail: jens.nipkau@rolls-royce.com

J. Beran et al. (eds.), *Advances in Mechanism Design II*,
Mechanisms and Machine Science 44, DOI 10.1007/978-3-319-44087-3_29

Apart from the extremely low structural damping level of blisks due to the lack of frictional damping, small but unavoidable differences of mechanical characteristics from blade to blade, which are denoted as mistuning can cause severe amplifications of the forced response compared to the ideal design with identical blades. Typical sources of mistuning are geometric deviations due to manufacturing tolerances, wear, damage or even strain gauge instrumentation. Engineers have been concerned with the mistuning phenomenon of bladed disks for about 50 years. As long ago as 1966 Whitehead [1] introduced a theoretical limit for an estimation of the maximum displacement amplification only depending on the number of blades. Martel and Corral [2] formulated a modified and less conservative limit in which the number of blades is replaced by the number of active modes in order to take into account the degree of modal coupling within a family of blade modes. In addition Figaschewsky and Kühhorn [3] assume normally distributed individual blade frequencies with a chosen standard deviation of mistuning. In doing so the mistuning strength is taken into account generally yielding a more realistic calculation of the forced response amplification due to mistuning. Petrov and Ewins [4] used optimization algorithms to find the worst forced response of bladed disks in terms of academic studies. However, the majority of analyses measured or preset mistuning patterns yielded amplification factors from 1 to hardly greater than 2 as exemplarily reported in [5].

Aiming at a reduction of vibration amplification amplitudes one idea has been to design blisks with intentional mistuning. Here the intention is to take advantage of the dependence of aerodynamic modal damping ratios on the inter-blade phase angle, which can yield an increased resulting damping level and lead to a reduction of the forced response level for particular engine order excitations even below that of the tuned counterpart [6]. In the current paper the effect of intentional mistuning is addressed with respect to a mitigation of the forced response. Reduced order models based on the subset of nominal system modes (SNM) [7] are employed in which mistuning is quantified by stiffness variations. Aeroelastic coupling effects are considered employing the method of aerodynamic influence coefficients (AIC) which are put into the SNM-model as described in [8]. Mistuning patterns which are derived from genetic algorithm optimizations are exemplarily analyzed for a 29-bladed high pressure compressor blisk rotor (Fig. 1a) with focus on the

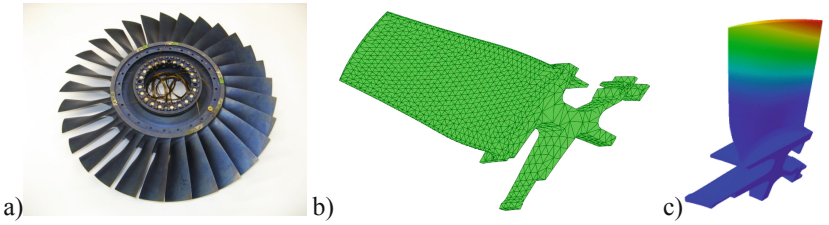

Fig. 1 **a** High pressure compressor blisk, **b** finite element sector model and **c** fundamental blade mode shape (1st flap)

fundamental blade bending mode. Additional random mistuning is superimposed in order to evaluate the robustness of the forced response reduction. Finally, the effect of aerodynamic mistuning is analysed.

2 Numerical Model

Aiming at a preparation of a numerical model for the forced response computation, a finite element sector model is set up in a first step representing the tuned and cyclic symmetric blisk with identical blades (Fig. 1). Subsequently an eigenvalue analysis is carried out in order to gain the relevant information about the basic vibration characteristics and blade mode families. Focusing on the frequency range around the first fundamental blade mode family, a basic SNM-model with just 31 degrees of freedom is derived. This basic modal model can be easily adjusted to arbitrary blade frequency mistuning by means of a stiffness adjustment of every blade, for details please refer to [7, 8]. These models are valid as long as no change of blade mode shapes appears. Hence, the SNM is well suited for quick forced response computations e.g. within probabilistic analyses.

Assuming small blade displacements and linear conditions, the AIC-technique is well suited to cover effects of fluid structure interaction in a simple way [8]. The computation of AIC starts with unidirectional coupled CFD-/FEM-calculations for an assembly of identical blades and stationary flow conditions. Only one blade, the reference blade, is forced to vibrate in a particular blade mode causing flow disturbances and consequently unsteady surface pressure distributions on all blades in the assembly. Subsequently, the modal forcing acting on each blade is computed and normalized with the modal displacement of the reference blade. This normalization yields the AIC which finally have to be transformed from blade individual coordinates into coordinates of the subset. In this way the whole aeroelastic information is considered in the aerodynamic impedance matrix $\mathbf{Z}$ appearing in the equation of motion as follows:

$$[-\Omega^2\mathbf{M} + j\Omega\mathbf{D} + \mathbf{K} + \mathbf{Z}]\mathbf{q}(j\Omega) = \mathbf{F}^F. \tag{1}$$

$\mathbf{M}$, $\mathbf{D}$ and $\mathbf{K}$ denote modal mass, modal structural damping and modal stiffness matrices, $\mathbf{F}^F$ the vector of external modal forcing and $\mathbf{q}$ the vector of modal displacements. If external forcing and structural damping are neglected, Eq. (1) represents an eigenvalue problem which yields the aeroelastic natural frequencies and aerodynamic damping values given in Fig. 2. Note that if a tuned blisk is excited in a particular engine order only one mode characterized by a particular number of nodal diameters (ND) and assigned to one aerodynamic damping ratio is responding. In case of a mistuned blisk the response is composed by a linear combination of several ND-modes so that the resulting aerodynamic damping deviates from the ‘regular’ value of a pure response in only a single ND.

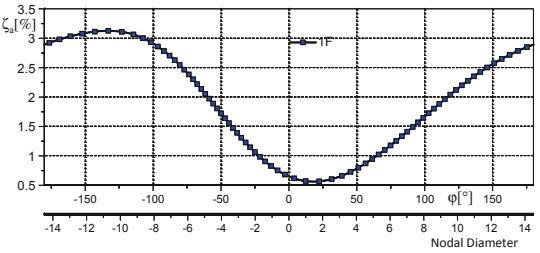

Fig. 2 Aerodynamic damping versus inter-blade phase angle φ and nodal diameter (maximum take off conditions)

3 Real and Intentional Structural Mistuning

The real mistuning distribution has been experimentally determined for the blisk shown in Fig. 3a by use of a patented approach via blade by blade ping tests [6]. It was found that the blade to blade stiffness variation is ranging between ±0.75 %. However, the maximum forced response amplification of the tuned reference is appearing moderately with an 8 % (γ = 1.08 at EO 26) rise in the worst case (Fig. 3c). On the contrary large alternating intentional mistuning (ΔE = ±6.09 %, Fig. 3b) comes along with tremendous differences (Fig. 3c): extreme values are a 115 % rise (γ = 2.15 at EO 13) and a drop of about 40 % (γ = 0.60 at EO 25). Such a behavior is explainable by a modified aerodynamic damping level. In the latter case an EO 25 corresponds to an aliased EO-4 excitation, which excites a ND 4 mode in case of a tuned system. However, since strong mistuning is present, other NDs are involved which contribute more aerodynamic damping (Fig. 2) and hence strongly increase the resulting aerodynamic damping level. Obviously this increased damping contribution works against the commonly response amplifying

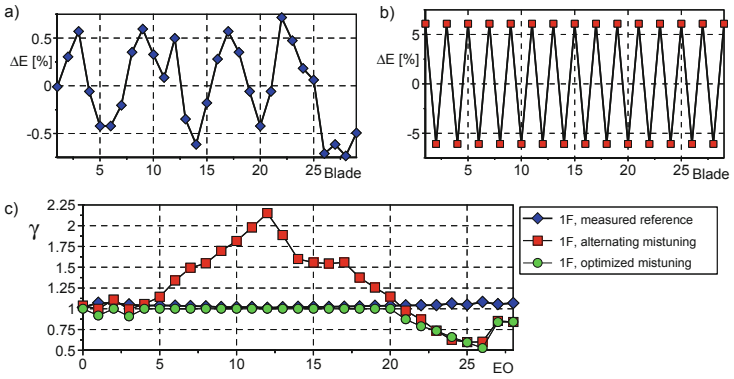

Fig. 3 **a** Measured and **b** alternating mistuning patterns, **c** maximum amplification of mistuned forced response versus engine order (EO)

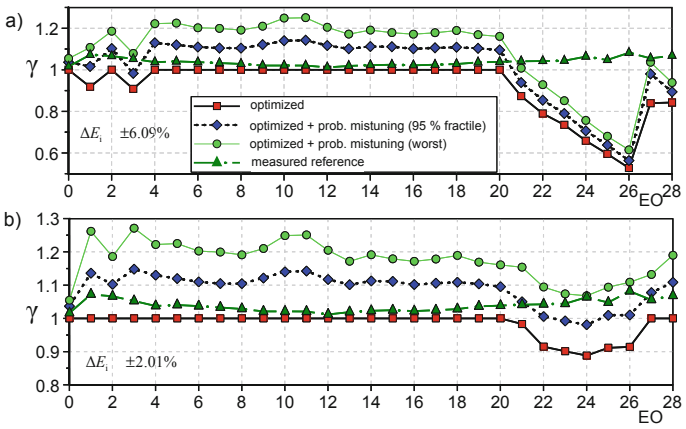

Fig. 4 Amplification of max. blade displacements—optimized intentional mistuning combined with additional random mistuning (50000 samples): **a** large, and **b** small intentional mistuning

effect of mistuning and even causes a mitigation of forced response below that of the tuned counterpart. Similar results are achieved with intentional mistuning patterns ($\Delta E = \pm 6.09$ % allowed) being individually optimized for each EO via genetic algorithms [6]).

Uncertainties within the manufacturing process cannot be avoided even in case of intentional mistuning. For that reason it is assumed that additional and evenly distributed random mistuning ($\Delta E = \pm 1$ %) will be present in order to prove the robustness of the optimized intentional mistuning patterns to reduce the forced response. Again considering large intentional mistuning ($\Delta E = \pm 6.09$ %), the gain achieved for mistuning patterns optimized with respect to EO-excitations from 21 to 28 is the same since the responses remain always below that of the measured and largely below the tuned reference (Fig. 4a). However, this is not the case for small intentional mistuning ($\Delta E = \pm 2.01$ %) where the benefit of the optimization gets widely lost and hence the robustness is not given (Fig. 4b).

4 Aerodynamic Mistuning

Apart from structural mistuning additional aerodynamic mistuning is considered via small random perturbations of AICs. Hence, small perturbations of features like blade stagger angles or the distance of adjacent blades are taken into account. Similar to the approach presented in [9] random perturbations are included in the impedance matrix of Eq. (1) considering three different maximum random deviations: 1, 3 and 10 %. In combination with large intentional mistuning patterns

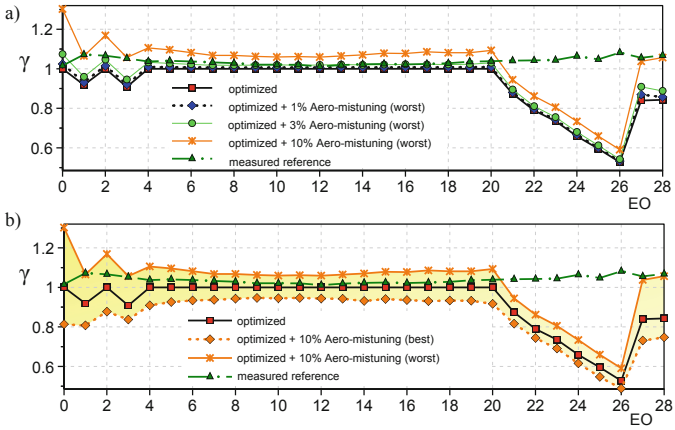

Fig. 5 Amplification of maximum blade displacements—optimized intentional mistuning combined with additional aerodynamic mistuning (50000 samples): **a** varying, **b** 10 %

($\Delta E = \pm 6.09$ %) 1 and 3 % aerodynamic mistuning only marginally affects the forced response (Fig. 5a), which agrees with the findings shown in [9]. Whereas allowing 10 % aerodynamic mistuning both, a partly significant rise and drop of the forced response may occur (Fig. 5b). Nevertheless, the gain achieved with optimized, large intentional mistuning is retained between EO 21 and 28, since the maximum response amplification is never exceeding that of the measured reference.

5 Conclusions

The use of intentional mistuning has been analysed for a compressor blisk rotor in terms of a mitigation of the forced response. It could be shown that even a response reduction beneath the level of the tuned counterpart design is possible for particular engine order excitations for optimized mistuning patterns. In case of large intentional mistuning the potential of encouraging reduced forced response levels has been proven to be robust with respect to additional moderate but realistic random structural and aerodynamic mistuning.

Acknowledgments The research was conducted as a part of the joint research program "COOREFLEX-turbo (AG Turbo)". The work was supported by the Bundesministerium für Wirtschaft und Energie (BMWi) under FKZ 03ET7021. The authors gratefully acknowledge AG Turbo and Rolls-Royce Deutschland for their support and permission to publish this paper. The responsibility for the content lies solely with its authors.

References

1. Whitehead, D.S.: Effect of mistuning on the vibration of turbomachine blades induced by wakes. J. Mech. Eng. Sci. **8**, 15–21 (1966)
2. Martel, C., Corral, R.: Asymptotic description of maximum mistuning amplification of bladed disk forced response. J. Eng. Gas Turb. Power **131**, 1–10 (2009) (022506–1)
3. Figaschewsky, F., Kühhorn, A.: Analysis of mistuned blade vibrations based on normally distributed blade individual natural frequencies. In: Proceedings of ASME Turbo Expo 2015, GT2015-43121, Montréal, Canada, 13–19 June 2015
4. Petrov, E.P., Ewins, D.J.: Analysis of the worst mistuning patterns in bladed disk assemblies. J. Turbomach. **125**, 623–631 (2003)
5. Chan, Y.-J., Ewins, D.J.: The amplification of vibration response levels of mistuned bladed disks: its consequences and its distribution in specific situations. J. Eng. Gas Turb. Power **133** (10), 1–8 (2011) (Paper 102502)
6. Beirow, B., Kühhorn, A., Giersch, T., Nipkau, J.: Optimization-aided forced response analysis of a mistuned compressor blisk. J. Eng. Gas Turb. Power **137**(1), 012504 (2015)
7. Yang, M.T., Griffin, J.H.: A reduced-order model of mistuning using a subset of nominal system modes. J. Eng. Gas Turb. Power **123**, 893–900 (2001)
8. Giersch, T., Hönisch, P., Beirow, B., Kühhorn, A.: Forced response analysis of mistuned radial inflow turbines. J. Turbomach. **135**(3), 031034-1-9 (2013)
9. Besem, F.M., Kielb, R.E., Key, N.L.: Forced response sensitivity of a mistuned rotor from an embedded compressor stage. J. Turbomach. **138**(3), 031002-1-10 (2016)

Flat Flexural Vibration of Drill-String with an Initial Curvature

A.S. Sergaliyev and L.A. Khajiyeva

Abstract Drill-string vibration is one of the major causes for a deteriorated drilling performance. It is crucial to understand the complex vibrational mechanisms experienced by a drilling system in order to better control its functional operation and improve its performance. This work is devoted to modeling of nonlinear dynamics of the drill-string taking into account initial curvature and finiteness of deformations. The drill-string is considered as a one-dimensional rod of a symmetric cross-section compressed by an axial force applied at the top end of the rod. The equation of motion is derived using the theory of finite deformations of V.V. Novozhilov and the Hamilton–Ostrogradsky's variational principle. The initial curvature is modelled as a random shape that can be approximated by a finite series of smooth functions. All numerical calculations are carried out in the environment of symbolic mathematical computations—Wolfram Mathematica. The obtained results allow to study the influence of initial curvature on excited flexural vibrations in the drill-string in order to improve its performance and avoid of severe and destructive oscillations.

Keywords Drill-string · Dynamics · Flexural vibration · Finite deformations · Nonlinear model

1 Introduction

Intensive development of the Earth's interior is characterized by the growth of oil and natural gas production. Construction of vertical wells by drilling is the most widespread way of production of oil products in countries with developed mining industry. It is safe and effective in a variety of geological conditions. However, the

A.S. Sergaliyev · L.A. Khajiyeva (✉)
Al-Farabi Kazakh National University, Almaty, Kazakhstan
e-mail: khadle@mail.ru

A.S. Sergaliyev
e-mail: almaz.ss@gmail.com

J. Beran et al. (eds.), *Advances in Mechanism Design II*,
Mechanisms and Machine Science 44, DOI 10.1007/978-3-319-44087-3_30

practice of construction of oil and gas wells shows that there are cases when there are some factors, which jeopardizes the possibility of its use. One of these factors can be geometrical imperfections of structural elements.

As mentioned in [1] the real structural elements can have an initial curvature, for this reason attached forces act with a certain eccentricity. These factors can significantly affect the behavior of the system. The study of such systems with initial imperfections is important, first of all, from a practical side as allows us to approach mathematical models to real structures. Of course the listed factors are usually random, therefore reasonably it is possible to estimate their effect only with attraction of statistical methods.

Theoretical study of influence of initial imperfections on the dynamic behavior of the structure is developing in two directions. The first direction—deterministic, based on the fact that the amplitude and shape of the initial geometric imperfections are known for each case. The second direction—it is assumed that the initial perturbations are random field [2, 3]. In this paper the nonlinear dynamics of a drill-string with a random shape of initial curvature is investigated.

2 Problem Statement

The problem of flat bending of the drill-string of length l with an initial curvature is studied. The drill-string is considered as an isotropic rod of circular cross-section compressed by an axial force $N(t)$ applied at the top end of the string. Due to the small cross-sectional size relative to the length of the drill-string, it is represented as one-dimensional rod where the axis of OZ is directed along a rod axis.

The model of elastic deformation of the drill-string is based on the nonlinear theory of elasticity of Novozhilov [4]. The second system of simplifications by V.V. Novozhilov and the hypothesis of flat cross-sections is applied to components of strain tensor. According to the last cross sections of the rod at deformation remain flat and perpendicular to its deformed axis, and normal tension on planes parallel to the rod axis are negligible. In this case, equations of elastic displacements, relative elongations and rotation angles of the rod elements have the form:

$$\begin{aligned} U(x,y,z,t) &= u(z,t) + u_0(z); \\ V(x,y,z,t) &= 0; \\ W(x,y,z,t) &= -\frac{\partial u(z,t)}{\partial z}x + \frac{du_0(z)}{dz}x, \end{aligned} \tag{1}$$

where $U(x,y,z,t), V(x,y,z,t), W(x,y,z,t)$—displacement components along the axes OX, OY, OZ, respectively; $u(z,t)$—a complete bending that occurs during deformation; $u_0(z)$—initial curvature.

The functional of elastic deformation have the form:

$$\Phi = \frac{G}{1-2v}\left[(1-v)e_{zz}^2 + e_{zz}\omega_y^2 + \frac{1}{2}\omega_y^4\right], \tag{2}$$

where v—Poisson's ratio, e_{xx}, e_{yy}, e_{zz}—relative elongations parallel to the axes OX, OY, OZ, respectively; e_{xy}, e_{yz}, e_{zx}—shifts; $\omega_x, \omega_y, \omega_z$—rotation angles around respective axes.

To derive the main differential equations of movement defining transverse displacements of the drill-string, relative to its initial undeformed position, methods of the variation principle of Ostrogradsky-Hamilton is used [5].

The potential energy of deformation is defined as follows:

$$\mathrm{U}_0 = \frac{G}{1-2v}\int_0^l \left[(1-v)J\left(\frac{\partial^2 u}{\partial z^2} - \frac{d^2u_0}{dz^2}\right)^2 + \frac{F}{2}\left(\frac{\partial u}{\partial z} - \frac{du_0}{dz}\right)^4\right]dz. \tag{3}$$

The potential of external loading is defined as work of the external loading force on mutual shift of the ends of the rod to the direction of force of N. Then the potential of external loading have the form:

$$\Pi = \frac{1}{2}\int_0^l N\left[\left(\frac{\partial u}{\partial z}\right)^2 - \left(\frac{du_0}{dz}\right)^2\right]dz. \tag{4}$$

The kinetic energy of the rotating rod in global system of coordinates is defined as follows:

$$T_{kin} = \frac{1}{2}\rho\int_0^l \left[F\left(\frac{\partial u}{\partial t}\right)^2 + J\left(\frac{\partial^2 u}{\partial z \partial t}\right)^2\right]dz, \tag{5}$$

where F—area of cross section of the drill-string, J—axial moment of inertia.

Applying the variational principle of Ostrogradsky-Hamilton:

$$\delta Q = \delta\int_{t_1}^{t_2}(T_{kin} - U_0 + \Pi)dt = 0. \tag{6}$$

the main equation of movement of the drill-string is obtained:

$$\rho\left(-F\frac{\partial^2 u}{\partial t^2}+J\frac{\partial^4 u}{\partial z^2\partial t^2}\right)-\frac{\partial}{\partial z}\left(N\frac{\partial u}{\partial z}\right)-EJ\frac{\partial^4 u}{\partial z^4}+\frac{EF}{(1-\nu)}\frac{\partial}{\partial z}\left(\frac{\partial u}{\partial z}-\frac{du_0}{dz}\right)^3=-EJ\frac{d^4u_0}{dz^4}; \tag{7}$$

where E—Young's modulus.

The equation of movement (7) has the nonlinear character caused by geometrical nonlinearity of the drill-string and consider the influence of its initial curvature on behavior of the system.

3 Solution Method and Shape of an Initial Curvature

Well known the Bubnov-Galerkin's variational method of separation of variables was used to determine the solution of (7) with a simply-supported boundary conditions. In [6] has been shown that this method allows to successfully analyze the behavior of drill-strings used for oil production in the vertical and deviated wells. According to the Bubnov-Galerkin's method the solution of the system is defined as:

$$u(z,t)=\sum_{i=1}^{n} f_i(t)\sin\left(\frac{i\pi z}{l}\right), \tag{8}$$

where $f_i(t)$—unknown functions of time, $\sin(i\pi z/l)$—modes of flexural vibrations of the rod.

It is obvious that initial curvature has the smooth form. Thus, it can also be represented as the same series of trigonometric functions. Considering that it guessed that the initial curvature has a random shape it assumed the coefficients of the trigonometric series have a random character.

$$u_0(z,\xi)=\sum_{i=1}^{n} A_i(\xi)\sin\left(\frac{i\pi z}{l}\right), \tag{9}$$

where $A_i(\xi)$—are independent Gaussian random coefficients.

After substitution of the series (8), (9) in Eq. (7) the nonlinear system of differential equations of the second order with respect to the unknown functions $f_i(t)$ is obtained.

4 Numerical Results

The implementation of the Bubnov-Galerkin method and the further numerical solution were made in the applied program for symbolic computation—Wolfram Mathematica 10. The stiffness switching method was applied to implement the numerical solution of the equations.

Numerical calculations were carried out for the steel drill-string at the following values of parameters: $E = 2.1 \times 10^5$ MPa, $\rho = 7800$ kg/m^3, $\nu = 0.28$, outer diameter of the rod $D = 0.2$ m, inner diameter $d = 0.12$ m, $F = 2.01 \times 10^{-2}$ m^2, $N = 2.2 \times 10^3$ N, $J = 6.84 \times 10^{-5}$ m^4, $l = 200$ m. In addition, it is assumed that a compressive load is constant and distributed along the length of rod.

Calculations were carried out up to 12 modes and it can be seen that the main contribution to the dynamics of vibrations make the first modes. With the growing number of modes its contribution is reduced (Fig. 1). Moreover, if there is no the initial curvature it can be shown that the flexural vibrations will not appear on the even modes [1]. Figure 2 shows four simulations at fixed cross-section ($z = 0.5\ l$), where $u_1(t)$ solution of (7) in case of no initial curvature and other $u_2(t)$, $u_3(t)$, $u_4(t)$ are solutions with random shape of curvature. Maximum of amplitudes of random shapes lie in the range from 0.5 to 2 cm. Figures 3 and 4 show the same

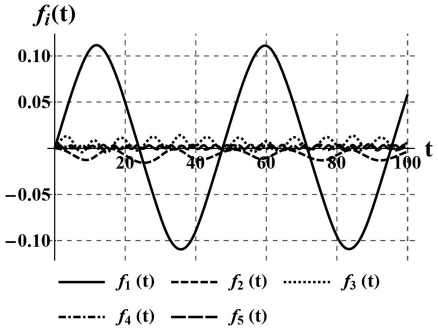

Fig. 1 First five modes at fixed cross-section

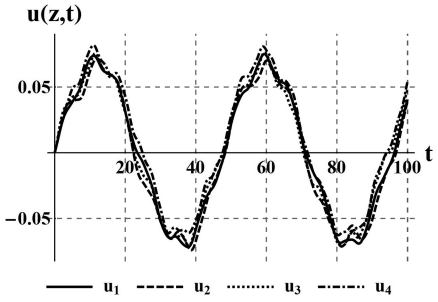

Fig. 2 Four simulations at fixed cross-section

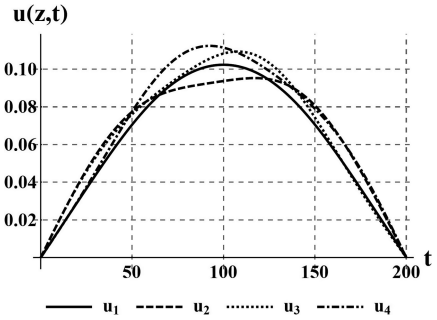

Fig. 3 Four simulations along the entire length at t = 200 s

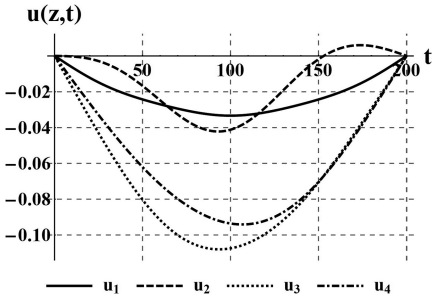

Fig. 4 Four simulations along the entire length at t = 600 s

solutions along the entire length at t = 200 s and t = 600 s, respectively. It can be seen that a small initial curvature slightly affects the amplitude of vibration of the system, but it considerably affects the frequency characteristics.

5 Conclusions

In this paper the spatial movement of compressed drill-strings with no restrictions on the size of their deformations was modelled. The model is based on application of the Ostrogradsky-Hamilton variation principle and the theory of finite deformations of V.V. Novozhilov. The Bubnov-Galerkin method was applied for converting the original system of nonlinear equations with distributed parameters in a system of nonlinear ordinary differential equations. The initial curvature is modelled as a random shape approximated by a finite series of trigonometric functions. The calculation procedure of the mathematical model was developed and implemented in the environment of Wolfram Mathematica 10.

It was observed that small initial curvature leads to slightly increasing of the amplitude of vibrations and considerably affects the frequency characteristics of the system, thereby there is no destructive oscillations. However, the picture could change significantly if we consider the real initial curvature of structural elements.

Nevertheless, the developed approach will allow to estimate it, it is only need to make other assumptions about the nature of distribution of random coefficients based on statistical data. This may serve as further development of this work. It is also planned to consider the non-flat case when the drill-string is rotating at a constant angular velocity.

Acknowledgments This research work has been done within the framework of the "Development of nonlinear dynamic models of deformable media and their practical application for solution of drilling problems in oil and gas industry taking into account ambiguities, complicating factors and influence of the environment" scientific project (2015–2017), funded by the Ministry of Science and Education of the Republic of Kazakhstan.

References

1. Sergaliyev, A., Umbetkulova, A.: Numerical simulation of drill-string dynamics with an initial curvature. Appl. Mech. Mater. **799–800**, 523–527 (2015)
2. Wenbin, Y., Hodges, D.H., Volovoi, V., Cesnik, C.E.S.: On Timoshenko-like modeling of initially curved and twisted composite beams. Int. J. Solids Struct. **39**, 5101–5121 (2002)
3. Kala, Z.: Stability problems of steel structures in the presence of stochastic and fuzzy uncertainty. Thin-Walled Struct. **45**, 861–865 (2007)
4. Novozhilov, V.V.: Foundations of the Nonlinear Theory of Elasticity. OGIZ, M.-L (1948)
5. Kudaibergenov, A., Kudaibergenov, A., Khajiyeva, L.: Stability analysis of drill rods as shells in the gas stream. Appl. Mech. Mater. **665**, 593–596 (2014)
6. Vaz, M.A., Patel, M.N.: Analysis of drill strings in vertical and deviated holes using the Galerkin technique. Eng. Struct. **17**, 437–442 (1995)

A Design of the Two Architectures of Electromagnetic Vibration Energy Harvesting Devices

M. Maták, M. Gašparík, P. Šolek and M. Margetin

Abstract This paper presents two architectures of electromagnetic vibration energy harvesters. The first presented architecture of vibration energy harvester is comprised by a coil rotationally moving in magnetic field. Design goal is to produce the harvester capable of effective operation in wide range of frequencies and able to utilize vibrations from all directions in one plane. This architecture is capable of utilizing the low frequency vibrations as well. During the experiment, a peak voltage of approximately 1.2 V has been measured at 25 Hz harmonic excitation. The second architecture is comprised by cylindrical magnet moving inside the PMMA tube, along the axis of a coil wound around this tube. Magnetic mass of the harvester is suspended on magnetic springs on both sides. Ease of manufacture and customization of the harvester are emphasized in the design to allow fitting the parameters of the harvester to existing condition of vibration source.

Keywords Vibration energy harvesting · Electromagnetic induction · Energy scavenging

1 Introduction

Energy harvesting (or energy scavenging) is process of transformation of ambient energy into useful electric energy. In past decade, energy harvesting has become a viable source of power for low-powered systems. These systems include various

M. Maták (✉) · M. Gašparík · P. Šolek · M. Margetin
Slovak University of Technology, Bratislava, Slovak Republic
e-mail: marek.matak@stuba.sk

M. Gašparík
e-mail: marek.gasparik@stuba.sk

P. Šolek
e-mail: peter.solek@stuba.sk

M. Margetin
e-mail: matus.margetin@stuba.sk

J. Beran et al. (eds.), *Advances in Mechanism Design II*,
Mechanisms and Machine Science 44, DOI 10.1007/978-3-319-44087-3_31

sensors and devices operating in remote areas. Utilizing the energy from ambient sources greatly enhances usability of such devices by making them practically maintenance-free and fully autonomous.

Sources of ambient energy that can be artificially harvested an their respective available power densities are: solar energy—approximately 15000 μW/cm^2 (outdoor, sunny day), mechanical vibrations—375 μW/cm^3, fluid flow—380 μW/cm^3, temperature variation—40 and 1 μW/cm^3 for both acoustic and radio frequency energy [1, 2].

2 Electromagnetic Energy Harvesting Devices

The source of ambient mechanical energy can be either movement of industrial structure due to its operation, movement of human body or fluid flow. The frequency of mechanical motions depends on its source and in general can be considered less than 10 Hz for human movements and approximately 30 Hz for machinery vibrations [1].

From point of view of transduction mechanisms used to transfer the kinetic energy of vibrations to electricity, four options are available: piezoelectric, electromagnetic, electrostatic and magnetostrictive. According to various authors [3, 4], piezoelectric generators are best suited for microscale applications, while for situations where miniature dimensions are not necessary, electromagnetic generators are preferred because no smart materials are required and electromagnetic generators are robust and sturdy.

2.1 Principle of Operation

From point of view of mechanics, most vibration energy harvesters are 1DOF systems with base excitation (Fig. 1). From point of view of mathematics, the system is described by 2nd order differential equation.

$$M\ddot{z} + b\dot{z} + kz = -m\ddot{y} \tag{1}$$

Multiplying Eq. (1) by relative velocity $\dot{z}$ we get the flow of mechanical power in the system. In Eq. (2), the first member represents the change of kinetic and

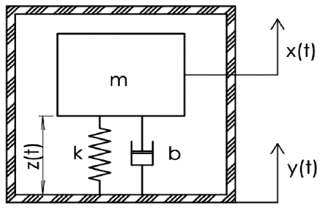

Fig. 1 Physical model of electromagnetic generator

potential energy, and the second member represents the power dissipated by the damper [5]. The members on the right side represent the power flow into system through spring and damper.

$$\frac{d}{dt}\left(\frac{m\dot{x}^2}{2}+\frac{k(x-y)^2}{2}\right)+b(\dot{x}-\dot{y})^2=b(\dot{x}-\dot{y})\dot{y}+k(x-y)\dot{y} \tag{2}$$

Damping in system is provided either by mechanical damping inherent to the structure and by electromagnetic damping, which occurs during transduction of mechanical energy to electric energy.

$$b=b_m+b_e \tag{3}$$

The expression $b\dot{z}^2$ in Eq. (2) represents all the power drawn from the system and only portion of it is available for transfer to electric power.

For harmonic excitation and steady state solution, we get following expression for the amplitude of relative displacement

$$Z=\frac{m\omega^2 Y}{\sqrt{(k-m\omega^2)^2+b^2\omega^2}}=\frac{r^2 Y}{\sqrt{(1-r^2)^2+(2\xi r)^2}} \tag{4}$$

The average power draw from the system is defined as

$$P_{av}=\frac{m\omega_0^3 Y^2\xi r^6}{(1-r^2)^2+(2\xi r)^2} \tag{5}$$

The maximum power draw from the system occurs at frequency ratio r defined as

$$r_{max}=\sqrt{2-4\xi^2-\sqrt{16\xi^4-16\xi^2+1}} \tag{6}$$

Maximum power draw from the system with given parameters occurs at frequency defined in Eq. (6). However, in design process, more important question is not the frequency ratio at which is the power output maximal for given generator, but the frequency ratio of harvester generating maximum power at given frequency of base excitation specific for the source. The generator should be tailored for the vibration source and not otherwise [3]. Using Eqs. (4) and (5) to redefine the average power P_{av} as a function of spring stiffness k, the r of the optimal generator is defined as:

$$r_{\max,k}=\sqrt{\frac{3}{1-2\xi^2+2\sqrt{\xi^4-\xi^2+1}}} \tag{7}$$

As Eqs. (6) and (7) show, the optimal generator for given frequency of source is operating at frequency ratio $r > 1$. A clear conclusion can be drawn from Eq. (5) that the higher angular frequency of the generator ω_n and larger amplitude of base excitation Y, the higher average harvested power. This means that it is much easier to get serious amount of power at higher frequency and therefore direct comparison of generator designs using only generated power as criterion is not always appropriate. Since machine vibrations occur at lower frequencies [6], it is important to present generator design capable of utilizing these vibrations effectively

2.2 *Architectures of Generators*

The vast majority of vibration generators use the effect of resonance to get the maximum possible power output. This fact makes them inherently narrowband [3]. The use of nonlinear springs to widen the resonance bandwidth is common. Design intent of both presented architectures is to produce a generator with broad bandwidth and the ability to operate effectively at low frequency.

2.2.1 Architecture 1

The architecture 1 is an attempt to produce generator capable not based on resonance principle with the added benefit of being able to harvest energy equally from all directions in plane of the generator. It is in concept similar to generator presented in [7], but with different arrangement. The generator uses the movement of the coil in magnetic field and its layout resembles the hard disk drive actuator arm. The generator is depicted on Fig. 2b. Two variants of this architecture (marked as type 1 and type 2) have been assembled and tested, the only difference between them being the arrangement of the magnets.

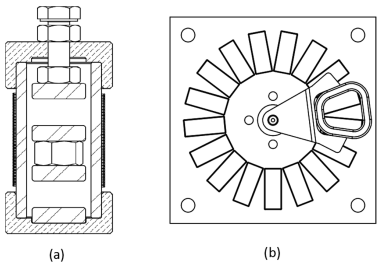

Fig. 2 Architectures 1 and 2 of proposed harvesters

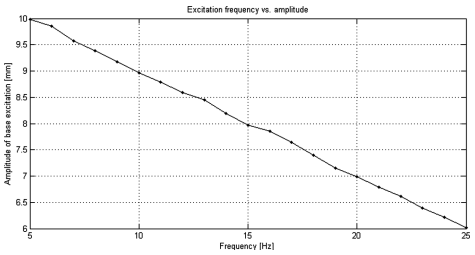

Fig. 3 Amplitudes of harmonic excitation

2.2.2 Architecture 2

The second architecture is a translational generator utilizing the motion of magnet inside the coil. The repelling force of neodymium magnets has been used as a nonlinear spring [8]. The generator has been designed with adjustable preload of magnetic springs and various configurations of inner magnets has been considered as well. Two samples (marked V1 and V2) with different dimensions and inner magnetic members has been assembled and tested. The layout of harvester is pictured in Fig. 2a.

2.3 Measured Results

Both architectures of generators have been tested on hydraulic actuator. Since our interest lies in low frequency range, the harvesters has been excited by harmonic signal with frequency range from 5 to 25 Hz. The measured data have been obtained using the NI myDAQ device. Measured physical parameter was voltage. The amplitudes of excitation are depicted in Fig. 3. Figure 4 shows the raw measured data for both architectures and variants. After processing the measured data using Matlab, average harvested voltages and powers have been calculated for both

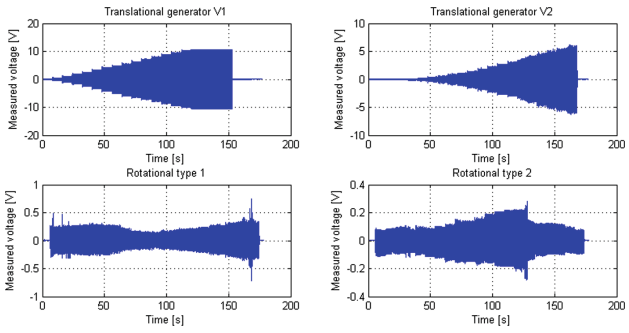

Fig. 4 Raw measured data

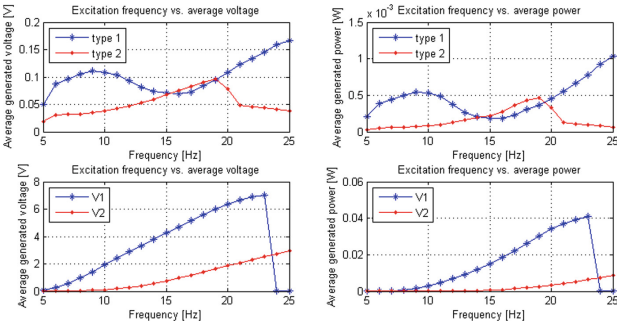

Fig. 5 Processed results for architectures 1 and 2

types of generators for both architectures. Average voltages and powers for architectures 1 and 2 are shown in Fig. 5.

3 Conclusion

As the measured results show, both harvesters of architecture 1 struggle to get usable voltage. On the other hand, architecture 2 has performed above expectations with V1 harvester even exceeding the voltage limit of NI myDAQ used to measure the output voltage. The results shown in this article are from initial testing, there is a solid potential for further growth.

Acknowledgments The authors would like to thank the Ministry of Education of SR for financially supporting this research under contract VEGA 1/0742/15

References

1. Priya, S., Inman, D.: Energy Harvesting Technologies. Springer Science+Business Media, New York (2009). ISBN 978-0-387-764463-4
2. Galchev, T.V.: Energy Scavenging from Low Frequency Vibrations. University of Michigan (2010)
3. Spreeman, D., Manoli, Y.: Electromagnetic Vibration Energy Harvesting Devices: Architectures, Design, Modeling and Optimization. Springer Science+Business Media (2012). ISBN 978-94-007-2943-8
4. Chalasani, S., Conrad, J.M.: A survey of energy harvesting sources for embedded systems. In: IEEE Southeastcon 2008. ISBN 978-1-4244-1883-1
5. Stephen, N.G.: On energy harvesting from ambient vibration. J. Sound Vib. **293**, 409–425 (2006)
6. Sardini, E., Serpelloni, M.: An efficient electromagnetic power harvesting device for low-frequency applications. Sens. Actuators A **172**, 20161 (2011)

7. Spreeman, D., Folkmer, B., Mintenbeck, D., Manoli, Y.: Novel non-resonant vibration transducer for energy harvesting. PowerMEMS (2005)
8. Tan, Y.K.: Sustainable Energy Harvesting Technologies. InTech, Rijeka (2011). ISBN 978-953-307-438-2

Acoustic Solution for a Car Cab Interior

P. Němeček

Abstract The paper describes a process focused on sound acoustic issues inside a car cab ("enclosed space"). The problem is solved experimentally with the use of noise measurements and interior-panel-vibration measurements with the aim to reduce noise at such a level that would allow a comprehensive communication among passengers.

Keywords Car interior · Noise · Language comprehension · Verbal communication among passengers

1 Introduction

Noise solutions in "enclosed space" represent a wide topic—covered mainly by so called "Building acoustics" and are defined by specific quantities and solutions, which are based on insulating materials. In the view of Acoustics, the car interior is quite specific space. Its "particularity" is defined by relatively small dimensions and space volume, space design based on structural principles, defined "acoustic" surfaces (e.g. glass panels), objects (e.g. seats), people and noise-sources location (e.g. engine, wheels etc.), commercially lead "interior" design (an esthetic issue), a certain similarity of car interior designs and quite contradictory requirements of a structural interior design [1, 2].

1.1 Physical Ground

Technical acoustic is based on measurements and data processing mainly. Exact and quality measurements are a ground for modelling and value(s) definitions used

P. Němeček (✉)
Technical University of Liberec, Liberec, Czech Republic
e-mail: pavel.nemecek@tul.cz

J. Beran et al. (eds.), *Advances in Mechanism Design II*,
Mechanisms and Machine Science 44, DOI 10.1007/978-3-319-44087-3_32

further on for data evaluations. Most of such models are based on equations mentioned below (1) and (2). Acoustic pressure at any point within certain space must meet the wave equation:

$$\frac{\partial^2 p}{\partial x^2} + \frac{\partial^2 p}{\partial y^2} + \frac{\partial^2 p}{\partial z^2} = \frac{1}{c^2} \cdot \frac{\partial^2 p}{\partial t^2}. \tag{1}$$

The relation between acoustic velocity and acoustic pressure in the direction of r "carrier" within certain space is described by the motion equation:

$$\frac{\partial u}{\partial t} = -\frac{1}{\rho} \cdot \frac{\partial p}{\partial r} \tag{2}$$

Equations (1) and (2) arise from the acoustic energy spread theory and put together acoustic pressure and acoustic velocity depending on environmental constants and on time. Equations (1) and (2) are usable for theoretical solutions but in real applications they cope with unavailability of an acoustic pressure description (a concrete one) and its dependency on "the" location and "the" time. Nevertheless, these equations are valid in a universal point of view—thus for the car interior, as well.

Than it is necessary to define two theoretical forms of a sound field. A sound field is space through which sound waves are spread out.

1. Free Sound Field—a sound is spread out from a sound-source in the form of waves, where levels of acoustic pressure, acoustic velocity and sound intensity are equilibrated in relation to the "size" of relative values):

$$L_P = L_M = L_I \tag{3}$$

2. Diffusion Field—represents an omnidirectional sound-wave incidence. Levels of acoustic quantities are not equilibrated:

$$L_P \neq L_a \neq L_I \tag{4}$$

2 An Acoustic Situation Inside a Car-Cab

It should be noted that the self-supporting coachwork is composed of flexible components, which have significant resonance frequencies, components of 2D or 3D symmetry (bonnets, roofs)—so that modal characteristics (locations of nodes and antinodes) are exacerbated—and of cavities through which acoustic energy spreads out easily. So, we can observe that supporting parts without acoustic (anti-noise) modifications exacerbate noise conditions. A vehicle can be divided into 3 sections as regards acoustic (anti-noise) modifications. We consider a car

with an engine in the front, with a front-wheel drive and a separate trunk in the rear, so the mentioned sections are:

(1) Engine Space
(2) Car-cab (the interior space)
(3) Trunk (the luggage space)

There are sound-absorbing materials "used" with a car. They are applied (practically) inside the whole car and are thought for inner-and-outer noise reduction. Generally speaking, sound-absorbing materials represent a compromise for contradictory requirements as regards their applications (e.g. a vehicle weight/a vehicle price/further processing/ecological issues—like disposal, design features etc.).

3 Interior Measurement Possibilities

3.1 RASTI Method

The car interior is designed for passenger transport (primarily) aiming at comfort and safety issues. An easy-communication requirement is in fact a minimal language-signal disturbance requirement. The RASTI (**RA**pid **S**peech **T**ransmission **I**ndex) method represents a universal method that is used to evaluate a concrete (artificial) language-signal in a noisy background in relation to the speaker location. The RASTI Index (in the range of 0–1) "classifies" an interior according to its sound quality—and places the interior into one of 5 groups (1 is for excellent comprehension, 0 is for bad comprehension).

3.2 Articulation Index

The index arises from a mathematically processed noise-spectra measurement at a given point of an interior. It evaluates only the "state" at the given point (not the transmission or the source). The space is not "aroused" by a special signal (as with the RASTI Method), but its features are evaluated through masking a frequency spectrum of a speech-signal by a background noise.

4 Solution Steps

4.1 Problem Definition

The anti-noise applications in the car cab are based on a combination of sound-absorbing materials and objects according to given requirements—criteria as

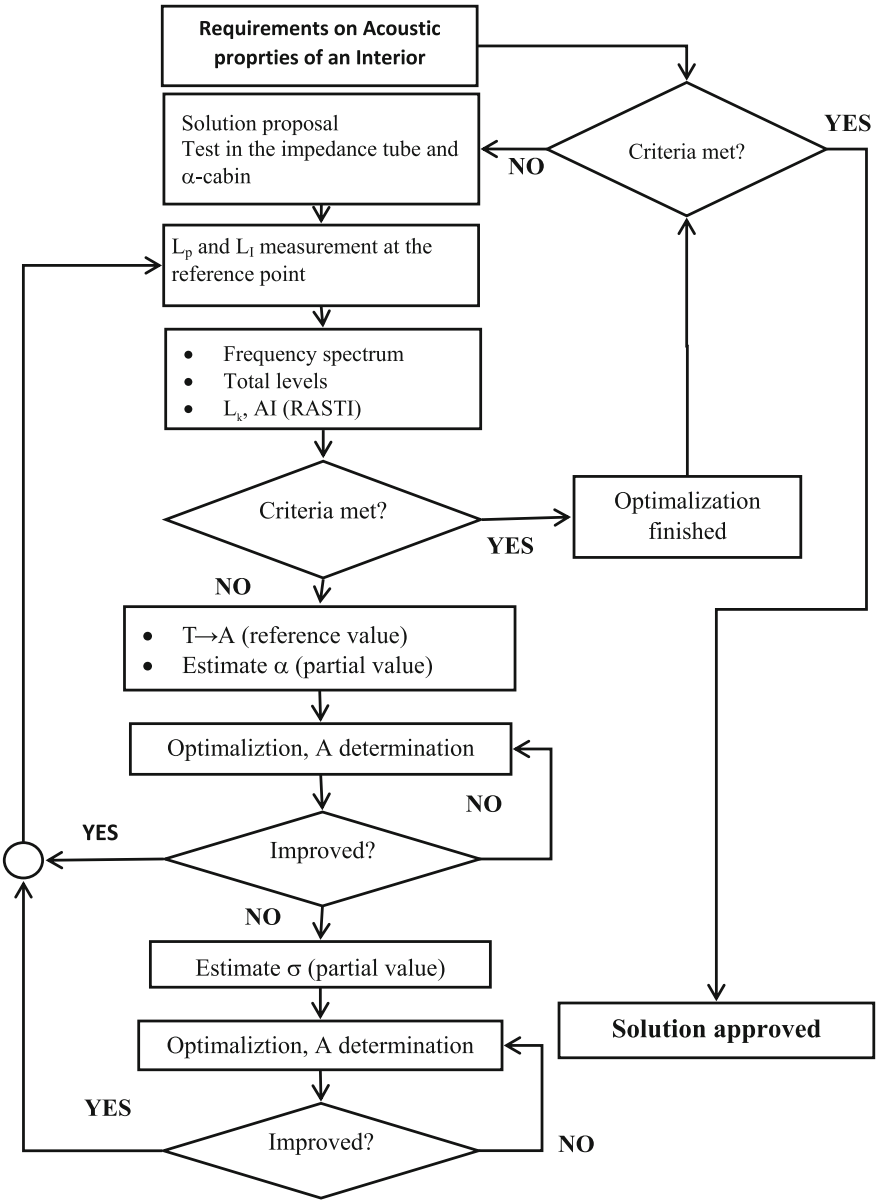

Fig. 1 Flow chart of an acoustic solution made for a car cab interior

regards functions, a safety and an operation of a vehicle. The noise evaluation is made after the a.m. criteria are met. A problem of such noise is its "changeability" in source acoustic performance as regards sound-level and frequency (an engine, wheels, air-conditioning etc.). (Fig. 1).

4.2 Proposed Procedure

(1) To determine targets to be achieved
(2) To use all noise-reducing possibilities primarily (in a vehicle). It means to use components of low-acoustic performance, low vibration levels, flexible mounting etc.
(3) To accept the interior design
(4) To describe the features of an interior with the use of acoustic quantities
(5) To propose measures to improve acoustic parameters
(6) To realize such proposals/applications
(7) To verify impact of the final realization/applications

An important complication for such acoustic improvements and applications is the interior design. Its shape, dimensions and location of glass panels and limitations in use of anti-noise (acoustic) materials. We can recommend a measurement of 5 "crucial" quantities to describe a car interior:

(1) Levels of acoustic pressure dB (A) and third octave sound frequency spectra. Articulation indexes and other needed data can be derived from such measured values. The measuring points are located above passenger heads.
(2) RASTI values for individual couples of communicating passengers. As in the previous case, it is not an "established" value.
(3) Sound termination time (a direct criterion of sound-absorption α) is crucial for next steps
(4) Sound-absorption measurements—A—of individual interior panels
(5) Transmission Coefficient Measurement σ—calculating vibration change of boundary surfaces into acoustic energy

Physical restriction of a technical solution:

- Engine speed revolution frequency and doubled harmonic revolution frequency are both within the range of 50 to 100 Hz. To reduce acoustic features of these frequencies we would need a material of 900 to 1700 mm thickness—which is unthinkable. So, "acceptable" primarily modifications of engine and its mounting are recommended.
- Considering a concrete insulation material thickness to be e.g. 20 mm, we can work with frequencies above 5 kHz. Nevertheless, objects of a higher thickness are applied in the vehicle e.g. passenger seats, sound absorption of which, cannot be determine with α.

4.3 Procedure Application

(1) It is necessary to determine the reference point (the center of front seats at the level of passenger heads).

(2) Noise level and sound intensity at the reference point (in 3 directions) with reference revolutions (mostly 3000 min^{-1}) and RASTI index are measured then.
(3) The Articulation Index and The Reactivity Index are determined from acoustic pressure levels and sound intensity.
(4) An estimate of component acoustic absorption is derived from the Reactivity Index

I would like to point out that the correlation of AI and RASTI is very good in car cab ("enclosed space").

5 Sound Transmission Estimate of Vibrating Panels

Noise coming from individual sources (engine, wheels and their suspensions etc.) gets into the car cab directly through coachwork parts or it is indirectly transmitted by panel(s) vibrations. These panels must be identified and their primary insulating features must be evaluated. It is recommended to cover them with a material that will increase their inner acoustic (it is a material, which will muffle them). We work on the assumption that acoustic power is proportional to acoustic impedance of air, surface, Square of effective vibration velocity and transmission coefficient σ. The coefficient is increasing with increasing frequency and therefore it is necessary to decrease that at higher frequencies. It is possible with the use of shape modifications like ribbing or breaking surface symmetry or applying highly muffling materials on panel surfaces.

6 Conclusion (Solution Summary)

A problem was defined in the given space (a car cab interior) and a procedure of a possible solution was described. Concrete steps represent a combination of objective methods to describe acoustic field in the car cab interior. The targeted outcome is a comprehensive communication of passengers and thus improvement of their safety. A comprehensive communication will be "arranged" with the use of suitable and appropriate insulating materials and by their right application.

References

1. Apetaur, M., Ráfl, J.: Konstrukce automobilů díl I – Hluk motorových vozidel. Vydavatelství ČVUT, Praha (1994). ISBN 80-01-01224-7
2. Stěnička, J.: Šíření a vyzařování hluku konstrukcemi. ČSVTS, Praha (1990). ISBN 80-02-00016-1

Possibilities for Reducing Car Gearbox Vibration and Noise

E. Tomeh

Abstract This article deals with the possibilities for reducing car gearbox vibration and noise in connection with the production quality of its parts on machine tools. The technical condition of these machine tools is monitored by vibration diagnostics. The article explains as well the method of gear pinion machining. The accuracy of manufacture, installation and adjustment of the gearbox mechanisms and the method of machining gearbox pinion (grinding or superfinishing) contribute significantly to the overall level of car gearbox vibration and noise. The location of gears and bearings has also a similar effect. The level of production, assembly and the superfinishing method in processing the gearbox pinion are shown in the vibration spectrum as affecting the reduction of gearbox noise and vibration.

Keywords Vibration · Noise · Gearbox · Grinding · Superfinishing

1 Introduction

The technical diagnostics of machines and equipment is mainly based on vibration measurements and analysis of all critical components of these machines for predefined operation conditions and at the stage of installation of the new machine and its subsequent operation. One of the possible noise sources in the car is the drive system, which includes the gearbox.

Frequency analysis of vibration spectra is a modern tool for the process of identifying the mechanical defects that affect the quality of production, assembly and overall noise in car gearboxes. The analysis of vibration spectra is performed using frequency analysis methods and means of technical diagnostics that monitor the influence of gears and rolling element bearings in a complex gearbox.

The article deals with the possibilities of reducing car gearbox vibration and noise in connection with various methods of machining the pinion (grinding, superfinishing) with bearing diameter 32h5 (see Fig. 1). The bearing is fitted to the diameter

E. Tomeh (✉)
Technical University of Liberec, Liberec, Czech Republic
e-mail: elias.tomeh@tul.cz

J. Beran et al. (eds.), *Advances in Mechanism Design II*,
Mechanisms and Machine Science 44, DOI 10.1007/978-3-319-44087-3_33

Fig. 1 Grinded pinion diameters

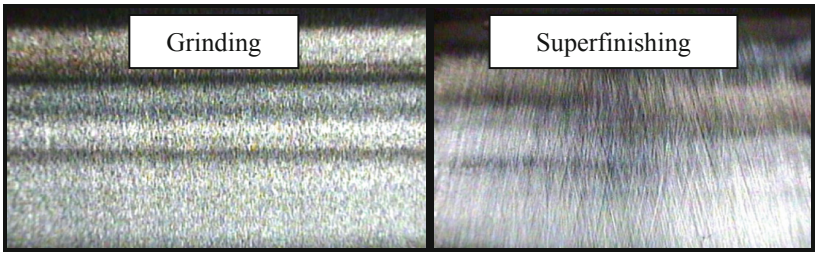

Fig. 2 The difference in machining a gearbox pinion

32h5 without an inner ring, so that the cylindrical pin serves as the inner rolling surface of the bearing. The difference in machining a grinded and super-finished pinion is shown in Fig. 2.

2 Measurements Analysis

On the stand (see Fig. 3) and using a measuring instrument—the vibration analyser—the noise of the gearbox with an accordingly machined gear pinion was evaluated. The next steps were to remove the pinion from the gearbox, then to

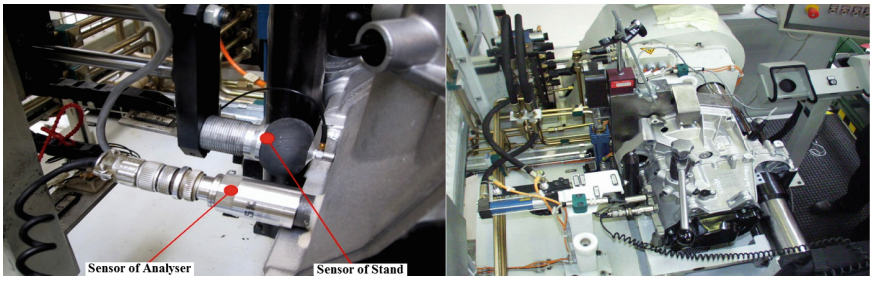

Fig. 3 Determination of measuring points

Table 1 Resulting overall values of bearings noise amplitude

Velocity	Pinion grinding a_{ef} [G_s]—envelope method		Pinion superfinishing a_{ef} [G_s]—envelope method	
	In traction	Backward	In traction	Backward
1	0.216	0.192	0.034	0.028
2	0.163	0.144	0.023	0.021
3	0.164	0.181	0.025	0.020
4	0.187	0.201	0.025	0.029
5	0.200	0.258	0.029	0.045

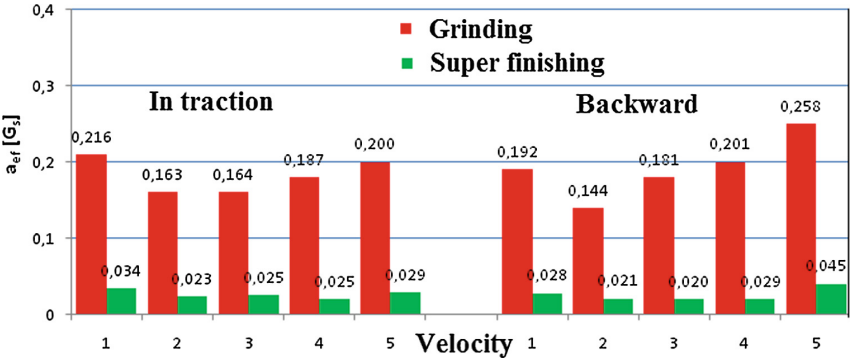

Fig. 4 Graphical comparison of noise for a grinded and super-finished pinion

super-finish it on the superfinishing machine, to mount it back in the gearbox, to measure it and to evaluate the gearbox noise once more. The analysis of the spectral envelope measurements shows that superfinishing a cylindrical diameter of 32h5 has decreased gearbox noise (see Table 1 and Fig. 4).

3 Measurement Protocols of Gear Parameters

The gearing involute profile and pitch helix curves were measured including the nominal values of the above parameters. The measurement informed us about the components kinematics (throw, pitch). The drawing tolerance of the parameters is also included in the measurement protocol.

4 Example of Measured Noise Spectra

The first example refers to the first gearing speed level, where gearing noise tolerance parameters didn't significantly comply. The parameters fHβ exceeded by about 50 μm and fHα by about 10 μm. Figure 5 shows measured spectrum—MIX—In Traction.

The picture shows the difference between this case (the red curve) and the serial measurement of non-defective gearboxes of the same day (black line).

The measured spectrum shows the whole continuous spectrum as relatively elevated. The first harmonic frequency (Ord 14), corresponding to the first gearing speed level, is within the norm in comparison with non-defective gearboxes. But the second (28 Ord) and the third (42 Ord) harmonic frequencies of this gearing are in comparison with others increased by up to 10 dB.

The second example relates to the missing process. On the assembly line, a gear of the third speed level was released without performing the final process of teeth finishing (grinding)—the gear was therefore only milled. This defect was very much reflected on the gearbox measured spectra. The noise level was increased not only when the mention third gear was loaded (Fig. 6) but also in all other gears, even when the third one was not loaded. In the measured spectrum of the third gear, increased component harmonic frequencies are displayed including their sidebands.

In the other gears, the harmonic frequencies belonging to the mentioned third speed level were evident.

As a demonstration, here is noise spectrum MIX for the fifth speed level In Traction (Fig. 7). It is evident that the manifestation of the first (35 Ord—106 dB) and the second (75 Ord—103 dB) harmonic frequencies of the defective gear are identical to that when the gear was loaded.

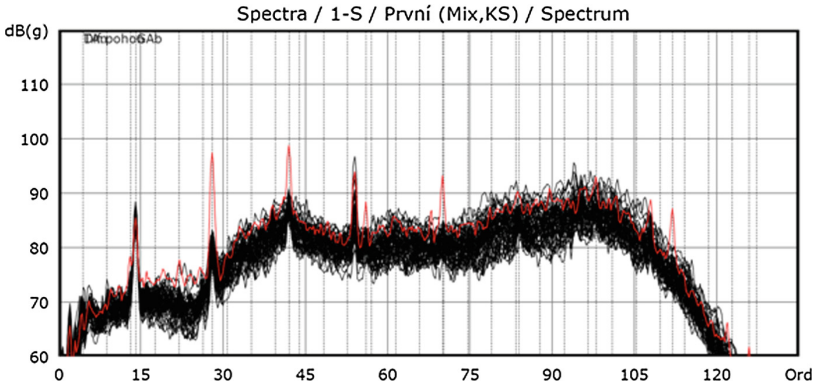

Fig. 5 Noise spectrum 1-S (MIX)

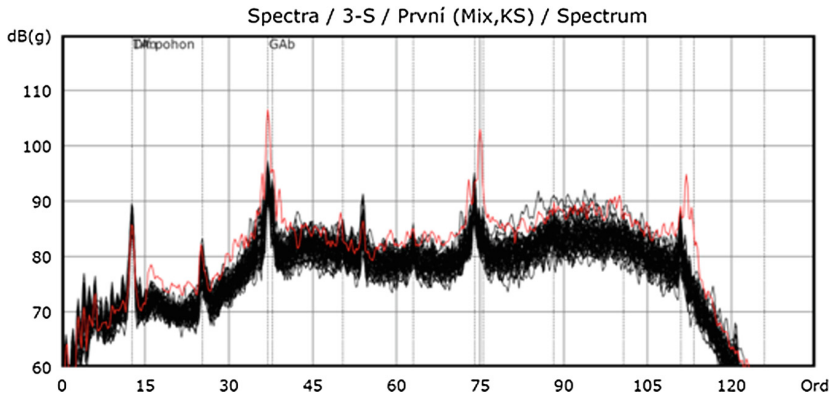

Fig. 6 Noise spectrum 3-S (MIX)

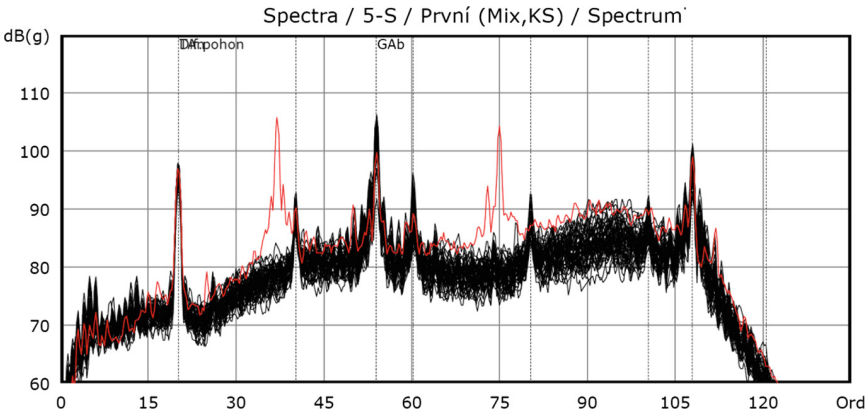

Fig. 7 Noise spectrum 5-S (MIX)

The grinded pinion on stand showed increased noise at all speed levels and for In Traction and Backward (Fig. 8). The green curve is for the super-finished pinion, the black one is for the grinded pinion.

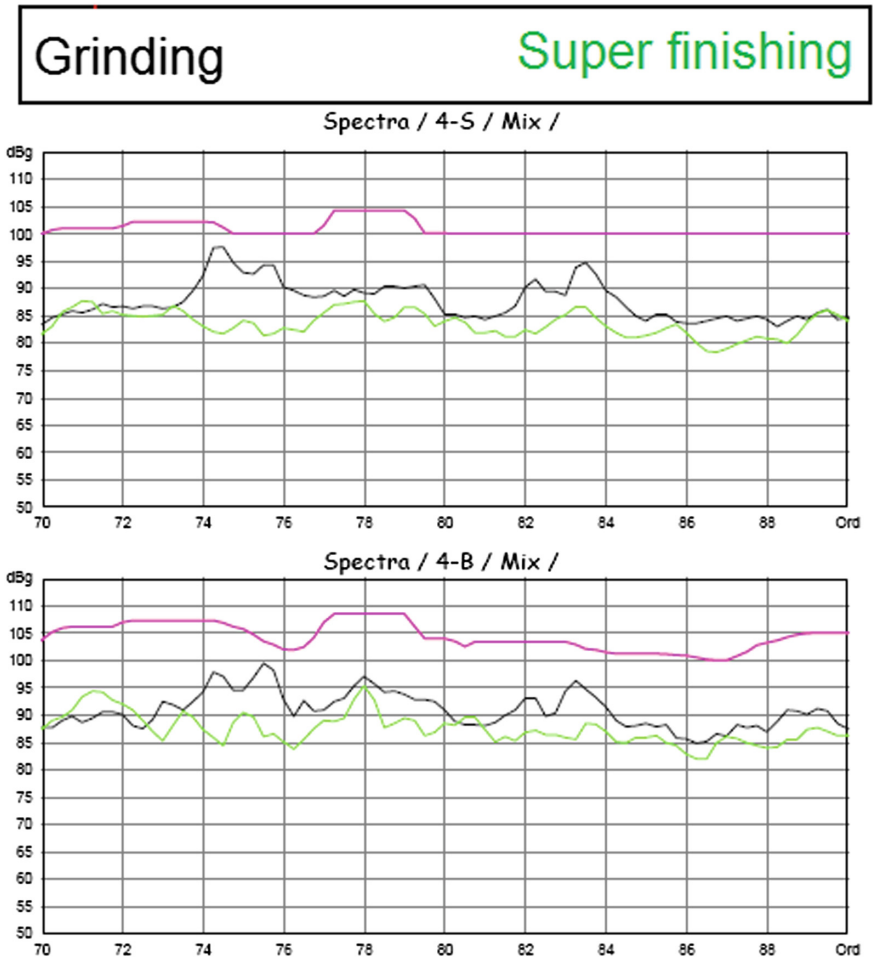

Fig. 8 Order analyses for 4th and 5th speed levels in traction and backward

5 Conclusions

The article discusses the influence of the processing methods (grinding or super-finishing) for a pinion with a 32h5 bearing diameter on the resulting car gearbox noise. For both mentioned technologies, measurements of the overall vibration levels on the stand, as well as the frequency and envelope analyses were evaluated for each gear speed.

The most effective influence on decreasing the overall vibration levels in a gearbox appeared in the analysis of spectral envelopes on a pinion of 32h5 diameter, which serves as inner ring of bearing. It was reduced by 86 % on average. Furthermore, comparing orders analyses on the stand, the noise was reduced on the

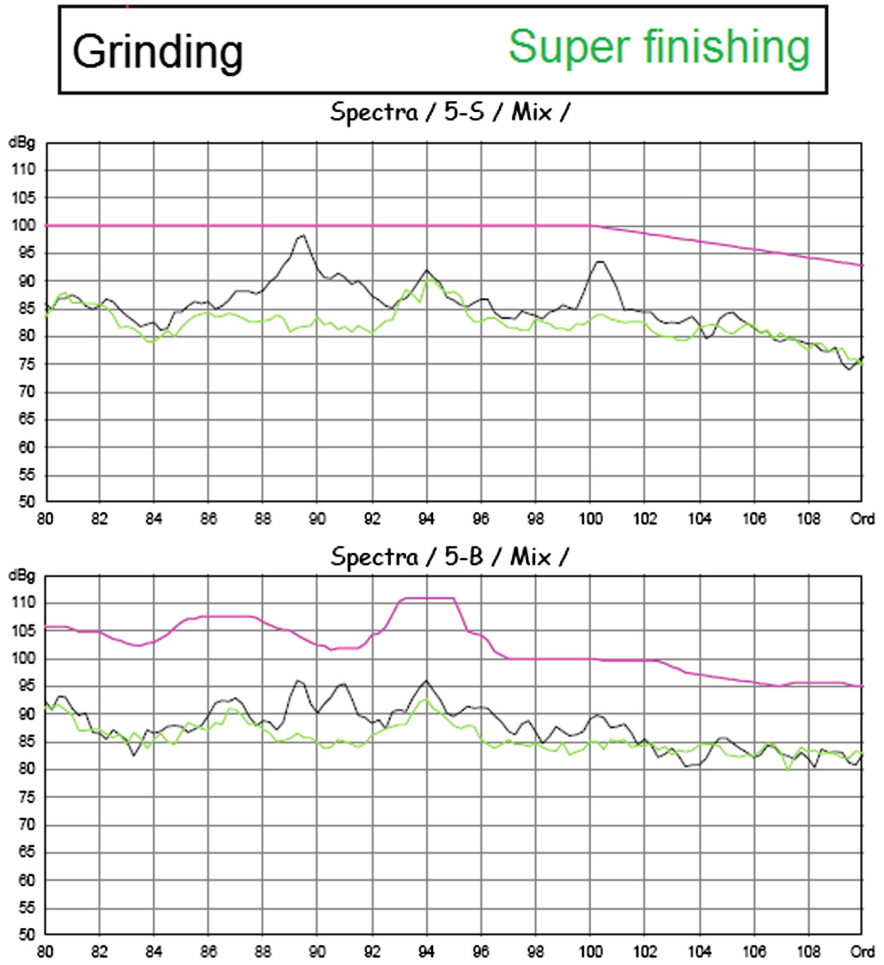

Fig. 8 (continued)

super-finished pinion by up to about 15 dB in some orders. For these reasons, it is possible to state that superfinishing has a great impact on the overall noise of car gearboxes.

Acknowledgments The paper has been elaborated with financial support of TUL in the framework of specific university research competition.

References

1. Tomeh, E.: Technická diagnostika: vibrační diagnostika strojů a zařízení. Skripta TU v Liberci, p. 220 (2015). ISBN 978-80-7494-174-0
2. Tomeh, E.: Identify the sources of vibration and noise on cars gearbox by spectral analysis. In 54th International Conference of Machine Design Departments, p. 6, Sept 2013. ISBN 978-80-7372-986-8
3. Tomeh, E.: Diagnostic Methodology of Rolling Element and Journal Bearings, p. 66. Textbook TU in Liberec (2007). ISBN 978-80-7372-278-4
4. Moravec, V.: Konstrukce strojů a zařízení II. Montanex a.s. (2001)

Reduced Order Analyses of Multi-stage Coupled Structures with Main Focus on Disk-Dominated Modes

R. Weber and A. Kühhorn

Abstract Rotors manufactured as blisk (Blade Integrated Disk) has become state-of-the-art in turbomachinery. This integral design saves a lot of mass and enables higher rotational speeds allowing for higher pressure ratios and hence an increased efficiency. The advantage comes along with the drawback that the structural damping level is extremely low. Nowadays, the dynamics of single-stage rotors is well-investigated, as dynamical analysis of cyclic structures is one of the most important subjects in applied research in turbomachinery. However, the stage-to-stage coupling effect is neglected in most cases. The importance of proper interstage treatment is obvious for adequate multi-stage analyses. Hence the structural dynamics of a multi-stage assembly has recently become an important area of research. In this paper, some multi-stage effects are discussed and three different reduced order techniques are summarized and demonstrated on a multi-stage assembly of academic blisks. The findings are compared to a FE-solution. Particular attention must be paid to disk-dominated modes, which are highly affected by multi-stage behavior. Mistuning modeling is not considered, because it mainly influences blade-dominated vibrations.

Keywords Turbomachinery · Blisk vibration · FEM · Reduced order model · Multi-stage coupling

1 Introduction

In turbomachinery, rotating structures are assessed by dynamic analyses of their operating behavior. Dynamic analyses of high pressure compressors assume some simplifications. First of all, it is common to fulfill stage by stage analyses. It is then possible to investigate the complete cyclic structure by analyzing an elementary

R. Weber (✉) · A. Kühhorn
Brandenburg University of Technology, Cottbus, Germany
e-mail: robby.weber@b-tu.de

A. Kühhorn
e-mail: kuehhorn@b-tu.de

J. Beran et al. (eds.), *Advances in Mechanism Design II*,
Mechanisms and Machine Science 44, DOI 10.1007/978-3-319-44087-3_34

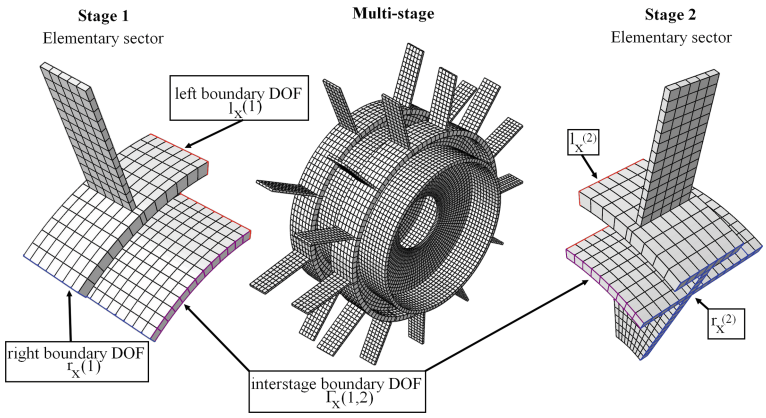

Fig. 1 Elementary sectors (rotor 1 and 2) and multi-stage assembly

sector using cyclic symmetry boundary conditions [1]. However, due to manufacturing or material tolerances, there are no identical blades. In order to consider small mistuning and to estimate resulting amplification factors, various reduced order models (ROMs) are invented [2, 3], adapted and advanced.

Since stage methods will not predict dynamic behavior of the assembled compressor with adequate accuracy. Stage-to-stage coupling effects may significantly impact eigenfrequencies and modes. A priori, disk-dominated modes are highly affected whereas blade-dominated modes hardly contribute to interstage coupling [4].

This paper summarizes different methods [2, 5, 6] to calculate Multi-stage modes at moderate costs. Aiming at a drastic reduction of the DOF-number, different reduced order models are applied. These techniques are demonstrated by means of academic sample rotors, shown in Fig. 1. Since every ROM implies errors compared to a full FE-model, results from a full analysis are used as reference.

First, the dynamic of the assembly is characterized and interesting modes, which demonstrate the need of a Multi-Stage analysis, are identified. Since the main focus of this paper is on disk-dominated Multi-Stage modes and blade individual mistuning particularly modify blade-dominated modes, mistuning is neglected here. However, there are ways to consider small deviations (e.g. material property), if the interaction between blade induced mistuning and stage-to-stage coupling were discussed.

2 Dynamics of the Multi-stage Assembly

Figure 1 depicts a two staged academic compressor, which is evaluated in this paper. The geometry is quite simple; however basic characteristics (e.g. blade-dominated, disk-dominated modes and interactions) appear.

Although Rotor 1 consists of 9 blades and Rotor 2 is composed of 13 blades, the assembled mesh is compatible. Thus, FE-meshes of both rotors are matching along

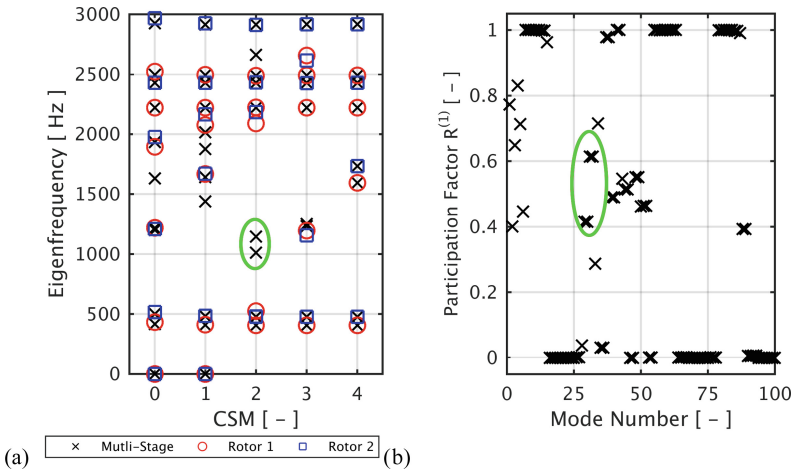

Fig. 2 Influence of interstage coupling: **a** eigenfrequency versus periodic index map **b** relative stage participation (Color figure online)

the interstage boundary. If the meshes are incompatible, multipoint constraints are used to ensure interstage coupling.

The dynamics of the assembled structure is determinate by a modal analysis. Furthermore, single stage modal analyses with cyclic symmetry boundaries of both rotors are performed. Figure 2a shows the eigenfrequencies versus the corresponding periodic parameter (cyclic symmetry mode). Even though single stage modal analyses yield passable results in blade-dominated mode families, there are critical inaccuracies in disk-dominated regions (e.g. green mark in Fig. 2a).

Figure 2b reflects the relative participation of stage 1. The Participation Factor $R_k^{(s)}$ [4] expresses the portion of elastic strain energy for the *k*th mode of stage (s). Values around 1.0 indicate that main fraction of elastic energy is concentrated on stage 1. Values near 0.0 imply stage 2 dominated modes. Obviously, there are mode families localized on a single stage, but there are mixed modes as well. One can find that mixed modes tend to be badly predicted in single stage analyses (e.g. Modes 29–33 are non-represented in the single stage cyclic symmetry analyses of Fig. 2a).

3 Reduced Order Model of Multi-stage Structures

Every ROM presented subsequently uses the mass and stiffness information from one elementary sector of each stage to build a reduced equation of motion of the unreduced assembly. The damped equation of motion (EOM) can be written as

$$\mathbf{M}\ddot{\mathbf{x}} + \mathbf{C}\dot{\mathbf{x}} + \mathbf{K}\mathbf{x} = \mathbf{f_e}. \tag{1}$$

The coupling of both stages is the cornerstone. It can be achieved by introducing geometrical constrain **A** between interstage degrees of freedom (DOF)

$$\Delta^{\Gamma}\mathbf{x} = \mathbf{A} \cdot {}^{\Gamma}\mathbf{x}^{(1)} - {}^{\Gamma}\mathbf{x}^{(2)} = 0. \tag{2}$$

3.1 Multi-stage Multi-level Craig-Bampton Approach

Basically, this ROM (*msmlcb*) [2] differentiates between inner ${}^{i}\mathbf{x}$ and outer ${}^{b}\mathbf{x}$ DOF. Here, the outer DOF contain left and right boundary DOF as well as interstage DOF. The EOM of an elementary sector is rearranged as

$$\begin{pmatrix} {}^{ii}\mathbf{m} & {}^{ib}\mathbf{m} \\ {}^{bi}\mathbf{m} & {}^{bb}\mathbf{m} \end{pmatrix} \cdot \begin{pmatrix} {}^{i}\ddot{\mathbf{x}} \\ {}^{b}\ddot{\mathbf{x}} \end{pmatrix} + \begin{pmatrix} {}^{ii}\mathbf{k} & {}^{ib}\mathbf{k} \\ {}^{bi}\mathbf{k} & {}^{bb}\mathbf{k} \end{pmatrix} \cdot \begin{pmatrix} {}^{i}\mathbf{x} \\ {}^{b}\mathbf{x} \end{pmatrix} = 0. \tag{3}$$

The inner DOF can be expressed by eigenmodes $\mathbf{\Phi}$. Constraint modes $\mathbf{\Psi}$ are introduced to ensure the static solution. The reduction is executed as

$$\langle \mathbf{M}, \mathbf{K} \rangle_{CB} = \mathbf{T}_{CB}^{T} \cdot \langle \mathbf{M}, \mathbf{K} \rangle \cdot T_{CB} \tag{4}$$

with

$$\mathbf{T}_{CB} = \begin{pmatrix} \mathbf{\Phi} & \mathbf{\Psi} \\ 0 & \mathbf{I} \end{pmatrix} \quad \text{while} \quad \begin{matrix} \omega^2 \cdot {}^{ii}\mathbf{m} \cdot \mathbf{\Phi} = {}^{ii}\mathbf{k} \cdot \mathbf{\Phi} \\ {}^{i}\mathbf{x} = -{}^{ii}\mathbf{k}^{-1} \cdot {}^{ib}\mathbf{k} \cdot {}^{b}\mathbf{x} = \mathbf{\Psi} \cdot {}^{b}\mathbf{x} \end{matrix} \tag{5}$$

Once the reduction step is completed, the single stage system can be synthesized with another Boolean that connects adjoining sectors [2]. Both stages are reduced, but still uncoupled. However, there is a huge amount of DOF in ${}^{b}\mathbf{x}^{(s)}$, which are useless from now on. Therefore a second Craig-Banpton reduction can be performed. Thereby only the interstage boundary DOF are obtained physically. Equation 2 yields a constraint to the multi-stage system Eq. 6.

$$\langle \mathbf{M}, \mathbf{K} \rangle = \begin{pmatrix} \mathbf{I} & \mathbf{0} & \mathbf{0} & \mathbf{0} \\ \mathbf{0} & \mathbf{I} & \mathbf{0} & \mathbf{A}^{T} \\ \mathbf{0} & \mathbf{0} & \mathbf{I} & \mathbf{0} \end{pmatrix} \cdot \begin{pmatrix} \langle \mathbf{M}, \mathbf{K} \rangle_{CB}^{(1)} & \mathbf{0} \\ \mathbf{0} & \langle \mathbf{M}, \mathbf{K} \rangle_{CB}^{(2)} \end{pmatrix} \cdot \begin{pmatrix} \mathbf{I}\,\mathbf{0}\,\mathbf{0} \\ \mathbf{0}\,\mathbf{I}\,\mathbf{0} \\ \mathbf{0}\,\mathbf{0}\,\mathbf{I} \\ \mathbf{0}\,\mathbf{A}\,\mathbf{0} \end{pmatrix} \tag{6}$$

On that account the DOF in Eq. 1 are sorted as

$$\mathbf{x} = \begin{pmatrix} \mathbf{q}^{(1)} & {}^{\Gamma}\mathbf{x} & \mathbf{q}^{(2)} \end{pmatrix}^{\mathrm{T}}. \tag{7}$$

3.2 Multi-stage Cyclic Symmetry Method

This method (called *mscsm*) [5] forgoes physical DOF and transforms Eq. 2 in cyclic symmetry modes [1]. Prior to this, left intersector DOF of each sector ${}^{l}\mathbf{x}$ are eliminated with respect to the corresponding nodal diameter n

$$^{l}\mathbf{x} = \mathrm{e}^{\mathrm{j}2\pi n/N} \cdot {}^{r}\mathbf{x}. \tag{8}$$

The matrices are reduced in an equal way. The physical coordinates of the complete blisks are obtained by

$$\mathbf{x} = \mathbf{e}_n \otimes \tilde{\mathbf{x}}_n \text{ with } \mathbf{e}_n = \begin{pmatrix} 1 & \mathrm{e}^{\mathrm{j}2\pi/N} & \dots & \mathrm{e}^{\mathrm{j}(N-1)2\pi n/N} \end{pmatrix}^{\mathrm{T}}. \tag{9}$$

Assuming different numbers of sector $\mathrm{N}^{(1)}$ and $\mathrm{N}^{(2)}$, one find corresponding equivalent nodal diameters $n(p)$ [5]. Considering Eq. 2, the dynamics of the multi-stage structure of one nodal diameter p can be expressed as

$$\mathbf{T}_p^* \cdot \begin{pmatrix} \mathbf{M}_{n(p)}^{(1)} & \mathbf{0} \\ \mathbf{0} & \mathbf{M}_p^{(2)} \end{pmatrix} \cdot \mathbf{T}_p \cdot \ddot{\tilde{\mathbf{x}}}_p + \mathbf{T}_p^* \cdot \begin{pmatrix} \mathbf{K}_{n(p)}^{(1)} & \mathbf{0} \\ \mathbf{0} & \mathbf{K}_p^{(2)} \end{pmatrix} \cdot \mathbf{T}_p \cdot \tilde{\mathbf{x}}_p. \tag{10}$$

The transformation matrix $\mathbf{T}_p$ is defined by

$$\mathbf{T}_p = \begin{pmatrix} \mathbf{I} & \mathbf{0} & \mathbf{0} \\ \mathbf{0} & \mathbf{I} & \mathbf{0} \\ \mathbf{0} & \mathbf{0} & \mathbf{I} \\ \mathbf{0} & \mathbf{B}_p & \mathbf{0} \end{pmatrix} \text{ with } \begin{array}{l} \mathbf{B}_p = \left(\mathbf{e}^*_{N^{(2)},p} \otimes \mathbf{I} \right) \cdot \mathbf{A} \cdot \left(\mathbf{e}_{N^{(1)},n(p)} \otimes \mathbf{I} \right) \\ \tilde{\mathbf{x}}_p = \begin{pmatrix} {}^{i}\tilde{\mathbf{x}}_{n(p)}^{(1)} & {}^{\Gamma}\tilde{\mathbf{x}}_{n(p)} & {}^{i}\tilde{\mathbf{x}}_p^{(2)} \end{pmatrix}^{T} \end{array} \tag{11}$$

3.3 Multi-stage Modified Modal Domain Analysis

This analysis (*msmmda*) starts straightly in Eq. 1 by reading all information of mass, damping and stiffness from the Multi-Stage FE-model. Nevertheless, solving the problem itself is still too expensive. Rather, DOF are reduced with eigenmodes, calculated with elementary sector models extended with an additional connecting ring [6], which automatically guarantees mesh compatibility.

$$\mathbf{y} = \mathbf{\Phi} \cdot \mathbf{x} = \begin{pmatrix} \mathbf{\Phi}^{(1)} & \mathbf{\Phi}_f^{(1)} & \mathbf{0} & \mathbf{0} \\ \mathbf{0} & \mathbf{0} & \mathbf{\Phi}^{(2)} & \mathbf{\Phi}_f^{(2)} \end{pmatrix} \cdot \begin{pmatrix} \mathbf{x}^{(1)} \\ \mathbf{x}^{(2)} \end{pmatrix}. \tag{12}$$

$\mathbf{\Phi}^{(s)}$ denote eigenmodes of the stage (s) with the connecting ring having free end and $\mathbf{\Phi}_f^{(1)}$ are eigenmodes with the connecting ring having fixed end [6]. Equation 1 is written as

$$\mathbf{\Phi}^* \cdot \mathbf{M} \cdot \mathbf{\Phi} \cdot \ddot{\mathbf{y}} + \mathbf{\Phi}^* \cdot \mathbf{C} \cdot \mathbf{\Phi} \cdot \dot{\mathbf{y}} + \mathbf{\Phi}^* \cdot \mathbf{K} \cdot \mathbf{\Phi} \cdot \mathbf{y} = \mathbf{\Phi}^* \cdot \mathbf{f}_\mathbf{e}. \tag{13}$$

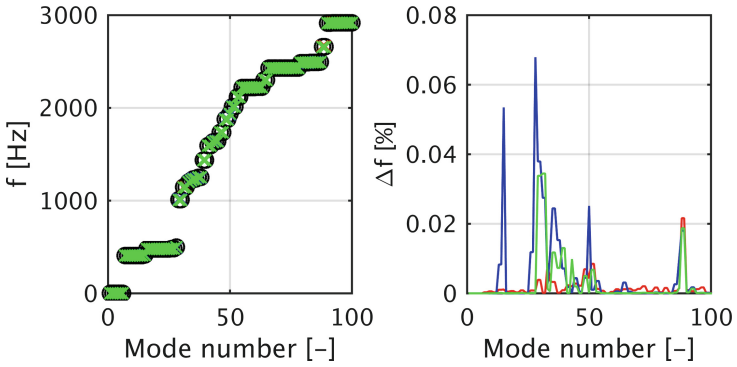

Fig. 3 Comparison between full 360° FE versus msmlcb (*red*), mscsm (*blue*) and msmmda (*green*) eigenfrequency and relative error in eigenfrequency versus full 360° FE-solution (Color figure online)

4 Conclusions

Three different ROM are presented in this paper. Figure 3a shows the eigenfrequencies from every ROM and full FE-solution. There are—even not in evidence—minute deviations. Figure 3b summarizes the relative error in eigenfrequency. As shown, the ROM implied error is extremely small. Depending on the individual task, one of the presented methods satisfies the requirements best. The *msmlcb* yields the best results, but is due to the constraint modes the most expensive one. The *mscsm* works quite fast and affords acceptable quality, but is limited to one-to-one nodal diameter modes. The *msmmda* represent a comfortable ROM, because all modes are implied and commercial FE-tools are intensively used. Moreover even geometric mistuning is conceivable.

References

1. Thomas, D.L.: Dynamics of rotationally periodic strucutres. Int. J. Numer. Methods Eng. **14**(1), 81–102 (1979)
2. Craig, R., Bampton, M.: Coupling of substrucutres for dynamic analysis. AIAA J. **6**(7), 1313–1319 (1968)
3. Yang, M.-T., Griffin, J.H.: A reduced-order model of mistuning using a subset of nominal system modes. J Eng. Gas Turb. Power **123**(4), 893–900 (2001)
4. Bladh, R., Castanier, M.P., Pierre, C.: Effects of multistage coupling and disk flexibility on mistuned bladed disk dynamics. J Eng. Gas Turb. Power **125**(1), 121–125 (2003)
5. Laxalde, D., Lombard, J.-P., Thouverez, F.: Dynamics of multistage bladed disks systems. J Eng. Gas Turb. Power **129**(4), 1058–1064 (2007)
6. Bhartiya, Y., Sinha, A.: Reduced order model of a multistage bladed rotor with geometric mistuning via modal analyses of finite element sectors. J. Turbomach. **134**(4), 041001-1–041001-8 (2012)

Part V
Optimization of Mechanisms and Machines, Mechanisms of Textile Machines

Composite Production and Industrial Robot Trajectory Calculation

T. Martinec, J. Mlýnek and M. Petrů

Abstract This paper discusses the problem of composite production. Composites often supplant traditional materials such as steel, iron, wood, etc. The most important advantages of composites are their high strength and flexibility, low weight, long lifespan and minimum maintenance. The technology used in this article is based on a winding of a carbon (or a glass) filament rovings on a polyurethane core which is a frame shape in 3D space with a circular cross section. The polyurethane frame is fastened to the robot-end-effector of the robot arm and during the winding process goes through a fiber-processing head on the basis of the suitably determined robot-end-effector trajectory. The fiber-processing head is fixed in robot working space and is composed of three guide lines with coils of carbon rovings. Quality production of described type of composite depends primarily on the correct winding of fibers on a polyurethane frame. It is especially needed to ensure the correct angles of the fibers winding on a polyurethane frame and the homogeneity of individual winding layers. The polyurethane frame is specified in the local Euclidean coordinate system E_3, the origin of this system is in the robot-end-effector. We use the matrix calculus to enumerate the trajectory of the robot-end-effector to determine the desired passage of the frame through the fiber-processing head. A practical example of the passage of a polyurethane frame through fiber-processing head is dealt with in the article. Of course, the determining calculation of the robot trajectory can be used in other applications of industrial robot use.

Keywords Robot trajectory planning and control · Composite manufacturing · Robotic fiber placement · Euler angles of rotations · Software implementation

T. Martinec (✉) · J. Mlýnek · M. Petrů
Technical University of Liberec, Liberec, Czech Republic
e-mail: tomas.martinec@tul.cz

J. Mlýnek
e-mail: jaroslav.mlynek@tul.cz

M. Petrů
e-mail: michal.petru@tul.cz

J. Beran et al. (eds.), *Advances in Mechanism Design II*,
Mechanisms and Machine Science 44, DOI 10.1007/978-3-319-44087-3_35

1 Introduction

There is a many possibilities how to make the composite materials and how to use it. Some analyses and, case studies and material properties are presented in [1, 2]. Composites are used in many areas, like in automotive industry, aircraft industry [3] or in space industry [4]. Specific area of composites production technologies are technologies, which uses the robots for fibers placing. Robots allows to produce specific composite products very effective [3]. In generally it is possible to use one of two different ways, how to make a composite using robots. For products with large open surfaces is suitable to use a prepreg tape. It is possible to activate the prepreg tape by pressure and temperature immediately after placement [5] and it is no needed moulding anymore. This article will discuss the other way, the winding technology. It follows the article [6], where winding technology is described. The computation method for offline trajectory planning and practical example with open-shaped core is also described in [6]. In this article we will discuss how to use this method for core with closed-frame shape.

First advantage of used method is fact, that it can be used in many program languages and development environments (because it is simple and it don't need special mathematical libraries or computation performance). Second great advantage is that we can generate variables, which are necessary to control the technology itself. In our case we needed to control also robots external axes. This three axes are to control of the winding speeds of three independent guide lines with coils (see Fig. 1). Positions of this guide lines along the main core defines the winding angles of fibers in all of three layers.

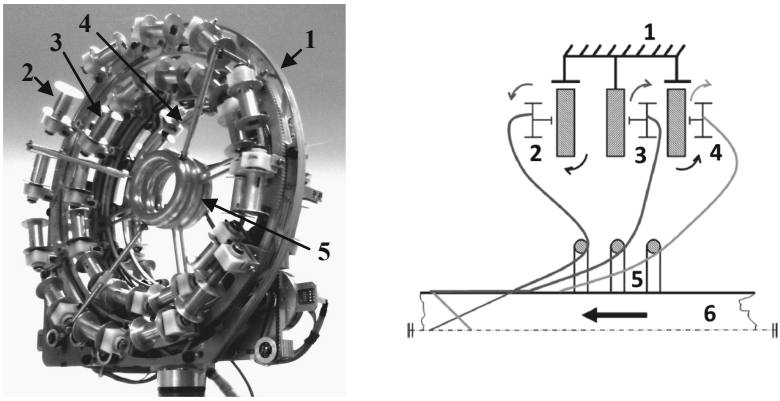

Fig. 1 Picture (on *left side*) and diagram (on the *right side*) of the winding solution principle of the working head: *1* non sliding core, *2*, *3*, *4* rotating guide lines with coils for winding at desired angles, *5* guiderings, and *6* moving core for winding controlled by the robot

2 Trajectory Calculation

In the first step of algorithm is necessary to find such set of transformations (translational and rotational), which ensures identity between the vectors (h1, h2) and (b1, b2) for selected point *Bi* (see Fig. 2). The final transformation is generally the product of translated matrix $\mathbf{L}_i$ and rotation matrix $\mathbf{Q}_i$, i.e.

$$\mathbf{T}_i = \mathbf{L}_i \cdot \mathbf{Q}_i. \tag{1}$$

We perform the calculation of the Euler angles of effector local coordinate system rotation in relation to robot basic coordinate system by decomposition of matrix $\mathbf{T}_i$. Each rotation matrix can be written as a product of the matrices of rotation around the coordinate axes z, y and x, i.e.

$$\mathbf{Q}_i = \mathbf{Rot}(z,\ a_i) \cdot \mathbf{Rot}\,(y,\ b_i) \cdot \mathbf{Rot}(x,\ c_i) \tag{2}$$

where matrices $\mathbf{Rot}\,(z, a)$, $\mathbf{Rot}\,(y, b)$ and $\mathbf{Rot}\,(x, c)$ are in form

$$\mathbf{Rot}(z, a_i) = \begin{pmatrix} \cos a_i & -\sin a_i & 0 & 0 \\ \sin a_i & \cos a_i & 0 & 0 \\ 0 & 0 & 1 & 0 \\ 0 & 0 & 0 & 1 \end{pmatrix}, \quad \mathbf{Rot}(y, b_i) = \begin{pmatrix} \cos b_i & 0 & \sin b_i & 0 \\ 0 & 1 & 0 & 0 \\ -\sin b_i & 0 & \cos b_i & 0 \\ 0 & 0 & 0 & 1 \end{pmatrix},$$

$$\mathbf{Rot}(x, c_i) = \begin{pmatrix} 1 & 0 & 0 & 0 \\ 0 & \cos c_i & -\sin c_i & 0 \\ 0 & \sin c_i & \cos c_i & 0 \\ 0 & 0 & 0 & 1 \end{pmatrix}$$

and a, b, c are the corresponding Euler angles. We note that the determination of Euler angles a, b and c is not unique [6]. Euler angles of rotation matrix

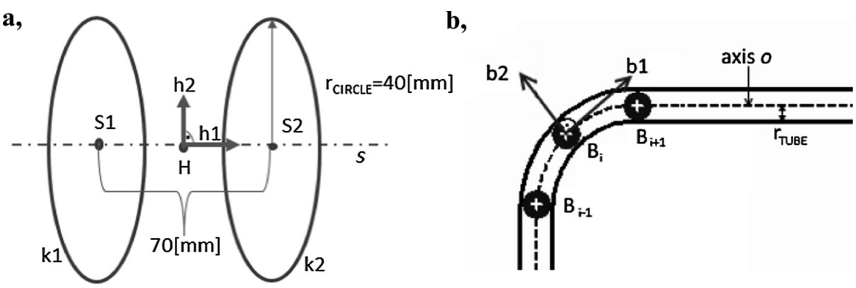

Fig. 2 Geometric scheme of the working head (on the *left*) and cross-section of the core (on the *right*)

$$\mathbf{Q}_i = \begin{pmatrix} q_{11}(i) & q_{12}(i) & q_{13}(i) & 0 \\ q_{21}(i) & q_{22}(i) & q_{23}(i) & 0 \\ q_{31}(i) & q_{32}(i) & q_{33}(i) & 0 \\ 0 & 0 & 0 & 1 \end{pmatrix}$$

can be determined by following relations (in detail see [6])

$$\begin{aligned} a_i &= ATAN2(q_{21}(i),\, q_{11}(i)), \\ b_i &= ATAN2(-q_{31}(i),\, q_{11}(i)\cos a_i + q_{21}(i)\sin a_i), \\ c_i &= ATAN2(q_{13}(i)\sin a_i - q_{23}(i)\cos a_i,\, q_{22}(i)\cos a_i - q_{12}\sin a_i). \end{aligned} \tag{3}$$

When calculating the angles of rotations a_i, b_i and c_i in relation (3) we use the ATAN2 function (part of the library of most programming languages), which calculates the value of the function arctangent for argument arg_1/arg_2 from two input parameters arg_1 and arg_2. Moreover, the signs of both input parameters are used to determine the quadrant in which the resulting value function is located (it is valid that $-\pi < \mathrm{ATAN2}(arg_1, arg_2) \leq \pi$).

Based on the knowledge of the translated matrix $\mathbf{L_i}$ and Euler angles we can determine a new tool-center-point position TCP_i. This position contains six values—three coordinates in Cartesian system (*X, Y* and *Z*) and three rotation angles (*A, B* and *C*). This values we can store in the robot native language. Described routine must be done for each of B_i points, $1 \leq i \leq N$. Range for variable N depends on the length of the axis o of the core and also on the distance between points (see [6]).

3 Practical Example

The considered composite with the closed frame-shaped profile (see Fig. 3a) serves for fastening of the window to the fuselage of the helicopter. This core is only 2D shape, so it is easy to show and understand how the algorithm works. But in general it is possible to use it also for 3D complicated shapes.

There are the basic measurements of the core on Fig. 3 and also there are marked values of the l variable. This variable is distance between start point B_1 (where $l = 0$, see Fig. 3a) and the selected point B_i. Distance is measured along the axis o. This variable helps us to determine proper positions of the guide lines with fiber coils (which are connected as an external axis of the robot). The winding angles and core diameter are given, so we can easily evaluate the external axis position for each B_i point, using l value for this point.

We used described algorithm of robot-end-effector trajectory calculation and generated source code in robot language. For our example we used a KUKA KR16 robot with KUKA KRC 4 controller. We implemented the algorithm in Delphi (Pascal language) and we generated source code in KRL (KUKA Robot Language). Generated code we tested in the KUKA Sim Pro software simulator first (see Fig. 5)

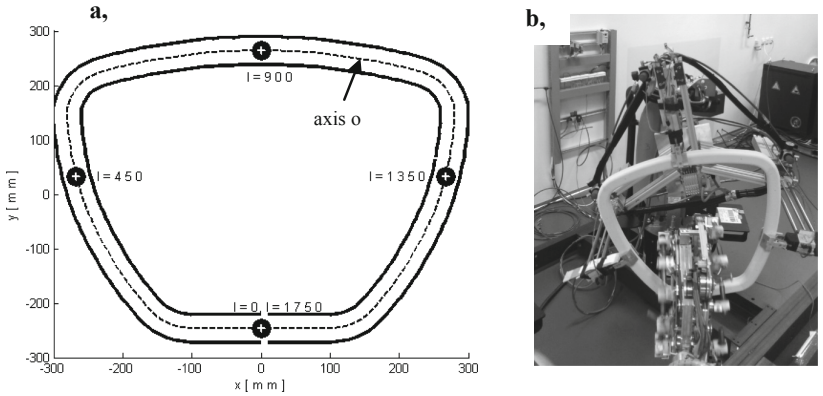

Fig. 3 Closed-frame-core—the sizes (on the *left*) and in the frame core connected to the robot-end-effector (on the *right*)

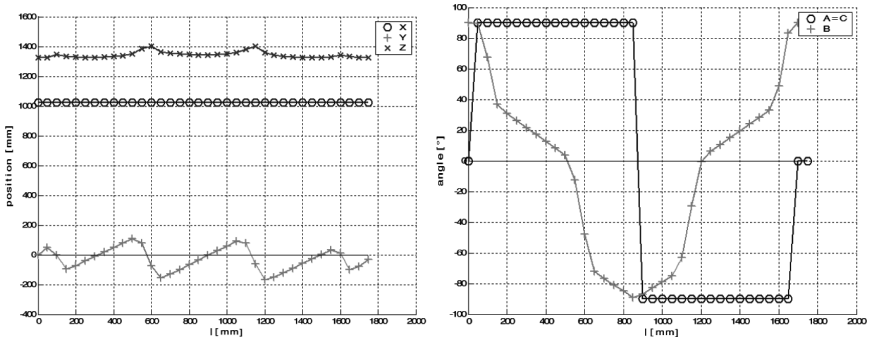

Fig. 4 Diagram showing the course of the TCP during the passage of the frame through the fibre-processing head—values of the first three parameters (on the *left side*) and values of the TCP angles (on the *right side*)

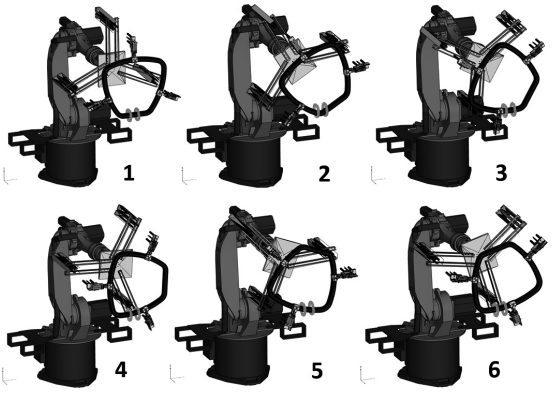

Fig. 5 Graphic simulation of the position of the robot and the frame during winding at selected points of the trajectory

and then on the robot in laboratory (see Fig. 3b). Obtained values are visualised on Fig. 4.

4 Conclusions

The described algorithm allows offline calculating the 3D trajectory of the robot-end-effector of the industry robot during the production of composites using the dry fiber winding technology on a core. The algorithm can be applied to any manufacturing process where it is necessary to determine the 3D trajectory of a robot-end-effector. Especially, this algorithm can be successfully used in the industrial production of specific composites, where is necessary to generate also trajectory for external equipment. The use of the described algorithm is completely independent of the type of production robot and software tools. The procedure for determining the trajectory of the robot-end-effector induces virtually no additional costs to the manufacturer and can significantly speed up the determination of the desired trajectory of the robot-end-effector.

Acknowledgments The research work reported here was made possible by project LO1201 financed with co-funding from the Ministry of Education, Youth and Sports as part of targeted support from the "National Sustainability Program I" programme, and "GESHER/MOST LJ14005—New applications in production technology and the use of composite frames fiber reinforced composites".

References

1. Gay, D., Hoa, S.V.: Composite Materials—Design and Applications, p. 550. CRC press, Taylor & Francis Group London (2007). ISBN 978-1-4200-4519-2
2. Agarwal, B.D., Broutman, L.J., Chandrashekhara, K.: Analysis and Performance of Fiber Composites, 3rd edn., p. 576 (2006). ISBN 978-0-471-26891-8
3. Groppe, D.: Robots improve the quality and cost effectiveness of composite structures. Ind. Robot: Int. J. **27**(2), 96–102 (2000)
4. Hana, P., Inneman, A., Daniel, V., Sieger, L., Petrů, M.: Mechanical properties of carbon fiber composites for applications in space. In: Proceedings of SPIE 9442, Optics and Measurement Conference 2014, 7 Jan 2015. doi:10.1117/12.2175925
5. Shirinzadech, B., Cassidy, G., Oetomo, D., Alici, G., Ang, M.H.: Trajectory generation for open-contoured structures in robotic fibre placement. Robot. Comput.-Integr. Manuf. **23**, 380–394 (2007)
6. Martinec, T., Mlýnek, J., Petrů, M.: Calculation of the robot trajectory for the optimum directional orientation of fibre placement in the manufacture of composite profile frames. Robot. Comput.-Integr. Manuf. **35**, 42–54 (2015). doi:10.1016/j.rcim.2015.02.004

The Pinion Teeth Temperatures Measured During the Different Power Levels Operation

M. Mazac and M. Maly

Abstract This paper deals with the temperatures of the automobile gearbox final drive pinion teeth during the performance in constant power levels. The temperatures are measured in the teeth of the pinion of the gearbox MQ100 final drive. The temperatures were measured during the mostly real operation conditions of the gearbox. The special temperature measurement equipment was used. The performance of the gearbox on the special designed testing stand was realized. The measurements were performed during many different power levels. The power levels were defined by torque and RPM. The temperatures measured during same power levels were compared. The main goal of this paper is comparing of the average temperature of the final drive pinion gearing measured during different power levels.

Keywords Gearbox · Temperature · Measurement · Teeth · Pinion · Final drive

1 Introduction

During the mechanical power transformation by gears a part of energy is dissipated. The quantity of dissipated energy can be a transformation quality parameter. Part of the energy is dissipated into heat. The dissipated energy changed the temperature of a gearbox parts. The question is a behavior of a gearbox parts during the higher temperature operation. The second question is the influence of mechanical power parameters on the temperature of gears. The final drive pinion gearing as a point of temperature measurements was chosen.

For the temperature measurements to design and manufacture the special equipment was necessary. The measurements were performed on commercial produced mechanical automobile gearbox MQ100 Škoda Auto a.s.. The temperature

M. Mazac (✉) · M. Maly
Technical University of Liberec, Liberec, Czech Republic
e-mail: martin.mazac@tul.cz

M. Maly
e-mail: miroslav.maly@tul.cz

J. Beran et al. (eds.), *Advances in Mechanism Design II*,
Mechanisms and Machine Science 44, DOI 10.1007/978-3-319-44087-3_36

was measured during several mechanical power levels. The several different torque and RPM were set during measurement, but ever power level was constant.

The main aim of this short paper should be description of experimental determination of final drive pinion gearing temperatures.

2 Equipment for Gearbox Loading

The special equipment for operating and loading was designed and manufactured. The stand is designed for the operating of gearbox in mostly real condition. The common combustion engine for the powering of the stand is used. All of the stand parts are connected by the shafts for the lowest temperature impacts. The gearbox is mounted on an engine block for the similar rigidity as in a car operation. The final loading of gearbox is realized by the electric dynamometer. The gearbox cooling by the electric fan is realized. The stand for testing is deeply described in papers [1, 2]. The stand and his main parts is depict on Fig. 1.

3 Equipment for Temperature Measurements

For the temperature measurements the special equipment was designed and manufactured. The temperature measurement on a rotating shaft is possible with this equipment. The NTC thermistors for the temperature measurement are used. The wires for the connection of NTC sensors are located in the middle hole of the shaft.

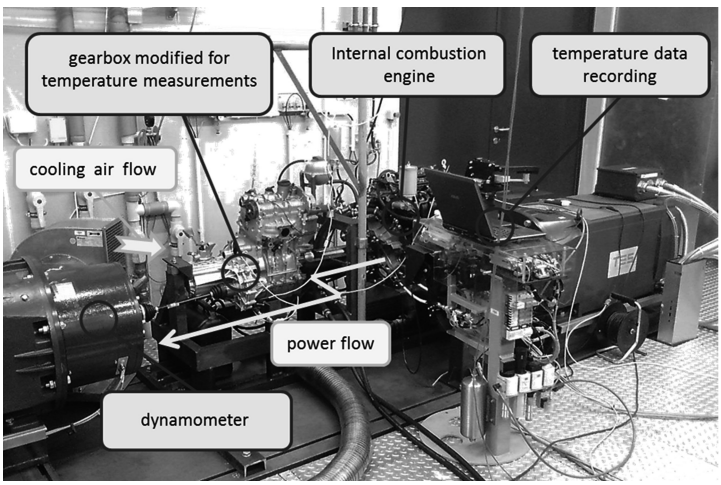

Fig. 1 The laboratory stand for automobile gearbox loading

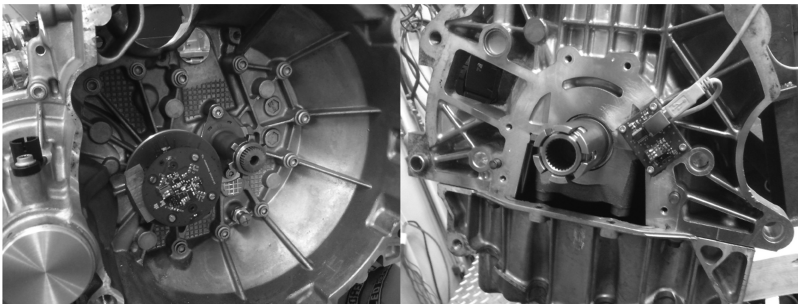

Fig. 2 The equipment for the temperature measurements—rotating parts (*left side*), static parts (*right side*)

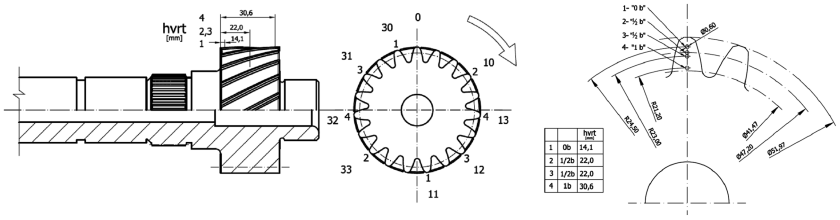

Fig. 3 The NTC sensors position in the teeth of the final drive pinion

The data about temperature are transported by the infrared optic method. The infrared diode is on the rotating part mounted in the axis of rotation. The static parts of equipment for temperature measurements are mounted in front of the infrared diode. The data from the static part are transported by USB to PC and loaded to the data file. For the final processing of the data the special program is used. All this equipment in the [3–5] is fully described. The equipment (rotor and stator) is on Fig. 2.

The temperature sensors were mounted to the teeth of the final drive pinion. The temperature was measured by the eight mounted NTC sensors. The position of every sensor is defined and it is depict on the little Fig. 3. The mounting of temperature sensors is described in [6].

4 Measurements

The measurements were realized in **9 power levels**. Every power level is defined by torque and RPM. The difference between torque and RPM was due to the shifted gear—the temperatures were measured during the operation in all five possible shifted gears. The table of the power levels is on Fig. 4.

P [kW]	1st Gear		2nd Gear		3th Gear		4th Gear		5th Gear	
	Torque [Nm]	RPM [min^{-1}]	Torque [Nm]	RPM [min^{-1}]	Torque [Nm]	RPM [min^{-1}]	Torque [Nm]	RPM [min^{-1}]	Torque [Nm]	RPM [min^{-1}]
7,46	337,0	211,4	180,8	394,1	117,5	606,4	88,7	803,0	73,7	967,3
9,07	337,0	257,3	180,8	479,5	117,5	737,8	88,7	977,0	73,7	1176,9
10,69	337,0	303,1	180,8	564,9	117,5	869,1	88,7	1151,0	73,7	1386,5
14,92	673,9	211,4	361,6	394,1	235,0	606,4	177,4	803,0	147,3	967,3
18,15	673,9	257,3	361,6	479,5	235,0	737,8	177,4	977,0	147,3	1176,9
21,38	673,9	303,1	361,6	564,9	235,0	869,1	177,4	1151,0	147,3	1386,5
22,37	1010,9	211,4	542,4	394,1	352,5	606,4	266,2	803,0	221,0	967,3
27,22	1010,9	257,3	542,4	479,5	352,5	737,8	266,2	977,0	221,0	1176,9
32,07	1010,9	303,1	542,4	564,9	352,5	869,1	266,2	1151,0	221,0	1386,5

Fig. 4 The table of the power levels with their parameters (Torque, RPM)

The **15 min** measurement cycles was realized in all power levels. The values of temperatures from the last **1 min** of the cycle for the final evaluation were used. Only **average value** from the temperatures measured by the seven sensors was used.

The gearbox was cooled by the constant air flow from the electric fan. The temperature of air in the room with the stand was regulated and it was **20 °C (68 °F)**.

5 Temperatures of the Pinion Gearing

The final measured data were evaluated by the special software and the final charts were created. All of the final charts are set for one constant power level. The final charts contain the RPM, torque and average temperature values. For all five possible set gears the measurements are realized. The parameters (RPM, torque, temperature) of all gears on the final charts are depicted. The charts for the lowest and the highest power levels are on Fig. 5.

The ranges of the average gearing temperatures are on Fig. 6. The border temperatures of the depicted gearing temperatures ranges are beginning and final temperatures of 15 min measurement cycles.

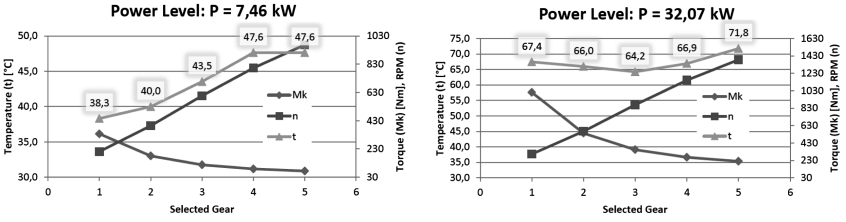

Fig. 5 The samples of the final charts of the average gearing temperatures measured during different power levels, minimal and maximal power level charts are depict

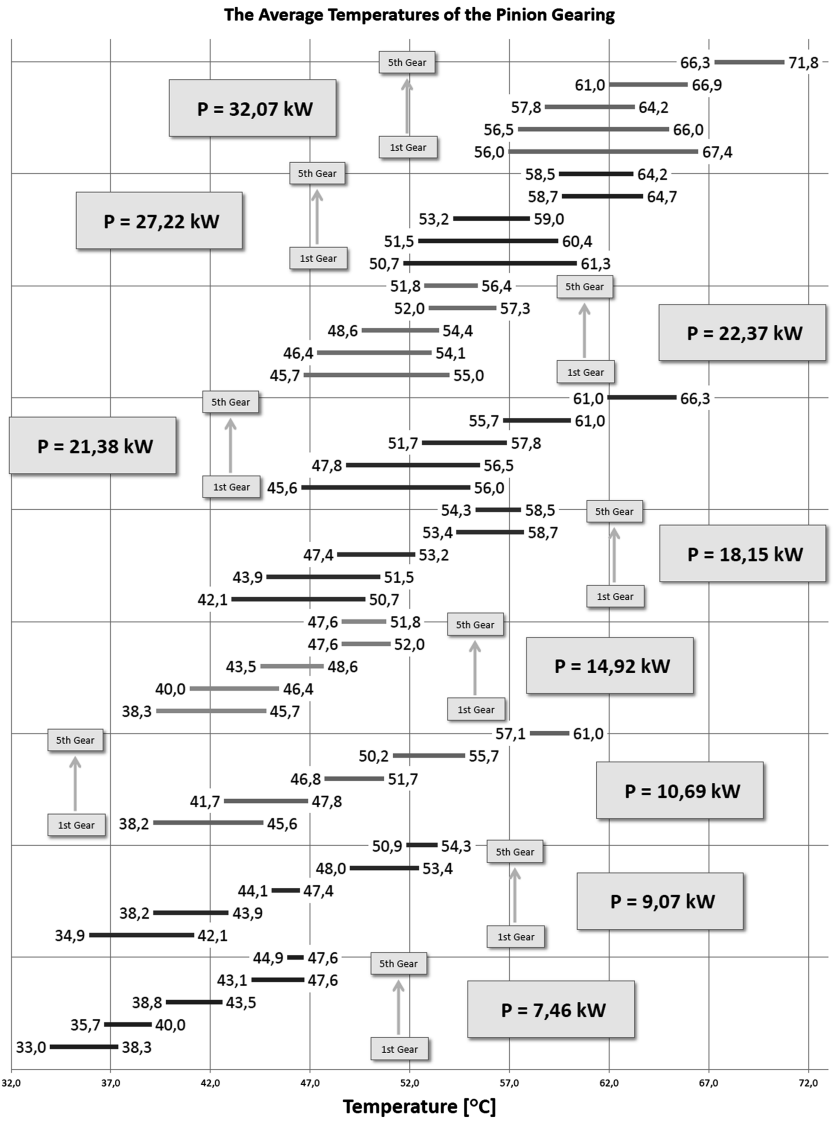

Fig. 6 The chart of the final drive pinion gearing average temperature ranges measured during the power levels

6 Conclusions

This short paper describes the temperature measurements realized in the final drive pinion gearing. The measurements were possible to realize due to special equipment for gearbox operating and for temperature measurements. The temperatures were

measured in several places of the pinion teeth. The measurements were realized during a few power levels operation. The beginning temperatures and the final temperatures measured during the 15 min cycle are summarized in the chart. The temperatures measured during the described test regimes are not danger for the condition of oil. The described measurement methodology is useful for other future testing.

Acknowledgments This publication was written at the Technical University of Liberec as a part of the project 21127 with the support of the Specific University Research Grant, as provided by the Ministry of Education, Youth and Sports of the Czech Republic in the year 2016.

References

1. Mazac, M.: Stand for measuring temperatures of the main gears of automobile differential. In: 54th International Conference of Machine Design Departments, Hejnice, Czech Republic, 10–12 Sept 2013. ISBN 978-80-7372-986-8
2. Mazac, M.: Stand for measuring temperatures of the main gears of automobile differential. In: Sevcik, L., Lepsik, P., Petru, M., Masin, I., Martonka, R. (eds.) Modern Methods of Construction Design, Book Series: Lecture Notes in Mechanical Engineering, pp. 139–144. doi:10.1007/978-3-319-05203-8_20 (2014)
3. Mazac, M., Herajn, P., Svoboda, M.: the equipment for temperature measurements near a gear tooth flank. In: 55th International Conference of Machine Design Departments (ICMD2014), Beroun, 9–12 Sept 2014. ISBN 978-80-01-05542-7
4. Mazac, M., Herajn, P., Svoboda, M.: The gear tooth flank temperature measurements system. In: Transactions on Electrical Engineering, vol. 4, no. 1, pp. 27–30 (2015). ISSN 1805-3386
5. Mazač, M.: Měření teplot ozubených kol v reálném provozu. *Studentská vědecká a odborná činnost 2014*, TUL, 28 May 2014. ISBN 978-80-7494-071-2
6. Mazač, M.: Zařízení pro měření teplot v blízkosti boků zubů ozubených kol – konstrukční řešení a stavba zařízení, *Studentská vědecká a odborná činnost 2015*, 3. červen 2015 Liberec. ISBN 978-80-7494-209-9

A Novel Four Wheel Vehicle

S. Pramanik and S.S. Thipse

Abstract A new arrangement of wheel location has been considered for a four wheel vehicle so that the turning radius can be reduced greatly. The front axle is to use one wheel only instead of two wheels of a conventional vehicle. The middle axle is to use two wheels and the rear axle is to use one wheel. The single wheels of the front and rear axle will be placed at the mid position so that the arrangement becomes symmetrical. This arrangement helps us to follow the law of correct steering for all angular positions. The steering mechanism will be such that the front and rear wheels will rotate equal amount but in opposite directions. A crossed four bar mechanism has been used to rotate the front and rear wheel while the vehicle is taking a turn. The rotation of each wheel will be 30° and the maximum steering error is 0.2° only. The wheels on the middle axle will not be rotated due to steering but are connected to the differential gear box to transmit motion. The intersection of the front and rear wheel axis will be always on the axis of the middle axle. Hence pure rolling will take place while the vehicle is taking a turn. The design enhances the life of the tires and parking of this vehicle will be easier. Each wheel of the middle axle shall have two tires so that it can bear more load and increases stability of the vehicle while taking a turn.

Keywords Kinematic synthesis · Steering mechanism · Hooke and Jeeves optimization · Four wheel vehicle

S. Pramanik (✉)
Symbiosis International University, Pune, India
e-mail: santiranjan_pramanik@rediffmail.com

S. Pramanik
College of Military Engineering, Pune, India

S.S. Thipse
The Automotive Research Association of India, Pune, India
e-mail: thipse.edl@araiindia.com

J. Beran et al. (eds.), *Advances in Mechanism Design II*,
Mechanisms and Machine Science 44, DOI 10.1007/978-3-319-44087-3_37

1 Introduction

Kinematic synthesis methods can be broadly classified into two categories: exact point approach and optimization techniques. In the exact point approach there are some precision points at which the function generated is exactly same as the required function. At other points there are deviations from the required function. This deviation is called the structural error. In order to reduce the structural error the number of precision points has to be increased. Generally the number of precision points is equal to the number of design parameters. The design parameters are the link length ratios and the angles used to define a mechanism.

A four-bar steering mechanism is generally used in buses and trucks. The mechanism is placed behind the front axle. This mechanism is called Ackermann steering. This mechanism is simple but has a drawback that there is divergent end behavior in the steering error curve. Fahey and Huston [1] modified a four-bar mechanism to an eight-bar mechanism in order to remove the divergent end behavior in an extended range of motion. They used an iterative method to achieve the final solution from the initial solution. But one link of the mechanism was small compared to other links. The wear in this small link joint may affect the accuracy of the mechanism greatly. The eight-bar mechanism provided seven precision points but is very complex.

De-Juan et al. [2] carried out optimal synthesis of function generation in steering linkages. They considered rack-and-pinion steering, four-bar steering, six-bar steering and double four-bar steering mechanism. In all these cases they considered leading configuration, trailing configuration, mixed-leading configuration and mixed-trailing configurations. However, they did not consider the mixed leading-and-trailing configuration of the four-bar mechanism. The present work is concerned about this mixed configuration and design of a new mechanism.

Zhao et al. [3] considered a planar five bar mechanism with two incomplete noncircular gears for steering of an automobile. The mechanism is able to follow the Ackermann equation exactly because the gears are designed in such a way. But the mechanism is mainly suitable for light carriages.

All the above works were done to reduce the steering error. But the present work uses a new arrangement of wheels so that the steering error can be eliminated completely and turning radius can be reduced greatly.

2 Crossed Four-Bar Mechanism

A crossed four-bar mechanism AGFB has been shown in mean position in Fig. 1. In this mechanism the links AG and BF are equal in size. These links are inclined to the lateral axis of the vehicle by equal angle β when the vehicle moves along a straight path. The angles GAK and FBH are equal to β. The extreme position of the

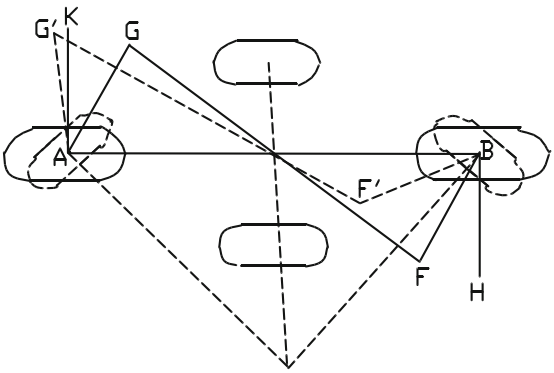

Fig. 1 A crossed four-bar steering mechanism during left turn of the vehicle

mechanism is shown by AG′F′B. Since the arms AG and BF rotate in the opposite directions the wheels at A and B will rotate in opposite directions due to steering.

3 Optimization Method

Figure 2 shows two wheels, front wheel A and rear wheel B. The steering mechanism AGFB has two design parameters. These are angle KAG (β) and steering arm length AG (r). The front wheel has been rotated by angle α (angle GAD) and then the rotation of the rear wheel (angle FBE) has been found out. Then the steering error has been calculated as follows.

The initial straight ahead position has two equal angles KAG and FBH. The two steering arms AG and FB are equal to r. The distance between the front wheel A and rear wheel B has been designated by d. The length of the coupler has been found as

$$GF = \sqrt{(d - 2r\,\sin\beta)^2 + (2r\,\cos\beta)^2}$$

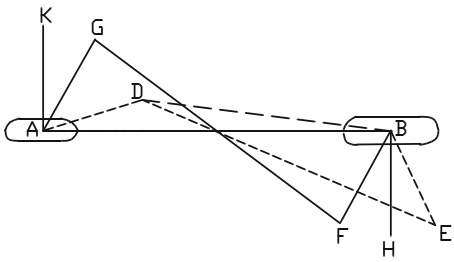

Fig. 2 Steering mechanism to be optimized

The distance DB is given by

$$DB = \sqrt{\{d - r\ \sin(\alpha + \beta)\}^2 + \{r\ \cos(\alpha + \beta)\}^2}$$

The angle DBE is given by

$$\text{Angle}\, DBE = \cos^{-1}\left[\frac{(DB)^2 + r^2 - (GF)^2}{2 \times DB \times r}\right]$$

The distance DF is given by

$$DF = \sqrt{\{d - r\ \sin\beta - r\ \sin(\alpha + \beta)\}^2 + \{r\ \cos\beta + r\ \cos(\alpha + \beta)\}^2}$$

The angle DBF is given by

$$\text{Angle}\, DBF = \cos^{-1}\left\{\frac{(DB)^2 + r^2 - (DF)^2}{2 \times DB \times r}\right\}$$

The rotation of the rear wheel is given by

$$Angle\, FBE = Angle\, DBE - Angle\, DBF$$

The correct angle of rotation of the inner wheel is given by

$$Angle\, FBE_{correct} = \alpha$$

The steering error is given by

$$Error = Angle\, FBE - Angle\, FBE_{correct}$$

The objective function is given by

$$Obj\, Fun = \sum (Error)^2$$

The Hooke and Jeeves optimization method has been used to minimize the objective function using the initial estimate as r = 2 units and β = 23.6°. The length (r) of the steering arm has been found as 2.147 units where the distance between hinge joints A and B is 10 units. The inclination (β) of the steering arms with the vehicle lateral axis is 24.069°. The steering error curve has been plotted in Fig. 3. The crossed four-bar steering mechanism has maximum steering error 0.2° at 30° rotation position of the front wheel.

4 Result

Figure 3 shows the steering error in Ackermann steering as well as in the proposed steering mechanism. The Ackermann steering mechanism produces a maximum steering error of 0.7° for inner wheel rotation up to 40°. But the wheel rotation in this proposed vehicle has been limited to 30° and the maximum steering error up to that is 0.2°. The steering error in the proposed mechanism is less than that of the Ackermann steering mechanism.

Figure 4 shows proposed vehicle wheel positions while turning. The size of the vehicle has been assumed considering the track to wheelbase ratio of four-tenth. The distance between front and rear wheel i.e. distance AC has been assumed as five meters. The axis of middle wheels is at a distance of 2.5 m from wheel A and C. At maximum rotation of 30° of front and rear wheels the angle IAC and angle ICA are 60°. Hence for maximum rotation position the triangle IAC is an equilateral triangle and side IA and IC are 5 m each. Hence the turning radius of the front left corner of the vehicle is (5 + 1.414) or 6.414 m. Here it has been assumed that the front wheel A is 1 m behind the front end of the vehicle and width of the vehicle is 2 m.

In Fig. 5 the existing Ackermann steering mechanism has been considered. The inner wheel rotates by 40° maximum. The rotation of the outer wheel is obtained 32° using Ackermann relation for track to wheelbase ratio four-tenth. The vehicle takes a left turn and the angle IDE is the rotation of the inner wheel. The rotation of the outer wheel is angle IAE. The instant centre of rotation is I for maximum wheel rotation position. The turning radius of the vehicle is the distance AI plus one meter

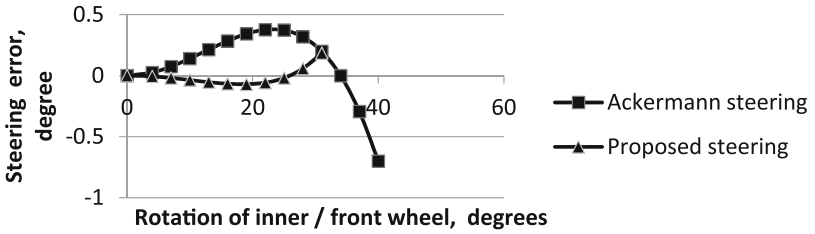

Fig. 3 Steering error curves

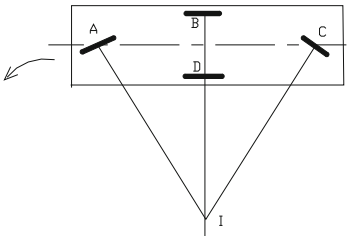

Fig. 4 Arrangement of wheel of the proposed vehicle

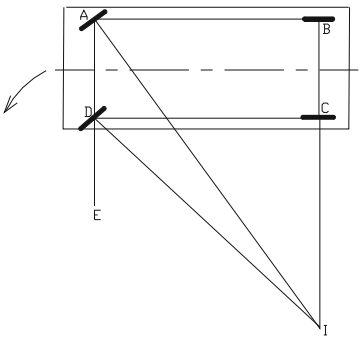

Fig. 5 Arrangement of wheel of vehicle with Ackermann steering

approximately. The wheelbase AB is five meters. Hence the distance AI is 5/Sin 32° i.e. 9.435 m. Hence turning radius is 10.435 m. Therefore, the reduction in the turning radius is 4.291 m and is 41 %.

5 Conclusion

The proposed steering mechanism is better than the conventional Ackermann mechanism because the steering error is less and the turning radius has been reduced by 41 %. The arrangement of the wheels has made the proposed vehicle capable of turning within smaller area and parking of the vehicle will be easier.

References

1. Fahey, S.O.F., Huston, D.R.: A novel automotive steering linkages. ASME J. Mech. Des. **119**, 481–484 (1997)
2. De-Juan, A., Sancibrian, R., Viadero, F.: Optimal synthesis of function generation in steering linkages. Int. J. Autom. Technol. **13**(7), 1033–1046 (2012)
3. Zhao, J.-S., Liu, X., Feng, Z.-J., Dai, J.S.: Design of an Ackermann-type steering mechanism. Proc. IMechE Part C: J. Mech. Eng. Sci. **227**(11), 2549–2562 (2013)

Cam Mechanism for Car Seat Testing

P. Srb, P. Kulhavy, V. Fliegel and P. Lepsik

Abstract This paper deals with optimization of a device designed for long-term dynamic testing of car seats. This kind of tests is important for car seat innovation with respect to improving safety and comfort of passengers. This type of testing is based on linear periodic movement of a car seat cushion on which a weight representing a passenger is placed. Movement of seat is generated by a cam mechanism. Several cam profiles were proposed by a computational software, in order to achieve acceleration occurring during a real car driving. Based on this information concept of the whole device was proposed. Thereafter the static and dynamic FEM analysis were carried out. Finally an optimization of the cam mechanism and the whole device was accomplished in order to achieve the best compromise of conflicting requirements of large acceleration at low frequencies.

Keywords Cam · Mechanism · Car seat · Cushion

1 Introduction

Testing of automobile seats and their parts is very important for increasing safety and comfort of passengers, but also for development of new design solutions. Evaluating of car seat comfort is a very complex issue because of great individual personal differences, like body structure, road conditions etc. Other important perceptions include visibility from the car, reachability of controls, vibrations, noise, temperature, humidity etc.

Among all these factors there are vibrations, one of the most important factors affecting the overall assessment of comfort and related safety. The whole body vibration (WBV) [1] manifests itself when a support of human body forms vibrant surfaces. The passenger sitting on a car seat is a typical example of the WBV

P. Srb (✉) · P. Kulhavy · V. Fliegel · P. Lepsik
Technical University of Liberec, Liberec, Czech Republic
e-mail: pavel.srb@tul.cz

J. Beran et al. (eds.), *Advances in Mechanism Design II*,
Mechanisms and Machine Science 44, DOI 10.1007/978-3-319-44087-3_38

exposure. The vibrations are transmitted to the torso through the seat and the backrest, to hands through the steering wheel and to legs through the car floor [2].

Good automobile car seats should provide particular support to passengers under all driving conditions and reduce vibration transmission from the car to human the body. Although the tolerance of the same level of vibration is individual for each, it turns significant increase of sensitivity in the frequency range 2–10 Hz [3] which corresponds to the natural frequencies of the vital organs, higher frequencies have a negative impact on the nervous system. The exposure of a human body to such vibration is contrary to the sense of comfort of the passengers, and negatively affects the concentration which is closely connected with safety. For these reasons design a car seat so as to provide comfort and safety parameters in sufficient amount for its entire lifetime is very important. Therefore, it is necessary to carry out endurance tests. However, to make this kind of tests in real conditions and with the entire car is expensive and very time consuming.

A testing device that will simulate real traffic loads is appropriate to create for these tests. These devices can operate continuously for long time and thus simulate loading of a car or its parts in less time.

2 Testing Device

The prototype testing device [4] (Fig. 1) was designed and built in cooperation with an international company producing car seats.

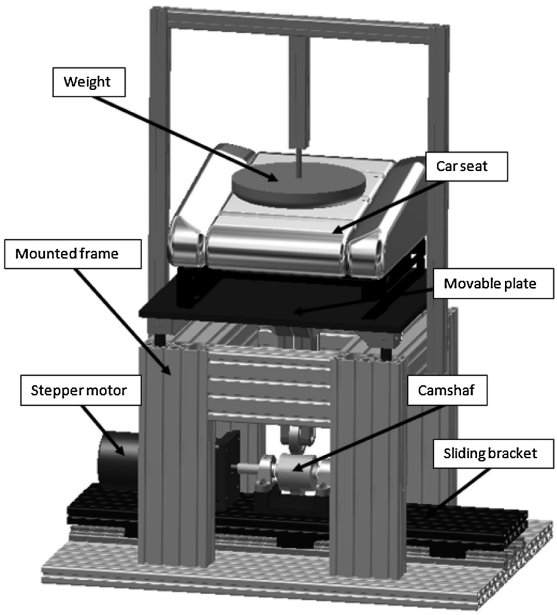

Fig. 1 First concept of testing device

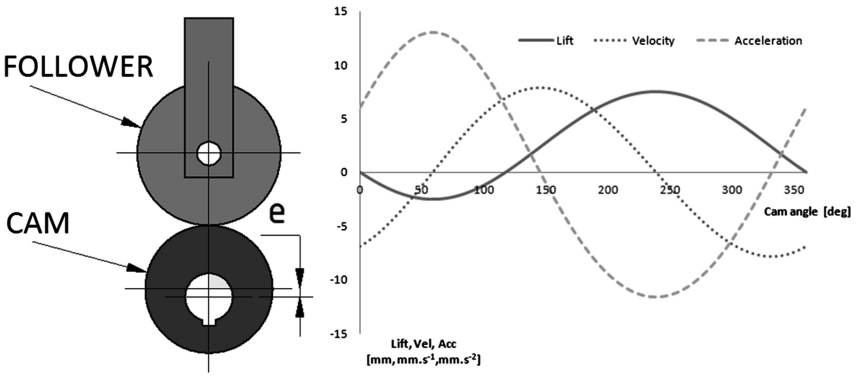

Fig. 2 Cam mechanism and lift, velocity and acceleration curves

A mounted frame made of aluminum profiles is the base part. On a base plate a sliding bracket is placed. On the sliding bracket an electric step motor is fastened which is connected to a camshaft module by a flexible coupling. The camshaft module contains three changeable eccentric cams. Into the frame a movable plate is inserted which is guided in four points. In the middle of the plate a support with a roller cam follower is placed which transfers rotation of the camshaft to reciprocating movement of the plate. On the plate a whole seat or a sample of polyurethane foam can be mounted. Additional weights representing the passenger load are placed on seat. During test it is possible to record position or acceleration of the seat frame and weights. An eccentric cam with diameter 80 mm and a rotating follower with diameter 90 mm were used in the first version. The eccentricities were 1, 2.5 and 5 mm, curves are shown in Fig. 2. To prevent bouncing of the follower from the cam the device was operated up to 120 rpm.

3 New Cam Designs

Later, the design requirements on the process of vibrations were defined more precisely: achieving pulses of acceleration 25 ms^{-2} with frequency of repetition 1–5 Hz. After considering several possibilities it was determined that for acceleration 25 ms^{-2} at the frequency 1 Hz a cam with diameter of hundreds mm is required and the whole device would be too heavy on a real engine power. For these reasons the requirements were revised and a compromise solution was proposed that there would be used three cams for three frequency bands. In this solution the initially required acceleration 25 ms^{-2} is achieved only at the frequency 15 Hz, but the requirements on the size of the device and engine power are acceptable [4].

The detailed design of the cam mechanism was made using a Design Accelerator which is integrated in the software Autodesk Inventor Professional 2015. The course of acceleration was chosen so that there will be two pulses of positive

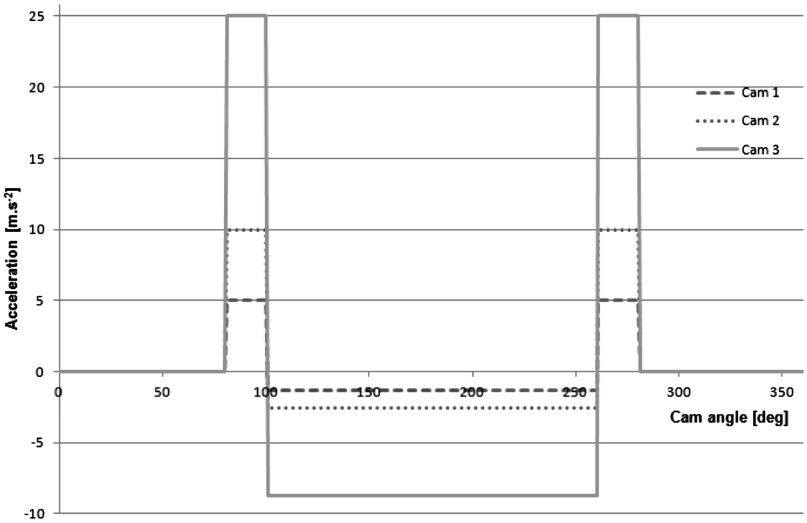

Fig. 3 Acceleration curves of new cams [4]

acceleration during one rotation of the cam, that are symmetrically distributed by 180° rotation of the cam as shown in Fig. 3.

From the viewpoint of force ratios on the whole structure the tangential force component on the follower is the most important. In Fig. 4 a force situation is shown where G is an action force from weight, N and T are component forces, angle φ is given by the shape of the cam and depends on the cam angle ψ.

The course of the tangential force T on the largest (the most unfavorable cam) is shown in the following graph Fig. 5.

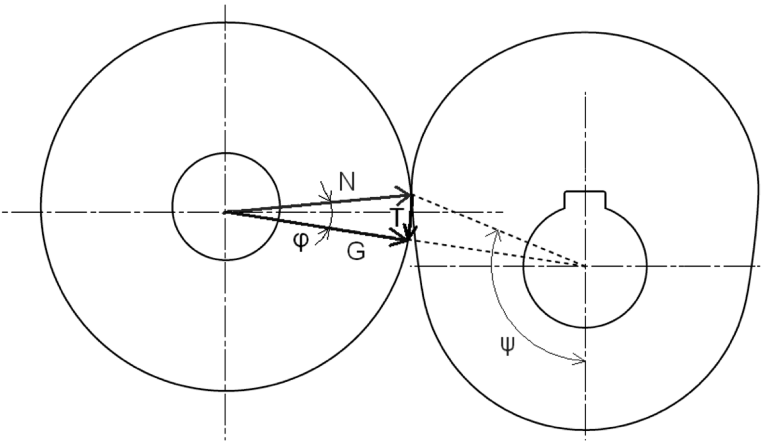

Fig. 4 Forces on cam mechanism

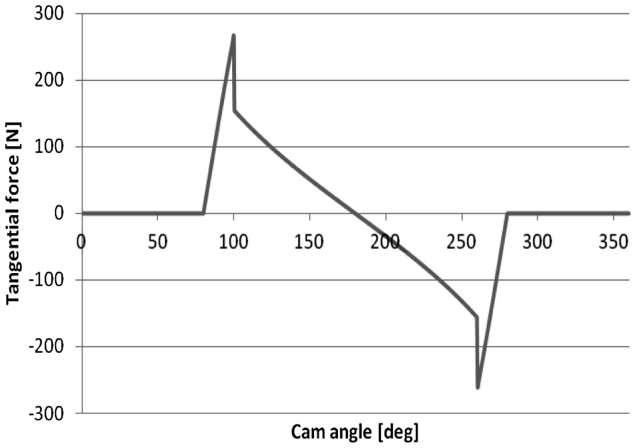

Fig. 5 Course of the tangential force

4 FEM Simulations

The simulations were performed in software CATIA V5. Guiding bearings were fixed and between bearings and guiding rods a frictionless contact was applied. The center of the top plate was constrained by a vertical movement. On the center of the follower a force was applied 300 N in the tangential direction and 1200 N in the vertical direction. The design was optimized after a first draft simulation where the values of deformation were unacceptable. The second simulation (Fig. 6) shows much better results, the maximal stress was 16 MPa and deformation was 0.2 mm on the holder of follower.

Fig. 6 Result of simulation

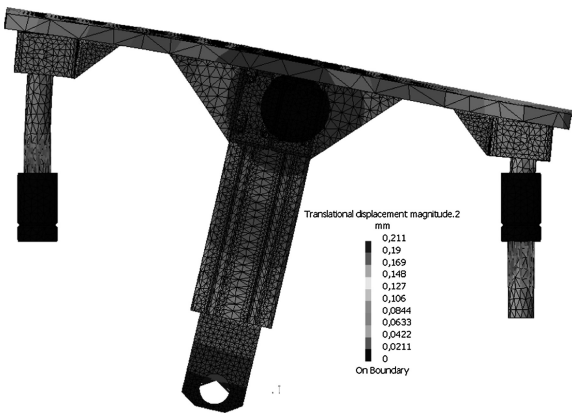

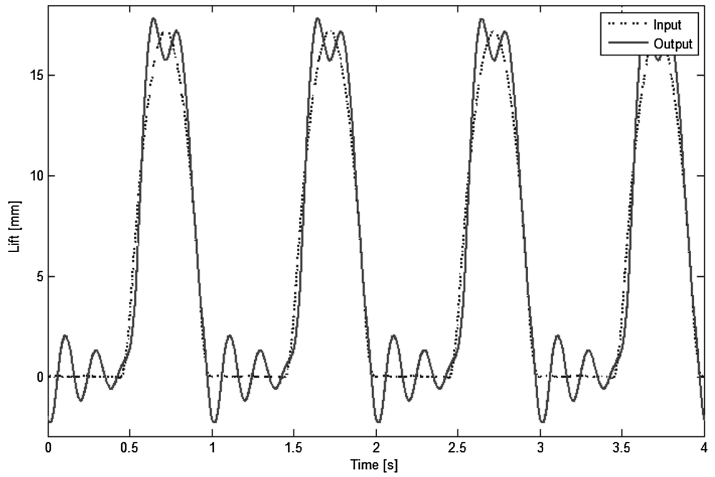

Fig. 7 Example of recorded data

5 Conclusions

The device for durability testing of automobile seats was optimized for increasing of stiffness of structure based on the FEM simulations. The new cam mechanism was designed by software Inventor. On Fig. 7 an example of measured values is shown where the dotted line represents the course of lifting of the car seat and the full line represents horizontal movement of the weights placed on the seat.

Acknowledgments The results of this project LO1201 were obtained through the financial support of the Ministry of Education, Youth and Sports in the framework of the targeted support of the "National Programme for Sustainability I".

References

1. Mackie, R.R.; Miller, J.C.: Effects of Hours of Service, Regularity of Schedules and Cargo Loading on Truck and Bus Driver Fatigue, Report HS 803 799. US Department of Transportation, Washington, DC, USA (1978)
2. International Standard Origination ISO 2631-1. Mechanical Vibration and Shock-Evaluation of Human Exposure to Whole-Body Vibration, Part 1: General Requirements (1997)
3. Barak, P.: Magic numbers in design of suspension for passenger cars. SAE Paper 911921 (1991)
4. Srb, P., Fliegel, V.: Vibration device for long-term testing of car seats. In: Modern Methods of Construction Design, Proceedings of ICMD 2013, Springer, New York, p. 189 (2014)

Offset of Natural Frequencies of Toothed Wheel by Means of Parametric Optimisation

J. Stadnicki and M. Głąbek

Abstract During the final stage of designing a toothed wheel which is exploited at different rotational speeds, it is occasionally necessary to offset natural frequencies from frequencies of excitations. The way of solving this problem by means of parametric optimisation of the toothed wheel profile, assuming small changes of its shape, is discussed in the paper. The problem is solved using finite element model with regard to monolithic toothed wheel of an aircraft gear.

Keywords Modal analysis · FEM · Parametric optimisation · Toothed wheel

1 Introduction

In high-speed aircraft gears, toothed wheels are often monolithic and, owing to the need to reduce the deadweight, shafts of such wheels are hollowed. An exemplary wheel form is shown in Fig. 1.

When designing a toothed wheel, gear teeth parameters, shape and dimensions of the envelope and the shaft are determined on the basis of the results of verification calculations, with consideration mainly to the criteria of safety, durability and design considerations. Compliance with these requirements sometimes results in the design of a toothed wheel whose natural frequencies are within the ranges of excitation frequencies which result from the ranges of the wheel rotational speeds occurring during operation, i.e. they lie in the areas of resonance. This applies particularly to gears that operate at different working speeds, for example, aircraft gears. Due to the fact that the wheel meets the requirements of safety, durability and design, there arises a problem of how to change the natural frequencies which lie in the areas of resonance, in other words, to offset some natural frequencies from excitation frequencies. Since solving this problem inevitably leads to changes in the shape and dimensions of the toothed wheel, whose project is already well advanced,

J. Stadnicki (✉) · M. Głąbek
University of Bielsko-Biala, Bielsko-Biała, Poland
e-mail: jstadnicki@ath.bielsko.pl

J. Beran et al. (eds.), *Advances in Mechanism Design II*,
Mechanisms and Machine Science 44, DOI 10.1007/978-3-319-44087-3_39

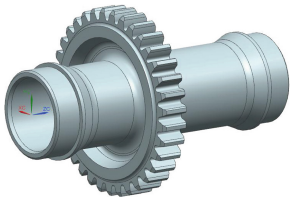

Fig. 1 An exemplary monolithic toothed with a hollowed shaft

such a solution is being looked for that minimally changes the design of the wheel. In practice, these parts of the wheel are indicated whose change does not affect the already fulfilled requirements of safety, durability and accepted design considerations.

2 Modal Analysis of Toothed Wheel of Aircraft Gear

Modal analysis of a toothed wheel of an aircraft gear (Fig. 1) provides a set of frequencies and forms of free vibrations, called a modal model. The analysis was carried out using the finite element method in the NX Nastran 9 environment [1].

2.1 Finite Element Model of a Toothed Wheel

Figure 2 shows the FEM model of a toothed wheel. The FEM model of a toothed wheel (Fig. 2a) consists of CHEXA 8-node solid elements. Support of the shaft in rolling bearings (Fig. 2b) was modelled with the use of RBE3 elements with dependent nodes on the circuit of the shaft cross section in the plane of the bearing rolling elements and with an independent node on the symmetry axis of the shaft. In points, where dependent nodes for the left and right bearing are located, coincident node pairs were formed and linked by zero-dimensional CELAS1 elements with three translational stiffnesses (in X, Y, Z direction) and one rotational stiffness (around X axis). Numerical values of the stiffnesses were assumed as large enough (respectively 1×10^{10} N/mm and 1×10^{10} N mm) to be treated as rigid when

a) b)

Fig. 2 **a** FE model of a toothed wheel of an aircraft gear, **b** the model of support

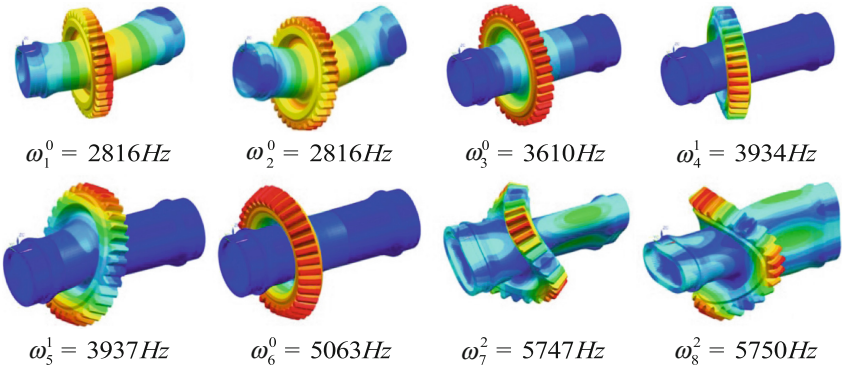

Fig. 3 Forms of free vibrations

compared to the shaft. Afterwards, one of the nodes of CELAS1 elements was deprived of all degrees of freedom. This way of support properly reflects real working conditions of a toothed wheel and eliminates over-rigidity of the FEM model. The developed model of a toothed wheel has 46 095 degrees of freedom.

The result of modal analysis of a toothed wheel FEM model is a set of eigen-frequencies and eingenforms of free vibrations. The values of a few of the first natural frequencies, important due to the possibility of resonance, and corresponding forms of vibration are shown in Fig. 3.

Natural frequencies and firms were determined according to ω_i^k—the convention where i is the ordinal number, whereas k is the number of nodal diameters around which there occurs the motion of the toothed wheel rim during vibrations. It can be noticed that the pairs of frequencies ω_1^0 and ω_2^0, ω_1^4 and ω_1^5, ω_7^2 and ω_8^2 are the same natural frequencies with the same corresponding forms shifted in a phase. At the same time, the phase shift in pairs ω_1^4 and ω_1^5, and ω_7^2 and ω_8^2 causes rotation of the form of vibrations of the toothed wheel rim around the axis of the wheel rotation, which is important for further analysis.

2.2 Campbell's Diagram

Engineering practice uses Campbell's diagram to compare the results of modal analysis of a toothed wheel—rotor with its rotational speeds which are the excitations of vibrations [2]. In the diagram, natural frequencies ω_i^k in Hz are given on the y-axis whereas rotations of excitation n are given in *rpm* on the x-axis. The analysed toothed wheel of an aircraft gear is operated at rotations corresponding to the following stages of operation: (minimum) $n_{\min} = 5500$ rpm, (flight) $n_p = 8500$ rpm, (climb) $n_w = 9500$ rpm (maximum) $n_{\max} = 11{,}000$ rpm (limiting 105 % max)

n_{gr} = 11,550 rpm. Campbell's diagram, shown in Fig. 4, shows the line of excitation by toothed wheel rotations (rotations growing from 0 to n_{gr} in Hz) and a line of excitation from meshing (for 35 wheel teeth, growing from 0 to $35 \cdot n_{gr}$ in Hz). The lines on the diagram corresponding to natural frequencies ω_4^1, and ω_7^2 are not horizontal like the other lines but include a certain range of natural frequencies (there are pairs of straight lines inclined at small angles). This is caused by the rotation of the toothed wheel—the rotor around its own axis. If the toothed wheel remained motionless, the lines of natural frequency would remain horizontal in the diagram. However, due to rotations of the toothed wheel, centrifugal force caused by the rotations of the wheel around its own axis affects the wheel movement relative to the nodal diameter. Depending on whether these actions are consistent or opposite in phase, the result is an increase or decrease of natural frequency. This phenomenon is observed by analysing the result of modal analysis. If different phase-shifted eingenforms, for which one can indicate nodal diameters, correspond to the same frequency of free vibrations of the toothed wheel (rim), we are dealing with the change of natural frequency caused by rotations of the wheel (this is called the stiffening effect cased by centrifugal forces). Then, in Campbell's diagram such an eigenfrequency is represented by two straight lines diverging from one point, with equation:

$$\omega_i^k(n) = \omega_i^k(0) \pm k \cdot n \tag{1}$$

In Campbell's diagram in Fig. 4, two points marked □ were identified, where there is a potential risk of resonance. More specifically, the lower straight line of resonance frequency ω_7^2 intersects the straight line of excitation from meshing in point 1 whose abscissa differs from the rotational speed during the climb n_w by 1.89 % of its value. However, the straight line of resonance frequency ω_6^0 intersects the straight line of excitation from meshing in point 2 whose abscissa differs from the rotational speed during the flight n_p by 2.12 % of its value.

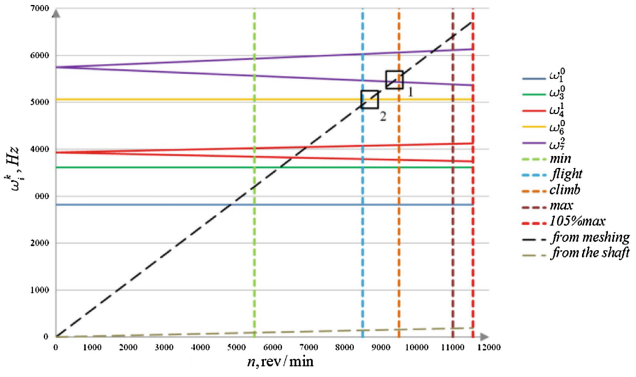

Fig. 4 Campbell's diagram of a toothed wheel

3 Parametric Optimization of a Toothed Wheel Shape—Offset of Resonance Frequencies

Since according to the adopted assumption, the offset of resonance frequencies must be performed with the least possible interference in the wheel envelope shape, the problem was solved using NX *Optimizer* for parametric optimization of the NX 9 programme. The toothed wheel, with an accuracy of gear teeth that cannot be changed, is axisymmetric. Parameters defining the profile in radial section of the wheel were assumed as decision variables of optimization problem. Figure 5 shows these profile parameters that will be subject to changes during optimization (p51 $= x_1$, p52 $= x_2$, p53 $= x_3$, p82 $= x_4$, p55 $= x_5$) and their initial values in mm. It should be noted that in order to maintain the profile integrity during the changes, suitable constraints are necessary. They are indicated in Fig. 5.

Since the eigenform for frequency ω_7^2 and the forms for frequencies ω_6^0 and ω_4^1 are the result of deformation of the toothed wheel rim, one can expect that these eigenfrequencies will be linked more strongly to one another than to the other ones. The offset of frequency ω_7^2 from the climb rotations n_w can be obtained by increasing or decreasing this frequency. Since the decrease causes the risk of resonance with maximum rotations $n_{\max}$, a better solution is to reduce ω_7^2, which also gives the chance to offset the frequency ω_6^0 from the flight rotations n_p. Thus, the criterion for optimization problem can be minimization of frequency ω_7^2.

$$Q_1(\bar{\mathbf{x}}) = \omega_7^2(\bar{\mathbf{x}}) \rightarrow \min, \quad \text{where} \quad \bar{\mathbf{x}} = [x_1, x_2, \ldots, x_5]^T \tag{2}$$

Solution to the problem (2) gave the following resonance frequencies: $\omega_1^0 = 2830\,\text{Hz}$, $\omega_3^0 = 3608\,\text{Hz}$, $\omega_4^1 = 3381\,\text{Hz}$, $\omega_6^0 = 4417\,\text{Hz}$, $\omega_7^2 = 5420\,\text{Hz}$. After having placed these values in Campbell's diagram (Fig. 4), one can notice that the adverse effect of the profile optimisation is the risk of resonance between frequency ω_4^1 (bottom line) and minimum rotations $n_{\min}$. In addition, optimisation

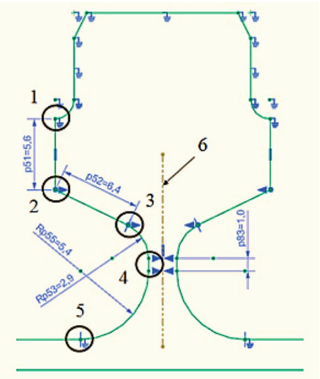

Fig. 5 Profile parameterization

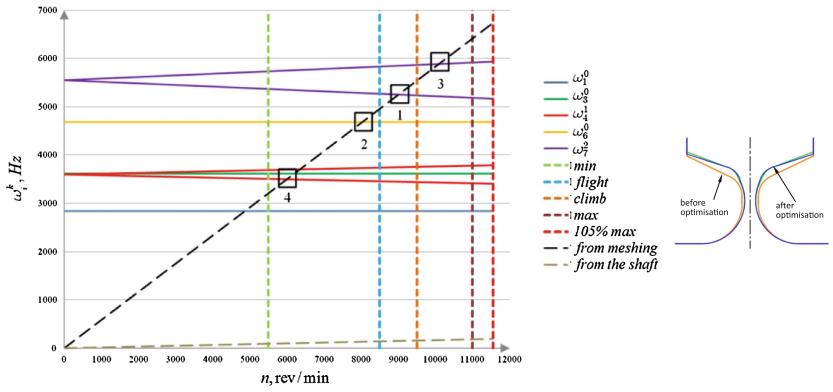

Fig. 6 **a** Campbell's of a toothed wheel after optimisation, **b** the profile—before and after optimisation

results confirmed the thesis that frequencies ω_4^1, ω_6^0 and ω_7^2, corresponding to eigenforms caused by the deformation of the rim, are interrelated. Taking into account the above conclusions, the following optimization problem was formulated

$$Q_2(\bar{\mathbf{x}}) = \omega_4^1(\bar{\mathbf{x}}) \rightarrow \max, \text{ with limitations} \tag{3}$$

$5540 \leq \omega_7^2 \leq 5550$ Hz, □ 1 (Fig. 4) halfway between the flight and the climb,

$\omega_6^0 \leq 4700$Hz, □ 2 (Fig. 4) sufficiently offset from flight rotations.

Figure 6a shows Campbell's diagram after the second optimisation whereas Fig. 6b presents the comparison of the toothed wheel profiles before and after optimisation. Numerical values of decision variables—profile parameters after optimisation and their percentage changes (%) in relation to the initial values are as follows: $x_1 = \text{p51} = 5.34$ mm (−4.6 %), $x_2 = \text{p52} = 5.76$ mm (−10 %), $x_3 = \text{p53} = 2.61$ mm (−10 %), $x_4 = \text{p83} = 0.98$ mm (−2 %), $x_5 = \text{p55} = 5.78$ mm (+7 %).

The toothed wheel with optimum profile dimensions met the requirements of security and stability as well as design requirements and in no range of operating rotations is there a risk of resonance.

4 Conclusions

The problem described in the article allows to draw the following conclusions:

– if the implemented project is in its final stage of development and yet it does not meet a particular requirement, such design parameters of the project should be

looked for that can be changed in a certain (usually small) range in order to meet all the requirements of the project,
- surfaces that are not dimensioned with fits and tolerances—free surfaces have the best chance to solve the problem of a small shape change in the final stage development of the project,
- a good way of introducing minor changes in the shape of the part in the final stage of the project development is parameterization of the part profile and then formulating and solving the problem of the optimal selection of the profile parameter according to the adopted criteria,
- modern tools for computer-aided design provide powerful tools for solving a parametric optimisation problem with the use of the FEM models of the project.

References

1. NX9 Nastran user's guide. http://nxtutorials.com/
2. Swanson, E., Powell, C.D., Weissman, S.: A practical review of rotating machinery critical speeds and modes. S&V **39**(5), 10–17 (2005)

Diagnosis of a Common Rail High Pressure Injector System

P. Starý

Abstract This article deals with the diagnosis of a Common Rail high pressure injector system and the determination of the causes of unstable fuel dosing in relation to operating temperature. The high-pressure injector is tested in a laboratory environment on an experimental stand, which able to detect the motion of the solenoid armature and the needle lift of the injector. This work is performed in two stages. The first stage involves a variability study and the second stage proposes design changes. Therefore, this paper does not provide a design solution that could lead to the removal of the high inter-cycle variability of the injector and incorrect fuel dosing at elevated operating temperatures.

Keywords Common rail · Injector · Experimental stand

1 Introduction

In recent years, Common Rail injection systems have increasingly been used in diesel engines. Due to greater demands on the minimization of harmful exhaust gas emissions it has been necessary to further develop the system of precise dosing of fuel into the cylinder.

The high pressure part of the Common Rail system ensures that the fuel pressure is regulated in the high pressure pump, this high pressure is maintained in the Rail and the volume of fuel in the injector is precisely measured.

The main task of the Rail is to supply enough fuel to the injector, the volume of which very rapidly compensates for any possible decrease in pressure in the injector

P. Starý (✉)
Technical University of Liberec, Liberec, Czech Republic
e-mail: petr.stary2@tul.cz

J. Beran et al. (eds.), *Advances in Mechanism Design II*,
Mechanisms and Machine Science 44, DOI 10.1007/978-3-319-44087-3_40

during injection and the design of which equalizes pressure impulses when opening and closing the injector needle to prevent any further spread towards the high-pressure pump or other injectors.

This ensures efficient delivery of fuel to the individual injectors with a minimum drop in pressure during the injection. The injection itself is then provided by the system's control unit, which precisely sets the time that the injector solenoid is activated. This helps achieve very accurate fuel dosing.

2 Measurement Description and Methods

During the testing of one of the developmental injectors on an combustion engine [1], and experimental stand [2–4], thermal instability of up to 30 % was determined when fuel was dosed at temperatures between 25 and 90 °C. The temperature was measured at the outlet of the waste dose from the injector. The flow of fuel heats the injector to its operating temperature of 80–90 °C. This heating changes the operating conditions of the injector either through dilation of individual parts or changes in the viscosity of the fuel used. However, a well-functioning injector should not react negatively in any way to these changes in operating conditions.

Due to the thermal instability, the injector becomes unmanageable in terms of the engine testing and cannot be run for the given engine tests. For these reasons, it was necessary to determine the cause of these instabilities which lead to further structural changes and eliminate the inter-cycle variability of the injector.

Micro Epsylon, LS 04 and Balluff BAW M08EI-UAD15B-BP03 sensors were installed on the high-pressure injector. Needle and armature lift measurements were taken on a single timeline in order to detect any time nuance from the values required by the unit when opening and closing the injector needle. Further variables i.e. voltage and current supplied to the solenoid coil, dynamic pressure on the inlet to the injector and in the Rail with a sampling rate of 0.2°CA and fuel temperature on the overflow, were measured to provide the overall conditions of the injector. Before installation, the average fuel dose cycles were measured in an opening time range of 200–1000 microseconds and pressure range of 600–1600 bar, see Fig. 1.

The injector was tested for 1000 microseconds at 1600 bar. The results of the measurements were evaluated taking into account the various injector temperatures i.e. 25, 50 and 88 °C (Fig. 2), which was the highest temperature reached on the injector overflow. The variability of the armature lift was also evaluated, see Fig. 3.

The results of the measurements show that an increase in temperature in the injector does not affect the total time for the armature to reach the solenoid or the value of the armature lift, which corresponds to 0.08 mm for the whole measurement duration. In terms of variability, no inter-cycle nuance was determined, which

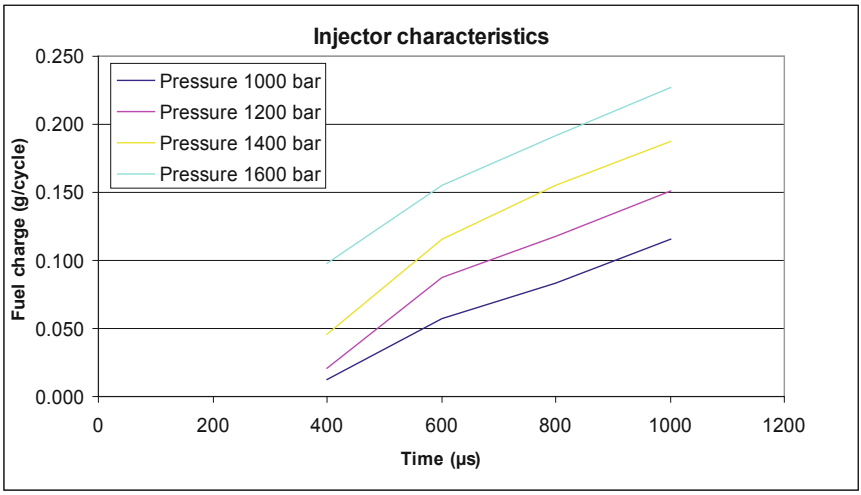

Fig. 1 Graph showing the average dose cycles

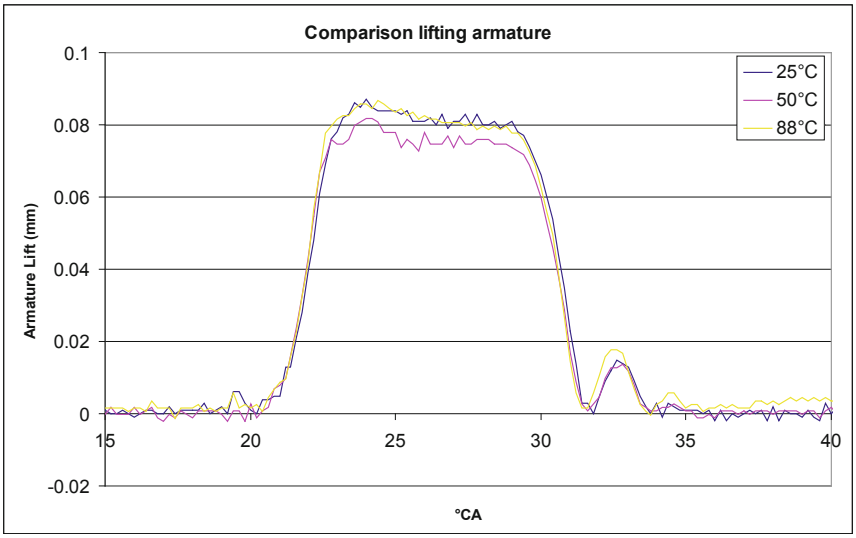

Fig. 2 Comparison of the armature lift in relation to the fuel temperature

shows that the armature has no temperature dependence on the open-close interval. The results show significant changes in the movement of the armature after it lands and subsequently rebounds when the ball valve is closed. This armature rebound movement occurs with an increasing operating temperature of the injector, see

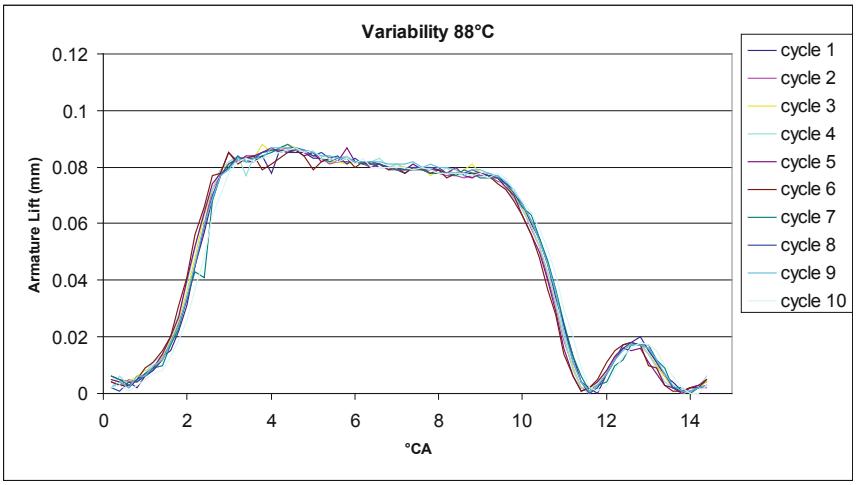

Fig. 3 Variability of the armature lift in 10 cycles

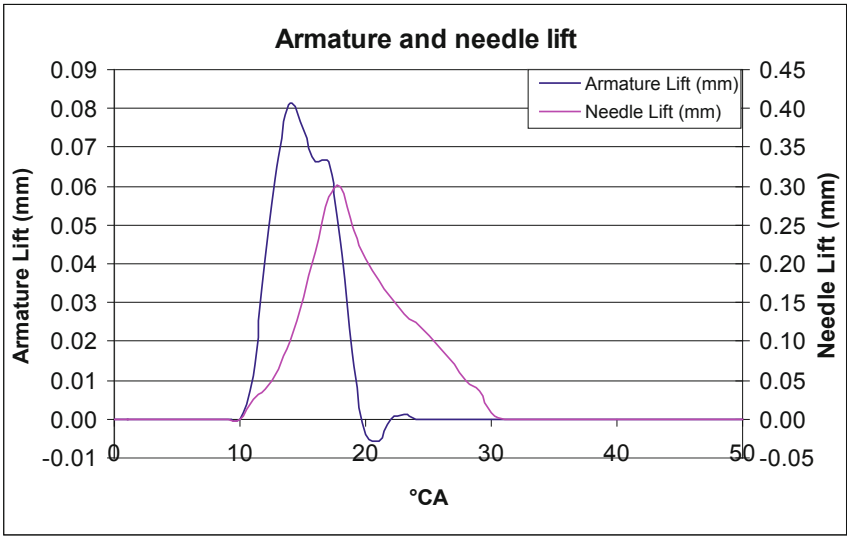

Fig. 4 Course of the armature and needle lift without solenoid armature rebound movement

Fig. 5. Therefore, it was necessary to also examine the behaviour of the needle lift. The results clearly show that even a small armature rebound movement when closing the ball valve can have an enormous effect on the total time it takes to open the main injector i.e. tens of percent, see Fig. 5.

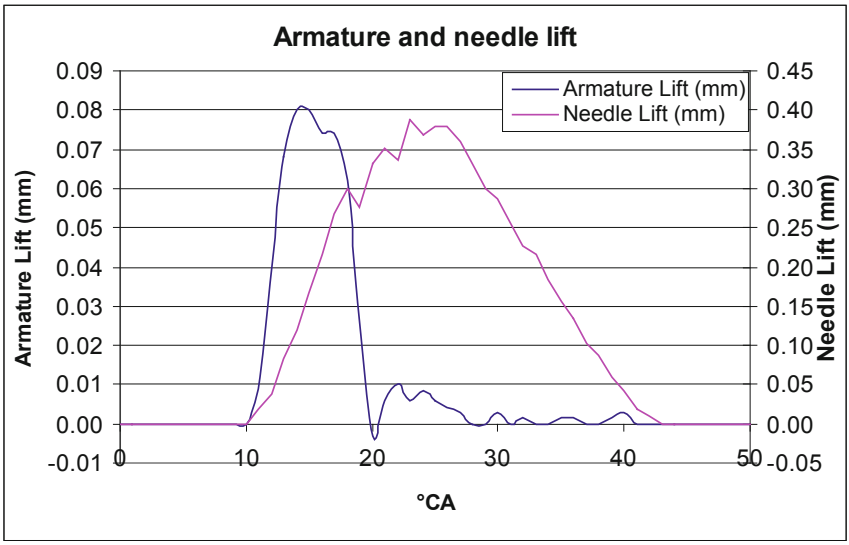

Fig. 5 Course of the armature and injector needle lift with solenoid armature rebound movement

3 Conclusions

Figure 4 shows the course of the solenoid armature and needle lift without armature rebound movement at a temperature of 25 °C. Figure 5 shows the behaviour of the armature at elevated temperatures of the waste dose in the range of 70–90 °C. The measured results show a significant effect on the dose cycle when the solenoid armature rebounds at elevated operating temperatures. This has an enormous effect on the opening time of the main injection nozzle and hence the total fuel dose. For these reasons, the injector becomes unstable and cannot be effectively operated on an internal combustion engine. Further development and measuring work on the injector will include a more detailed analysis of the basic operating parameters necessary to remove the problematic behaviour of the armature when closing the ball valve.

Acknowledgments The results of this project LO1201 were obtained through the financial support of Education, Youth and Sports in the framework of the targeted support of the "National Programme for Sustainability I" and the OPR&DI project Centre for Nanomaterials, Advanced Technologies and Innovation CZ.1.05/2.1.00/01.0005.

This paper was originated in cooperation with company Motorpal. It provided development and injector portion of the measured data.

References

1. Starý, P., Popelka, J.: Laboratory testing of a high-pressure common rail injection system. In: The 5th International Conference on Mechanics, Simulation and Control (ICMSC 2015) St. Petersburg, Russia (2015)
2. Scholz, C., Starý, P.: Experimental stand for research of common-rail injectors. In: XLI International Scientific Conference of Czech and Slovak Universities Departments and Institutions Dealing with the Research of Combustion Engines, Liberec, pp. 277–287 (2010). ISBN 978-80-7372-632-4
3. Scholz, C., Starý, P.: Common rail injector leak testing. J. Middle Eur. Constr. Des. Cars—MECCA **XI**(03), 22–28 (2013). ISSN 1214-0821, ISSN 1804-9338
4. Scholz, C., Starý, P.: Experimental study of common rail injection diesel engine fuelled with RME and diesel fuel. In: XLII International Scientific Conference of Czech and Slovak Universities Departments and Institutions Dealing with the Research of Combustion Engines, Zilina, pp. 277–287 (2011). ISSN 1337-8996

Design of a Tribometer for Piston Rings

R. Voženílek, S. Beroun and J. Břoušek

Abstract Reducing the energy loss associated with offsetting friction losses occurring on the contact surfaces of mutually moving parts is an important factor when correctly designing structures. A typical case of reciprocating sliding motion with significant friction losses on the overall mechanical losses of a machine is a piston group of internal combustion engines or compressors. One way to reduce friction is to use modern coatings on the surface of the friction pairs. Special testing equipment i.e. a tribometer is used to obtain information on the benefits of these coating layers. This paper deals with the design and verification of the functions of a special tribometer for identifying the losses of piston rings.

Keywords Tribometer · Piston ring · Stribeck curve · Mechanical losses

1 Introduction

Increasing the efficiency of machinery and equipment is associated with reducing the lost energy necessary to offset friction losses arising on the contact surfaces of mutually moving parts. The size of the friction losses depends on the load of the contact surfaces. At the same time, a significant role is played by the quality of the surface of the contact areas and the presence of lubrication between the "contact" surfaces of moving parts, as well as the relative speed of the moving parts (the dependence of these factors can be shown a in general form using a so-called Stribeck curve).

R. Voženílek (✉) · S. Beroun · J. Břoušek
Technical University of Liberec, Liberec, Czech Republic
e-mail: robert.vozenilek@tul.cz

S. Beroun
e-mail: stanislav.beroun@tul.cz

J. Břoušek
e-mail: josef.brousek@tul.cz

J. Beran et al. (eds.), *Advances in Mechanism Design II*,
Mechanisms and Machine Science 44, DOI 10.1007/978-3-319-44087-3_41

In cases where mutually moving pairs operate in a state of steady movement it is possible to achieve low friction losses using a suitable lubricant (i.e. to achieve an operating state using effective hydrodynamic lubrication)—such cases mostly concern rotational movement. In the design of machines, however, there are many cases where the sliding movement between pairs is at variable speeds and rapidly alternating directions. In these cases, the contact surfaces of the moving parts pass from marginal to hydrodynamic friction. In some cases of reciprocating sliding movement it is not possible to safely ensure that the movement between the pairs is under hydrodynamic friction—dry or semi-dry friction—then the friction loss increases and in these cases the quality of the surface of the contact area (surface roughness and coefficient of dry friction) significantly decreases due to these friction losses (Fig. 1).

A typical case of reciprocating sliding movement with significant friction losses on the overall mechanical losses of the machine is a piston group (piston with piston rings) in a piston combustion engine or in a piston compressor (Fig. 2).

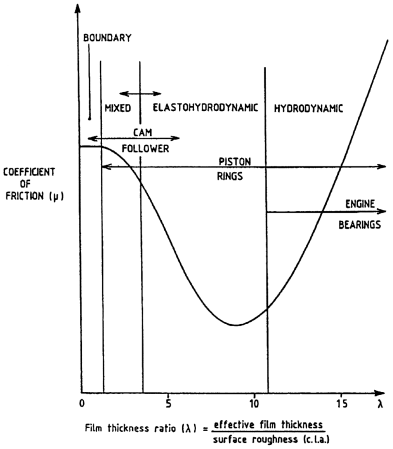

Fig. 1 Modified Stribeck curve and operating region of friction couples [1]

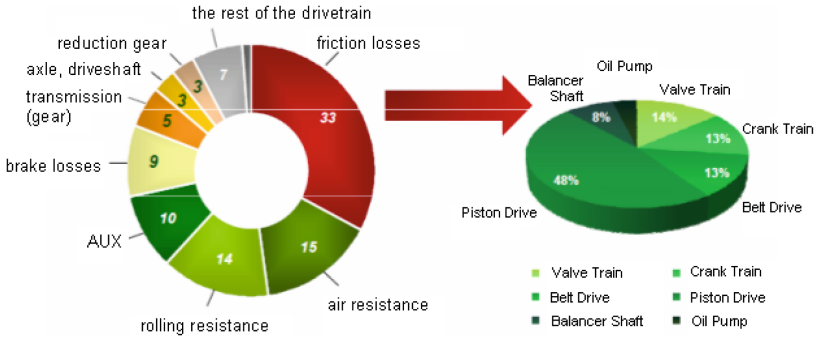

Fig. 2 Distribution of mechanical energy and friction losses [2]

It has been proven through experimentation that in spark ignition reciprocating internal combustion engines the piston group contributes to an overall mechanical losses in the engine of approximately 45 %, for diesel engines the share of the piston group is around 50 % of the total losses. It is therefore logical that in order to reduce mechanical losses in a reciprocating internal combustion engine one should focus on finding possible measures to reduce friction losses in the piston group. As a result, coating the sealing (friction) surfaces of piston rings and the friction parts of pistons offers a promising solution.

2 Tribometer Construction

Prior to designing the construction of the tribometer, research was performed on the test equipment, which involved testing friction properties and in particular a pair of piston rings and a cylinder engine. The test equipment works with a linear reciprocating motion with variable speed and only a cutout of an engine block and part of the piston ring were used for the test, as shown in Fig. 3.

The test equipment for measuring friction losses across the piston ring was structurally designed and physically implemented at the Technical University of Liberec. A Parker—PowerRod Actuator was used to create the linear reciprocating motion with variable speed. Therefore, no crank mechanism was used. The drive is created by connecting the rod with the piston and piston rings through the designed reduction. The cutout of the engine block is placed together with a base plate on a linear line with an extremely low friction coefficient. The base plate is connected to

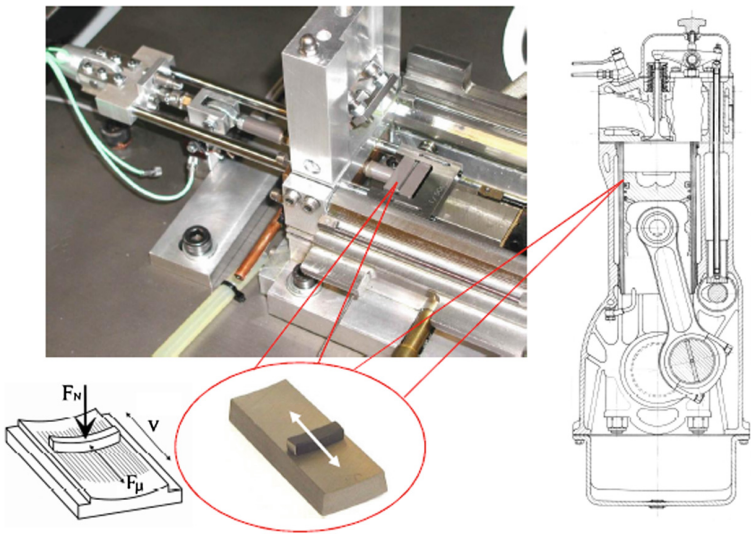

Fig. 3 Piston ring tribometer—VTT Technical Research Centre of Finland LTD [3]

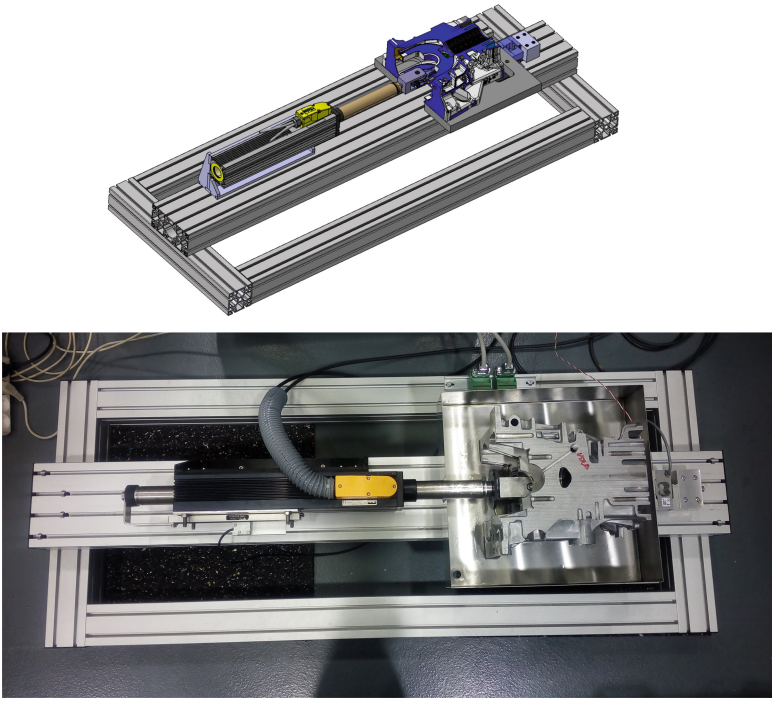

Fig. 4 Design and implementation of the construction of a tribometer with linear reciprocating movement

Table 1 PowerRod PRA38 drive parameters [4]

Parameter	Value
Peak force (at 25 °C ambient temperature) for 1 s (N)	1488
Continuous stall force (at 25 °C ambient temperature) (N)	276.2
Peak acceleration (based on a 33 mm stroke, without payload) (m/s^2)	391
Maximum speed (based on triangular move over maximum stroke, without payload) (m/s)	2.6

the frame of the structure through a force sensor. The whole of the test equipment is placed behind an aluminum profile frame to facilitate making adjustments when changing the test components. Oil circulation was also mechanically prepared for the system of external lubrication of the tested friction pairs, and can be used when needed (Fig. 4; Table 1).

A data collection system was created for the test equipment using an MGCplus (Hottinger) data logger, which records information about the strength of the rod axis motion (force sensor), the rod position (linear magnetic sensor) and temperature at selected points.

3 Verification of the Functions of the Tribometer and Selected Measurement Results

The measurements performed to-date indicate high repeatability and stability of the linear reciprocating motion on the measured sample. The graphs show the course of the force depending on the position. The maximum possible length of movement of the piston is given by the construction of the block of the internal combustion engine. The first tests of the test equipment were carried out with a stroke of 87 mm. For the selected combination of engine block cutout of the internal combustion engine, piston and piston rings, the electromagnetic actuator can be set at different levels of velocity in a range from 0 to 1.25 m/s. However, in order to ensure the required constant speed of the piston over a longer distance of its movement in the cylinder a lower speed is preferable during the measurement (Fig. 5).

Special software was prepared to evaluate the results, which calculated the average force in a given position or speed from multiple strokes, and subsequently only forces in the selected range are evaluated based on the selected criteria. This application will be used to evaluate different designs of rings and different ring surfaces used to reduce friction.

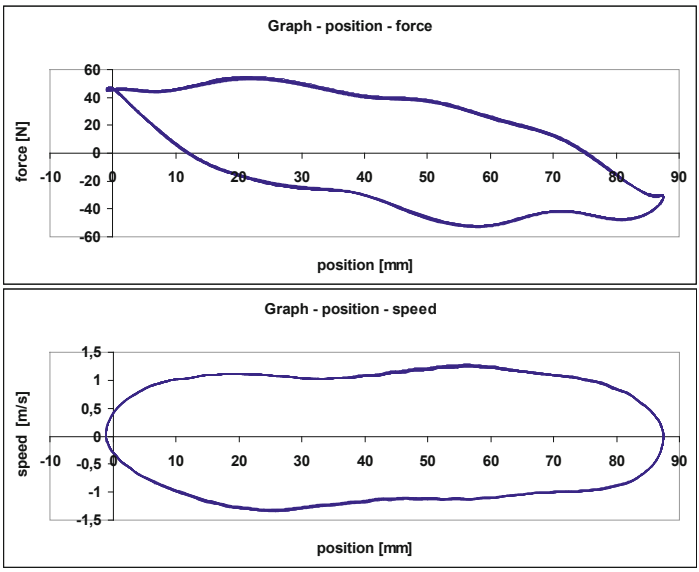

Fig. 5 Demonstration of the position/force and position/velocity of the measurement on the testing device (shown are measurements more cycles)—0 mm position is relative to the top dead center

4 Conclusions

The test equipment may be used for different sizes of piston groups. The advantage of the test equipment is the possibility to rapidly adjust the components for the different sizes of tested samples. The test equipment can also be used to measure individual piston rings separately, and it is therefore possible to determine the impact of the individual rings on the mechanical losses. Such measurements can be beneficial even for the verification of models of piston rings using different types of simulation software. In contrast to the real environment, however, forces caused by the combustion in the combustion chamber do not act on the piston rings. One advantage can be that a linear actuator is used for the linear reciprocating movement, which prevents the formation of normal forces on the piston during movement. These may arise due to imperfect mounting of the components on the test equipment. However, they can be determined by measurement and subsequently subtracted during the measurements with piston rings. A certain disadvantage of the test equipment (tribometer) may be the limited speed range, as the mean velocity of the piston in a conventional internal combustion engine can reach values of up to one order of magnitude higher.

Acknowledgments The results of this project LO1201 were obtained through the financial support of the Ministry of Education, Youth and Sports in the framework of the targeted support of the "National Programme for Sustainability I" and the OPR&DI project Centre for Nanomaterials, Advanced Technologies and Innovation CZ.1.05/2.1.00/01.0005.

References

1. Priest, M., Taylor, C.: Automobile engine tribology—approaching the surface. Wear **241**(2), 193-203 (2000). ISSN: 0043-1648
2. Basshuysen, R., Schäfer, F.: Internal Combustion Engine Handbook, Chapter 9. Vieweg Verlag, Berlin (2002)
3. http://www.vttresearch.com/services/business-essentials/pilot-plants-and-r-d-infra/machines-and-vehicles-research-facilities/tribology-research-facilities
4. Catalog PARKER: PowerRod—Actuators and components: 192-570006 N2/UK Version 2, (2006)

Mathematical Model of Elastic Heald

M. Bílek, Š. Kovář and J. Skřivánek

Abstract The paper is concerned with description of the mathematical model meant for an analysis of the movement of healds during the weaving cycle. The paper deals with the assessment of the current construction design fastening the heald into the heald shaft. The present condition is characterized by the increased heald loading which is caused by its impact on the supporting wire. As a result of this, the healds get considerably worn out and their service life of the heads is reduced. There is a possibility for passive resistance involvement to reduce the velocity of the heald impact on the supporting wire. In this variant of the solution, the friction between the heald and the supporting wire is used for the decreasing of the impact.

Keywords Weaving loom · Heald · Mathematical model · Shedding motion

1 Introduction

The means for realization of the paper objective has been a complex description of the system elastic heald—supporting wire, employing a verified mathematical model. Regarding the wide spectrum of diverse arrangement options for the system individual parts, the article does not intend to suggest any particular parameters of the construction design. However, the primary aim is to specify possible ways, which lead to its optimization.

It is not possible to find a larger amount of the papers which are focused on this theme in the case of the shedding motion analyzes. Some of them have been dealt

M. Bílek (✉) · Š. Kovář · J. Skřivánek
Technical University of Liberec, Liberec, Czech Republic
e-mail: martin.bilek@tul.cz

Š. Kovář
e-mail: simon.kovar@tul.cz

J. Skřivánek
e-mail: josef.skrivanek@tul.cz

J. Beran et al. (eds.), *Advances in Mechanism Design II*,
Mechanisms and Machine Science 44, DOI 10.1007/978-3-319-44087-3_42

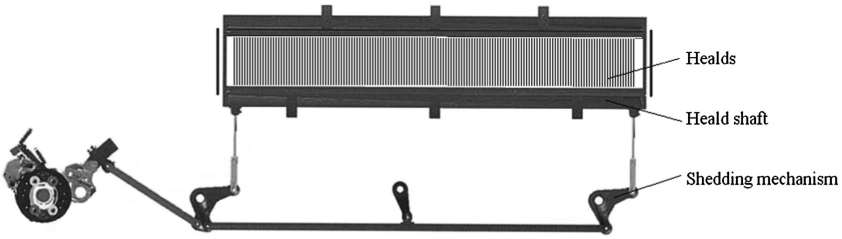

Fig. 1 Shedding mechanism

theoretically or experimentally with emphasis on the analysis heald frame [1, 2] or shedding motion [3, 4].

In general, the shedding mechanism can be classified into two sections: the driving section and the transforming section. In most cases the transforming section of the shedding mechanism involves joint mechanisms, which convert the rotational motion of the driving section into reciprocating motion of the heald shaft. Heald frame motion characteristics depend on the type of shedding motion.

The heald shaft is the frame in which there are fastened the healds operating warp threads (Fig. 1). The healds are fastened in this frame with a necessary designing play. Because of textile technology reasons, this play must enable axial displacement of the heald along the supporting wire. As the heald shaft performs reciprocating movement, the system of healds gets transferred during the weaving cycle. This transfer produces a load on the supporting wire upon which the healds impact, bringing as a consequence an increased stressing of the whole shedding mechanism.

2 Mathematical Model of the Elastic Heald

The studies realized up to now [5, 6] have shown that the heald is one of the most important part of the shedding motion and it exerts an important effect upon its dynamic loading. Because of this reason, it also constitutes one of the limiting elements, which impede the increase in its operational revolutions.

The heald is subjected to many forces, which determine the connection with the supporting wire. The most important ones are the dynamic forces of the heald, the warp forces in the sense of the shaft movement and the heald weight.

The analysis of the heald behaviour during the operating cycle has been realized using derived models of the heald. The motion equations describing the movement of the heald during the weaving process are complemented with motion equations of the shedding motion. In all compiled models, the mass of the heald mn is

concentrated in one particle. The force T_o from the warp operates in the position of the thread eyelet. The action point of this force is located in one particle. It is possible to disregard the bowing of the heald due to its lateral loading. The derived models proceed from the assumption that the movement of the particle substituting the heald is carried out on a straight line.

At present, there are used flat healds made of a flat steel band by pressing process. The healds are contoured in the positions of their suspension eyes; however, it reduces their stiffness. Because of this reason, mathematical models have included different rigidities of the upper and lower sections of the heald (k_{nD}, k_{nH}) and different damping (b_{nD}, b_{nH}). In the mathematical model of the heald, Newtonian impact theory is employed. The drop description of the heald upon the supporting wire employs the presumption of a perfectly elastic impact.

There is a possibility for passive resistance involvement to reduce the velocity of the heald impact on the supporting wire. In this variant of the solution, the friction between the heald and the supporting wire is used for the decreasing of the impact. The proposal of the structural design using friction force for reducing the relative velocity of heald with respect to supporting wire is mentioned in [7] and scheme is on Fig. 2. In the referred design proposal, parts of inner surfaces of end eyelets are curved concavely, in order to create conditions for a slip of the end eyelet along a convex surface formed on the supporting wire. The relative velocity of the heald is reduced by effect of the friction force, and at the same time, the direction of the heald movement changes. In the solved case, there has been taken into account the calculation of the friction force according to this design proposal. In the following text, this mathematical model is referred to as the model 4.

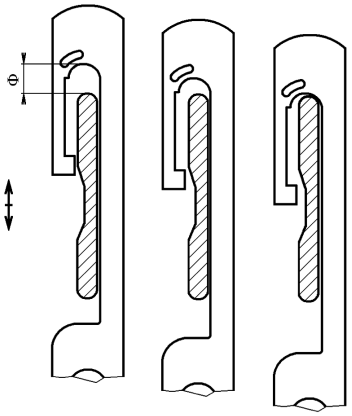

Fig. 2 Scheme of the design using friction force

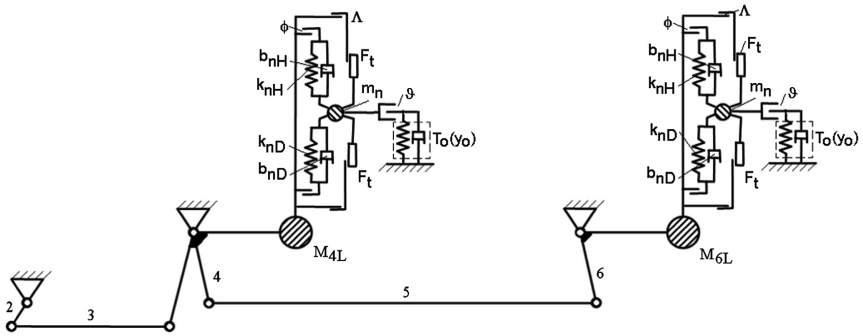

Fig. 3 Schematic model of the system shedding motion—elastic heald

The mathematical model of the system with the impact damping of heald upon supporting wire is obtained by modification of the preceding model [5, 6]. The whole solved system can be represented schematically according to the Fig. 3. The motion equation describing the behavior of the heald during a revolution of the weaving loom has been complemented with a term characterizing the magnitude of the friction force.

The motion equation of this case can be written in the following form:

$$\begin{aligned} m_n \cdot \ddot{y}_{in} = T_o - m_n \cdot g + H \cdot k_{nH} \cdot (y_h - y_n) + H \cdot b_{nH} \cdot (\dot{y}_h - \dot{y}_n) \\ - D \cdot k_{nD} \cdot (y_n - y_d) - D \cdot b_{nD} \cdot (\dot{y}_n - \dot{y}_d) + H_2 \cdot F_{ty} \end{aligned} \quad (1)$$

The constants H, D and H_2 determine which members of the equation will be applied in the calculation.

The initial conditions of the solution proceed from the presumption that the heald is held on the upper supporting wire, and both its velocity and acceleration are identical with those of the upper supporting wire. The individual mathematical models has been solved using derived software. The solution of compiled differential equations describing the shedding motion coupled with an analysis of the heald movement during the weaving cycle has been effected by the Runge-Kutta method of the 4th order [5]. During the calculation, there have been studied the courses of the principal kinematic and force quantities of the system. The control algorithm of the calculation checks the position of the heald with respect to the supporting wire of the heald shaft. As mentioned above, there can arise six possible states which have been studied and on the basis of which there has been realized the calculation of the heald movement (Fig. 4).

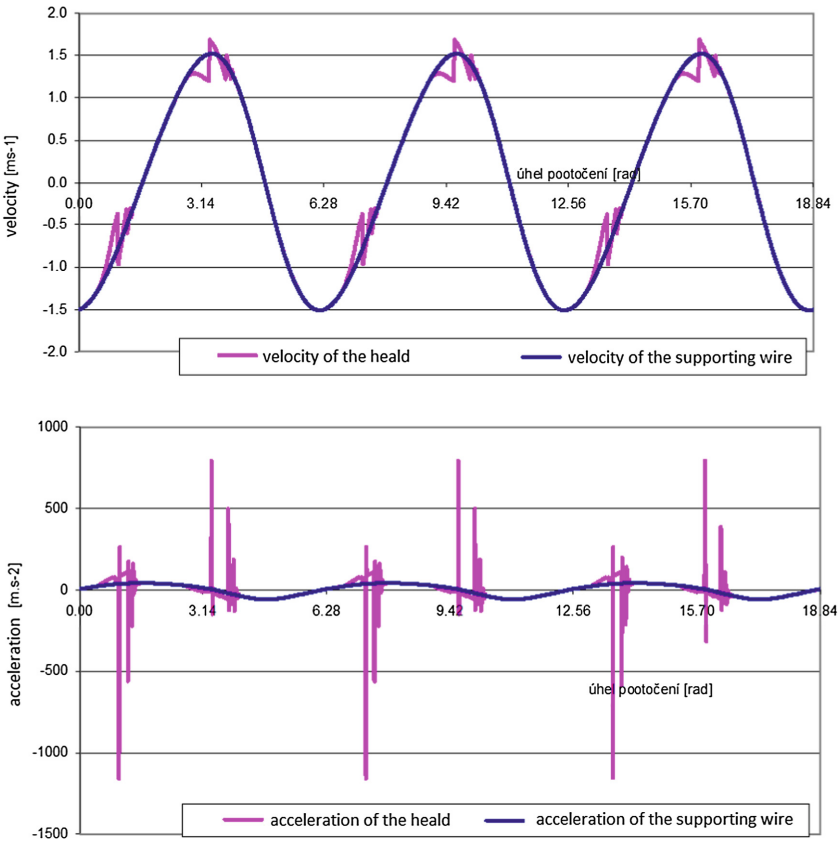

Fig. 4 The courses of velocity and acceleration of the heald shaft and of the heald for the operating velocity of the shedding motion 300 rpm

3 Conclusions

In order to reduce the impact velocity of heald on supporting wire, the friction between the heald and the supporting wire can be used, too. The friction force brings into the system a force effect, which causes a reduction of relative movement of the heald with respect to the supporting wire. In this order, the friction force does not affect the heald after its separation from the supporting wire, because the normal force between the heald and the supporting wire in this moment amounts to zero.

The use of passive resistances for reducing the velocity of heald impact upon the supporting wire proves to be less effective than the usage of a damping element [6]. The effect of the friction force is more significant with lower operating velocities. With increasing operating velocities, the effect of the friction force on the reduction of the maximum value of heald acceleration decreases.

Table 1 Maximum values of heald acceleration after its impact on upper support wire

	150 rpm of the shedding motion (m s^{-2})	300 rpm of the shedding motion (m s^{-2})	450 rpm of the shedding motion (m s^{-2})
Model 2	1.220	1.340	1.477
Model 3	746	963	1.066
Model 4	984	1.160	1.313

Table 2 Acceleration of heald after its impact on lower support wire (m s^{-2})

	150 rpm of the shedding motion (m s^{-2})	300 rpm of the shedding motion (m s^{-2})	450 rpm of the shedding motion (m s^{-2})
Model 2	671	906	1.080
Model 3	294	533	711
Model 4	567	783	955

Tables 1 and 2 shows maximum and minimum values of the heald acceleration after its impact upon upper and lower supporting wires, ascertained by means of the models 2 (without damping and friction force [5]), model 3 (heald with damping element [6]) and model 4 (design of heald with friction force). If we compare the courses of the heald acceleration obtained via the individual mathematical models, it is possible to state that the maximum reduction is achieved when employing the damping element [5, 6]. From the analysis there follows that the use of the friction force also reduces the maximum values of acceleration in comparison with a system without damping; however, this reduction is less significant than in case of the damping element.

Acknowledgments This publication was written as part of the project "Research of the processes of textile and single-purpose machines" with the support of the Specific University Research Grant and also the Institutional Endowment for the Long Term Conceptual Development of Research Institutes, as provided by the Ministry of Education, Youth and Sports of the Czech Republic.

References

1. Lee, D.G., Lee, C.S., Oh, J.H., Jeon, H.S.: Composite heddle frame for high-speed looms. Compos. Struct. **47**(1–4), 507–517 (1999). doi:10.1016/S0263-8223(00)00012-X
2. Xu, S., Feng, Z.: Modal analysis of heald frame and experimental verification. J. Soochow Univ. Eng. Sci. Ed. **28**(2), 34–36 (2008)
3. Guha, A., Amarnath, C., Kurien Issac, K., Talukdar, M.K., Joshi, S.: Linkage driven dobby with dwell. Text. Res. J. **79**(9), 804–809 (2009)
4. Eren, R., Aydemir, A.: Kinematic design method for six-bar linkage sley drive mechanisms in weaving. Indian J. Fibre Text. Res. **30**(3), 243–251 (2005)

5. Bílek, M., Skřivánek, J.: Mathematical modeling of the system shedding motion—heald—warp. AUTEX Res. J. **14**(2), 42–46 (2013). ISSN 1470-9589
6. Bílek, M., Skřivánek, J.: Mathematical model of the heald with damping element. AUTEX Res. J. **15**(1), 2–7 (2015). ISSN 1470-9589
7. Technical University of Liberec, Bílek, M., Kovář, Š.: Nitěnka pro tkací stroj (Loom heald), patent, CZ 305126

Dynamic Model of the Mechanical System of the Needle Bar

J. Komárek

Abstract The paper deals with description of dynamic behaviour of the mechanical system of the needle bar on the basis of mathematical modelling. The equation of motion of the system which is a part of a sewing machine are described by Lagrange equations of second order. Contacts between individual parts of the system are described using boundary conditions based on the geometry of the mechanical system. The equations were solved using the software Matlab Simulink. The knowledge obtained from the dynamic analysis can be used in the optimisation of the mechanical system of the needle bar.

Keywords Mathematical model · Dynamic analysis · Needle bar · Sewing machine

1 Introduction

Requirements of manufacturers of sewing machines aim to reduce the time of the sewing process and increase the productivity. Other important requirements that should fulfil today's sewing machines are silent running, minimum vibration, long lifetime and easy to operate. A sewing machine which contains the mechanical system of the needle bar uses the floating needle system to produce a hand stitch represented in Fig. 1.

The floating needle system uses a double pointed needle with an eye in the middle as represented in Fig. 2. By the use of two mechanical systems of the needle bar, one above and one below the work plate, a threaded needle is passed through the material on every stitch. The mechanical system of the needle bar performs a rectilinear reverse movement which is realized by a cam mechanism. However, in case of high operating speeds machines produce high level of noise and vibrations. This unfavourable effect should be reduced. The dynamic model described in this

J. Komárek (✉)
Technical University of Liberec, Liberec, Czech Republic
e-mail: jiri.komarek@tul.cz

J. Beran et al. (eds.), *Advances in Mechanism Design II*,
Mechanisms and Machine Science 44, DOI 10.1007/978-3-319-44087-3_43

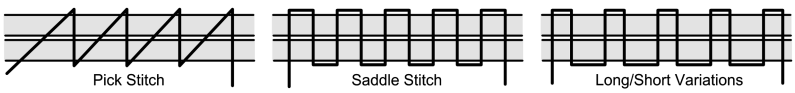

Fig. 1 Hand stitch types

Fig. 2 Double pointed needle

article enables the analysing of the mechanical system of the needle bar and it will help with its optimization. A detailed description of the sewing machine is included in the work [1].

2 Description of the Mechanical System of the Needle Bar

The cross-section of the mechanical system of the needle bar is shown in Fig. 3. The floating needle *20* is held by collets *12* inside the mechanical system of the needle bar. The collets are made up of two balls whose axial movement is controlled by a cylinder *4*. The balls are pushed into a conical hole in a shell *2* due to the pressing force of the springs *11*, *15*. This situation is shown in Fig. 3a. The release of the needle is started in a moment when the control element (assembled from parts *1*, *3*, *6*, *10*, *11*, *16*, *17*) collides with the machine frame *18*. The impact is absorbed by the rubber pad *10*. The influence of stiffness of the rubber pad on absorbing of the impact is described in [2]. After the impact, the shell *2* continues its movement towards the bottom dead centre position, whereby the balls are released in the enlarged area of the conical hole. This situation is shown in Fig. 3b. A more detailed description of the mechanical system of the needle bar is in [1].

There has been carried out an experimental measuring of compression of springs in response to applied force for the purpose of determining the stiffness of the springs. There has been obtained values of stiffness of the spring *11* k_2 = 900 N/m and the spring *15* k_3 = 690 N/m. There has been also experimentally determined dependence of deformation of the rubber pad in response to the applied force. The dependence is nonlinear and its obtained values has been approximated by a polynomial of third degree (1), where x_{20} denotes the deformation of the rubber pad and F_{20} the applied force. The values of damping of the springs and the rubber pad has been determined by the actual behaviour of the mechanical system of the needle bar which corresponds to the high-speed camera recording. The values of damping of the spring *11* b_2 = 13.15 N s/m, the spring *15* b_3 = 3.32 N s/m and the rubber pad b_{20} = 28.5 N s/m. Obtaining of values of stiffness and damping is described in detail in [3].

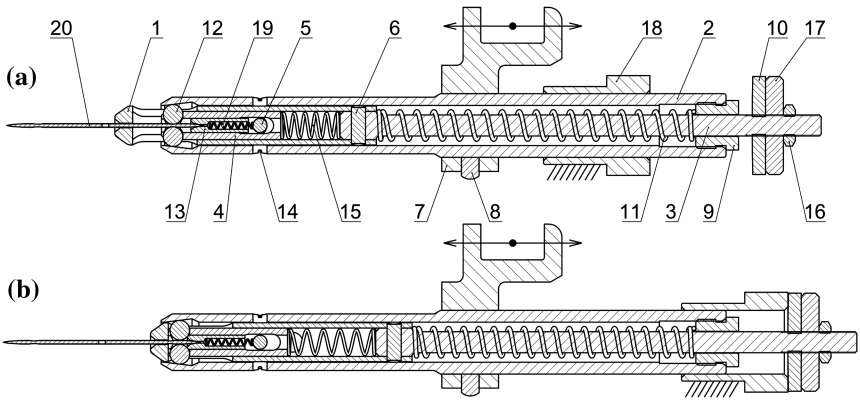

Fig. 3 Cross-section of the mechanical system of the needle bar **a** Holding position, **b** Release position

$$F_{20} = 15{,}739 \cdot 10^8 x_{20}^3 + 445{,}150 x_{20} \tag{1}$$

3 Description of the Dynamic Model

The dynamic model of the mechanical system of the needle bar is illustrated in Fig. 4. The real system has been simplified to six bodies of masses m_1, m_2, m_3, m_4, m_5 and m_6. The body 1 represents the shell, the body 2 represents the control element, the body 3 represents the collets, the body 5 represents needle and bodies 4 and 6 represent needle guides. The individual parts of the model are considered as rigid bodies with the mass concentrated in one point. Gravitational acceleration is neglected. The springs and rubber pad are described by means of stiffness k_2, k_3, k_4, k_6, nonlinear stiffness k_{20} and damping b_2, b_3, b_4, b_6, b_{20} and their masses are neglected. Modelling of contacts between bodies is based on the idea that due to contact between bodies occurs the reflection that is caused by the elasticity of real bodies. In the model, the elasticity of the bodies is replaced by the spring. The transformation of the part of kinetic energy to deformation energy is simulated using a damper. The values of stiffness and damping have been chosen so that the behaviour of the dynamic model as close as possible to the real system.

Using Lagrange equations of second order [4] were compiled equations of motion of the system in the form:

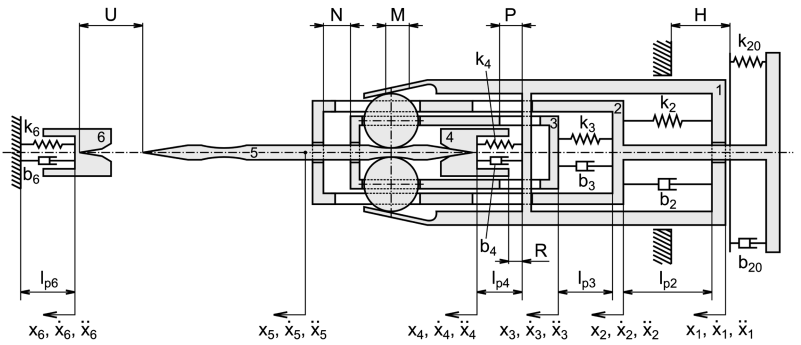

Fig. 4 Scheme of the mechanical system of the needle bar

$$\begin{aligned} m_1\ddot{x}_1 = {} & -k_2\left(x_1 - x_2 + l_{20} - l_{p2}\right) - k_4\left(x_1 - x_4 + l_{40} - l_{p4}\right) \\ & + L_{21}k_{21}(x_2 - x_1) - L_{13}k_{13}(x_1 - x_3 - P) + L_{31}k_{31}(x_3 - x_1) \\ & - L_{14}k_{14}(x_1 - x_4 - R) - b_2(\dot{x}_1 - \dot{x}_2) - b_4(\dot{x}_1 - \dot{x}_4) \\ & + L_{21}b_{21}(\dot{x}_2 - \dot{x}_1) - L_{13}b_{13}(\dot{x}_1 - \dot{x}_3) + L_{31}b_{31}(\dot{x}_3 - \dot{x}_1) - L_{14}b_{14}(\dot{x}_1 - \dot{x}_4) \end{aligned} \tag{2}$$

$$\begin{aligned} m_2\ddot{x}_2 = {} & k_2\left(x_1 - x_2 + l_{20} - l_{p2}\right) - k_3\left(x_2 - x_3 + l_{30} - l_{p3}\right) \\ & - L_{20}\left(15,739 \cdot 10^8 (x_2 - H)^3 + 445,170(x_2 - H)\right) - L_{21}k_{21}(x_2 - x_1) \\ & + L_{32}k_{32}(x_3 - x_2 - N) + b_2(\dot{x}_1 - \dot{x}_2) - b_3(\dot{x}_2 - \dot{x}_3) \\ & - L_{20}b_{20}\dot{x}_2 - L_{21}b_{21}(\dot{x}_2 - \dot{x}_1) + L_{32}b_{32}(\dot{x}_3 - \dot{x}_2) \end{aligned} \tag{3}$$

$$\begin{aligned} m_3\ddot{x}_3 = {} & k_3\left(x_2 - x_3 + l_{30} - l_{p3}\right) - L_{32}k_{32}(x_3 - x_2 - N) + L_{13}k_{13}(x_1 - x_3 - P) \\ & - L_{31}k_{31}(x_3 - x_1) - L_{35}k_{35}(x_3 - x_5) + b_3(\dot{x}_2 - \dot{x}_3) \\ & - L_{32}b_{32}(\dot{x}_3 - \dot{x}_2) + L_{13}b_{13}(\dot{x}_1 - \dot{x}_3) - L_{31}b_{31}(\dot{x}_3 - \dot{x}_1) - L_{35}b_{35}(\dot{x}_3 - \dot{x}_5) \end{aligned} \tag{4}$$

$$\begin{aligned} m_4\ddot{x}_4 = {} & k_4\left(x_1 - x_4 + l_{40} - l_{p4}\right) + L_{14}k_{14}(x_1 - x_4 - R) - L_{45}k_{45}(x_4 - x_5) \\ & + b_4(\dot{x}_1 - \dot{x}_4) + L_{14}b_{14}(\dot{x}_1 - \dot{x}_4) - L_{45}b_{45}(\dot{x}_4 - \dot{x}_5) \end{aligned} \tag{5}$$

$$\begin{aligned} m_5\ddot{x}_5 = {} & L_{35}k_{35}(x_3 - x_5) + L_{45}k_{45}(x_4 - x_5) - L_{56}k_{56}(x_5 - x_6 - U) + L_{35}b_{35}(\dot{x}_3 - \dot{x}_5) \\ & + L_{45}b_{45}(\dot{x}_4 - \dot{x}_5) - L_{56}b_{56}(\dot{x}_5 - \dot{x}_6) \end{aligned} \tag{6}$$

$$m_6\ddot{x}_6 = -k_6x_6 + L_{56}k_{56}(x_5 - x_6 - U) - b_6\dot{x}_6 + L_{56}b_{56}(\dot{x}_5 - \dot{x}_6) \tag{7}$$

where l_{02}, l_{03}, l_{04}, l_{06} are lengths of the unloaded springs and l_{p2}, l_{p3}, l_{p4}, l_{p6} are lengths of the springs after installation. Positions of individual objects are labelled in equations as x_1, x_2, x_3, x_4, x_5 and x_6. The Fig. 4 shows the system in the initial state, where the distances between the contacts are lettered H, N, P, R, U, M. The distances are also taken into account in the equations of motion.

The states when contacts between bodies occur are described by the boundary conditions:

$$If\ x_2 - H \geq 0 \quad then \quad L_{20} = 1; \quad If\ x_2 - H < 0 \quad then \quad L_{20} = 0 \tag{8}$$

$$If\ x_2 - x_1 \geq 0 \quad then \quad L_{21} = 1; \quad If\ x_2 - x_1 < 0 \quad then \quad L_{21} = 0 \tag{9}$$

$$If\ x_3 - x_2 - N \geq 0 \quad then \quad L_{32} = 1; \quad If\ x_3 - x_2 - N < 0 \quad then \quad L_{32} = 0 \tag{10}$$

$$If\ x_1 - x_3 - P \geq 0 \quad then \quad L_{13} = 1; \quad If\ x_1 - x_3 - P < 0 \quad then \quad L_{13} = 0 \tag{11}$$

$$If\ x_3 - x_1 \geq 0 \quad then \quad L_{31} = 1; \quad If\ x_3 - x_1 < 0 \quad then \quad L_{31} = 0 \tag{12}$$

$$If\ x_3 - x_1 + M \geq 0 \quad then \quad L_{35} = 1; \quad If\ x_3 - x_1 + M < 0 \quad then \quad L_{35} = 0 \tag{13}$$

$$If\ x_1 - x_4 - R \geq 0 \quad then \quad L_{14} = 1; \quad If\ x_1 - x_4 - R < 0 \quad then \quad L_{14} = 0 \tag{14}$$

$$If\ x_4 - x_5 \geq 0 \quad then \quad L_{45} = 1; \quad If\ x_4 - x_5 < 0 \quad then \quad L_{45} = 0 \tag{15}$$

$$If\ x_5 - x_6 - U \geq 0 \quad then \quad L_{56} = 1; \quad If\ x_5 - x_6 - U < 0 \quad then \quad L_{56} = 0 \tag{16}$$

If the condition L_n is equal to 1, then there is contact between the bodies. The numbers in a lower index of conditions n correspond to the bodies that are in contact.

4 Results

The system is kinematically excited at the body 1. As stroke function the modified sine acceleration was selected. The stroke function corresponds to 250 rpm of the sewing machine. The equations of motion were solved using the software Matlab Simulink. To illustrate the results of the solution, the dependence of velocity of the bodies 1 and 2 is shown in Fig. 5. The influence of stiffness of the spring k_2 in response to velocity of the control element in the moment its collides with the machine frame is investigated. The instant value of velocity influences the value of kinetic energy in the moment of collision. The decreasing stiffness k_2 significantly increases maximum value of velocity of the control element. A graph with a corresponding acceleration is shown in Fig. 6.

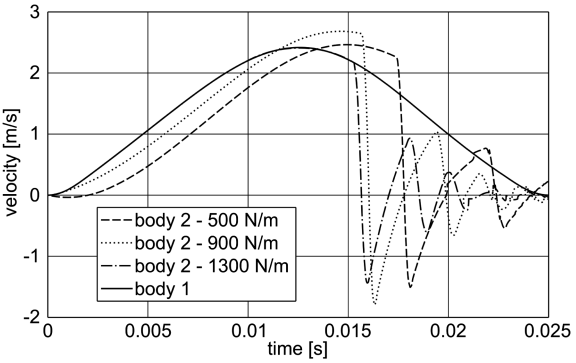

Fig. 5 Velocity of bodies 1 and 2

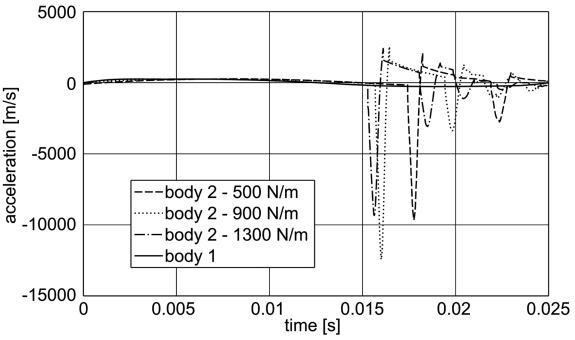

Fig. 6 Acceleration of bodies 1 and 2

5 Conclusions

The dynamic analysis of the mechanical systems of the needle bar can be investigated using the described dynamic model. It can examine the influence of various parameters on the dynamic behaviour of the system. For example, the influence of weight parameters or the influence of stiffness of individual parts. The dynamic model may be useful in selecting an appropriate stroke function. The knowledge obtained from the analysis can be used for design optimisation of the system, for example, the optimisation of the stiffness of the springs.

Acknowledgments This publication was written at the Technical University of Liberec, Faculty of Mechanical Engineering as part of the project "Research of the processes of textile and single-purpose machines" with the support of the Specific University Research Grant and also the Institutional Endowment for the Long Term Conceptual Development of Research Institutes, as provided by the Ministry of Education, Youth and Sports of the Czech Republic in the year 2016.

References

1. Komárek, J., Beran, J., Lima, M., Machado, J., Silva, J.: Finding the optimal setting of the sewing needle transfer mechanism using simulation software. In: Proceedings of TRS 2012, the 41st Textile Research Symposium, pp. 401–404. Guimaraes, Portugal, 12–14 Sept 2012. ISBN 978-972-8063-67-2
2. Komárek, J.: Influence of the rubber pad stiffness on the noise of the needle transfer mechanism. In: Proceedings of IV International Conference Mlodzi Naukowcy, pp. 135–139. Jelenia Góra, 19–20 May 2010. ISBN 978-83-61719-86-1
3. Pejchar, K., Beran, J.: Optimization of the needle bar mechanism. In: Proceedings of X. International Scientific Conference Transfer 2009, pp. 44–49. Trenčín, Slovak Republik, 17–18 Nov 2009. ISBN 978-80-8075-414-3
4. Juliš, K., Brepta, R.: Mechanika. Díl 2., Dynamika. Technický průvodce 66. SNTL, Praha (1987)

Electronic Link Between the Needle Cylinder and the Dial of the Small Diameter Knitting Machine

J. Skřivánek, M. Bílek, O. Baťka and M. Kašpárek

Abstract The article is focused on verification of the applicability of individual drives in the design of small diameter knitting machines. The current arrangement of the drive ensures the mechanical transmission between the needle cylinder and the dial is via a central servomotor; this mechanical link raises limitations in terms of efficient utilisation of these elements of the machine. The new drive system eliminates the mechanical link and allows separate operation of the individual aggregates used in the knitting process. From the technical viewpoint, it is necessary to ensure compliance with the manufacturer's prescribed maximum deviation of rotation between the needle cylinder and dial during the working cycle. For this reason, the article discusses an experiment verifying the capability of the new drive system to achieve the above-stated rotation deviation.

Keywords Drive · Position · Knitting machine · Mechanical link · Knitting process

1 Introduction

Improvement of the mechanical structure of the machines is currently progressing far much more slowly and with much more difficulty than development in the areas of electronics, control and computer technology. This faster development of electronics creates an opportunity for deployment of electrical control drives on knitting

J. Skřivánek (✉) · M. Bílek · O. Baťka · M. Kašpárek
Technical University of Liberec, Liberec, Czech Republic
e-mail: josef.skrivanek@tul.cz

M. Bílek
e-mail: martin.bilek@tul.cz

O. Baťka
e-mail: ondrej.batka@tul.cz

M. Kašpárek
e-mail: michal.kasparek@tul.cz

J. Beran et al. (eds.), *Advances in Mechanism Design II*,
Mechanisms and Machine Science 44, DOI 10.1007/978-3-319-44087-3_44

machines and hence elimination of mechanical transmissions. These transmissions are already at the limit of their possibilities and as compared to the past, they are becoming a limiting factor in the area of increase of dynamics and precision. Every small improvement of their properties is counterweighted by very high development costs and efforts, while in the electro-technical field, development is far much more dynamic. Further, when considering the trends to reduce not only the production, but also operating costs, the expansion of the electronic base of the machine pays off for many design applications since the use of long kinematic chains increases machine input while the power transmission efficiency declines. Further, the huge importance of the use of unit drives consists in the actual simplification of the design due to the reduction of mechanical transmissions [1, 2].

The article builds on the study solved in [3], where the first of the two basic knitting modes was examined, specifically, the return run of the already new knitting system in terms of the drive, resulting in the considerable simplification of the structure of the entire drive system, reduction of electric input and dynamic effects and achievement of higher efficiency in the use of the needle cylinder, dial and circular cutting blades. The cited modification of the system has a constraint consisting in the electronic replacement of the mechanical link since at present the transmission of power is, on standard basis, being realised through a system of gears and shaft, which ensure not only the transmission of the power to the needle cylinder and dial, but also their correct mutual setting, which is fundamental in the second basic knitting mode, specifically during synchronous rotation during the operation known as simultaneous transfer. The value of the maximum position deviation between the needle cylinder and the dial, in the relay of working speeds corresponding to the solved mode, should not reach more than 0.3° for this type of machine.

The arrangement of the drive in Fig. 1 shows the new structure of the small diameter knitting machines. From the viewpoint of the main drive, this drive can be

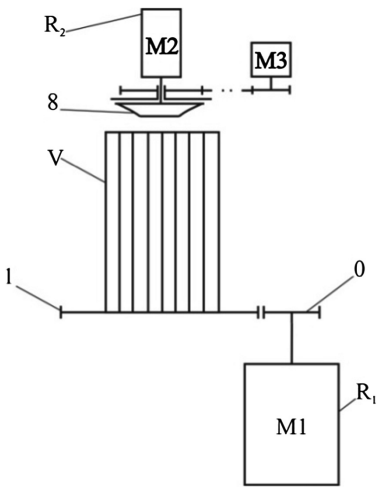

Fig. 1 New drive system for small diameter knitting machines

divided into three basic driving aggregates. In the first aggregate, the needle cylinder (V) is driven by a servomotor (M1) and gears (0, 1). In the second, the servomotor (M2) drives the dial (8) and in the last, a stepped motor (M3) drives the circular cutting blade used to cut the ends of the threads. Since the article discusses only the motor synchronisation mode during the simultaneous transfer, the solved area is only focused on the drives (M1) and (M2) and the aggregates, which they drive. The replacement of the mechanical links with the electronic links was already solved in the past and described in articles [4, 5].

2 Test Equipment for Simulation of the Drive of a Small Diameter Knitting Machine

Figure 2 shows the test equipment, which consists of three main parts. Part one (1) is the power part and contains the drives on which the flywheels are installed (2 and 3). The second part (4) contains the power supply and control of the drives by means of frequency converters. The last part (5) is the controller, where the essential input parameters are entered via PC.

The test equipment in Fig. 2 is used to simulate two motion regimes, in which the knitting process runs. The first regime is the return run of the system based on the assumption of the required motion of the flywheel (2) according to the applied stroke dependence based on the entered position of the needle cylinder. In the second regime, i.e. steady rotational motion (synchronous run of the needle cylinder and dial), which is represented by the flywheel (3), the monitored parameter at the moment of deployment of the dial is compliance with the maximum position deviation at the constant rotation speed of both flywheels.

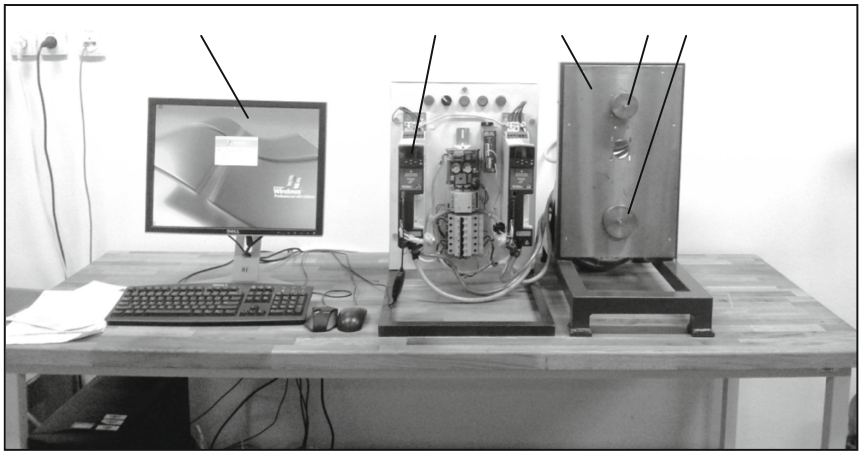

Fig. 2 The apparatus used during the measurement—measurement workstation

The measuring equipment, unlike the real machine, does not have any gears. In order to affect this gear between the needle cylinder and the dial, flywheel (2) representing the needle cylinder rotates at six-fold the angular speed of the flywheel (3) representing the dial. The results obtained from the following measurements shall be related to the needle cylinder as the main working element using the gear between the needle cylinder and dial.

3 Measurement in Synchronous System Regime

Verification of the use of unit drives within the framework of modification of the drive of the small diameter knitting machine was done by measurement of the mutual position deviation between the needle cylinder and the dial at constant rotation speed of both components. During the measurements, various simultaneous transfer speeds typical for these machines were tested, i.e. from 100 to 220 rpm in steps of 20 rpm; for experimental reasons, the speeds of 300 and 400 rpm were tested. In the real case, the standard speeds are in the range of 160–200 rpm, where the specific speed is derived from the mechanical properties of the material used for knitting. The stepped build-up of machine speed was chosen for experimental reasons as an extreme state for the system and subsequent possibility to assess the stabilisation of the position deviations.

A demonstration of the behaviour of the position of the needle cylinder for a simultaneous transfer speed of 180 rpm is given in Fig. 3, which shows the overall measured behaviour and detailed part of the behaviour of the synchronisation of motion between the needle cylinder and the dial. The visualisation already includes the gears between these working elements.

Figure 4 shows the details of the behaviour of the position deviation at standard speed range during simultaneous transfer. It is possible to state that the servomotors are capable of maintaining the mutual position settings in relation to the maximum

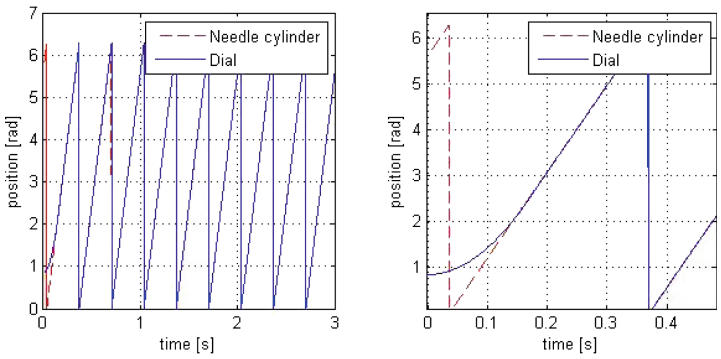

Fig. 3 Behaviour of the position of the needle cylinder and dial at a speed of 180 rpm

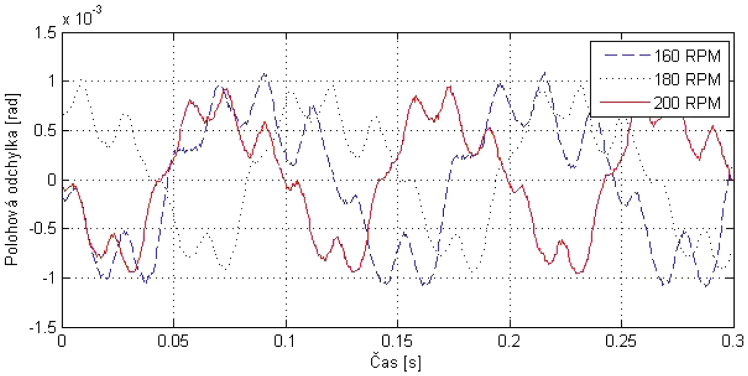

Fig. 4 The behaviour of the position deviation of the needle cylinder and dial for the applied speeds

permissible deviation. In the real knitting machine system, a component of the drive is an in-line gear from the servomotor on the needle cylinder, thanks to which the resultant value is expanded by the value of tooth play in the gear.

4 Conclusions

Within the framework of the verification of the possibilities of application of virtual electronic cams to the new knitting machine structure, the possibility of precision synchronisation of two electronically linked drives with embedded virtual gearbox was experimentally verified. Precision was tested both in terms of the range of the normally used rotation speeds as well as at higher rotation speeds of the needle

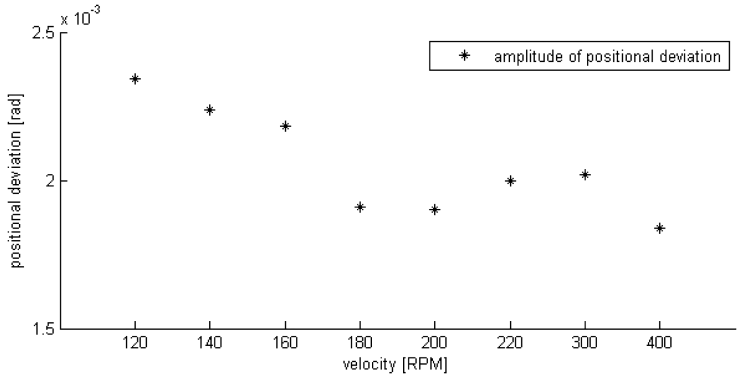

Fig. 5 Dependence of the amplitude of the position deviation on a speed of 120–400 rpm, during simultaneous transfer, after settling of the transition phenomenon

cylinder (up to 400 rpm). With regard to the drives used with a working speed range of 4000 rpm, their suitability for use in low-speed applications with a requirement for high precision and uniformity of speed was proven. With increasing working drive rotations, the synchronisation deviation dropped and at the used speeds and higher speeds, the requirement for the maximum permissible deviation was fulfilled.

The graph in Fig. 5 clearly shows that the position deviation declined with increasing speed up to a speed of 180 rpm. This phenomenon can also be attributed to the more suitable operating conditions of the drives, particularly for the drive of the dial, which rotates at six-fold the speed of the drive of the needle cylinder.

Acknowledgments The paper has been elaborated with the financial support of TUL in the framework of specific university research competition.

References

1. Skřivánek, J., Bílek, M.: New structure of the drive of small-diameter knitting machines. AUTEX Res. J. **12**(1), March 2012 © AUTEX (2012). ISSN 1470-9589
2. Skřivánek, J., Bílek, M.: Analysis of dynamic model of the drive of small diameter knitting machines Ange 18.1. Acc J. XVII 2011, Liberec, 2011 (2011). ISSN 1803-9782
3. Skřivánek, J., Bílek, M., Kašpárek, M.: Control optimization of the new drive of small diameter knitting machines. AUTEX Res. J. **17**(3), September 2016 © AUTEX (2016). ISSN 1470-9589 [ahead of printing]
4. Vaclavik, M., Jirasko, P.: Research and application of displacement laws of electronic cams. In: Proceedings of the 13th IFToMM World Congress, Besancon, France, 18–21 June 2007
5. Tesar, D.: Intelligent mechanical systems, plenary paper. In: Proceedings of the 11th IFToMM World Congress in Mechanism and Machine Science, Tianjin, China, 1–4 Apr 2004

Utilization of Magnetic Accumulators for the Traversing Rod of the Yarn Winding System on Rotor Spinning Machines

J. Valtera

Abstract The paper focuses on utilization of magnetic springs to the central traversing system of the yarn winding system that is used on rotor spinning machines. The aim of this research is to reduce the longitudinal deformation of the traversing rod in the dead centres of its rectilinear motion with variable stroke. For this purpose, a magnetic system with specific repelling force characteristic was designed. At the same time, the mathematical model of the traversing rod equipped with sets of these magnetic systems was created and a dynamic analysis of this system was carried out. The distribution of the magnetic system on the traversing rod was analysed for a range of operating speeds. The most promising variant, from minimal deformation and number of used magnetic sets point of view, was chosen for experimental verification. Both the tests and the dynamic analyses proved the magnetic system to contribute significantly to deformation reduction. In conclusion, the potential of this non-contacting means of dynamic force reduction for modern high-performance rotor spinning machines was discussed.

Keywords Rectilinear motion · Magnetic spring · Magnetic accumulator · Winding

1 Introduction

The central traversing system on rotor spinning machines provides the guidance of yarns, which are wound upon the output cross-wound bobbins [1, 2]. The required rectilinear movement of the traversing rod is delivered from the central drive unit, which is placed at one side of the machine. The traversing rod is formed out of serially-coupled one-section-length rods and reaches a length over 50 m. Despite of using rods made of advanced materials (carbon composite or high-strength

J. Valtera (✉)
Technical University of Liberec, Liberec, Czech Republic
e-mail: jan.valtera@tul.cz

J. Beran et al. (eds.), *Advances in Mechanism Design II*,
Mechanisms and Machine Science 44, DOI 10.1007/978-3-319-44087-3_45

aluminium alloy [3]), the excessive dynamic force limits this system for modern machines with more sections and/or high operational traversing speed [2, 4]. Therefore several systems of dynamic force reduction of traversing rod [5–7] are investigated and analysed. This article describes the utilization of a new magnetic system and its optimal distribution on the rotor spinning machine in order to enhance its dynamic behaviour at high operational speeds.

The traversing reciprocating motion is characterised by linear and transition sections. The latter one is defined by the parameter γ which describes the necessary length of the stroke (or virtual cam angle) for the moving elements to deaccelerate towards the dead-centre position and accelerate from it. Generally, the traversing motion consists of the main stroke of e.g. 148 mm and additional one, called the reversal point shift (*RPS*). It provides slight shift of the end of the traversing stroke from the inner reversal point (rp_{in}) towards the outer reversal point (rp_{out}). This additional motion is commonly described by means of harmonic function with the amplitude of e.g. 4 mm and enables diminution of the negative impact of non-zero transition section on winding quality [8]. Generally, there are two basic types of RPS on rotor spinning machines. The conventional type of RPS is generated by means of e.g. cam mechanism supplemented with additional crank mechanism. The stroke boundaries of this type are shown in Fig. 1a. In Fig. 1b, the variable RPS is generated by means of electronical control of e.g. a belt mechanism or a linear drive.

Previous results of carried-out analyses with sets of magnetic-mechanical accumulators proved that the implementation of this system enables significant reduction of the dynamic force and total deformation [7]. However, it also showed a new negative phenomena of losing the value of RPS with inappropriate distribution

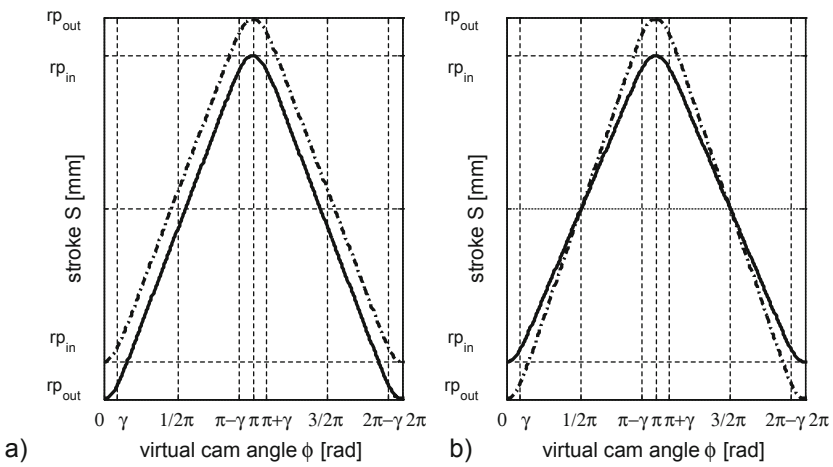

Fig. 1 Modification of the traversing movement due to the reversal point shift (*RPS*) [from the *inner* reversal point (rp_{in}) to the *outer* one (rp_{out})]. **a** Conventional. **b** Variable [7]

of accumulators on the traversing rod. For further implementation of this system it is therefore essential to define appropriate setting of magnetic accumulators for defined range of traversing speed.

2 Magnetic Accumulator

The scheme of the magnetic accumulator [9] in a symmetrical arrangement is shown in Fig. 2. The system consists of the moving parts (rod *2*, magnet *4L*, fixing element *3* and magnet *4R*) that form a magnetic spring with left and right static parts (the static parts consist of the frame *1*, magnets *5L, 5R* and pole pieces *6L, 6R*). All permanent magnets are magnetized axially: parts *4L* and *4R* with the same direction, while the magnets *5L* and *5R* are magnetized with opposite direction to the magnets *4L* and *4R*. Figure 3 shows the end-stroke detail of the repelling magnetic

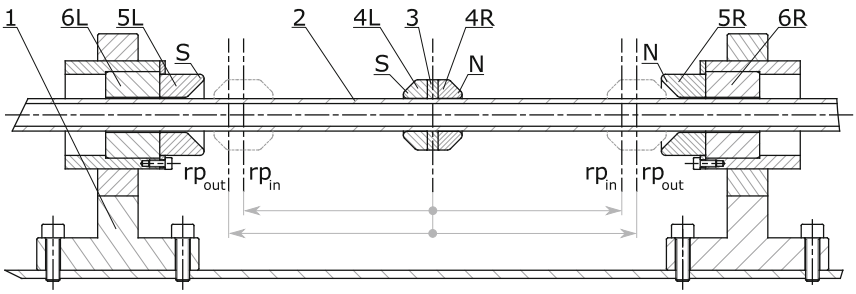

Fig. 2 Scheme of magnetic accumulator for the traversing rod of the rotor spinning machine

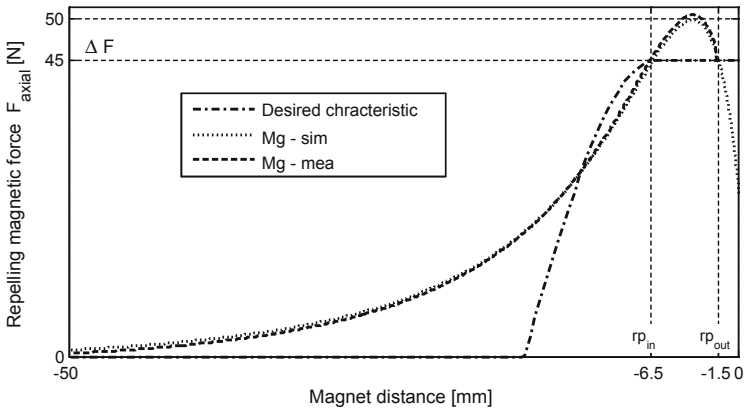

Fig. 3 The force characteristic of the magnetic spring of the magnetic accumulator

force characteristic of the analysed model (MG-sim) and measured prototype (MG-mea). Due to the specific geometry of magnets (obtained by magnetic analysis [9]), the repelling force increases to certain maximum value, from which it decreases slightly. Due to that, the force difference ΔF within the *RPS* is only 10 % of the maximal value and thus it partially respects the desired force characteristic of the mechanical system. The geometry of magnets and their force characteristic was designed with respect to measurement results of the traversing system with 20-section long rod and a cam mechanism (with the $\gamma = 32°$), while the layout of one magnetic system per section was chosen.

3 Dynamic Analysis of the Traversing System

For the mathematical description of the studied system, the discrete model of the traversing rod was used. The model, created in MSC Software, module Adams View is described in [3]. For the purpose of cam mechanism, kinematic excitation describing the required motion by means of the defined acceleration of the first element was used. The force characteristic $F_m(x)$ of the devised geometry of magnets was solved in the model carried out in software Ansys/Maxwell and applied to appropriate rod elements as displacement-depended force. The mathematical description of the model can be expressed by differential Eq. (1), where matrices (with size 320 × 320) represents: *M*—elements mass, *B*—viscous damping, *K*—stiffness, vectors F_v—passive resistance and *x*—element displacement. The presumptions of the model are: the difference in ideal-stiff excitation of the model and cam mechanism can be neglected; dynamic magnetic effects between the static permanent magnets and translating rod sections which are made of conductive material are neglected.

$$\mathbf{M} \cdot \ddot{\mathbf{x}} + \mathbf{B} \cdot \dot{\mathbf{x}} + \mathbf{K} \cdot \mathbf{x} + \mathbf{F_v} + \mathbf{F_m}(\mathbf{x}) = 0 \tag{1}$$

Dynamic analyses were carried out for the range of traversing speeds from 100 to 200 dspm (1.6–3.3 Hz) (dspm—double-stroke per minute).

There were several various layouts of magnetic systems analysed. Out of them the one with 9 systems applied in the middle of the 1st, 2nd, 3rd, 5th, 7th, 9th, 12th, 15th and 18th section was evaluated as the most promising one. The evaluation was based on the minimal reaction force, minimal total deformation and minimal losing of RPS point of view. Results of dynamic analysis of this layout are shown in Fig. 4. Figure 4a illustrates the reaction force *F* along the traversing rod with respect to the traversing speed and RPS. Figure 4b then illustrates the difference in the dead end position *DP* along the traversing rod with respect to traversing speed and RPS.

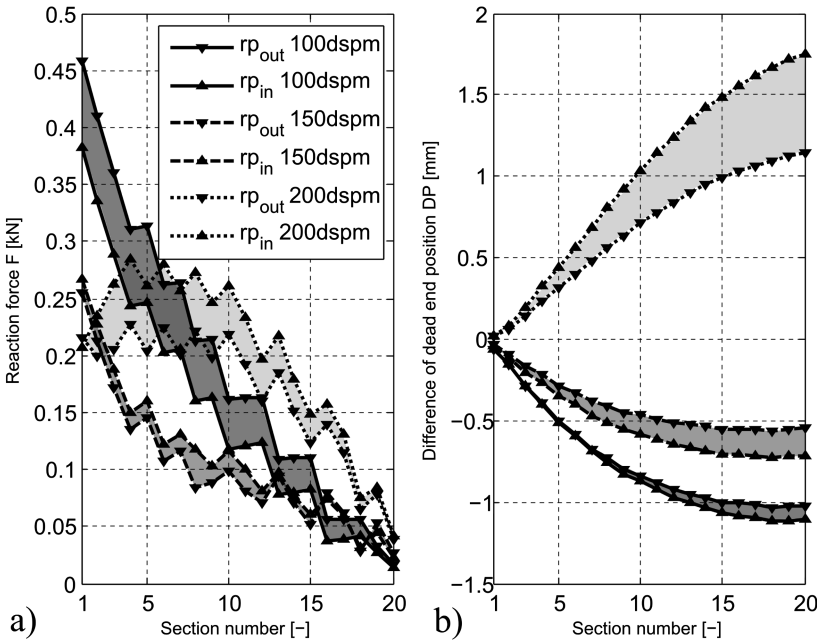

Fig. 4 Dynamic analysis results: parameter dependence on the section number with respect to the traversing speed and RPS. **a** Reaction force. **b** Difference in dead *centre* position

4 Experiments

Measurement of the traversing rod was carried out on the test rig with 20 section-length rod. As the driver a new system with linear drive was used. The measurements was carried out for two variants of traversing rods: 1: traversing rod without any magnetic systems (*v0*), 2: traversing rod with magnetic systems in layout according to the selected variant from dynamic analyses (*v9*). In Fig. 5, comparison of results of these two types for both the simulation and the measurement is shown. Figure 5a illustrates the maximal force $F_{\max}$ with respect to the traversing speed. Figure 5b shows the maximal difference of the dead centre position $DP_{\max}$.

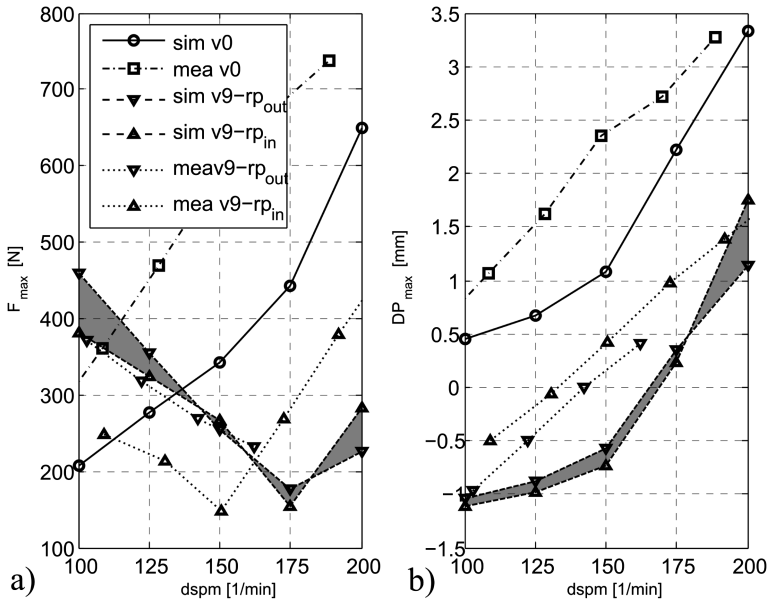

Fig. 5 Comparison of measurement and analysis results: selected parameters dependence on the traversing speed with respect to RPS and traversing system type (*v0*—without any magnetic system, *v9*—with 9 magnetic systems) **a** Maximal force, **b** Maximal difference in dead *center* position

5 Conclusion

The simulation and the measurement results show the relative equal decrease of both evaluated parameters when applying the magnetic systems to the traversing rod in the selected layout. At the speed 200 dspm, the $DP_{\max}$ was reduced from approximately 3.3 mm to values bellow 1.75 mm. The average value of the maximal difference of $DP_{\max}$ due to the RPS change is in both cases bellow 0.55 mm, which is within 7 % of the given overall RPS stroke. Despite of that, the model results does not fully corresponds to the measurements, which may be caused by the different stiffness of the linear drive and ideal kinematic excitation of the model. Improving of the mathematical description of the system will be therefore the subject of the further work.

However, presented paper shows, the magnetic systems applied to the central traversing system of the rotor spinning machine in the appropriate layout improves the dynamic behaviour considerably. Similar approach can be applied to modern high-performance machines with more spinning units and higher operational speeds.

Acknowledgments The research presented in this article was supported by the Ministry of Education, Youth and Sports in the framework of the targeted support of the "National Programme for Sustainability I" LO 1201 and the OPR&DI project "Centre for Nanomaterials, Advanced Technologies and Innovation", CZ.1.05/2.1.00/01.0005.

References

1. Ernst, H.: The Reiter Manual of Spinning—Rotor Spinning, vol. 5. Rieter Machine works Ltd. ISBN 13 978-3-9523173-3-4 (2014)
2. Kaniok, J.: New trends in mechanisms for the distribution of yarn in textile machines. In: Proceedings of 6th International Scientific Conference Transfer (2004)
3. Valtera, J., Beran, J.: Mathematical model of the long traversing rod with a discrete flexible link utilization. In: Proceedings of the International Conference Transfer (2011)
4. Černohorský, J.: Extreme dynamics on eCAM linear drive. In: Proceedings of 14th International Power Electronics and Motion Control Conference EPE-PEMC (2010)
5. Foune, F., et al.: The influence of magnetic accumulators equipped with permanent magnets on the drive of a mechanical system with the periodical reciprocating movement and its behaviour. In: Proceedings of 10th International conference of Vibration problems ICOVP (2011)
6. Valtera, J., Beran, J.: Magnetic-mechanical accumulator of kinetic energy. Autex Res. J. **14**(1), 1–6 (2014). doi:10.2478/v10304-012-0038-0
7. Valtera, J., Žabka, P., Beran, J.: Enhanced central system of the traversing rod for high-performance rotor spinning machines. Autex Res. J. (2015). doi:10.1515/aut-2015-0038, November
8. Beran, J, Valtera, J.: Yarn distribution process during winding thereof onto a bobbin located in a winding mechanism of a textile machine workstation and apparatus for making the same, patent number: 304685 (2014)
9. Valtera, J.: Design of magnetic spring characteristic with finite element method utilization. In: Proceedings of the conference Výpočty konstrukcí metodou konečných prvků MKP (2015)

Mechatronic Model for Traversing Rod Longitudinal Vibration Analysis

P. Žabka

Abstract The paper deals with analysis of vibration of traversing rod on rotor spinning machines. The rod is part of winding system and it should provide a precise motion in order to ensure quality package. However the rod is subject of dynamic load that excites detrimental longitudinal vibrations. In order to better understand the behaviour of the rod a mathematical model in Matlab/Simulink is used to describe the system. The traversing rod was described using finite element method while a dq model was used for the permanent magnet synchronous motor description. To verify the mathematical model the simulation results were compared to experimental data. Results from the simulation proved the model to be well suited for the system description.

Keywords Traversing rod · Longitudinal vibration · Yarn winding · dq model

1 Introduction

The paper deals with analysis of vibration of traversing rod on rotor spinning machines. The rotor spinning is after ring spinning the second most used technology in yarn production [1]. Once the yarn is produced it is stored in packages by winding mechanisms that are incorporated directly into rotor spinning machines. The machines are equipped either with individual winding mechanisms or with central winding system. The winding process consists of two motions: rotation of the package and traversing motion of a yarn guide. When a central system is used the traversing motion is generated by a central mechanism and it is distributed along the machine by the traversing rod.

The traversing rod is assembled from sections of aluminium alloy rods and carbon composite rods. It is placed along the whole length of the machine that can reach almost 50 m. With the diameter of 12 mm the length to diameter ratio of the

P. Žabka (✉)
Technical University of Liberec, Liberec, Czech Republic
e-mail: petr.zabka@tul.cz

J. Beran et al. (eds.), *Advances in Mechanism Design II*,
Mechanisms and Machine Science 44, DOI 10.1007/978-3-319-44087-3_46

rod reaches 4000. During the operation the rod is subject to dynamic load and longitudinal vibrations are excited. These vibrations can have detrimental effect on the quality of output packages and the lifetime of the system [2].

To obtain cross wound package the yarn guide must follow a periodical rectilinear motion, see Fig. 1. Each period consist of section with constant velocity and motion reversion near dead-centres. In order to ensure high quality package, two additional motions are included: anti-patterning and stroke displacement. Anti-patterning ensures that the yarn does not create pattern zones that are hard to unwind while stroke displacement compensates for yarn accumulation near package edges [1]. Both of these additional motions are slow compared to the main traversing motion [3].

Several systems can be used for generating the required traversing motion such as cam mechanism, belt mechanism or mechanism with linear motor [4, 5]. For the analysis of the rod a system with crank mechanism was used. The scheme of the winding system is shown in Fig. 2.

The traversing rod is placed along the packages that are shown on the right side. The main motor marked with M is a permanent magnet synchronous servomotor. It ensures main traversing motion along with anti-patterning motion. Because the crank mechanism has fixed dead-centre positions an additional motor with an eccentric is used for stroke distortion.

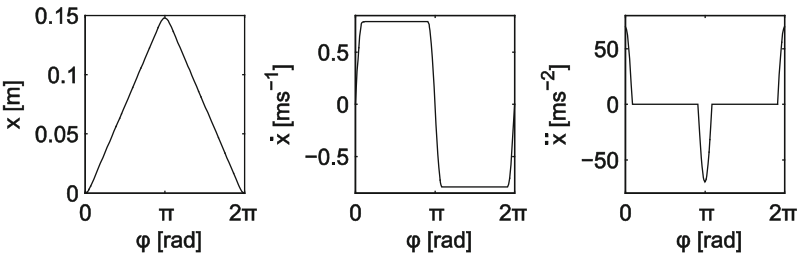

Fig. 1 Stroke, velocity and acceleration diagrams of the required motion (for 150 rpm)

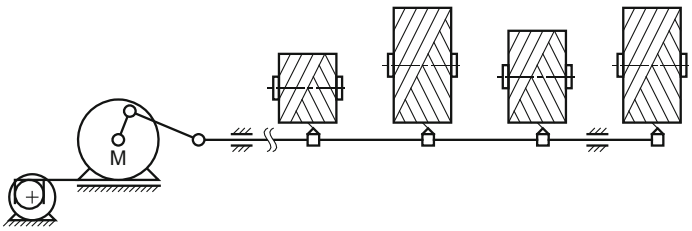

Fig. 2 Scheme of the traversing system with crank mechanism

2 Mathematical Model

In order to better understand the behaviour of the system a mathematical model in Matlab/Simulink was created. Traversing rod is described using finite element method while for description of the servomotor a dq model is used. The overall structure of the model is shown in Fig. 3.

Where MS is a master system, AP is an anti-patterning mechanism, SD is a stroke displacement mechanism, DR is a driver, SM is the servomotor with regulation, CM is the crank mechanism and TR is the traversing rod. The forward arrows represent kinematic actuation while the arrows in backward direction represent force feedback.

The model was created with several assumptions and simplifications such as omitting temperature influence. However the main simplification is that the rod is considered to be 1D body in 1D space. It means that the model does not cover transverse vibration of the rod.

The traversing rod is described by a differential equation:

$$\mathbf{M}\ddot{\mathbf{x}} + \mathbf{B}\dot{\mathbf{x}} + \mathbf{K}\mathbf{x} + \mathbf{f} = \mathbf{0} \tag{1}$$

where **M** is a mass matrix, **B** is a damping matrix, **K** is a stiffness matrix, **f** is a vector of external passive forces and **x** is a vector of node positions.

For description of the permanent magnet synchronous motor a dq model [6] was used. The equations were simplified with assumption that the servo driver ensures zero current in the direct direction $I_d = 0$. With this consideration the motor torque is defined by equation:

$$M = \frac{3}{2} p_p \Phi_B I_q \tag{2}$$

where p_p is number of pole pairs, Φ_B is permanent magnet flux linkage and I_q is current in q direction witch can be obtained from differential equation:

$$U_q = R_S I_q + L_q \frac{\mathrm{d}I_q}{\mathrm{d}t} + p_p \Phi_B \omega \tag{3}$$

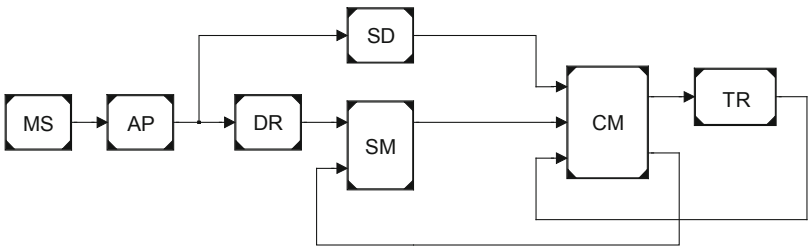

Fig. 3 Scheme of the Simulink dynamic model structure

where R_S is the stator phase resistance and L_q inductance in q direction and ω is rotor angular velocity. Once the motor moment is known the rotor angular acceleration can be computed:

$$\frac{\mathrm{d}\omega}{\mathrm{d}t} = \frac{M - M_Z}{J} \tag{4}$$

where M_Z is load torque on the shaft and J is rotor moment of inertia.

The equations describing crank mechanism express the ratio between input and output position of the mechanism. Moreover the dynamic forces from the movement of the mechanism are included.

3 Experiment

In order to verify the mathematical model the simulations results was compared with an experiment [2]. The measuring set-up is shown in Fig. 4. A rod of 20 sections was used with the overall length of 47 m. The system was measured with speeds in range from 100 to 190 rpm. The stroke was 148 mm and for the sake of simplicity anti-patterning and stroke displacement motions were disabled during the measurement.

The measured parameters were the position and acceleration on selected sections along the rod and the force on the first section between the rod and the crank mechanism. For measuring acceleration inductance sensors were used while the force was measured by means of industrial force transducer. Beside that several parameters such as crank position and motor current were read from servo drive.

Fig. 4 Measuring set-up with long traversing rod

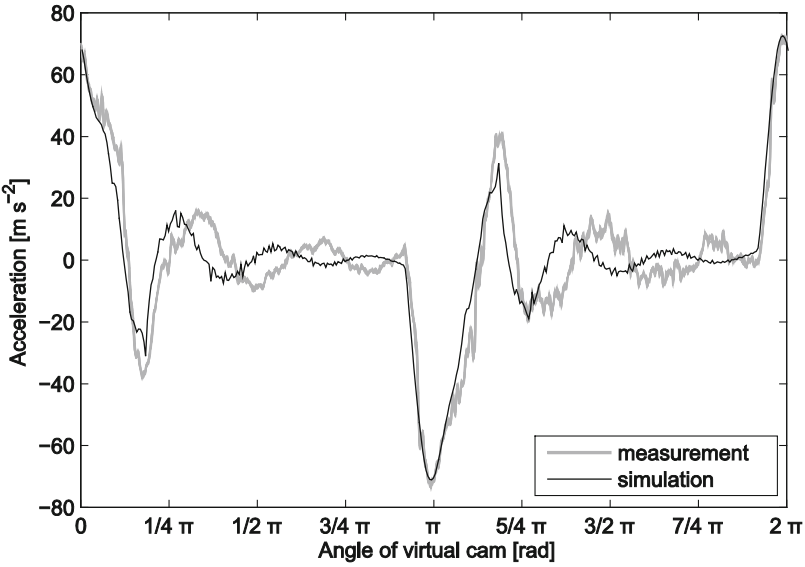

Fig. 5 Acceleration of the first section (for 150 rpm)

4 Results

Number of data was obtained from the measurement as well as from the simulation. To enable comparison of the mathematical model with the measurement, the mathematical model was provided with parameters of the testing set-up. Even the masses of sensors were included. For obtaining all the necessary parameters additional tests were performed.

Results of acceleration on the first section are shown in Fig. 5. One plot depicts the measurement data while the other shows results of the mathematical simulation. The acceleration is selected because the differences between both plots as well as the appearance of residual vibrations are best noticeable.

From Fig. 5 a good match could be seen between the measurement and the simulation. The peak values are matched almost precisely. Some difference is in the frequency of residual oscillation where the mathematical model exhibits higher frequency than the measurement.

5 Conclusion

A mathematical model of a system with the traversing rod was created. The model includes both servomotor and the traversing rod. The complexity of the model is important as both parts influence dynamic behaviour of each other.

In order to verify the model the simulation results were compared with measurement on testing set-up. Results of comparison provided a good match in all measured quantities. It means that the model properties were set correctly and all assumptions were appropriate for the purpose. The simulations proved to provide a reliable description of the real system.

The created model can be used for understanding of the behaviour of current systems as well as for designing new systems. Results of the simulation are fast and inexpensive compared to an experiment. The model can be employed in design modification, dimensions optimization or servo-drive control testing.

Acknowledgments The research presented in this article was supported by the Ministry of Education, Youth and Sports in the framework of the targeted support of the "National Programme for Sustainability I" LO 1201 and the OPR&DI project "Centre for Nanomaterials, Advanced Technologies and Innovation", CZ.1.05/2.1.00/01.0005

References

1. Ernst, H.: The Rieter Manual of Spinning—Rotor Spinning, vol. 5. Rieter Machine Works Ltd., Winterthur (2014). ISBN 13 978-3-9523173-5-8
2. Žabka, P., Valtera, J., Beran, J.: Dynamic properties of traversing rod. In: XI International Conference on Theory of Machines and Mechanisms, TMM2012, p. 469. Springer, Liberec (2012). ISBN 978-94-007-5124-8
3. Valtera, J., Beran, J.: Magnetic-mechanical accumulator of kinetic energy. Autex Res. J. **14**(1), 1–6 (2014). ISSN (Print) 1470-9589. doi:10.2478/v10304-012-0038-0
4. Beran, J., Valtera, J., Žabka, P.: New trends in yarn distribution systems on spinning machines. In: STRUTEX 2008, Liberec, 2008, p. 579 (2008). ISBN 978-80-7372-418-4
5. Černohorský, J.: Extreme dynamics on eCAM linear drive. In: Proceedings of 14th International Power Electronics and Motion Control Conference EPE-PEMC (2010)
6. Rydlo, P.: Řízení elektrických střídavých pohonů. TUL, Liberec (2006). ISBN 80-7372-117-1

Adaptive Timing of Relay Nozzles of an Air Jet Weaving Loom

J. Žák

Abstract In this paper we present our approach to optimize air jet usage by using an adaptive timing of nozzles, with some excursion to the general theory of air jet weft insertion. Our algorithm of adaptive timing of relay nozzle valves relies on this theory of weft introduction. By exploiting only the potential of digital control of the loom and without any single change to its mechanics, we succeeded in saving of about 20 % of compressed air. In addition, other textile technology parameters, such as number of weft breaking, also went increasing.

Keywords Air jet loom · Energy saving

1 Introduction

The first task was to provide both air consumption of individual systems of weft introduction and the impact of these systems on its quality. When determining consumption of main nozzles and relay nozzles we started from previous measurements made in VÚTS earlier. Moreover, it was possible to use certain analogies and similarities for the tandem nozzle (hereinafter identical to main nozzles) and for so-called "auxiliary weak-jet" and for the tensioning nozzle. It was therefore concluded that the air consumption of each individual nozzle in a steady mode depending on the air pressure was known. It was also necessary to determine the sensitivity of weft introduction on the input parameters. For evaluation of quality of the pick weft arrival time was chosen, more precisely the angle of the machine in a circular diagram (terms of "time" and "angle" further used indifferently thus). This value is provided as a statistical average of an arbitrarily large set of data of weft arrival time acquired by the control system of the loom. Variable input parameters were the pressure on the individual nozzles and their opening times. At the very beginning we have rejected the possibility of changing the position of the nozzles

J. Žák (✉)
VÚTS, a.s. Liberec, Liberec, Czech Republic
e-mail: josef.zak@vuts.cz

J. Beran et al. (eds.), *Advances in Mechanism Design II*,
Mechanisms and Machine Science 44, DOI 10.1007/978-3-319-44087-3_47

and their possible shape optimization. This has been done many times before, both in VÚTS, as well as by other manufacturers or research institutes, and it was clear that textile-technological constraints would not allow any major breakthrough in this domain.

2 Analysis of the Problem

At this stage, experiments were performed to determine the sensitivity of the quality of the pick on the fore mentioned parameters. The measurements became the basis for a deeper analysis of the influence of variable parameters on the movement of the weft in the shed, the results, however, fall out of the scope of this work.

Due to the number of relay nozzles (up to 36, divided into 5–7 independently timed sections) the overall sensitivity (Jacobian) matrix of the pick was not evaluated analytically. This analysis was done in a very simplified manner by gradually shutting down of individual sections.

The performed sensitivity analysis has given the following conclusions:

- Main nozzle pressure sensitivity is high. However, this fact is known and is used to control the time of weft arrival to satisfy the textile-technological requirements by setting this pressure.
- Sensitivity to the opening time of main nozzle is surprisingly low.
- The pressure at the inlet to the relay nozzles (the same for all sections) and the time of their opening have minimal influence on the angle of arrival.

In carrying out the experiments, however, it became clear that chosen pick quality criterion, this is angle of arrival, is not sufficient. Especially when sensitivity measurements of parameters of relay nozzles being carried out the repetitive "short pick", i.e. incomplete introduction of the weft into the shed, happened frequently, although the statistical average angle of arrival $\bar{t}$ remained at the required value, it was not influenced by changes of parameters of relay nozzles. It was therefore necessary to establish additional criteria of pick quality. For this criterion the standard deviation was selected:

$$\sigma = \sqrt{\sum_i (t_i - \bar{t})^2}$$

Given the global air consumption analysis, sensitivity analysis, and also with regard to the technical limitations we made the following conclusions, which were the basis for the next steps:

- Pressure on main nozzle will remain independent parameter, as a mean of automatic regulation the angle of weft arrival; although its impact on consumption is not negligible, it is the only parameter by means of which weavers can control the textile-technological requirements of the pick.

– Pressure on the relay nozzles has a big impact on overall air consumption, costs associated with the installation of an electronically controlled throttle valve on new machines, however, are high and this is a hardly realizable modification on existing machines. In the future, there is likely to use it, for now this option was postponed.
– Air consumption of all nozzles is directly proportional to the time of opening of the relevant nozzle valves. Their timing is controlled by a digital control system and it is therefore relatively easy to vary this timing to reduce air in comparison with a fixed setting. This fixed valve timing has to cover all the possible timings of the weft being driven into the shed. The quality of the weft, however, changes with time, e.g., depending on the unwound length of the yarn or on the wear of the reed and on changes of its aerodynamic characteristics, or is subject to mechanical errors of other picking devices, such as feeder or weft brake (ABS).

Our goal, thus, will be to adjust adaptively the timing of the relay nozzles so that at any moment of the pick only the necessary number of valves be open, and this depending on the actual operating conditions.

3 Mathematical Model of the Weft Introduction

To be able to optimize nozzle timing for each picking jet, we need to know at any moment the position of the weft in the channel. For a description of the movement of the weft pick at the air we came out of the work [1, 2]. Basically, to solve the motion equation for the position of weft head L versus time:

$$\int_L c_D \cdot \rho(\xi,t) \cdot \left(c(\xi,t) - \dot{L}\right)^{\alpha} \cdot d\xi = (\lambda + f_O) \cdot \left(\left(\dot{L}\right)^2 + L \cdot \ddot{L}\right) \tag{1}$$

Given that α, λ and c_D in this equation are the material constants of the weft at a given time, describing its inertial properties and interaction with the air jet; in general it would be necessary to determine them for each type of weft. Furthermore, the density ρ (ξ, t) and speed c (ξ, t) are difficult to determine, either in position and either in time varying parameters of the airflow. Parameter f_O describes simply the empirically determined drag of the feeder and ABS. Analytical solution of this integral-differential equation is therefore virtually impossible.

Actual procedure of solving this equation of motion, used in the machine control system, was presented at 30th conference Computational Mechanics 2014 in Železná Ruda, see [3], here let us mention only the resulting relationship, used in the next presentation:

$$L(t) = v_\infty \cdot \left(t - 2 \cdot B + e^{-\frac{t}{B}} \cdot (t + 2 \cdot B)\right) \tag{2}$$

Meaning of the parameters of this function is obvious: v_∞ is the finite speed of weft and B is a certain time constant.

4 Adaptivity of Relay Nozzles Timing

As previously stated, our goal was to enable the control system continuously respond to changes in the quality of the pick. The first step was to integrate an algorithm evaluating the quality of the pick into the existing control system. As mentioned above, for the quality measure standard deviation of angle was chosen. As our goal was to respond to constantly change in the pick quality, the values of $\bar{t}$ and σ are calculated as the floating value of the last n values.

It should be noted that the time of arrival of the weft does not meet exactly normal probability distribution. However, since the values of n are chosen sufficiently high, normally n ≅ 50, the normal probability distribution can be used.

To find the actual optimum settings we accepted the following considerations:

- The main propulsive force in introducing the weft is the drag of the main nozzle. Relay nozzles create a sort of "dragless" environment in picking channel. But then, it is just sufficient to open only those relay nozzles over which the head of the weft is moving. However, the problematics is somewhat more complicated, more profound analysis lies out of scope of this abstract.
- Theoretical position of the current weft pick is known at any time due to the approximation of the measured values of coil times by using the function (2), see also [3].
- Times of arrival of individual picks differ and analogically differ the times of passage of weft over individual relay nozzles. The time probability distribution of passage over a given point will also follow a normal probability distribution. Standard deviation from nominal mean value increases linearly from 0 for the L = 0 up to σ for L = width of picking.

To derive the algorithm of relay nozzle timing it was still necessary to solve the problem of fast calculation of v_∞ and B. As mentioned above, it is possible to use some of regression techniques, but this practice is not suitable due to nonlinearity of function (2). During the theoretical calculations, however, it was found that it should be possible to find values sufficiently accurately approximating as follows:

$$v_\infty = \frac{L_{N-1} - L_2}{T_{N-1} - T_2} \tag{3}$$

$$B = \frac{1}{2} \cdot \left(T_{N-1} - \frac{L_{N-1}}{v_\infty}\right) \tag{4}$$

In these relationships N is the total number of coils, L_2 and L_{N-1} are the positions of the weft head after unwinding 2 and N − 1 coils (known total length of the windings up to 2 and to N − 1) and T_2 and T_{N-1} are the times of passage over these positions (values read by the sensor on the feeder) respectively. This approximation is based on the fact that conventional wefts, at least wefts woven on air looms, achieve the speed v_∞ very quickly, practically during the first coil unwinding. For extremely heavy, slowly accelerating wefts or for small width, for which N could be less than 4, it would be necessary to modify this approximation.

The implementation itself into the control system utilizes certain geometrical properties of the construction of the loom; these values are available in the control system. Relations (3) and (4) then take the form:

$$v_\infty = \frac{N + q_{12} - 1}{N \cdot (\alpha_D - \alpha_0)} \cdot L$$

$$B = \frac{q_{12} - 1}{N \cdot v_\infty} \cdot L$$

Here L is the woven width, q_{12} is the ratio between the duration of the first and second coil. α_0 and α_D are times (angles) of the beginning and the end of the pick (time of arrival of the weft). Theoretical transit time through the position L_i for i ≥ 2, this is for second and subsequent coils, then is:

$$T_i = \alpha_0 + \frac{L_i}{v_\infty} + B$$

Given the assumption of a normal distribution probability of passage of the weft head over a given point, this is the mean value of the time passage. If we want to "cover" the entire confidence interval of passage of the weft head p ≥ P, P = 1 − 1/n, where n is the number of reliably introduced wefts, it is necessary to extend the interval of opening of the respective valve by k-times σ according to the empirical rule of k − σ. If we choose e.g. k = 4, then will be n = 15,787. The value of σ increases linearly with the value L_i. As the requirements for operational reliability of the weft introduction are in the magnitude of about 1 short pick to 10,000 picks, the choice is obvious. Then time (more precisely angle) interval of the opening of the nozzle is:

$$\left\langle T_i - k \cdot \sigma \cdot \frac{L_i}{L}, T_i + k \cdot \sigma \cdot \frac{L_i}{L} \right\rangle$$

Note: Implementation of the algorithm into the control system of VERA and CAMEL looms was somewhat more complicated, since it was necessary to take into account the grouping of relay nozzles into sections with different numbers of nozzles per valve. In addition, because of the conservatism of some users it always allows manual entry of additional opening times, both before and after automatically calculated minimum interval. The following Fig. 1 shows an example of timing of a pick.

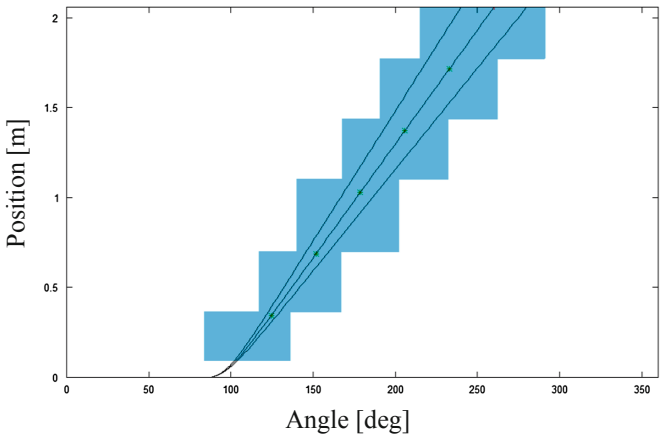

Fig. 1 Example of relay nozzles timing

5 Results and Conclusions

A theoretical estimation of air saving, particularly for the case of relay nozzles grouped into sections, is difficult to quantify, however, without knowledge of the exact scatter of weft properties and thus without knowledge of changes of σ during weaving. Bigger the scatter of weft properties is and thus σ is high, bigger the air saving can be.

This algorithm has been implemented into the existing control system of 10 weaving machines CAMEL, installed by a customer. After performing operational tests of 5 weeks of continuous duty it was achieved a saving of around 20 % of the compressed air while maintaining or improving other quality indicators.

Acknowledgments The research work reported here was made possible by the program LO 1213-Excelentní strojírenský výzkum (2013-2018 MSMT), LO-NPÚ 1.

References

1. Pilipenko, V.A.: Pněvmatičeskije mechanismy prokladyvanija niti. Legkaja industrija, Moskva (1973)
2. Škop, P.: Kontrolní, informační a řídící systémy prohozních ústrojí vzduchových tryskových tkacích strojů, Kandidátská dizertační práce. Vysoká škola strojní a textilní, Liberec (1985)
3. Žák, J., Kolář, J.: Simulation of an air jet weft pick. In: Book of Extended Abstracts of Computational Mechanics 2014, pp. 157–158. University of West Bohemia, Plzeň (2014)

Part VI
Mechatronics, Control and Monitoring Systems of Machines

The Testing Stand of the Direct Linear and the Torque Servo Drives Siemens Controlled by the Simotion C

J. Antoš

Abstract Conception of ball screw, gearbox, pinion and rack are commonly used for linear and rotary axes of machine tools. Issues of these applications are backlash, increased moments of inertia and friction. These disadvantages can be eliminated by using of direct drive motors. In this case, it has to be taken into account that the entire mechanical stiffness of the axis is formed only by closed loop control. Before using of this technology, required properties and behavior of motors has to be practically tested in specific situations on real device. The first goal of this project was design and implementation of unique stand for testing of direct linear and direct torque drive motors in order to use in special-purpose machine tools. The second goal was design and implementation of complete control system for testing of dynamics and position accuracy. Both of the test stand and the control system based on Siemens Simotion C controller were successfully constructed and implemented in accordance with the design. Created solution allows measuring of position accuracy, speed and torque for standardized displacements law and it can be done in manual or automatic mode. It also allows developing and evaluating the quality of the control system. Attention was paid to the new method of transmission data of displacement law from the USB flash memory to the controller based on the Client-Server communication. Result of this project is decision about recommendation of this concept for practical application for special-purpose machine tools.

Keywords Direct linear drive · Direct torque drive · Simotion · Displacement law

1 Introduction

Demands for linear movement with high dynamic performance and for accuracy and elimination of backlash and increased moments of inertia caused by conventional mechanical conceptions can be solved by usage of linear motor. Linear

J. Antoš (✉)
VÚTS, Liberec, Czech Republic
e-mail: jaroslav.antos@vuts.cz

J. Beran et al. (eds.), *Advances in Mechanism Design II*,
Mechanisms and Machine Science 44, DOI 10.1007/978-3-319-44087-3_48

motors simplify mechanical design, increase affordability and durability and improve handling of the machine by elimination of mechanical transmission elements. Direct torque motor which transfers force not trough gearbox but directly on the workpiece was already successfully used by VÚTS Company for BRV300 radial cam grinder [1]. First issue is if replacement of Mechanical transmission elements by direct servo drives is effective option for particular application of single purpose machine-tools. Second issue is if control system and created application meet demands for dynamics testing of both servo drives. The benefit of this concept is to study and identifying the behavior of electric motors on the real equipment for research in cooperation with the Technical university of Liberec. Tests is already underway feedforward regulation on this machine. Especially, the benefit of using the knowledge from this concept in a dedicated new CNC machine tool with direct drives follow-up to this project. Direct drive components have been designed, engineered and manufactured to order in our research institute. For example a sliding surface of the linear model holding the probe following the cam. This metallic cam has also been produced in VÚTS.

2 Mechanical Part

The flywheel has a function of load as well as reduction for cam clamping on Siemens 1FW3150 [2]. Stroke length of the linear motor is 450 mm and is determined by six permanent magnets Siemens 1FN3050. Feedback from absolute encoder by using Heidenhain LC483 is indispensable for closing of control loop [3] (Fig. 1). Measuring probe MSL50.152KA is used for accurate measuring of the length coordinate in short measuring range. Measuring step is 5.0 µm. Siemens Simotion C control system was selected because of this system satisfies demands for controlling of multiaxis systems with possibility of design and modification of displacement laws within program execution. Speed and current loop control are closed here [4]. Specific requirement is controlling of the motors by pendant control station with hand wheel. General safety supplemented by special circuit for safe

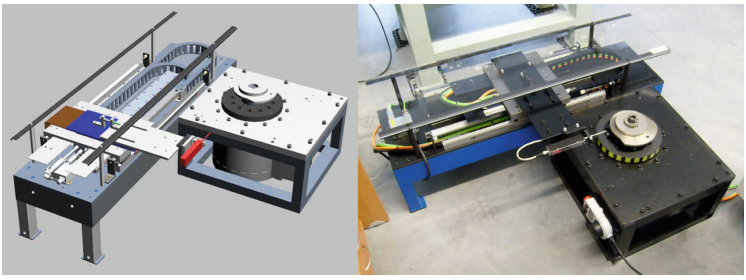

Fig. 1 3D model of the testing stand of the direct servo drives Siemens and real stand

servo drives switching off by safety integrated. Double motor module uses enable pulse which determines if sequence of functions like timer and OFF3 will be started. Function OFF3 ensures safe stop of servo motor via ramp function.

3 Software Part

Software architecture is decomposed into manual mode, the operator of cam panel and automatic mod. Monitoring of position, speed, positioning, jog, homming, enable axes, synchronization the virtual and the real axis alllows manual mode. Upload displacement law with USB portable memory, display it for inspection and then exported to the memory controller allows cam panel. All synchronization of the three axes are using the gear and cam handles automatic mode. The whole system is controlled by a single virtual axis. Virtual gear rotational axis is attached virtual axis. Displacement law between the rotational axis and a linear is use. First, parameters and hardware configuration were set during program initialization. Then, the stops were solved. Real system contains mechanical stops which are supplemented by virtual ones 10 mm earlier and programmed ones 20 mm before real stop. That means triple protection against collision between linear and torque motor. In the case of program error and moving into virtual stop, motor goes immediately into disable state. Remedy is deleting of position error, putting motor in enable state and leaving the restricted area with negated speed. This information is displayed by LEDs on electrical switchboard and on HMI panel throughout remedy. Errors can be acknowledged on HMI panel. Conventional total stop on electrical switchboard and on pendant control station is supplemented by software stop. The safety integrated function is activated during emergency stop of the motor and it executes delayed switching off. This makes possible to stop motor with defined deceleration.

Visualization and controlling by using Weintek 8070iH HMI and Simotion PLC are based on Client-Server communication. Although these two systems do not support each other, because the motion control system Simotion uses the indirect (symbolic) addressing, bidirectional communication can be established by means of this application. Application of “Client-Server” based on functions in a development environment EasyBuilder and Siemens Scout is described in report Client-Server application for the operator panel Weintek and the control system Siemens Simotion [5].

Source data of displacement law are saved in controller memory. That is standard practice. Large attention is paid to the new method for displacement law data transfer via USB to the Simotion controller memory. This transfer is based on mentioned unique Client-Server communication and on Weintek HMI panel usage. This new technique allows user friendly data transfers from any USB flash memory directly into Simotion memory. Simotion unlike Weintek uses indirect addressing and so this option is not standardly possible. Typical situation for dynamic tests is displacement law modification on system input. Within few seconds, displacement

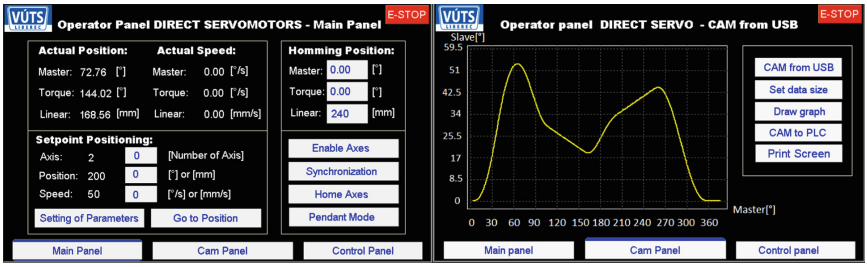

Fig. 2 Operator panel direct servomotors—main panel and cam panel

law can be uploaded, displayed for checking and exported into the controller during RUN mode and without any change of programme in the PLC. That is possible thanks to the Client-Server method [5].

Application for the testing stand of the direct linear and the torque servo drives Siemens is divided into the three basic windows: Main panel, Cam panel (Fig. 2) and Control panel. The first window (Main Panel) is responsible for: axes positioning, actual position and speed showing, axes homming, axes enabling, synchronization between three axes and activate of pendant mode. Particular axes, theirs multiple of position, jog and hand wheel are possible to be selected on pendant control station. Because of security, operator has to use both hands and be pushing enable pulse button with defined pressure.

The second window (Cam Panel) is designed to select one of the predefined displacement laws for the electronic cam. Electronic cam is alternate option to the conventional mechanical cams. Quick change of displacement law is one of the biggest advantages of the electronic cam. Solving of cam movement dynamics is on the contrary disadvantage. Periodic type of cam from VDI 2143 standard was used for electronic cams dynamics testing [6]. This cam has high dynamics and interval with constant nonzero speed. Relation between positions of master and slave axes (displacement law) is saved in *.xls format and sampling step of master axis is 0.5°. Therefore, one displacement law in 0–360° range with two axes with mentioned sampling period needs 1440 elements. Data file on USB flash memory has to be in *.emi format and its name has to be in range EM0-EM9. Conversion from *.csv format to *.emi format is done by Recipe Editor [7]. Particular elements of the data field are in float type and the file is saved into root of USB flash memory. After this, the data are ready to be connected into HMI panel. After connection of the flash drive to the panel, this memory is as accessible as inner memory with EM0-EM9 attributes. File saving is done by data transfer function with definition of source (EM0.emi), destination for saving into HMI panel memory registers (LW514), uploaded data size (1440) and mode (touch trigger). Afterwards, the USB flash memory can be removed without losing of data. Rendering of the electronic cam displacement law on the HMI screen is done by plot function with definition of rendered data size. Four bytes are necessary for every position value. Information about displacement law is carried by slave axis so 2880 elements are necessary.

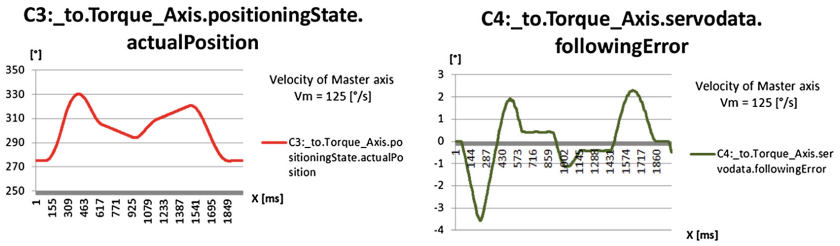

Fig. 3 Position and following error of torque motor

Size of the field is always used as a multiple of 512. Here is divided into 6 parts with size of 512 due the limitation of maximal field size during Client-Server communication. Displacement law which is saved in the inner HMI panel registers is saved into field of 3072 size. Afterwards, two times nested for loop is used for sending the packets of 512 Byte size. Communication channel on the 9001 port is reserved for this.

The third window (Control panel) allows showing of actual position and speed of all axes, showing and acknowledging of errors of the axes selected electronic cam type. This window defines the master axis speed set point and active automatic mode and finally switching the main contactor in front of the frequency converter.

This mode is block of instructions that are executed automatically. Initial assumptions are successful enable of the motor with zero errors and activated active line module contactor. Two automatic modes were used in this project. First one tests dynamic parameters of both motors. These parameters are position, speed, torque and position error of standardized VDI 2143 displacement law with 1800 values per one revolution. These points are linearly interpolated. Testing system has virtual master axis. This axis is rotating at a constant speed 125°/s and is synchronized with real torque axis by displacement law. Resulting graph on the Fig. 3 presents displacement law of linear and torque motor.

Second automatic mode simulates machining for measuring the zero position error of the measuring probe. Synchronization of particular axes (real and virtual) is done by displacement law. Whole process is separated into approach, machining simulation and departure. Approach and departure is done by moving at 120°/s into the safe distance. Then the speed is decreased at 3°/s due to the safe movement on required position.

Synchronization of all three axes is realized during this process. Double synchronization is made for machining simulation. Entire system is controlled by master axis speed which revolves real torque axis via gearbox with 1:1 ration. Electronic cam defined by 1800 values is between torque and linear motor. Real steel asymmetric cam was manufactured thanks to known x and y coordinates and it was placed directly on the torque motor. Linear motor was mounted with measuring probe. Torque motor rotates at constant speed 3°/s and linear motor copies contour of the cam.

4 Conclusions

The first goal of the project, assembling of the stand, was successively and completely accomplished. The biggest attention was paid to the perpendicularity of linear rails and to the accuracy of air gap between primary and secondary section in whole range. Concept of contact between measuring probe and cam is area where further development is required. Radial stress acting on measuring probe is bigger than 0.2 N. That can bring difficulties during higher speeds. Solution of this issue can be application of measuring probe with roller, contactless measuring, etc. Nevertheless, the used concept of measuring probe with sphere was fully sufficient for required speeds.

The second goal of the project, design and implementation of complete control system for testing of dynamics and position accuracy, was successfully accomplished. The biggest attention was paid to the safety and to the transmission of displacement law. This new transmission method facilitates and speeds up manufacturing process. Its next application can be transfer via company network from office computer to the production hall using the same principle.

Fulfillment of these goals had allowed testing of dynamic properties of motors in real situations. It also proved that replacement of conventional conception by direct motors is proper solution and that control system fulfills all demands and therefor can be recommended.

References

1. Jirásko, P.: Metodika aplikací elektronických vaček v pohonech pracovních členů mechanismů výrobních strojů. Liberec (2010). Available from:http://www.fm.tul.cz/files/autoreferat_jirasko.pdf
2. Souček, P.: Servomechanismy ve výrobních strojích. Vydavatelství ČVUT, Praha (2004). ISBN:80-01-02902-6
3. Heidenhain: linear encoders for numerically controlled machine tools. Measuring principles [online]. 2016 [cit. 2016-04-18]. Available from: http://www.heidenhain.de/fileadmin/pdb/media/img/571470-28_Linear_Encoders_For_Numerically_Controlled_Machine_Tools.pdf
4. Lindr, D.: Řízení servopohonů v dynamicky náročných aplikacích. Liberec (2011)
5. Antos, J., Busek, M.: Client-server application for the operator panel weintek and the control system Siemens Simotion. Mechatronika. VÚTS a.s. Liberec [online]. (2014) [cit. 2016-04-18]. ISBN 978-1-4799-3527-7. Available from: http://ecopyright.ieee.org/xplore/down.html
6. VDI 2143, Bl. 1: Blatt 2 Motion rules for cam mechanisms; practical application. VDI-Fachbereich Getriebe und Maschinenelemente (2002)
7. Weintek: Professional in human maschine interface [online] (2012) [cit. 2016-04-18]. Available from:http://www.weintek.com/global/download/Download.aspx?wFun=byM&c=Manuals&S=HMI_0002

New Method of Contactless Measurement and Analysis of CNC Machine Spindle Lopping

Z. Braier, P. Šidlof, V. Čejka and P. Žďárek

Abstract This article is focused and describes a system of a contactless measurement and analysis of a spindle lopping of CNC machines with horizontal axis orientation. The spindle lopping is caused by changes of spindle and headstock deformation during the spindle longitudinal travel and it has a considerable importance for precise CNC machine. The measurement system results from the research and development of a contactless measurement method using a laser source. The laser source is mounted in the CNC machine spindle and rotates together with the spindle. The laser beam goes to the sensor box placed at a specific distance from the spindle. Inside the sensor box, the beam is split into two paths and their traces are recorded by two cameras situated in a position that the beam path total length is different for each camera. The spindle lopping is calculated and analyzed from the camera records using appropriate software equipment. The form and application of the new measurement method is protected by patent CZ305542 (B6).

Keywords Measurement · Contactless method · CNC machine · Spindle lopping · Laser beam

1 Introduction

During extension of a horizontal spindle out of a headstock, the spindle sinks due to the effect of gravity force—i.e. the bending of the spindle and change of deformation of its mounting occurs. These inaccuracies are significant especially in the

Z. Braier (✉) · P. Šidlof · V. Čejka · P. Žďárek
VÚTS, a.s., Measurement, Liberec, Czech Republic
e-mail: zdenek.braier@vuts.cz

P. Šidlof
e-mail: pavel.sidlof@vuts.cz

V. Čejka
e-mail: v.cejka@seznam.cz

P. Žďárek
e-mail: pavel.zdarek@vuts.cz

J. Beran et al. (eds.), *Advances in Mechanism Design II*,
Mechanisms and Machine Science 44, DOI 10.1007/978-3-319-44087-3_49

case of precise production. At present, the process of lopping is usually measured with respect to a clamping table of a particular machine [1]. However, during that process errors occur, caused by the inaccurate position of the original axis of the spindle with respect to the clamping table, as well as by inaccuracies of the clamping table or its shifting. Another disadvantage is also the fact that the process of lopping of a spindle cannot be measured until the headstock is installed on a particular machine tool and until it is adjusted.

According to new principle, a laser beam source is mounted to the spindle of the CNC machine and laser beam traces are scanned by sensors in the specific position from the spindle end for several spindle extensions. Spindle lopping and angle are evaluated from the differences of point of laser beam incidence. In order to increase accuracy the spindle is rotated during measurement and the center of path transcribed by laser beam is evaluate.

The principle practical realization demands solution a few problems, some of them are: (a) The laser source must be battery powered due to the spindle rotation and the laser beam diameter should be minimized in wide range of distances. It is difficult to realize such requirement, therefore the laser beam is focused in a specific distance and the beam diameter increases out of this point. Therefore the laser beam image is relatively large. (b) Interference stripes are detected due to various factors. (c) The laser beam source outputs polarized light and additional partial polarization happens after reflection at mirrors and semi permeable mirrors in the sensor box. The laser beam intensity is varied during the spindle rotation.

These problems are solving in hardware or software. For example, the laser beam records are filtrate using two dimensional FFT for elimination of the interference stripes and the software evaluation is using many image processing principles. The measurement and evaluation principle is still being improved.

2 Measurement and Evaluation Method

The measurement and evaluation of the spindle lopping is calculated for various spindle extensions and for various weights simulating the spindle mass load at the end. At first the reference measurement is made without weights and fully retracted spindle state. Then, the measurement is repeated for partial or full spindle extension. The same scheme is used for the weight influence measurement. Figure 1 shows fully extended spindle with weights 50 kg, info and details of CNC machine and measurement are described in [2]. Each evaluation of the spindle lopping is compared with the reference measurement without weights.

Schematic illustration of the spindle inclination and lopping measurement principle including dimensions for calculation is shown in Fig. 2. The laser beam, which is skew to the spindle rotation axis in general, transcribes a rotational hyperboloid during the spindle rotation. The cuts of hyperboloid by recording planes have elliptical shape (in Fig. 2 shown in rotated state). The centers of ellipses are evaluated from paths of laser beam at the sensor and changes of their position after

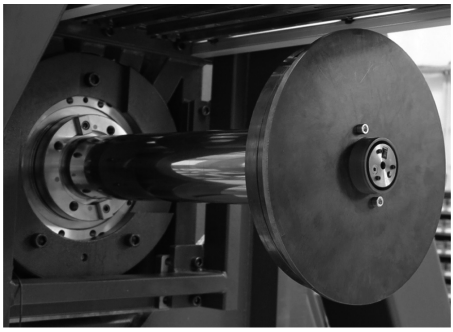

Fig. 1 Photo of extended spindle of CNC machine with weights and laser beam battery source

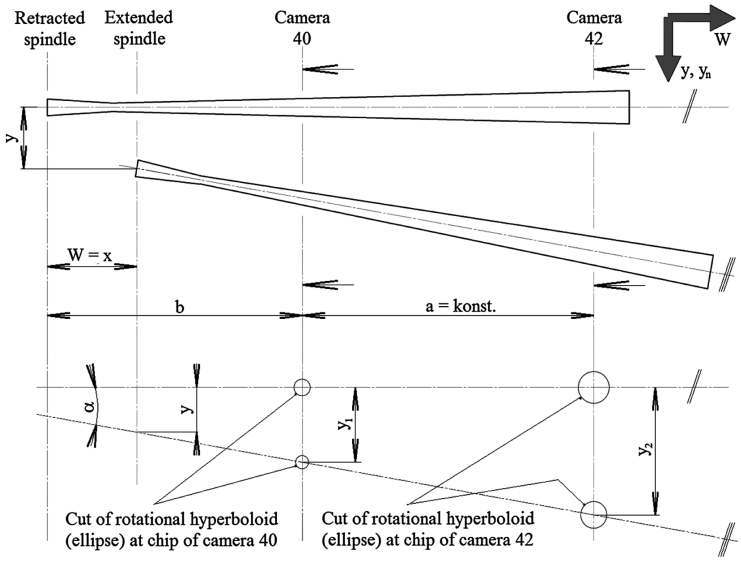

Fig. 2 Schema of measurement principle with scanning of laser beam paths by two cameras (indexes 40, 42)

extension are marked y_1 and y_2. The centers of ellipses are not identical with the intersection of the spindle axis in the recording plane, but errors are maximally in hundredths of µm under given conditions. Therefore the results of the spindle inclination α and spindle lopping y are calculated according to the Eqs. (1) and (2).

$$\tan \alpha = \frac{y_2 - y_1}{a} \tag{1}$$

$$y = y_1 - (b - x) \tan \alpha = y_1 - (b - x) \left(\frac{y_2 - y_1}{a}\right) \tag{2}$$

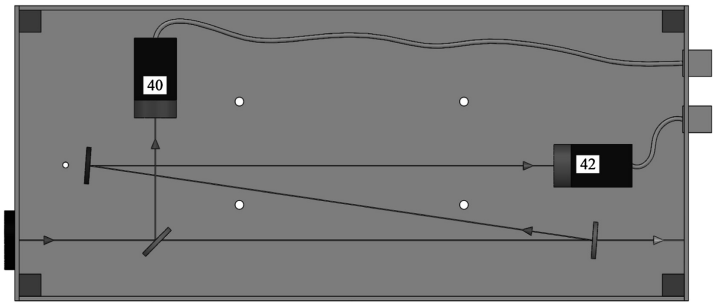

Fig. 3 Schematic figure of sensor box with two cameras (indexes 40, 42) and laser beam trace

The laser beam paths are a little complicated in the real sensor box, which is schematically shown in Fig. 3. Input laser beam is split into two paths in first semipermeable mirror. The first camera (index 40) is situated in nearer optical distance from spindle. Distance of laser beam trace to the second camera (index 42) is extended by using another two mirrors.

Images from both cameras are pre-processed (two dimensional FFT filter, finding the optimal brightness value, image defects elimination, etc.), then the laser beam traces centroid is evaluated by software with focus on threshold parameters and changes of image intensity. Two dimensional matrix of the centroids coordinates is approximated by a general ellipse using SVD method (Singular Value Decomposition) for linear regression. The deviation (diffusion) of points and ellipse parameters (center, the length of semi axis, the angle of main axis) can be extracted from the SVD.

3 Measurement and Evaluation of Results

Measurement, analysis and evaluation were prepared and realized with minimal rpm of the CNC machine spindle. An example of the laser beam traces evaluation of the camera 42 sensor (in retracted and extended states) is shown in Fig. 4. One pixel is 2.2 μm. Measured points, fitted ellipses as well as their major axes indicating the ellipses centers are drawn. Calculation were carried out from 620 points (images of each camera) measured at approximately 5 rpm of spindle. It is evident that a small displacement occurred even in the horizontal direction. The overall spindle lopping evaluation with 50 kg load from 0 to 800 mm extension is displayed in Fig. 5.

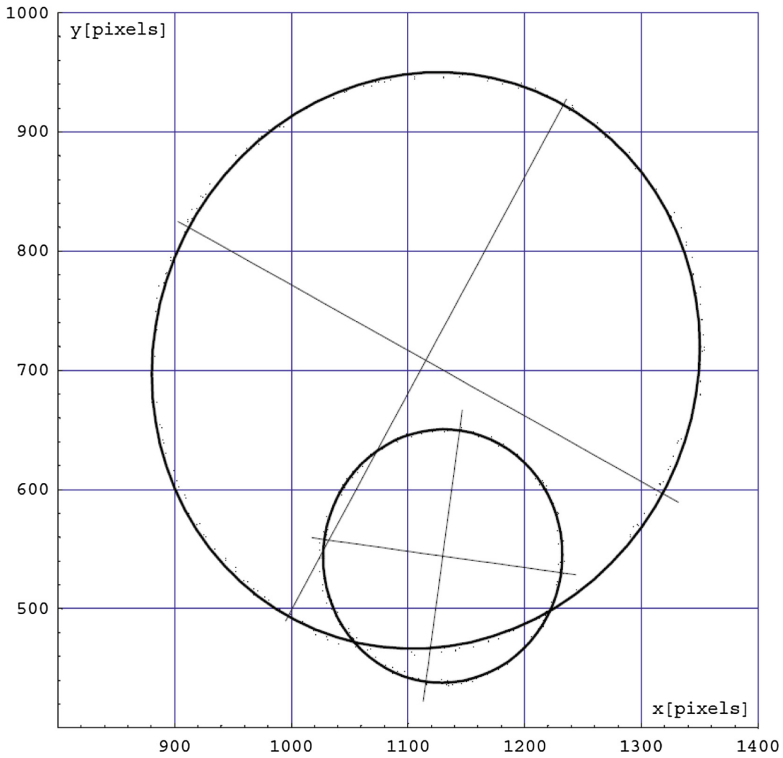

Fig. 4 Example (zoom) of laser beam trace at camera 42 sensor. *Large ellipse* corresponds to retracted state, *small ellipse* corresponds to extended state of spindle. Ellipses major axes are drawn

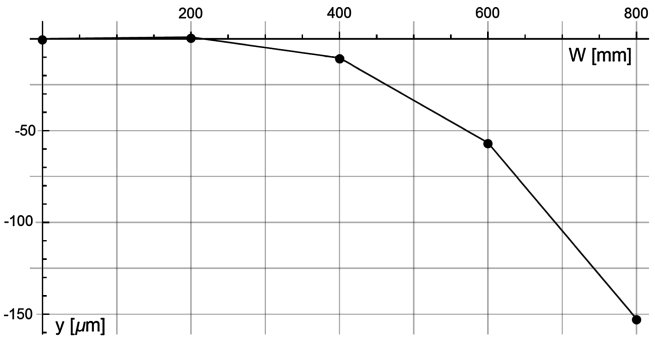

Fig. 5 Spindle lopping versus extension for 50 kg load

4 Conclusions

New method of contactless measurement and analysis of CNC machine spindle lopping was tested on a real machine. Crucial factor for precise and accurate measurement and analysis is sufficient quality of laser beam and necessary quality optics of the sensor box with cameras. It is also important to set the camera exposure time adequately to the spindle extension. It is equally important to eliminate distortions and process of laser beam trace on camera sensor by software, where opportunities for improvement are still open. The described method also allows an inverse way of measurement, e.g. a table machine with attached sensor box is moving (sliding) instead of the spindle. However, the performed measurements and analyses show applicability and usefulness the new methods of measurement and analyses in practice. The form and application of the new measurement method is protected by patent [3].

Acknowledgments The research work reported here was made possible by the Czech Ministry of Education, Youth and Sports, project LO1213.

References

1. Česká technická norma ČSN ISO 230-1, 20 0300, Test code for machine tools—Part 1: Geometric accuracy of machines operating under no-load or quasi-static conditions, ISO 230-1:2012, ÚNMZ, (2014)
2. Richter, A., Vencl, T., Škop, P., Braier, Z., Žďárek, P.: Modulová řada vřeteníkových jednotek obráběcích strojů nové generace. Program TIP, ev. no. of project FR TI4-182, Zpráva o řešení k 17.8.2015 v rámci projektu TIP, report no. AUT-01/2015, VÚTS, a. s. (2015)
3. Patent CZ305542 (B6): Šidlof, P., Škop, P.: Method of determining lopping and/or lopping characteristic and/or determining angle of incline and/or incline characteristic of horizontal or skew spindle, especially machine tool horizontal or skew spindle, and pick-up device for making the same, VÚTS, a.s., publication info 25 Nov 2015

Smart Rehabilitation Splint

J. Cernohorsky and M. Cadek

Abstract In the scientific papers there are various mechatronic devices, with smart sensors, biofeedback systems and high end components. These system are mostly designed like replacement after amputation. The second are aim to exoskeleton concept, where the human capability is increased. Our rehabilitation device aim to area of temporary rehabilitation or recondition. The conventional motorized splint has limited possibilities for advance control and typically has no diagnostic functions.

Keywords Splint · Rehabilitation · Knee · Motion control

1 Introduction

The rehabilitation process is very important process, with two basic aspects. At first, the return of the post traumatic patient to active life, which have financial aspects for him as well as for the society and psychical aspect, that active movement and physical load produce endorphins that help patient to be motivated and also influence him and his surroundings.

The conventional physiotherapeutic care is irreparable, in one hand, because physical contact and human care also helps the patient psychical mood at the other the skilled personnel use own perception system and own muscular system to use proper forces and movement limits according to actual possibilities of the patient. The mechatronics systems in rehabilitation are more and more popular nowadays; the motivation is mainly physiotherapist overload and independent validation of rehabilitation progress.

J. Cernohorsky (✉) · M. Cadek
Technical University of Liberec, Liberec, Czech Republic
e-mail: josef.cernohorsky@tul.cz

M. Cadek
e-mail: milos.cadek@tul.cz

J. Beran et al. (eds.), *Advances in Mechanism Design II*,
Mechanisms and Machine Science 44, DOI 10.1007/978-3-319-44087-3_50

2 The Anatomy and Modelling of Knee Joint

The knee is the biggest joint in human body with quite complicated anatomical structure, include bones, cartilages, muscles and ligament, skin and other structures. There are tree bones are femur, tibia and patella (Fig. 1).

This joint can be segmented into femorotibial and femorpaterlar part. The femorotibial jon hase medial and lateral part with meniscus divided to femor-omenikal and meniskotibial part.

In the literature there are many models of joints generally and knee joints as well. The releology model is one of used and this model is easy to understand to people with technical knowledge, because it is based on terms like stress, stench, viscosity, plasticity and deformation. This description has usually time varying parameters, therefore the overall description is more difficult to e.g. metallic material description [2].

The knee joint is one of the most loaded joint in human body. The flat ground walking is described in many papers, the load depends a little on movement stereotype [3].

The phases of the motion can be described by diagram. The motion start with heel strike (HS), than slide flexion to reduce the shock during impact to floor up to maximum stance flexion MSF, and then extension to maximum stance extension MSE. In this part of the motion the most of the torque is applied. After this phase, the two "passive" phases are followed which moves leg to start position to next heel strike to start new cycle. These swings operates with leg mass, not with human body mass, therefore the torque are lower. This description is suitable only for flat surface, in case of stairs or even knee bend exercise is load much higher then Fig. 2. The next problem is in locomotion speed, where dynamic of movement influence overall energy.

The movement stereotype are slightly different person to person too, but overall gait cycle description in general is well known. In our further design we focus to rehabilitation device, the highest demands are similar or lower to regular flat gait.

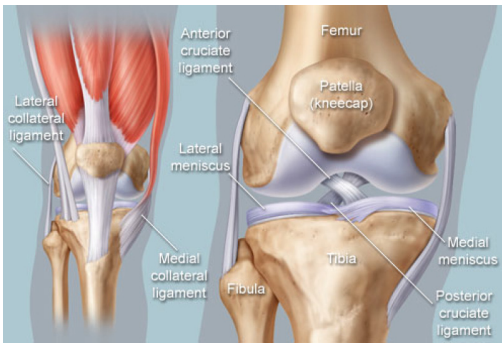

Fig. 1 Skeletal and musculovascular description of knee joint [1]

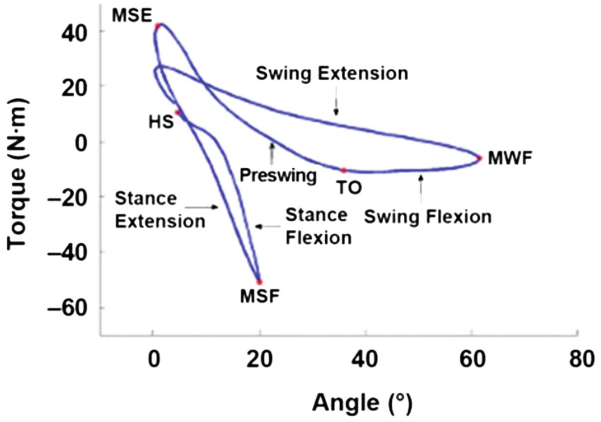

Fig. 2 Motion diagram of one step [3]

3 Rehabilitation Devices

The post traumatic therapy is very important phase in healing, there are two general goals, to increase the limited movement abbilitity to pre traumatic state. The bending limits are extended in proper way, e.g. the people can place the leg to next stair. The second goal is enhance the performance of the joint, where pretraumatic limits are reached at least with little limitation, e.g. the people is able to move the mass to healed leg and go up-stairs without help. The dynamic movement, running, volleyball spikes are really long term processes. The combine injury with neural system illness is a problem, the special devices combine locomotion and functional electrostimulation is applied. The multichannel electro stimulators are capable to emulate electrical signal in channels to create the step forward. In our case we focused to simple mechatronic device, which can helps with rehabilitation and measure the progress of exercises.

There are several types of exoskeletons on the market, which are worth to mention. For instance ReWalk, which is wearable robotic exoskeleton, which belongs between untethered, active, lower-body exoskeletons. ReWalk is licensed by the FDA in the USA, it has CE mark and it is licensed in Canada. This exoskeleton has motors at knee and hip joints and it's designed for people suffering from spinal cord injury. Suit should enable people with this kind of injury to stand, turn around, walk and even run or climb stairs. Unfortunately the climb stairs function is not currently available in the US. ReWalk offers two versions of exoskeleton, personal for use at home and rehabilitation for use at specialized ReWalk clinics. Both devices are controlled by remote wrist-worn control (Fig. 3).

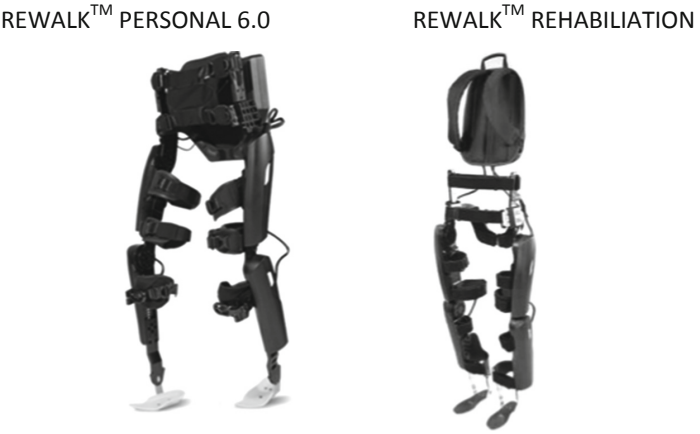

Fig. 3 ReWalk exoskeletons [4]

4 Design of Rehabilitation Splint

The key element of rehabilitation splint is electric motor. We have selected Maxon motor ECDC flat motor. This motor has high moment of inertia to other non-flat motors, but low profile, with is important for mechanical design. The output torque is about 0.5 Nm and speed less than 3000 RPM. The motor is equipped with harmonic gearbox with ratio 100. It means, that we are able to fulfill the load during gait cycle with one motor. The encoder system is built-in and has 3600 puls/turn resolution. The motor controller is Maxon Epos 2, that is not programmable motion controller, but there is option to control the drive via CANopen. The main control system can be arrange like PC based system or industrial controller. We have used the entry level PLC made X20CP1380. The main benefit of this system is low power consumption and wide spread of input and output modules.

In our first design of rehabilitation splint we assume to use two motors, each from one side of the splint and use drives without gearboxes for low torque rehabilitation. In current version with gearbox we suppose to use only one drive for knee, node id2, the second motor node id3 will be implemented for hip joint.

Mechanical design depends on the type of the device. Currently, there are two types of exoskeleton like devices being developed. Both are designated for rehabilitation, both are untethered and for the lower-body. First has two EC flat motor concentric with a knee joint. Second has one motor, which is located on the outside of a knee joint. Another motor is located at the hip joint. Work on the second kind of design is still in progress and it's not part of this paper. Both designs uses Maxon EC flat motors combined with Maxon harmonic gearboxes. Such harmonic drives and motors allows the design to be light and compact with appropriate dynamics.

Fig. 4 Robotic orthosis composite and metallic variant

There are currently two pre-designs of wearable robotic orthoses with two motors being concentric at the knee joint. Design of orthosis (Fig. 4 left) is based on composite materials, such as carbon fiber, which could be shaped to achieve ergonomic surfaces as on the CAD model below. Another advantage of such materials is indisputably strength/weight ratio, which could be very high compared to metallic materials. The alternative solution (Fig. 4 right) is based on cheaper metallic materials and cheaper manufacturing process.

The final version of the design is modular, which means that modules with gearbox and motor can be easily replaced by joint with bearing. The orthosis can be easily adjusted for left or right leg and the motor is on outer side of the orthosis. The configuration of positive motion and other adjustment is made in configuration menu.

5 Control of Rehabilitation Splint

The control algorithm has several operation modes. The first of them is simple passive mode. The splint is fixed to patient knee and after that the patient and physiotherapist set motion limits, the maximal flexion and extension. The limit values are displayed in HMI interface and can be freely modified.

The next operation mode is conventional motorized splint mode, where number of cycles is set. The velocity and acceleration of this motion can be adjusted according to patient feeling. The special feature is the continual torque measurement, where e.g. spasm can be detected.

The other operation mode is the releology diagnostic mode, where the load is applied to patient leg and the output data are torque characteristic of the knee.

This characteristic has hysteresis shape and the hysteresis can be used for performance description.

The multi task system is one feature of used PLC system, however in our case we use only two task. One for drive control via CANopen thru PDO objects. The

basic configuration via SDO object is made in special program this program is in longer task. The visualization realized in 400 ms task class. The response of the visualization interface in not very impressive thanks to low computing power of PLC, where the visualization is processed in idle time. The key communication interface is CANopen. The Maxon Epos and used Maxon Epos2 used CANopen, Epos3 is EtherCAT based. The CANopen communication is quite simple and thanks to process data object are important data cyclically updated. The PDO configuration can be made inside Automation Studio.

6 Conclusion

The control software uses position control and torque diagnostic is made, the mechanical design is made in two variants. The manufacturing process in now in progress. The overall concept is validated in no load operation. In the future must there must be designed the battery pack and model is ready for higher model predictive control to utilize the orthosis to actual motion stereotype, walk, stairs and run.

Acknowledgments The results of this project were obtained through the financial support of the Ministry of Education, Youth and Sports in the framework of the targeted support of the "National Programme for Sustainability I LO1201" and the OPR&DI project "Centre for Nanomaterials, Advanced Technologies and Innovation CZ.1.05/2.1.00/01.0005".

References

1. The knee joint [online]: Jointace C2 [cit. 2016-02-28]. Available from:http://jointacec2.com/the-knee-joint/
2. Martinez-Villalpando, E.C., Herr, H.: Agonist-antagonist active knee protehesis: a preliminary study in level–ground walking. J. Rehabil. Res. Dev. **46**, 361 (2009)
3. Sifta P, Bittner V.: Measurement of reologic properties of soft tissue (muscle tissue) by device called myotonometer. In: 6th World Congress of Biomechanics (WCB 2010), vol. 31, p. 1020 (2010) WOS:0003067161100260
4. ReWalk 6.0 [online]: © 2016 ReWalk Robotics [cit. 2016-02-28]. Available from:http://rewalk.com/

Implementation of Specific Displacement Diagrams for the Control of Kinetic Sculptures with Yaskawa Electronic Cams

P. Dostrašil

Abstract Electronic cams are used for different manufacturing systems, but in terms of displacement diagrams, they have common characteristics. The emphasis is usually placed on maximum accuracy, the machine cycle time and the displacement diagram has a simple shape. This paper addresses a completely different case, which shows that the use of electronic cams is very diverse. A Yaskawa's electronic cam was used to control the kinetic art sculptures. It was necessary to develop an implementation that will be able to accommodate a large number of very long and complex displacement diagrams. Sculptures contained up to 150 interpolating axes and their programs took up to half an hour. The proposal builds on the basic animation and designer's demands, but it must comply with all limits of the mechanism (maximum speed, torque, etc.). The classic electronic cam uses a data table and interpolation function. This approach has been replaced with a new feature that composes the movement from polynomial of the 5th order. For this purpose, it was developed an independent software tool. The final displacement diagram is composed by defining the 0th, 1st, and 2nd derivatives at the key points. This method of design has proved to be very effective, and in addition, this implementation brought a significant saving of memory and reducing of computational complexity.

Keywords Electronic cam · Displacement diagram · Polynomial function

1 Introduction

For production systems, displacement diagrams are usually supplied by the contracting authority or generated by specialized software tools (in VÚTS, we use our own tools KINZ and KINZ2 [1]). Displacement diagrams (Fig. 1) can be composed

P. Dostrašil (✉)
VÚTS a.s., Liberec, Czech Republic
e-mail: pavel.dostrasil@vuts.cz

J. Beran et al. (eds.), *Advances in Mechanism Design II*,
Mechanisms and Machine Science 44, DOI 10.1007/978-3-319-44087-3_51

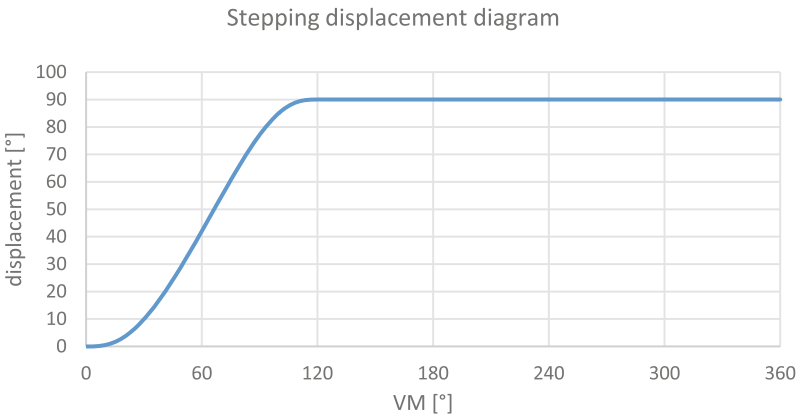

Fig. 1 Displacement diagram used e.g. for rotary table

from different functions (higher order polynomials, trigonometric functions, exponential, and combinations thereof). In the PLC (Programmable Logic Controller), data are stored in a table where the first column contains the coordinates of independent variables, i.e. the virtual master (hereinafter referred to as VM). The second column represents rotation of the output shaft of the motor. The next columns contain higher derivatives which are used to improve the regulatory process. A step of the VM can be constant or variable.

In the system of Yaskawa electronic cam, it is for proper operation necessary to know the values of displacement for any rotation of VM. It uses the internal FGN function that implements binary search in the field of input data and then linear interpolation between the nearest points.

Based on the contract for the controlling of kinetic sculpture [3], it was necessary to revise the above approach. Displacement diagrams were supplied in the form of data, but it cannot be directly used for the electronic cam. Data were created in graphic software tools, so they did not apply continuity of higher derivatives (velocity and acceleration) and they did not take into account the physical limits of the mechanism (maximum speed, etc.). In total, there were up to 75 servo motors controlled by one PLC and the whole scene lasted nearly half an hour. The approach used for production machinery would exceed the computational and memory capabilities of the PLC.

2 Division on Polynomials

The displacement diagram was divided into sections which were replaced with individual functions. As a general replacement, it was chosen to the 5th degree polynomial. The function is determined by conventional notation [2].

$$y = c_5x^5 + c_4x^4 + c_3x^3 + c_2x^2 + c_1x + c_0 \tag{1}$$

For implementation in the control system, it is used notation according to Horner scheme.

$$y = ((((c_5x + c_4)x + c_3)x + c_2)x + c_1)x + c_0 \tag{2}$$

This implementation guarantees the most effective method of calculation. It used only 5 additions and 5 multiplications, the computational complexity in the control system is lower than, for example, calculation of the sine function.

The 5th degree polynomial can also be very intuitive and easy to define using the boundary conditions. Practically, it is about to enter the 0th, 1st and 2nd derivatives at the endpoints. Sharing these points between the adjacent functions ensures the continuous shape resulting displacement diagram, including the first two derivatives. Calculation of individual coefficients using the boundary conditions is demonstrated by the following relations (3) to (8), where boundary points are labeled 0 and 1.

$$c_0 = y(0) \tag{3}$$

$$c_1 = y(0)' \tag{4}$$

$$c_2 = \frac{y(0)''}{2} \tag{5}$$

$$c_3 = \frac{1}{2(x(1) - x(0))}\left(20\frac{y(1) - y(0)}{(x(1) - x(0))^2} - 4\frac{2y(1)' + 3y(0)'}{x(1) - x(0)} + y(1)'' - 3y(0)''\right) \tag{6}$$

$$c_4 = \frac{1}{2(x(1) - x(0))^2}\left(-30\frac{y(1) - y(0)}{(x(1) - x(0))^2} + 2\frac{7y(1)' + 8y(0)'}{x(1) - x(0)} - 2y(1)'' + 3y(0)''\right) \tag{7}$$

$$c_5 = \frac{1}{2(x(1) - x(0))^3}\left(12\frac{y(1) - y(0)}{(x(1) - x(0))^2} - 6\frac{y(1)' + y(0)'}{x(1) - x(0)} + y(1)'' - y(0)''\right) \tag{8}$$

A specific example composition of displacement diagrams from two polynomials is shown in Fig. 2, which was captured directly from the applications developed for the design of displacement diagrams.

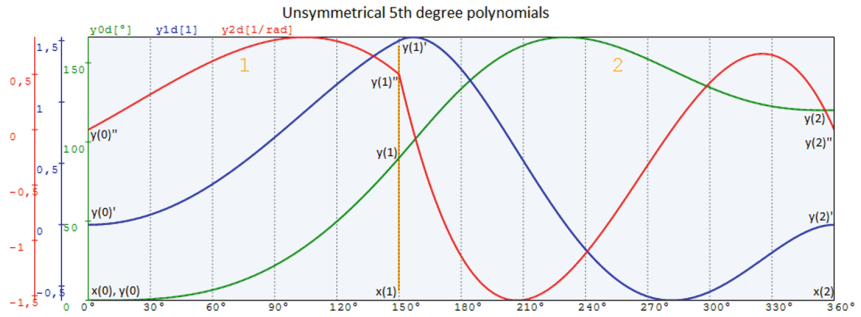

Fig. 2 Creating of displacement diagram by folding polynomials

3 Implementation in the Control System

Based on the data from the customer's animation software, physically realizable displacement diagrams were created by specialized software tools. Curves are usually made up of many functions (in some cases up to 60 functions) of the 5th order polynomial. The software tool also implements a library with a Modbus TCP communication protocol, which allows direct communication with the PLC, as shown in Fig. 3. Displacement diagrams or more precisely parameters of functions are directly transmitted as data frames, stored in a predefined format (see Fig. 4) into the PLC memory. For a definition of one polynomial, there are necessary seven coefficients (x-coordinate of the end point and 6 polynomial coefficients).

The control program in the PLC in the first step (before starting the electronic cam) searches the currently used polynomial by the position of the VM. Subsequently, displacement is calculated according to (2) until the interval of the current polynomial is exceeded. Due to the length of polynomials and the step size of the VM, we can safely assume that we always change no more than one polynomial.

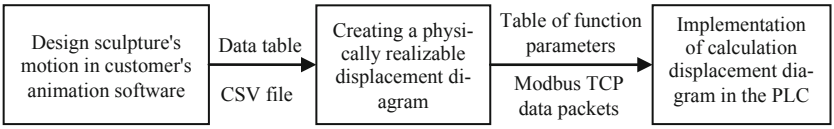

Fig. 3 Data flow diagram in the creating of displacement diagram

Polynomial 0							Polynomial 1							…
x_1	c_{00}	c_{01}	c_{02}	c_{03}	c_{04}	c_{05}	x_2	c_{10}	c_{11}	c_{12}	c_{13}	c_{14}	c_{15}	…

Fig. 4 Transmitted data frame

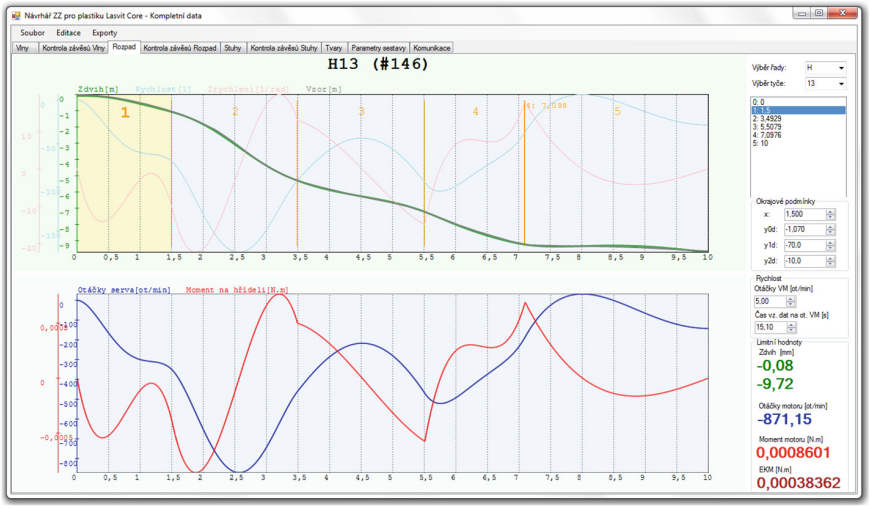

Fig. 5 Practical demonstration creating of displacement diagram (*green* stroke, *blue* motor speed, *red* motor shaft torque) (Color figure online)

Consider the already mentioned situation when we want to control the 75 drives. The displacement diagram has a shape as shown in Fig. 5 and it is replaced by 5 polynomials. If we calculate similar complexity also for other axes, we can estimate the overall memory demands according to the following relation (9) to the 2625 coefficients.

$$\begin{aligned}\text{num. of coeff.} = 7 \times \text{num. of polynomials for displacement diagram} \\ \times \text{num. of controlled axes}\end{aligned} \tag{9}$$

Although the reduction of memory demands is clear, we cannot objectively compare these numbers because it is always an approximation of the original displacement diagrams. Determining when it is a sufficient approximation and when not is always subjective, especially in this case when the aim is the artistic impression rather than accuracy.

4 Conclusion

The realization of kinetic sculptures brought completely new requirements for implementation of displacement diagrams. In place of a simple but strictly defined displacement diagram, it was necessary to effectively implement complex movements whose purpose is not to create a product, but the artistic impression.

At first, the developed method divided the displacement diagram to individual sections which are replaced by the 5th order polynomial. This approximation is sufficient to preserve the character of the movement and also very efficient from a technical perspective. The displacement diagram keeps continuity to the second derivative (acceleration) and its memory and computational requirements are relatively small.

The practical outcome is a graphical software tool for a rapid assembly of a displacement diagram based on data from the customer graphical tool. It also implements a communication library for the direct memory access to control the system of electronic cams which realized calculation of displacement. Everything has been practically applied in the implementation of two kinetic sculptures and is ready for use in other similar systems.

References

1. Dostrašil, P.: Kinetostatic synthesis of stepping mechanism with a classical and electronic cam. Liberec 2014. Dissertation, Technical University of Liberec, Faculty of Mechatronics, Informatics and Interdisciplinary Studies (2014)
2. Koloc, Z., Václavík, M.: Cam Mechanisms, 1st edn. Elsevier, Amsterdam (1993). ISBN 04-449-8664-2
3. Lasvit: Supernova [online]. [cit. 2016-04-06]. http://lasvit.com/bespoke-glass-installations/e-motions/supernova–309/about

Semi-automatic Transmission in a Car

M. Gašparík, M. Černý, P. Šolek and M. Maták

Abstract Automatic clutch may be seen as the latest achievement of the modern times, however this is not always the case. The history of automatic and semi-automatic transmission is as extensive as the history of the car itself. Nowadays there are many different solutions for clutch control in cars with manual transmission. The clutch control system described in this paper is particularly unique with very specific properties. There is a similar device to the aforementioned which allows automatic control of the clutch pedal and is mainly used for physically disabled drivers. However, this concept has never been selected for mass production. Electro-hydraulic cylinder will be connected to the original hydraulic clutch system without impairing its functionality. This will enable the driver to select the mode in between the conventional pedal clutch control and an automatic intelligent clutch control. This article discusses the different measurement methods of input parameters of the control system and different ways of controlling the clutch mechanism. The first part of the article is focused on measurement of the force applied directly to the gear shift stick when shifting gears manually. The subsequent parts will address the measurement of the gear shift stick position, measuring chain principle, processing of the measured values and the design of a control unit for controlling the clutch mechanism.

Keywords Clutch · Gearbox · Clutch control · Strain gauge · Accelerometer · Electro-hydraulic cylinder · Measuring chain

M. Gašparík (✉) · M. Černý · P. Šolek · M. Maták
Technical University of Bratislava, Bratislava, Slovak Republic
e-mail: marek.gasparik@stuba.sk

M. Černý
e-mail: michal.cerny@stuba.sk

P. Šolek
e-mail: peter.solek@stuba.sk

M. Maták
e-mail: marek.matak@stuba.sk

J. Beran et al. (eds.), *Advances in Mechanism Design II*,
Mechanisms and Machine Science 44, DOI 10.1007/978-3-319-44087-3_52

1 Introduction

Automatic clutches may seem to be a product of modern times, however this is not always the case. History of automatic clutches is as wide as history of automobiles itself. Some of the car manufacturers are moving not only towards automatic gearboxes but also towards cheaper versions called sequential gearboxes. These are ordinary manual gearboxes. The only difference is that moves such as controlling the clutch stick or mechanical clutch are not controlled by humans and are instead controlled by the control unit with electric motors. This idea of controlling the manual clutch is used by a number of companies. Those companies are making and installing the equipment into the cars with manual clutches in order to make cheap cars available for people with physical disabilities.

Following the aforementioned content about devices allowing the automatic control over the clutch pedal in cars for people with physical disabilities, this article will discuss the different measurement methods for the control systems and clutch mechanisms [1].

Nowadays there are many solutions out there to operate clutch in a vehicle with manual gearbox. Clutch control system mentioned in this article is unique with specific properties. Figure 1 shows the connection between electro-hydraulic cylinder and original hydraulic clutch system without overriding its functionality. This gives the driver the ability to choose between control of clutch by using pedal or intelligent clutch control without requiring driver to intervene. The present article is looking at the development of a measuring system, which could estimate and determine the position and force action of controlling gearstick for following control of clutch system. The device will be based on electro-hydraulic cylinder which will be controlling hydraulic clutch system. Control and display panel, measuring system and control unit for processing and operation of the whole process are also critical parts of the system. Block assembly schematics for all required electronic components can be seen on Fig. 2. In the process of collecting experimental data, it is necessary to assemble the measuring chain so that the measured data meet the demands of accuracy and temporal association signal. A metered chain consists of measuring card NI 9215 accompanied with acceleration

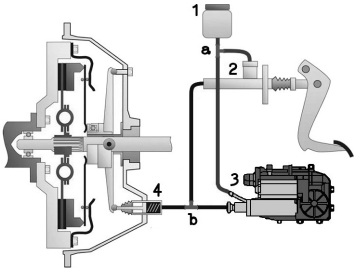

Fig. 1 Hydraulic system. *1* Liquid container, *2* main clutch cylinder, *3* electromechanic clutch cylinder, *4* auxiliary clutch cylinder, *a–b* parallel connection to native system

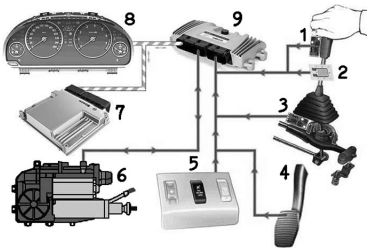

Fig. 2 Electronic system. *1 3* Accelerometer, *2* strain gauges, *4* clutch pedal, *5* controller, *6* electromechanic clutch cylinder, *7* engine control unit, *8* display panel, *9* ECU of clutch system

sensor MMA7361L and unified signal from the strain gauges to measure force. In addition to this, input/output interface for PID controller and program controller itself to control the hydraulic cylinder were also designed [2].

2 Design of Measurement System on a Gear Stick

Physical value is a value defined by physical law. Electric measurement of physical value, in general implements measure chain shown in Fig. 3. Measure chain is based on two separate parts and those are sensor of measured value, which is in direct contact with measured object and device to process electric signal.

2.1 Measuring the Force Exerted on the Gear Stick

Resistive sensor converts the measured value to change the electrical resistance. Its main advantage is the ease of transformation. The electrical resistance increases by the prolongation of the metal wire. Magnitude of the change depends on the geometry size and material properties. This phenomenon is used for resistive strain gauge [3]. Input power on the gear stick is the human hand. It influences many factors when choosing the right method of measuring the power load on the gear stick. The gear stick has seven different positions, causing different values of operating uniaxial strength. The arrangement of the gears of the letter H indicates that it is sufficient to measure the force required for changing gear in one direction.

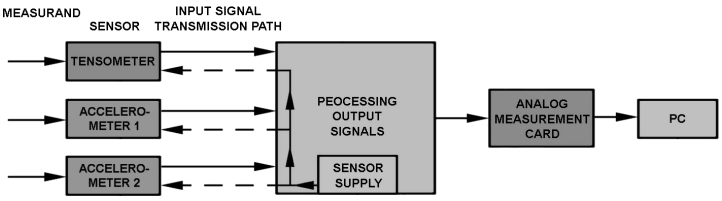

Fig. 3 Block schematics of measuring chain

For measuring on the gear stick, it will be used the special Wheatstone-bridge assembly for measuring the deformation clamped beam. This connection is used for the measurement of small loads. This is a simple cantilevered beam with four strain gauges in which the two are fixed to the upper surface of the beam and two on the lower surface of the beam. All four strain gauges are parallel to the axis of the beam. Given that the change in resistance of strain gauge is very small and therefore it has small change in voltage, voltage signal must be amplified. It is more convenient to measure the change in voltage with differential amplifier. It is possible to use any operational amplifier. To accurately measure it is recommended to use an integrated circuit INA122 displayed in Fig. 4. The advantage of such devices is that they have the necessary components and filter built directly inside the circuit. Small integration ensures little interference from the environment and increases accuracy. In the mentioned circuit, it is simple to alter its amplification with resistor R1 and set offset with resistor splitter R2 and R3. This way, the output signal transforms into a voltage signal between 0 and 5 V, with a median 2.5 V which determines idle state.

Omega strain gauges will be used on the gear stick, which are originally attached to a custom aluminum profile. The principle of operation as well as the measuring member is shown in Fig. 5.

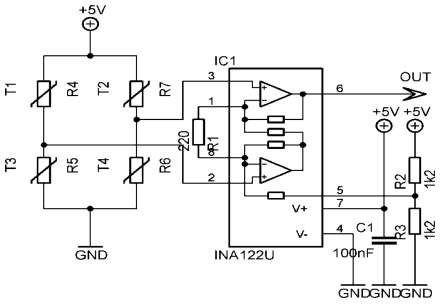

Fig. 4 INA122U circuit schematics

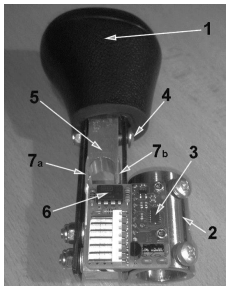

Fig. 5 Test design of measurement system. *1* Force created by operators hand, *2* gear stick attachment, *3* accelerometer, *4* idle state setting screw, *5* crumple element, *6* signal adjustment, *7 a*, *b* strain gauges

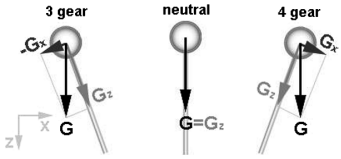

Fig. 6 Graphical view of layout of the gravitation force on gear stick

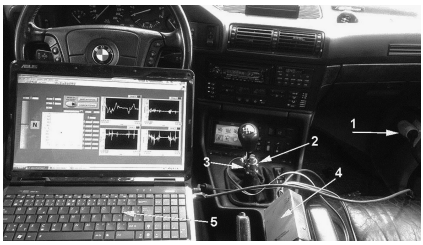

Fig. 7 Description of the measurement chain in practice. *1* Energy source, *2* force and acceleration sensor, *3* signal processing, *4* analog measurement card, *5* PC-data evaluation

2.2 Measuring the Gear Stick Acceleration

For easy determination of the position of the gear stick, two accelerometers are used. Their property of measuring direction of gravitational force in idle state will be used. The first accelerometer is attached to the body of the car and the car will measure acceleration in three axes. The second accelerometer is mounted on the gear stick to measure its acceleration. A simple comparison of the measured values and subsequent subtraction shows precise acceleration of the gearstick in an uneven movement of the car. The gear stick trajectory describes letter H. In the neutral position, the gravitational force is parallel to the axis of the accelerometer and therefore the value of the X and Y axes are zero. In other positions of the gear lever, R, 1, 2, 3, 4, 5, the force of gravity is distributed among the x, y, z axis. Processing and comparison of these values determines exact position of the gear stick by application program. Figure 6 is the visual layout of gravity force in two axes of N, 3 and 4 gears. When the selected gear is 1, 2, 5, R, the power is distributed to the third component y. Figure 7 shows the entire measurement system that is equipped on a gear stick.

2.3 Evaluation Method of Measured Data

The chosen application program for evaluation of measured data is LabView. Given that programing environment is very intuitive, it was easy to experiment with measured data. In order to visibly interpolate the measures, all four analog inputs were adjusted with simple filters [4].

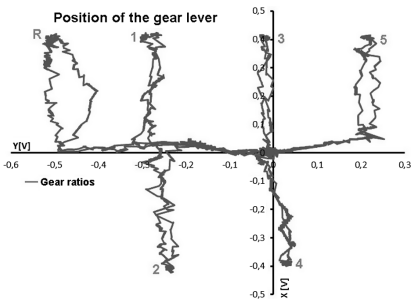

Fig. 8 Gear stick position in the coordinate system x, y

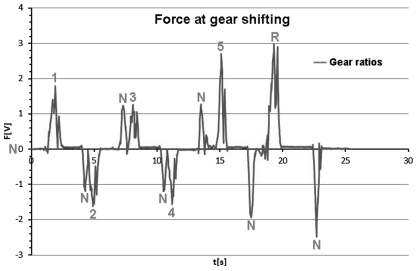

Fig. 9 Graphical illustration of power when shifting gears

Measured data were saved to.txt file, from where the measured characteristics have been drawn. The following graphs—Figs. 8 and 9—are the expected objectives of this measurement. They interpret the force action of a human hand on a gear stick and also gear stick position in gear units.

3 Conclusions

The present article is a contribution towards improved understanding of power interactions when shifting gears in the car. It explains a proposal for design of the measuring system of a device, which is able to measure the effects of power and acceleration of human hand on gear stick in its linear movement. Simultaneously, it critically assesses the numerous issues raised when processing and evaluating the measured data collected from different types of sensors.

References

1. Minh, V.T., Rashid, A.A.: Automatic control of clutches and simulations for parallel hybrid vehicles. Int. J. Aut. Technol. **13**(4), 645–651 (2012)
2. Wang, X., Xie, X., Wu, X., Yu, T.: Precise position tracking control based on adaptive neuron PID algorithm for automatic clutch driven by DC motor. In: IEEE Vehicle Power and Propulsion Conference (VPPC), Harbin, China, 3–5 Sept 2008

3. Klement, J., Plánička, F., Vlk, M.: Modelová podobnosť, elektrická oporová tenzometrie, experimentální určování zbytkový chnapětí, vyhodnocenie xperimentálně získaných dat. Fakulta aplikovaných věd, Plzeň (2004)
4. Klementev, I., Kyška, R.: Elektrické meranie mechani kých veličín. Alfa, Bratislava (1990)

Improvement of Dynamic Characteristics of the Car in the Light of Technological Evolution

F. Palčák

Abstract The Member States of European Union are required to enact the Vibration Directive [4] into national legislation. This paper describes the development of car technology aiming to reduce the impact of unwanted forced vibration on a change of position of the chassis when car is passing over bumpy road. It is about the transition from the preset (passive) mechanical suspension to the adaptive (active) mechatronical suspension. The new breakthrough solution without compromises uses the rules, procedures and tools of the TRIZ approach. Adaptive car provides the best ride comfort and driving safety at the same time.

Keywords Dynamics · Ride comfort · Driving safety · TRIZ approach

1 Effect of Vibration on the Car Driver

Despite constant improvements to passenger and commercial vehicles, the number of accidents caused by driver drowsiness is increasing, even though the requirement for enforced resting time has been complied with. The reason that the driver gets tired while driving and while waiting at the border with the engine idling may also be that the low-frequency forced vibration from the road (below 8 Hz) and high frequency forced vibration of the engine at idle speed (above 20 Hz) acts on him adversely.

If forced vibration were located in the spectrum of natural frequencies of the internal organs (eyes 20–25 Hz, stomach: 3–8 Hz,…), even though the driver is unaware of the internal organs attempt to reduce their amplitudes, a few hours of vibration exposure results in fatigue and a reduction of the driver's attention sufficient enough to cause a crash. The driver is most sensitive to vibration in the band 4–8 Hz, therefore, an essential requirement for car dynamic characteristics in terms of ride comfort is that vibration frequency should be outside this area.

F. Palčák (✉)
Slovak University of Technology, Bratislava, Slovakia
e-mail: frantisek.palcak@stuba.sk

J. Beran et al. (eds.), *Advances in Mechanism Design II*,
Mechanisms and Machine Science 44, DOI 10.1007/978-3-319-44087-3_53

Vertical ride comfort describes the ability of the vehicle to absorb road excitation so, that car body vibration is minimized. The basic evaluation measure for ride comfort criteria in ISO 2631 [1] is the root-mean-square value $RMS(a_w)$ of weighted acceleration a_w:

$$RMS(a_w) = \sqrt{\frac{1}{N}\sum_{1}^{N} a_w^2(n)} \tag{1}$$

where N denotes the total length of the signal of segments n,

$$a_w^2 = \sum_i k_i^2 a_{wi}^2 \tag{2}$$

k_i is the weighting factor for different position

$$a_{wi} = \sqrt{\int_0^{\infty} \phi_i(\omega) d\omega} \tag{3}$$

where

$$\phi_i = C_i^2 W_i^2(\omega) |H_i(\omega)|^2 G_u(\omega) \tag{4}$$

is modified PSD, C is the factor for the stochastic excitation, W_i is frequency weighting function, H_i is the transfer function from the tire patch to the i position and G_u is the power spectral density of the excitation from the road. The accepted ride comfort has a value $RMS(a_w) < 0.315 \left(\mathrm{m/s}^{-2}\right)$ according to British Standard (BS) 6841. In the Fig. 1a the ride comfort is denoted as normalized body acceleration $A = a_w/g$.

Driving safety, denoted on Fig. 1b as $B = F_{zD}/F_{zS}$, depends on the normalized tire load variation is F_{zD}/F_{zS}, where F_{zD} is dynamic normal tire force, and F_{zS} is static tire force. The normal tire force F_{zD} is calculated using the formula:

$$F_{zD} = m_{wh} g + c\left(l_f \varphi_y - u_z\right) + d\left(l_f \dot{\varphi}_y - \dot{u}_z\right) \tag{5}$$

where m_{wh} is the wheel mass, g is the acceleration of gravity, l_f is the distance from the center of mass to the front axle, c is the suspension spring constant, and d is the suspension damping constant, u_z, resp. $\dot{u}_z$ is the vertical displacement, resp. velocity of the center of gravity of the car body, φ_y is pitch angle and $\dot{\varphi}_y$ is pitch angular velocity (Figs. 2, 3, 4 and 5).

The driver is most sensitive in the bandwidth 1–2 Hz (eigenfrequency of car body-sprung mass) and about 6–8 Hz (eigenfrequency of wheel suspension-unsprung mass), so this low ride comfort is in contradiction with high

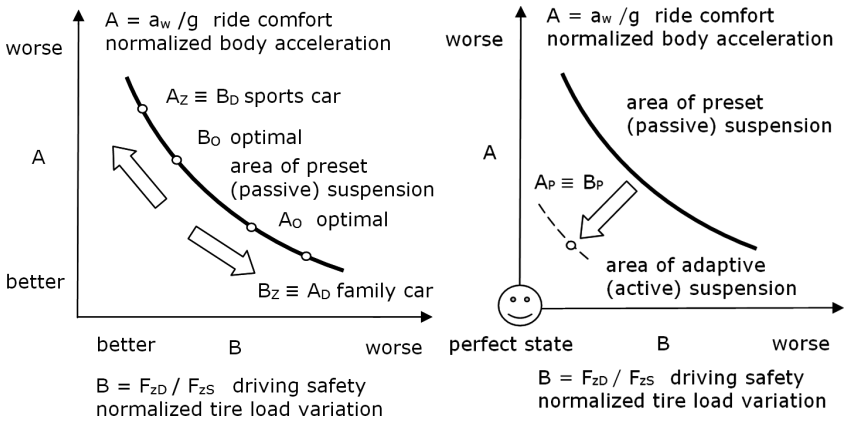

Fig. 1 Target conflict between ride comfort A and driving safety B for **a** passive suspension, and for **b** active suspension

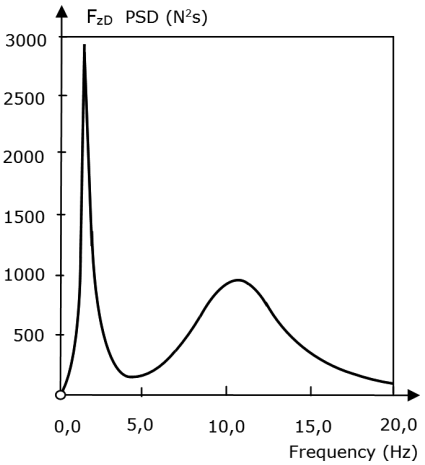

Fig. 2 PSD of the normalized tire load

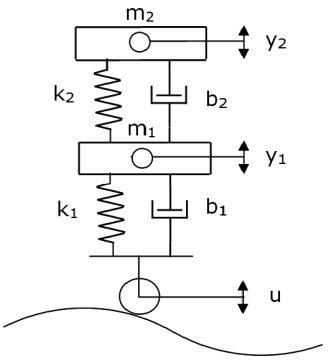

Fig. 3 The two mass passive suspension

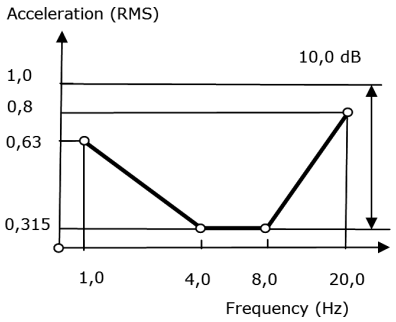

Fig. 4 Vertical vibration exposure curve

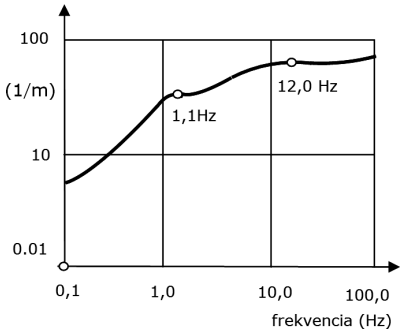

Fig. 5 Car frequency response function

driving safety due to the highest values of PSD of normal tire force [2]. Peaks in frequency response PSD of normal tire force are unwanted, because they cause discomfort to the driver. The damping of the main shock-absorber has the main influence on the ride comfort (70 %), while for driving safety the tire stiffness is actually the most sensitive parameter (70 %) [3].

Vehicle suspension system performance is typically rated by its ability to provide improved road handling (driving safety) and improved passenger ride comfort. The fixed setting of passive suspension properties is always a compromise between ride comfort and driving safety for given road conditions on the one hand and payload suspension parameters on the other. When developers attempt to improve car driving comfort (A) so that no sudden changes in the position of the car body (under minimum acceleration), this deteriorate driving safety (B) in the form of undesirable jumps of the wheels. Thus arose the concept of family car that has good ride comfort (A_D) on Fig. 1a, but bad driving safety (B_Z) and sports car that has good driving safety (B_D), because it maintains the wheels in constant contact with the road (without jumps), but it has poor ride comfort (A_Z).

The only possible solution for improving the dynamic properties of a car has long been regarded the optimization, but it results in compromise: either optimal family car (A_O), or optimal sports car (B_O). The main objective of suspension systems is to reduce movement of the car body (sprung mass). Then the challenge for breakthrough perfectioning of driving performance of a car is to overcome the

contradiction (opposing ride comfort and driving safety) and to achieve the best possible ride comfort and driving safety ($A_P \equiv B_P$) in Fig. 1b simultaneously.

2 Laws and Procedures of the TRIZ Approach

The acronym TRIZ means Theory of the resolution of invention-related tasks. Altshuller developed the TRIZ approach after study of patterns of invention in the global patent literature [4], and today a lot of problem-solving, analysis and forecasting tools is derived from it. An important mission of the TRIZ approach is to reveal patterns of evolution expressed on the Law of least action. Thus, everything in nature has an innate desire to get as close to the unreachable goal, which is perfect efficiency as a result of perfect purposefulness and perfect economy (Fig. 6). TRIZ approach allows to drive the problem solving process with higher effectiveness and efficiency, because of its logic oriented towards the overcoming of conflicts rather than accepting trade-offs among requirements. In the TRIZ approach the essence of the generic steps (need, benefits, procedure, and use) for systematic perfection of creations is to recognize and remove contradictions:

- The managerial-administrative contradiction on the level of intention for a change: the director will invite developers to enhance the driving characteristics of the car to be successful in the market. This is contradiction between the requirements to improve the car and the absence of the conditions to do so (need to identify the targets, acquire knowledge of the process and ensure proper resources). The principle for overcoming the managerial-administrative contradiction is to seek out and remove the global-technical contradiction.
- The global-technical contradiction on the system level of creation is the conflicting relationship between the features of the parts of the whole creation when improving one part (driving comfort A on the level of car body) worsens

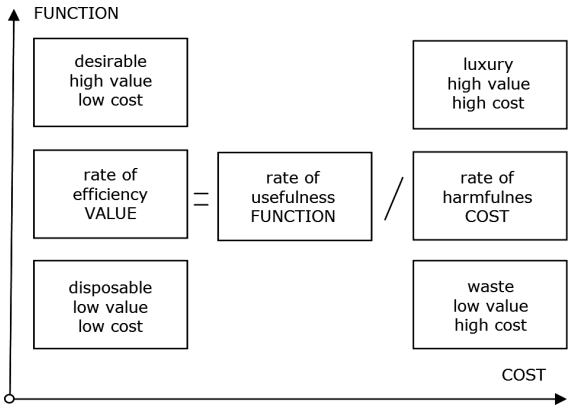

Fig. 6 The value of creations is a measure of cost effectiveness for the fulfillment of their function

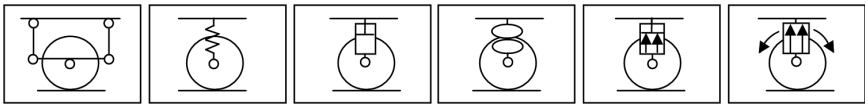

Fig. 7 The individual steps for breakthrough improvement of car suspension

the second part (driving safety B on the level of wheel). The overall principle for overcoming global contradiction is to search and remove the local-physical contradiction when one part satisfies conflicting properties simultaneously.

– The local-physical contradiction on the single part level: the suspension of the car body has to ensure zero change in the force transmitted to the car body for its desirable zero heave, and at the same time to ensure non-zero change in the force which pushes the wheel onto the road. Then the car provides the best possible ride comfort and driving safety ($A_P \equiv B_P$) on Fig. 1b simultaneously.

An expert on cars, who works without knowledge of the TRIZ approach, uses only his area of knowledge, therefore he tries to remove a local conflict through new resources (additional equipment to produce force). The result is of high value but high costs (Fig. 6) Magic Body Control system [5] with a camera which scans irregularities of the road ahead. Then the Active Body Control system uses a hydraulic piston to act on each steel coil spring to quickly and independently adjust the suspension on each wheel and provide the best possible ride comfort and driving safety ($A_P \equiv B_P$) on Fig. 1b simultaneously. The Master of the TRIZ approach has the mission to guide the car expert how to intentionally search for initiatives in successful patents from all areas of knowledge and warns that the removal of local conflict has to be to take advantage of local resources (drive and braking torque) which makes it possible to achieve high value at low cost (Fig. 6).

Figure 7 shows the transition from preset (passive) features of a mechanical suspension to a hydraulic suspension with self-adaptable change of a magneto rheological fluid properties, to a hydro-pneumatic suspension, to the adaptable (active) suspension with electronic management of features, toward the recent removal of unwanted movements of the car body (vertical heave, yaw, roll and pitch) for desirable ride comfort by quick control of the drive and braking torque acting on the wheel motors (LEAF [6]) and ensuring necessary wheel load simultaneously.

3 Conclusions

The example of the use of the TRIZ approach for improving the dynamic of the car in this paper explains why successful universities and companies have already integrated Computer Aided Innovation (CAI) based on the TRIZ approach into education and research. The benefit of the TRIZ approach is that it leads to the

creation a necessary interdisciplinary overview, and to better systemization and exploitation of existing knowledge. The cooperation of company experts with Masters of the TRIZ approach results in a breakthrough and patentable innovations.

Acknowledgments This work was written within the objectives of the Civic Association TRIZ SK (www.triz.sk) thanks to the support of the company SOVA Digital, Inc., Bratislava.

References

1. Mechanical vibration and shock—evaluation of human exposure to whole-body vibration—Part 1: general requirements, ISO 2631, Directive EU 2002/44/EC—vibration (1997)
2. Strandemar, K.: On Objective Measures for Ride Comfort Evaluation, Royal Institute of Technology (KTH), ISSN 1404-2150, Sweden (2005)
3. Kvasnička, P., Palčák, F.: Optimization of the suspension damper on a quarter car model using ride comfort criteria in a multiobjective function, Strojnícky čas. **55**(2), 15 (2004)
4. Altshuller, G.S.: 40 Principles: TRIZ Keys to Technical Innovation. Translated by Lev Shulyak, Technical Innovation Center, Worcester, MA (1998)
5. http://www.cartrade.com/blog/2015/car-automobile-technology/mercedes-active-body-control-1462.html
6. http://www.nissan-global.com/EN/TECHNOLOGY/OVERVIEW/new_chassis_control.html and http://www.nissan-global.com/EN/NEWS/2016/_STORY/160302-01-e.html (2013)

Rotary Table Machine Input Parameters Optimization

A. Richter and J. Ondrášek

Abstract This paper deals with a mechatronic model of a rotary table machine. An ideal course of movement of the carousel plate during the working cycle is obtained by modification of the input parameters of the servo drive. The simulation also shows power and torque demands and bearing loading.

Keywords Rotary table machine · Mechatronic system · Optimization · Axial cam

1 Introduction

Growing demands on the production efficiency require very fast and precise machines. In our case, a demand for a rotary table machine (Fig. 1.) with an accuracy of 40 μm and a positioning time 0.5 s. Diameter of the table is 1000 mm and total moment of inertia is 100 kg m^2. For such a short positioning time, there is a problem how to determine a proper drive with a suitable control to avoid residual oscillation at the end of the cycle.

The carousel machine serves as a base of a multifunction machine tool. On the carousel plate, 16 beds for clamping workpieces are symmetrically distributed. Within 0.5 s the carousel moves to the exact position (rotation by 22.5°). Then follows a 0.5 s milling period, during which the carousel is stationary. The total cycle of the machine is 1 s. What is important is the positioning accuracy in establishing the plate before machining.

A. Richter (✉) · J. Ondrášek
VÚTS, a.s., Liberec, Czech Republic
e-mail: ales.richter@vuts.cz

J. Ondrášek
e-mail: jiri.ondrasek@vuts.cz

J. Beran et al. (eds.), *Advances in Mechanism Design II*,
Mechanisms and Machine Science 44, DOI 10.1007/978-3-319-44087-3_54

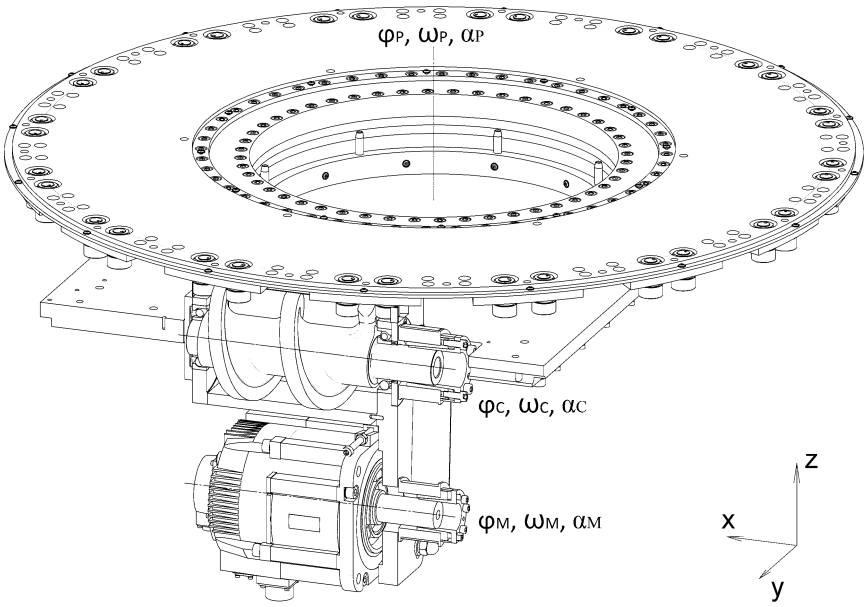

Fig. 1 Model of rotary table machine

2 Design of the Rotary Table Machine

From many design proposals, a variant was chosen that meets the criteria of high precision and short times—a cam mechanism.

The first estimates and calculations were based on the required parameters of the machine combined with the knowledge and experience of the designer with the problem. From the parameters affecting the dynamic properties of the system, the ideal gear and demands on the drive were determined using preliminary (no contact, no elastic links) calculations.

In order to ensure the accuracy of operation and programmable control, a servomotor was chosen. The motor drives the axial cam by a backlash free reduction belt gear. The cam rotates the carousel plate also with a reduction gear. When the theoretical ideal running, the dependencies of rotation (motor, cam, plate) are as follows: $\varphi_M = 1.25\varphi_C = 40\varphi_P$. Angular velocity is ω, acceleration is α (Fig. 1).

The main problem of the design was to correctly calculate and model the axial cam (Fig. 2). For the calculation, relations for the production coordinates [1] were used. The size of the axial cam was determined according to the static load and the stress-strain analysis (outer diameter 140 mm, length 326 mm, diameter of the rollers 30 mm). The resulting data, i.e. the coordinates of the points of the curves *x, y, z* were transferred into the SOLIDWORKS design program and a 3D model of

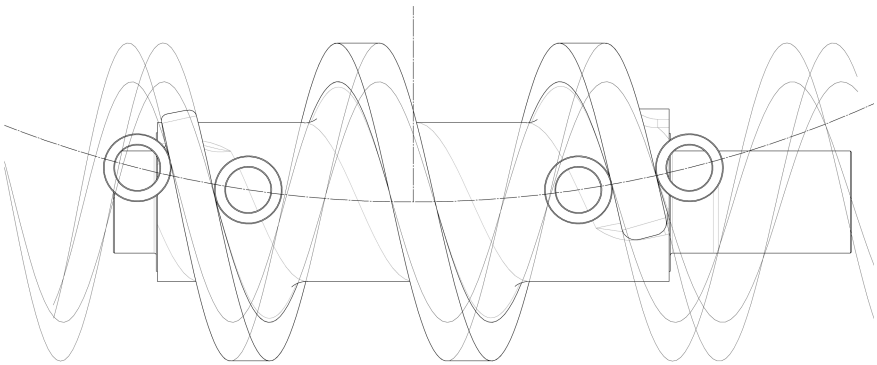

Fig. 2 Cam model, calculated (*grey*), designed (*black*)

the axial cam was modeled, as well as that of the carousel. The entire structure of the carousel machine was sufficiently dimensionally stiffened and strengthened for long durability.

3 Mechatronic Model

When creating a mechatronic model, design data from the SOLIDWORKS program were used and converted into MSC.ADAMS through a neutral format. Static members and assemblies that do not affect the dynamic properties of the system were neglected and excluded from the model. An elastic belt as well as friction in the main bearing were considered in the simulation of the contact between the axial cam and the rollers.

3.1 Mathematical Model of Drive

The scheme of a 3-phase motor comprises 3 identical subsystems whose effect is determined by a relative rotation by an electric angle of $2\pi/3$. The basic voltage equations supplemented by the interaction of the adjacent coils by mutual equally sized inductances M for each winding are, see [2, 3]:

$$\begin{aligned} u_U &= U_{EU} + R_s i_U + L_s \frac{di_U}{dt} + M\left(\frac{di_V}{dt} + \frac{di_W}{dt}\right), \\ u_V &= U_{EV} + R_s i_V + L_s \frac{di_V}{dt} + M\left(\frac{di_U}{dt} + \frac{di_W}{dt}\right), \\ u_W &= U_{EW} + R_s i_W + L_s \frac{di_W}{dt} + M\left(\frac{di_U}{dt} + \frac{di_V}{dt}\right) \end{aligned} \tag{1}$$

where L_s is leakage inductance of the stator winding, i is the current and R_s expresses the resistance of one phase of the stator winding. The Eq. (2) for internal induced voltage $U_{E\upsilon}$ of each coil with respect to the relative position of stator and rotor, which is expressed by an electrical angle θ are:

$$U_{EU} = K_E\omega_0 \sin\theta,\ U_{EV} = K_E\omega_0 \sin\left(\theta + \frac{2}{3}\pi\right),\ U_{EW} = K_E\omega_0 \sin\left(\theta + \frac{4}{3}\pi\right) \quad (2)$$

where K_E is the voltage constant of one coil of the motor and it is the same for all three coils. The relation between the electrical angular velocity ω_0—*rotational speed of magnetic field of the stator* and mechanical angular velocity ω—*rotational speed of the motor rotor* is given by the equation:

$$\omega = \omega_0/p_p \quad (3)$$

in which p_p indicates the number of pole pairs of the electromotor. Electrical angle θ is bound to mechanical angle φ by the number of pole pairs p_p by the equation: $\varphi = \theta/p_p$, which is based on the integration time of the dependence (3) of mechanical speed ω on the angular frequency of supply voltage ω_0. The expression for the resulting electromagnetic torque M_{ElMg} is:

$$M_{ElMg} = K_M\left[i_U \sin\theta + i_V \sin\left(\theta + \frac{2}{3}\pi\right) + i_W \sin\left(\theta + \frac{4}{3}\pi\right)\right], \quad (4)$$

where K_M represents the torque constant of one coil of the motor and it is the same for all three coils. The mathematical model of the synchronous servomotor is defined on the basis of Eqs. (1)–(4).

3.2 Controlled Mechanical System

In the vector control of this electromotor type, the cascade arrangement of the control circuit with three hierarchically arranged feedbacks: current, speed and positional, is almost exclusively used, see Fig. 3. Holding of the required value of position φ^*, angular velocity ω^* and current i^* is ensured by PID linear controllers. The control of the output quantity is done by the sum of the proportional, integral and derivative components of the controller. The relation between the output quantity—*action* (*control*) *quantity* $u(t)$ and the input quantity—*control deviation* $e(t)$ is defined by the equation:

$$u(t) = K\left(e(t) + \frac{1}{T_i}\int_0^t e(\tau)d\tau + T_d\frac{de(t)}{dt}\right),\ \ e(t) = w(t) - y(t). \quad (5)$$

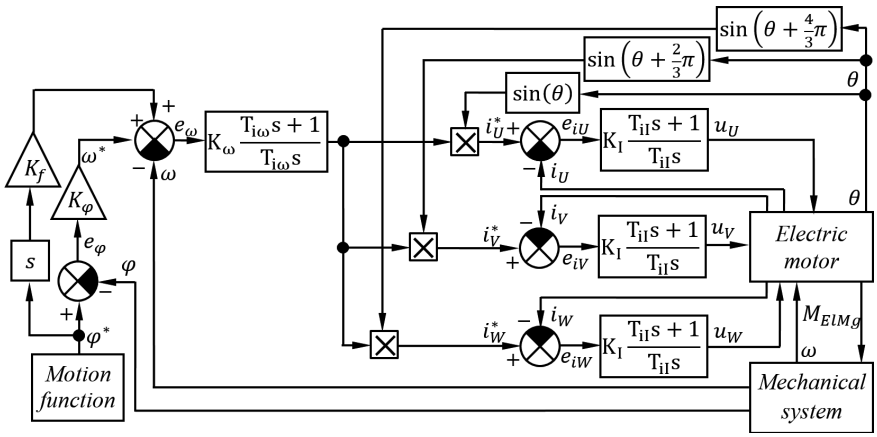

Fig. 3 Block diagram of cascade control loop with controllers

The proportional component of the PID controller is equal to K, the integral one is equal to the ratio K/T_i and the derivative one is equal to the product $K \cdot T_d$. Constant T_i expresses the integral time constant of the controller and T_d the derivative time constant. The control deviation $e(t)$ is given by the difference between the desired quantity $(w(t) \equiv \varphi^*, \omega^*, \mathrm{i}^*)$ and the actual output from the system—*controlled quantity* $(y(t) \equiv \varphi, \omega, \mathrm{i})$.

The Ziegler-Nichols experimental method was used for setting individual constants of the regulators, see, e.g. [4].

4 Input Parameters Optimization

To control the position of rotation of the carousel, the following motion functions were used: cycloidal, parabolic and fifth degree polynomial. Each of the control functions has its advantages and disadvantages. In terms of the smallest demands on starting torque, the best function is parabolic. However, it has the lowest positional accuracy and requires higher engine output. It is preferable to use the fifth degree polynomial. It has the lowest demands on engine performance and enables the carousel positioning most accurately in the given time.

By default, the parameters of the regulator caused a carousel deviation of 0.2 mm from the correct position. It was insufficient. By tuning the proportional component of the PID regulator (i.e. gradually increasing its value), a significantly higher accuracy was achieved, but at the cost of larger oscillations of the system. Eventually, a positional deviation of up to 0.01 mm with acceptable oscillations was attained (Fig. 4).

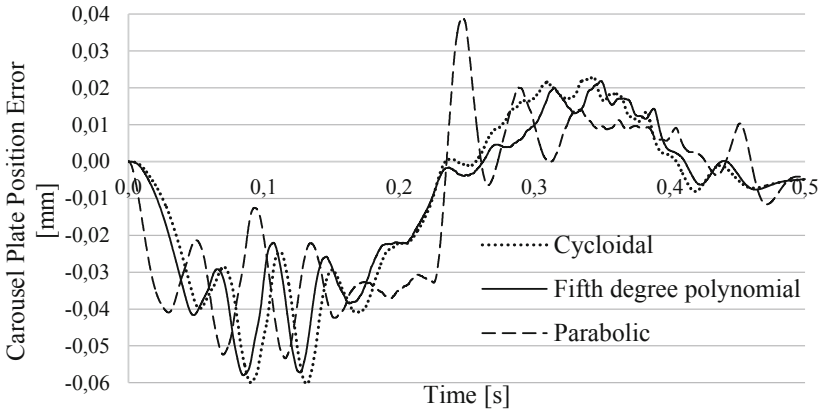

Fig. 4 Carousel plate position error versus time

Table 1 Power parameters of the drive

Control function	Driving torque (Nm)	Input power (kW)
Cycloidal	41	1.9
Fifth degree polynomial	38	1.6
Parabolic	30	2.0

Demands on the maximum torque and drive performance according to the individual starting functions are shown in Table 1. The SGMGV-44A engine from the manufacturer Yaskawa was chosen based on these results [5]. The simulation also showed the load on the bearings. The highest load was 2500 N in the axial direction and 1600 N in the radial direction.

5 Conclusions

A mechatronic model of a carousel machine with its control was created. Due to a proper setting of parameters of the controller and choosing the appropriate control function, the specified requirements for the machine cycle and its accuracy can be met. According to the simulation of required the drive maximum torque and power, a suitable servomotor was chosen. An appropriate bearing was chosen based on the calculated load of the bearings.

References

1. Koloc, Z., Václavík, M.: Cam Mechanisms, Elsevier, ISBN 0-444-98664-2 (1993)
2. Souček, P.: Servomechanismy ve výrobních strojích, Vydavatelství ČVUT, ISBN 80-01-02902-6, Praha
3. Bimal, B.K.: Modern power electronics and AC drives, Prentice-Hall, Inc. ISBN 0-13-016743-6 (2001)
4. Åström, J.K., Murray, M.R.: Feedback Systems: An Introduction for Scientists and Engineers, http://www.cds.caltech.edu/∼murray/FBSwiki
5. https://www.yaskawa.com/pycprd/products/sigma5-servo-products/rotary-servo-motors/sgmgv